CRANFIELD UNIVERSITY

YUN PENG YEH

SURFACE ENGINEERING FOR BIOLOGICAL RECOGNITION

PhD THESIS

Supervisors: Jeremy J. Ramsden
Hsi-Hsin Chien

April 2010

CRANFIELD UNIVERSITY

SCHOOL OF APPLIED SCIENCES

PhD THESIS

Academic Year 2009-2010

YUN-PENG YEH

SURFACE ENGINEERING FOR BIOLOGICAL RECOGNITION

Supervisors: Jeremy J. Ramsden
Hsi-Hsin Chien

April 2010

ABSTRACT

The underlying idea of this thesis is that the surface chemical and morphological nature of bacterial strains uniquely differentiates one from another and hence can be used as the basis for their identification and control. It follows that their interactions with an artificial substratum uniquely characterize them. In principle, potentially it is easier and faster to evaluate the interfacial energy between a bacterium and a substratum than to characterize its genome or determine molecular biomarkers characteristic of the strain, hence validation of this thesis opens the way to rapid screening and diagnosis. Auxiliary to this main idea, an advanced metrology for evaluating the interfacial energies has been developed, exploiting the power of kinetic analysis.

Keywords: identification; interfacial energy; kinetic analysis

ACKNOWLEDGEMENTS

First, I am grateful to my supervisors Professor Jeremy J. Ramsden and Professor Hsi-Hsin Chien who gave me the opportunity to work on this topic and closely followed my progress. I thank them very much for their patience, encouragement and understanding of my difficulties in the course of preparing this thesis. Special thanks to Professor Keng-Jeng Ma and Dr. John Chubb for their help and fruitful advices during my whole study period at Chung Hua and Cranfield Universities.

I would like to acknowledge the grant NSC 095-2917-I-216-001 from the Taiwan National Science Council for part financial support of this research work.

I am very grateful to Dr. Marcello Cacace for his precious help and initial assistance with the bacterial adsorption and many instructive scientific discussions as well as for his kindness and friendship during our evenings of strategy games.

I would like to thank Dr. Robert Horváth for his guidance and very practical help during my experiments. His knowledgeable explanations OWLS theory and practice gave a major impetus to the finalization of this work.

I would like to acknowledge Dr. Sarah Morgan for kindly providing *Escherichia coli* and *Lactobacillus plantarum* as well as guiding me in their cultivation and manipulation and Dr. Kaleem Khosa for providing the organometallic compounds used in the self-assembly experiments.

I am very happy to thank all my friends and colleagues (Megumu, James, Amir, and Farah) for their support and help during my work as well as for the nice time we have spent together inside and outside the lab.

This page would not be completed without mentioning the greatest support I have received from my parents Pu-Wen Yeh and Kuei-Ying Lui and my sisters Jui-Ping Wei and Chia-Jung Yeh, my brothers-in-law Jein-Zhi Wu and Huang-Chin Wu, my neice Peggy Wu and my nephew Da-Kuo Wu. Their presence has helped me to overcome the many hurdles and discouragements encountered during what has been, in many aspects, the hardest time of my life.

LIST OF CONTENTS

LIST OF FIGURES

LIST OF TABLES

LIST OF EQUATIONS

LIST OF STRUCTURES

LIST OF HYPOTHESES

The first two have been formulated at the beginning of the work.

NOTATION

(Principle symbolic, other than those used purely locally)

A	Adlayer
A_c	Cross sectional area of cuvette
A_H	Hamaker constant
A_h	Characteristic frequency of departure attempts
C	Cover medium
D	Diffusion coefficient
G	Free energy
ΔG_a	Free energy of adsorption, calculated from kinetics
$\Delta G^{\mid\mid}$	Free energy per unit area between two parallel planar surfaces
F	High refractive index waveguiding film
F_c	Volumetric flow rate
H	Polarization coefficient
K	Kinematic viscosity
L	Diffraction order
L_c	Length of the bacterium
M	Mass per unit area of adsorbed objects
N	Effective refractive index
$\tilde{N}$	Normalized N
N_0	Initial effective refractive index
$\tilde{N}_{sat}$	Saturation limit effective refractive index
N_A	Avogadro's number
R	Universal gas constant = $k_B N_A$
R_M	Molar refraction
S	Waveguide substrate
S_c	Distance along cuvette
T	Temperature
T_a	Slope
T	Absolute temperature
U	Factor for converting $\tilde{N}$ to b
V	Molar volume
X	Propagation direction of light
a	Area occupied by one bacterium derived from adsorption kinetics
$\bar{a}$	Projected area of one bacterium derived from microscopy
$\tilde{a}$	Orientation factor

b	Number of adsorbed bacteria per unit area
b_{sat}	Saturated number of adsorbed bacteria per unit area
b_w	Number of adsorbed bacteria per unit area remaining after flooding
c	Concentration, number of bacteria per unit volume
d	Layer thickness
k	Free space wavenumber= $2\pi /\lambda$
k_a	Adsorption rate coefficient
k_B	Boltzmann constant
k_d	Desorption rate coefficient
l_0	Equilibrium contact distance
n	Refractive index
r	Equivalent radius of one bacterium
t	Time
u	Fluid velocity relative to the bacterium
v_p	Phase velocity
v	Molecular volume
y	Dimensionless surface potential
z	Distance perpendicular to adsorbing substratum
z_0	Approaching distance when ΔG_{123} equals zero for the first time
α	Coupling angle
β	Propagation constant
ε	Dielectric constant
γ	Surface tension
δ_a	Characteristic adsorption distance
δ_d	Diffusion (hydrodynamic) boundary layer thickness
η	Viscosity
K	Dissociation constant
κ	Debye length $1/\kappa$
ϕ	Available area function
ψ	Electrostatic surface potential
θ	Occupied fraction of surface
θ_J	Surface coverage jamming limit
ζ	Electrophoretic zeta potential
υ	Appropriate attempt frequency
υ_d	Characteristic frequency of departure attempts
Λ	Grating constant
Γ	Dimensionless parameter $N_s\kappa/(4c_{ion})$

Chapter 1 Introduction

Starting point: The unsatisfactory nature of the current technology of bacterial identification.

The natural habitat of most bacteria is at an interface—a solid/liquid or solid/air interface—where in a real, heterogeneous environment they are most likely to survive and proliferate. Hence, the importance and topicality of bacterial adhesion are almost self-evident (for extensive reviews, see (Fletcher, 1996; Yuehuei H. An, 1998; Y.F. Missirlis and Katsikogianni, 2004; Yuehuei H. An and Friedman, 2000)). It is a matter of acute practical interest in hospitals, and wherever surgical operations are carried out. The adsorbent surfaces may be the walls of a ward, textile fibres, surgical instruments, and prosthetic implants. Retention of living bacteria on any of these surfaces may lead to chronic or acute health problems for patients. The adhesion of bacteria to teeth is a preoccupation for the entire population. Biofilm formation by adherent bacteria may impair industrial processes (e.g. (Kolari *et al.*, 2002)). Furthermore, bacterial adhesion (to clay particles, for example) is an essential component of understanding the microbiology of soil ecosystems, which has a technological aspect when bacteria able to metabolize environmental contaminants are artificially introduced into soils for remediation purposes. Bacteria may corrode engineered components (e.g., (Arnold *et al.*, 2004)), degrade building materials, and play an active role in the transformation of rocks and minerals.

Since the dispersal of bacteria in an environment generally takes place through a bulk (three-dimensional) phase (usually air or water), freely floating individual bacteria can be taken as the initial state. The first step in their interaction with a surface is arrival in its immediate vicinity (Figure 1.1), followed by adhesion, which in turn may be followed by the development of a biofilm, in which the bacteria embed themselves in a self-secreted matrix, which offers a great deal of protection from hostile environmental factors, as well as allowing nutrients adequate access to the bacteria.

To understand these processes is crucial to be able to control them. It can generally be supposed that the human agent has no direct control over the bacteria themselves other than through modifying their environment. It is likely to be much more effective to engineer potentially adsorbing surfaces than to control the presence (or absence) of selected chemicals in the bulk environment. Examples of designed surfaces include

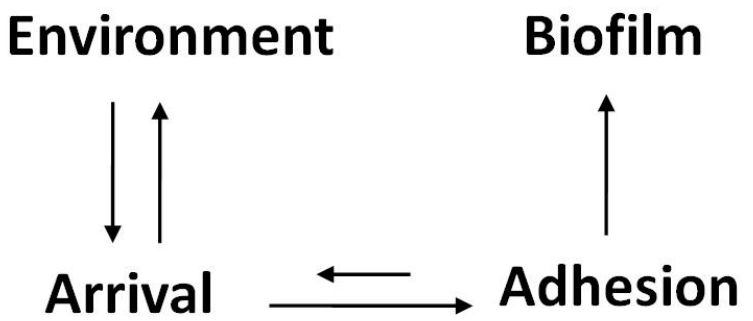

Figure 1.1 Sketch of the stages of bacteria interacting with surfaces. Note that the phenotype changes during passage through these stages. Note too that the successive stages become progressively less reversible.

repellent and bactericidal ones: If the bacteria cannot even arrive at the surface due to mutually repulsive forces, much less can they adhere and form a biofilm (e.g., (Harris *et al.*, 2004)); bactericidal surfaces, designed to kill adherent bacteria, typically work by releasing a toxicant (e.g., (Baveja *et al.*, 2004)), but this carries the risk that the bacteria may be induced to express resistance genes able to neutralize the toxicant, after which they can continue their proliferation without restraint, in the same way that resistance to antibiotics can be overcome. There is also a strong medical interest in the design of surfaces to which certain bacteria are able to selectively adhere. Enabling specific adhesion of bacteria leading to rapid identification would be of immense value for diagnostics.

Nevertheless, conventional bacterial identification methods are based on phenotype identification of microorganisms using cultivation, shape and morphological characterization, Gram staining and biochemical methods. The disadvantages of these methods are: that they can only be used for microbes that can be cultivated in vitro; the difficulties of recognizing the unique chemical characteristics of unknown microorganisms; furthermore, the procedures are complex, labour-dependent and take a long time (typically at least a week).

A more recent development is PCR to amplify the bacterial genome followed by microarray-based DNA identification. This is a molecular-level bacterial identification technique. Microarrays are however still expensive and difficult to design (S. Chumakov *et al.*, 2005), hence useless for the vast majority of bacteria whose genomes have not been sequenced.

The third possibility is to explore strain-specific surface properties. Although there is not much data on this, the evidence for a complex, chemically variegated surface of those bacteria that have been investigated. The hypothesis of this work is that all bacteria have a characteristic surface chemical signature (Hypothesis 1). Evidently binding to biopolymers (protein: antibody; nucleic acid: aptamer; polysaccharide) can be used to recognize bacteria. A possible assay procedure is therefore to coat a substratum sensitive to the presence of bacteria with appropriate biopolymers (Fleminger and Shabtai, 1995; Gfeller *et al.*, 2005; Haake *et al.*, 2000; Howell *et al.*, 2003). The disadvantage is that the most useful biopolymers for this purpose, notably antibodies, are expensive and fragile.

The aim of this thesis is to show that artificial nonbiological nanotextured surfaces can selectively bind diverse bacteria, and hence differential binding can be used as the basis of strain identification. In use, an unknown sample would be exposed to a variety of nanotextured surfaces; those retaining them would be characteristic of the bacteria in the sample. The knowledge acquired through the fulfilment of this aim is also expected to be useful for designing surfaces that deliberately repel or attract bacteria.

The novelty lies in the development of selectively binding nanostructured inorganic materials. A key necessity was the adaptation of a precise nanotechnology technique, OWLS, for measuring bacterial binding. The detection of differential binding to diverse substrata implies the need for such a high-resolution method, which has been previously developed for examining the binding of molecules to surfaces. The quantification of interfacial forces enabled by optical waveguide lightmode spectroscopy (OWLS) is, moreover, essential for arriving at a deeper understanding of the nature of bacterial life, whether benign or pathological, within host animals.

Chapter 2 Literature Review

This chapter reviews the theory of interfacial forces, it discusses how the surface energies can be measured and decomposed into components, it critically summarizes and reviews reported measurements of bacterial surface energies, it relates those energies to the chemistry of the bacterial coat, it examines how the kinetics of attachment and detachment of bacteria to a surface can be predicted from the interfacial interaction energy, and how the kinetics can be measured.

2.1 The interaction of bacteria with substrata

Bacteria are typically regular spheres or spherocylinders a few hundred nanometres in diameter. Assuming that the properties of their surface are uniform, their interaction energy with a planar adsorbent surface can be readily calculated from knowledge of the surface energies of the bacteria and the adsorbent. This model is the basis for the calculation of the interaction free energy $\Delta G(z)$, a typical example of which shown in Figure 2.1.

Since the dispersal of bacteria in an environment generally takes place through a bulk (three-dimensional) phase, freely floating individual bacteria can be taken as the initial state ($z \rightarrow \infty$, Figure 2.1). The first step in their interaction with a substratum is arrival in its immediate vicinity ($z \leq z_a$), and beyond this vicinal region, the potential is typically dominated by the longer-range interactions such as electron donor-acceptor(da) and electrostatic(el) (if the ionic strength is low). They are mostly repulsive since both the bacterium and substratum typically have electron-donating character. At short distances ($z = z_b$), attractive Lifshitz-van der Waals(LW) interactions dominate adhesion, corresponding to the transition point across the repulsive energy peak. This may be followed by the development of a biofilm, in which the bacteria embed themselves in a self-secreted matrix, which offers a great deal of protection from most environmental factors, while still as allowing adequate accessibility of nutrients.[1]

Arrival is encapsulated in Figure 2.1, which reviews the essential energetics of a bacterium approaching a surface. The rate of arrival is governed by the interfacial

[1] For a comprehensive interaction to interfacial force is aqueous media, see van Oss, C. J. (2006).

interaction potential $\Delta G_{123}(z)$, where the subscripts denote the surface, the intervening medium and the bacterium respectively, and z is the surface-bacterium distance.

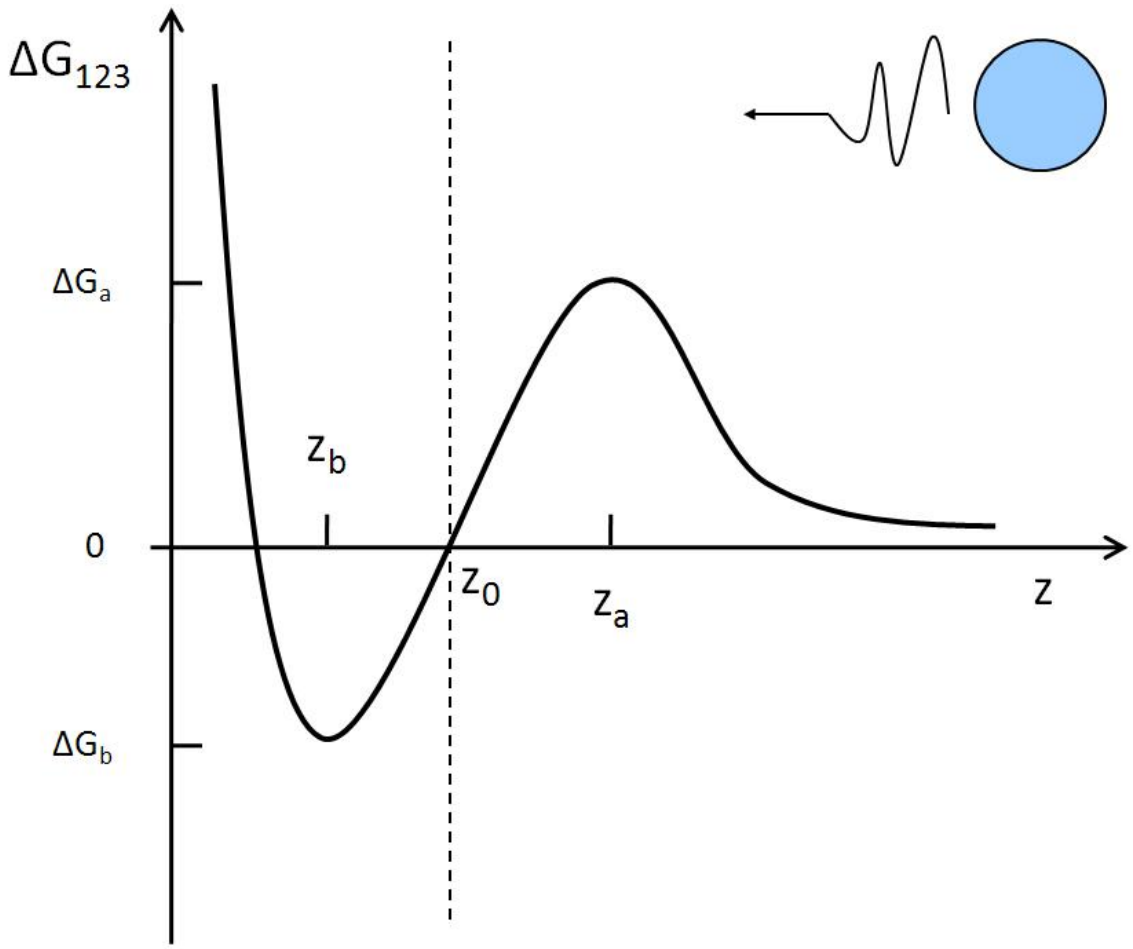

Figure 2.1 The net interfacial interaction potential between a bacterium and a surface, as a function of distance z from the surface. The vertical dashed line separates the "arrival" regime (to the right of the line) from the "adherent" one; adhesion implies that ΔG_{123} becomes negative. z_0 is the value of z at which ΔG_{123} equals zero for the first time when approaching the surface from infinity.

By matching the adsorbing particle concentration distribution near the surface (i.e., under the influence of interaction) with the equation for convective diffusion relevant at a greater distance from the surface, (Spielman and Friedlander, 1974) were able to derive an interaction length as the integral of the interaction potential:

$$\delta_a = \int_{l_0}^{\infty} \left[\exp\left(\frac{\Delta G_{123}(z)}{k_B T} \right) - 1 \right] dz \qquad (2.1)$$

assuming a large Peclet number; for *E.coli*, $Pe = uL_c/D$ (Al-Homoud and Hondzo, 2008), where u is the fluid velocity relative to the bacterium, L_c is the length of the bacterium, and D is the diffusion coefficient of the bacterium in the medium, from which the rate coefficient for arrival is defined:

$$k_a = \frac{D}{\delta_a} \qquad (2.2)$$

The full rate equation for arrival is then

$$\frac{db}{dt} = k_a c_b \emptyset(b) \qquad (2.3)$$

where b is the concentration of bacteria at the surface, i.e., the number per unit area (surface density), and c_b is the bulk concentration of bacterium (the number per unit volume). $\emptyset$ is the available area function, which gives the fraction of the surface still available for accepting bacteria.

Adhesion concerns the processes that ensue once the bacterium has surmounted the interfacial potential barrier and arrived in the adsorbed state (Figure 2.1). The bacterium now finds itself in an environment different from that of the bulk. It is very likely that the pH and the ionic composition will be different from the bulk values (Healy and White, 1978). In consequence, the water structure - as characterized by its degree of hydrogen bonding - is very likely to be different (Mentré, 2004; Wiggins, 2002). These changes may be registered by the bacterium, which may accordingly change its gene expression pattern (phenotype). It is very likely that the bacteria then start to form a biofilm, with a significantly different phenotype from the planktonic state (Vilain and Brozel, 2006).

Adherent bacteria are known to be very persistent residents at the solid/liquid interface. Nevertheless, it may happen that the interfacial forces dwindle away (e.g., if the bacteria die) in which case they may ultimately depart. A simple rate equation for departure is

$$\frac{db}{dt} = - k_d b \tag{2.4}$$

where k_d is the rate coefficient for departure, implying that b(t) decreases exponentially. A simple approximation for k_b assumes as an Arrhenius behaviour, i.e.,

$$k_d \approx \upsilon_d \exp\left(\frac{-(\Delta G_a - \Delta G_b)}{k_B T}\right) \tag{2.5}$$

where υ_d is the characteristic frequency of departure attempts.

2.2 The metrology of bacterial adhesion

The problems of metrology in this field can be divided into three groups. The first one is the determination of the bacteria adhering to a surface, most importantly the number per unit area, but also the actual force of adhesion. The second group concerns rate of arrival of bacteria from the bulk medium at the surface (which in fact underlies the number adhering). The third group comprises the measurement of the interfacial energetics (e.g., with atomic force microscopy), which essentially amounts to the determination of surface tensions (and, if the ionic strength is low, the electrostatic surface charge), from which the rate of arrival and the number of adhering may be predicted (Lower *et al.*, 2000; Otto, 2008).

2.2.1 Imaging

The most direct method is actually to observe, using a high-powered microscope, the surfaces on which the bacteria are adhering and actually count the numbers. Although this method can be useful for a rapid preliminary survey, it is rather tedious and, at the same time, automated image analysis is likely to be unreliable. A more severe limitation is that it is practically impossible to obtain high-resolution kinetics by this

method. Normally optical microscopy is considered; higher spatial resolution can of course be achieved using (scanning) electron microscopy (Arnold *et al.*, 2004), but at the price of laborious sample preparation, which may also result in some alteration of the salient sample features. Microscopy has been combined with the flow chambers to yield kinetic information on adhesion (Meinders *et al.*, 1995; Wiencek and Fletcher, 1995).

2.2.2 The kinetics of arrival and the numbers adhering

More significant and useful are the large family of non-imaging methods with which the number of bacteria adhering to the surface can be counted. Many of these methods are suitable for kinetic measurements. The basic problem, of counting particles at an interface, has been addressed in the context of proteins and abiotic nanoparticles (Ramsden, 1994). The simplest of these methods is simply to measure the depletion of bulk bacterial concentration due to adhesion, using nephelometry (Rijnaarts *et al.*, 1993). A slight increase in sophistication is obtained if the surface to which the bacteria may adhere is packed into a column through which the suspension of bacteria is passed; this method however requires the bacteria to the radiolabelled. Columns and nephelometry can be combined (Walker *et al.*, 2004).

Newer and more sophisticated methods are based on transducers sensitive to the presence of objects in their vicinity; for example, chemical sensors (see section 4.1 below)(Acharya *et al.*, 2006; Deisingh and Thompson, 2004; Fleminger and Shabtai, 1995; Grossman *et al.*, 2004; Hug, 2000; Ivnitski *et al.*, 1999; Lukosz, 1995). Using this approach, measurements can be carried out in situ. The most important family of such transducers are based on optical reflexion (scanning angle reflectometry, ellipsometry, and planar waveguide-based methods), of which the most sensitive and informative are optical waveguide lightmode spectroscopy (OWLS) based on grating couplers and optical waveguide lightmode interferometry (OWLI) based on the Mach-Zehnder interferometer and other devices (Ramsden, 1993; Ramsden, 2006; Mann, 2001; Lukosz *et al.*, 1988).

The main challenge with these methods is to determine the actual number of bacteria from the optical signals. Visible light (wavelength λ) is generally used in these transducers, but since bacteria typically have a diameter over ten times longer than the wavelength of the optical source, the uniform thin-film approximation (UTFA) is no longer valid (Mann *et al.*, 1997). One apparently has therefore the choice

of either analysing the optical signals using the UTFA, and applying a correction based on some independent calibration, such as microscopic counting, or using a more sophisticated analysis such as has been done for eukaryotic cells using the concept of effective volume (Ramsden *et al.*, 1995). In this work, however, we have developed a third way relying on the assumption the adsorption is random sequential (see section 4.3). In the one extant work that reports using waveguides to investigate bacterial adhesion (Horváth *et al.*, 2003), no attempt to count the bacteria was made.

Note that counting is not necessary for determining the energetics of the interaction, which depends only on the kinetics. However, if adsorption is allowed to continue to saturation, and this is equated with the jamming limit θ_J appropriate for the shape of the bacteria (which should be established from microscopic observation) (Viot *et al.*, 1992; Schaaf and Talbot, 1989), see section 3.2, we contend this provides a convenient and reliable estimation of the number adsorbed.

The initial rate. In this case the surface is empty (b =0) and $\phi(b)=1$. Departure may be neglected even if it is able to occur because b is close to zero. Hence, the surface can be considered to represent a perfect sink. If the fluid in which the bacteria are suspended is flowing laminarly over the solid/liquid interface, far from the interface the bacteria are transported by convection, but once they get closer than the hydrodynamic boundary (distance δ_d from the substratum surface) diffusion is faster (the overall process is called convective diffusion (Levich, 1962). Within the diffusion boundary layer Fick's law applies and we have

$$\frac{db}{dt} \approx c_b k_a \frac{D}{\delta_d} \tag{2.6}$$

Then ΔG_{123} can be obtained from k_a using Equations (2.1) and (2.2). Since this forms the basis of one of our main experimental methods, we go into more detail in chapter 3.

2.2.3 Direct measurement of interfacial forces

Atomic force microscopy can be used to directly measure the force between an abiotic cantilever tip and a lawn of bacteria immobilized on a rigid substratum (Razatos *et al.*, 1998; Ong *et al.*, 1999; Razatos *et al.*, 2000). However, a main disadvantage of this method is that the bacteria would need to be chemically fixed to the substratum, which may alter their surface properties.

2.2.4 Microbial adhesion to solvents (MATS)

Microbial adhesion to solvents (MATS) is based on the comparison between microbial cell affinity to a monopolar solvent and an apolar solvent and is a very convenient way to determine the surface energetics of bacteria. One simply measures the partitioning between a monopolar solvent (e.g., chloroform (a Lewis acid); ethyl acetate (a Lewis base)) and an apolar solvent such as decane (Bellon-Fontaine *et al.*, 1996; Briandet *et al.*, 1999). The method is a development of the earlier microbial adhesion to hydrocarbons (MATH) technique (Rosenberg *et al.*, 1980).

2.2.5 Experimental determination of single-substance surface tensions

Following Thomas Young, the measurement of contact angles of different fluids is a convenient way of measuring the surface tensions of unknown solid. For any given solids, there are in principle three unknown components, $\gamma^{(LW)}$, $\gamma^{\oplus}$ and $\gamma^{\ominus}$, the last two corresponding respectively to the electron-accepting and electron-donating components of the da force. Hence, three Young-Dupré Equations with different parameters must be solved simultaneously. The different equations are obtained from measuring the contact angles (which, except for very inert surfaces, must be the advancing angles) with fluids differing in their surface tension components. Convenient choices are water, α-bromonaphthalene and formamide (van Oss, 2006).

This approach can also be used for bacteria deposited as lawns on a substrate (see (van der Mei *et al.*, 1998)). However, the preparation of microbial lawn takes at least 30 minutes for drying and only a limited water is present on the surface, which might change the surface properties of bacteria.

2.3 The nature of bacteria

Bacteria are envelopes of cytoplasm surrounded by a membrane (the plasma membrane). Most bacteria are typically of the order of a micrometre in length (although there is great variety). Different strains (the word “species” is not generally used to describe different kinds of bacteria, because of the promiscuity with which bacteria can exchange DNA with one another) are characterized by different shapes: most typically spheres and spherocylinders (rods). The membrane has the basic structure of a lipid bilayer with embedded proteins, encapsulated within a tough polysaccharide (“exopolymer”) cell wall that may be tens of nanometres thick.

A useful classification of bacteria is into “Gram-positive”, which take up Gram’s stain, and “Gram-negative”, which do not. The former (Figure 2.2) have a structurally simpler cell wall: it essentially comprises a roughly 25-nm thick, possibly multilayered peptidoglycan (murein) and teichoic acid layer. Mureins are glycan heteropolymers-alternating residues of β-1,4-linked N-acetylglucosamine and N-acetyl muramic acid forming strands cross-linked by oligopeptides consisting of both L- and D-amino acids. Teichoic acids are polyols containing mainly of multiple hydroxyl, groups (glycerol, ribitol, and mannitol), and connected to the peptidoglycan in periplasm through covalent phosphodiester bonds. Structural details and composition vary considerably among different types of bacteria.

Gram-negative bacteria (Figure 2.3) have a roughly 3 nm thick peptidoglycan (murein) coating the membrane, encapsulated in turn by a roughly 8-nm thick outer membrane constructed from proteins, lipids, and lipopolysaccharides (LPS) (Kotra *et al.*, 1999). The LPS are fairly exotic molecules, consisting of a core (“kernoligosaccharide”) flanked by lipid A (which has six alkane chains constituting the apolar moiety) penetrating into the peptidoglycan, and O-side chains, consisting of repeated tetrasaccharide units, facing the exterior. The sugars themselves are typically found only in bacteria, molecules such as 2-keto-3-desoxyoctonate, heptose, and L-rhamnose. The peptidoglycan-containing zone between the two membranes is called the periplasma and is an aqueous compartment containing numerous proteins with transporter functions (Alcamo, 2001; Pelczar *et al.*, 1993).

In recent years, much effort has been spent on investigating the identities of specific molecules on the surface of bacteria responsible for particular pathogenicities. These molecules include sialic acid (Nagao and Benchetrit, 1999), lipopolysaccharides

(Walker *et al.*, 2004), proteins (Schwarz-Linek *et al.*, 2003; Beis *et al.*, 2004).

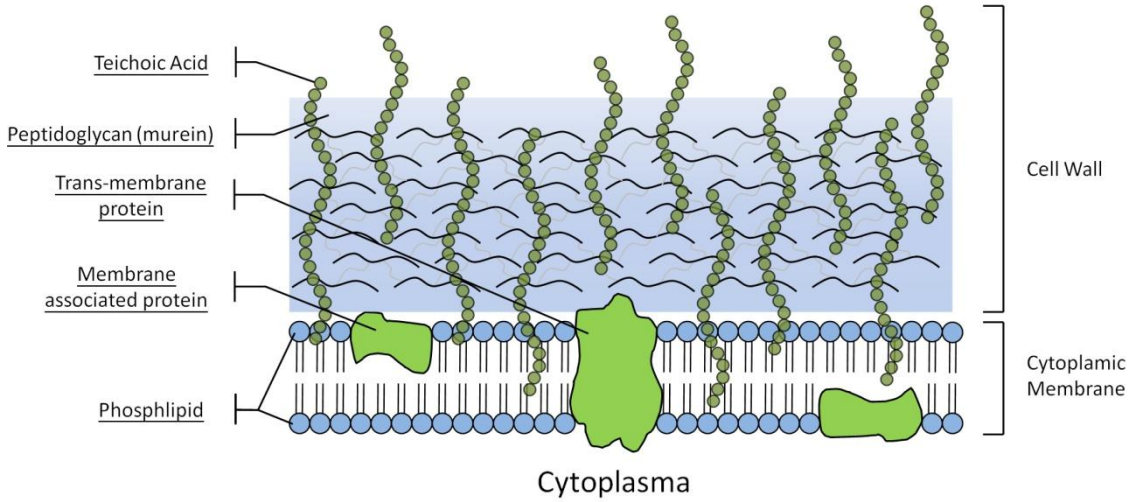

Figure 2.2 Sketch (approximately to scale) of the cell envelope of a Gram-positive bacterium.

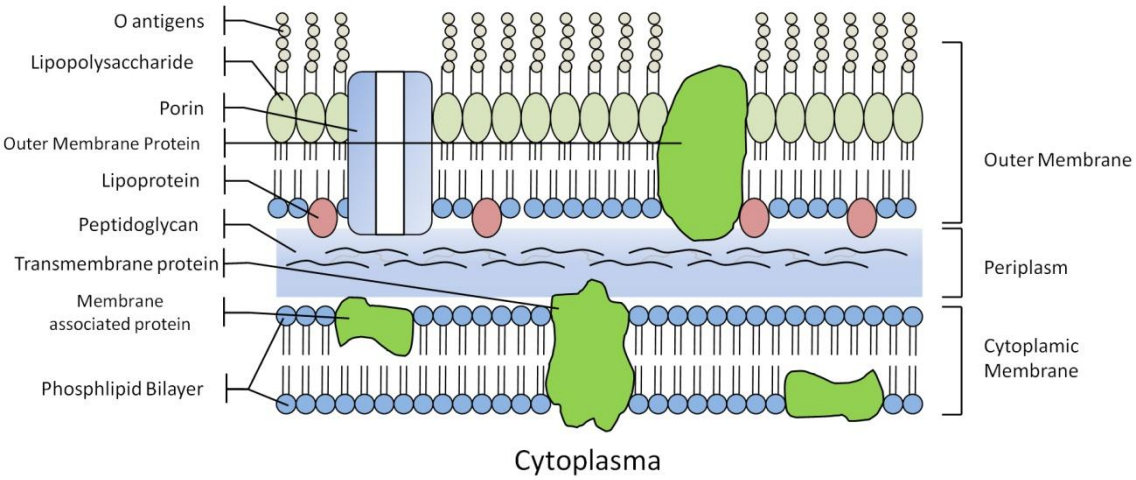

Figure 2.3 Sketch (approximately to scale) of the cell envelope of a Gram-negative bacterium.

Nevertheless, either type of surface coating may be in turn enveloped by an S-layer, constituted from a rather regular array of globular proteins (Schuster and Sleytr, 2000). The tough coatings of spores are of a similar nature (Gould *et al.*, 1970; Aronson and Fitz-James, 1976).

These two bacterial structures, the outer layers of bacterial spores (spore coats) that form the protective casing of dormant spores, and the S-layers that are found as the outermost cell envelope component of many bacteria, will be used as model surfaces for exploitation, i.e. as sources of proteins and as a source of understanding of the principles of multicomponent self-assembly. Both spore coats and S-layers share a number of similarities: protein composition, ordered arrays of protomeric subunits, self-assembly and protective properties. The robustness of bacterial spores is well known and they are therefore obvious candidates for being introduced into production processes hitherto dominated by purely synthetic materials. These coatings and layers are very sophisticated multicomponent, self-assembled, nanostructured materials.

Bacterial surface layer(S-layers)

Many prokaryotes including bacteria and archaea produce an S-layer, a surface-exposed paracrystalline layer surrounding the cell envelope. S-layers are monomolecular arrays composed of a single species of protein or glycoprotein subunits. As a first order self-assembly system, S-layer proteins form lattices with oblique, square or hexagonal symmetry, thus representing the simplest biological membrane developed during evolution (Sára and Sleytr, 1996; Schuster and Sleytr, 2000; Beveridge, 1997; Sleytr, 1997). S-layers can (a) form pores of defined size and morphology; (b) carry precisely aligned functional groups on the surface; (c) be induced to recrystallize on a variety of solid supports and lipid based membranes; and (d) be modified by genetic engineering to display novel functional groups (Messner, 1997; Rachel, 1997; Schar-Zammaretti and Ubbink, 2003; Beveridge, 1997). Thus, S-layers clearly offer new approaches for nanotechnology, particularly for nanopatterning of surfaces and the formation or ordered arrays.

Bacterial spores

Bacterial spores (endospores) are a unique natural material due to their extreme robustness—it is this that distinguishes bacterial spores from fungal spores (exospores) (Aronson and Fitz-James, 1976). As dormant metabolically inactive life forms, spores can survive indefinitely in a desiccated state, and indeed have been documented as surviving intact for 28 million years. The spore can resist temperatures as high as 90 °C as well as exposure to noxious substances (Gould *et al.*, 1970; Colwell, 1997). *Bacillus* species produce a single spore (endospore) within the bacterial cell by a process of differentiation requiring the coordinated action of hundreds of developmental genes (Chada *et al.*, 2003; Henriques and Moran, 2000; Nicholson, 2002; Nicholson *et al.*, 2000). Oral delivery of spores carrying a hybrid protein (a recombinant CotB-TTFC

chimera) to mice was sufficient to immunise and protect animals challenged with an otherwise lethal dose of tetanus toxin (Duc *et al.*, 2003; Ricca and Cutting, 2003).

The next section presents a selection of measured single-substance surface tensions for bacteria (from which the LW and da potentials can be derived), and some el data from electrophoretic mobility measurements.

2.4 Summary and analysis of bacterial adhesion data from traditional methods

Table 2.1 presents experimental and measured surface tension parameters for selected bacteria from literature. In the past, surface and bacteria have been classified as simply hydrophobic or hydrophilic (van Oss, 1997), but this is clearly an oversimplification with little predictive power.

Electrophoretic mobility data is much sparser, but both *Streptococcus thermophilous* B and *Leuconostoc mesenteroides* NCDO have been reported to have a mobility of -1.7×10^{-8} m^2 V^{-1} s^{-1} in 10 mM potassium phosphate buffer (pH 7) (Bellon-Fontaine *et al.*, 1996), which corresponds to a ζ-potential of approximately −20 mV (roughly estimated using the Helmholtz-Smoluchowski Equation). These two observations do not contradict the widely held belief that the surface charge of all bacteria is negative.

On the other hand, there is a wide variation among the ratio of electron donor to electron acceptor potentials. This variety confirms our hypothesis (Hypothesis 1) that different bacteria have different surface characteristics. Most, but by no means all, of the bacteria show a preponderance of $\gamma^{\ominus}$.

Table 2.1 Surface tension parameters (in mJ/m^2) for selected representative bacteria.

Strain	Gram	$\gamma^{(LW)}$	$\gamma^{\oplus}$	$\gamma^{\ominus}$	Ref.
Actinobacillus actinomycetemcomitans HG1099	Negative	33.5	3.2	0.2	[a]
Acinetobacter calcoaceticus MR-481	Negative	36.2	1.3	44.1	[a]
Acinetobacter calcoaceticus RAG-1	Negative	36.8	0.0	41.4	[a]
Leuconostoc mesenteroides NCDO 523	Positive	36.3	0.02	68.4	[b]
Serratia marcescens RZ37	Negative	10.5	310.0	46.7	[a]
Serratia marcescens RZ30	Negative	12.2	5.0	35.3	[a]
Staphylococci epidermidis NCTC 100892	Positive	26	6	49	[c]
Staphylococci epidermidis 3294	Positive	36.4	7.4	10.3	[a]
Streptococci cricetus H56	Positive	35.0	0.0	66.9	[a]
Streptococci mitis BA	Positive	35.8	5.8	3.8	[a]
Streptococci sanguis CR311VAR3	Positive	31.7	0.57	55.6	[a]
Streptococci sobrinus HG970	Positive	33.8	0.004	68.5	[a]
Streptococci oralis 34	Positive	37.2	2.4	43.7	[a]
Streptococci oralis PK1317	Positive	36.8	6.7	1.5	[a]
Streptococcus thermophilous B	Positive	37.9	0.03	62.1	[b]
Streptococcus thermophilous B	Positive	36.4	0.4	58.6	[a]
Pseudomonas aeruginosa AK1	Negative	34.7	4.8	5.8	[a]
Candida albicans ATCC10261 (37°C)	Positive	40.3	1.7	45.9	[a]

[a] (van der Mei *et al.*, 1998).

[b] (Bellon-Fontaine *et al.*, 1996).

[c] (van der Mei *et al.*, 1997)

2.4.1 Implications

The notion of equivalent chemistry. Knowing that the surface of bacteria is composed primarily of polysaccharides and proteins, the fraction of polysaccharides being *p*, bacterial surface chemical characteristics can be approximated as a mixture of these two components. Table 2.2 gives the surface tension parameters for two typical polysaccharides, the two most abundant blood proteins in humans, and the common lipid lecithin. Comparison with Table 2.1 shows that in fact the bacterial surface cannot be represented as an obviously simple combination of natural substances, in particular since $\gamma^{\ominus}$ for some strains exceeds even the electro-donor potential (dativită) of lecithin.

Table 2.2 Surface tension parameters (in mJ/m^2) for same common biopolymers (van Oss, 2006).

Substance	$\gamma^{(LW)}$	$\gamma^{\oplus}$	$\gamma^{\ominus}$
Agarose	41	0.0	27
Cellulose	44	1.6	17
Human serum albumin	27	6.3	51
Immunoglobulin G	34	1.5	50
Lecithin	29	2.7	60

2.4.2 Critique of DLVO theory

DLVO theory, which takes into account LW and el forces only, has been widely used to interpret bacterial adhesion (van Loosdrecht *et al.*, 1990; Hermansson, 1999; van Oss *et al.*, 1999; Y.F. Missirlis and Katsikogianni, 2004). However, as van Oss has pointed out (van Oss, 2006; Cacace *et al.*, 1997), under typical physiological conditions (e.g., bloodstream, cytoplasm) these two forces only account for five to ten percent of the interfacial energy. The balance is made up from the Lifshitz-van der Waals(LW), electron donor-acceptor (da) and electrostatic (el) forces (see earlier sections of chapter 2). Therefore these DLVO papers are wrong, in the same that they neglect the da interactions.

Chapter 3 Development of a New Paradigm for Measuring Bacterial Adhesion

The novel concepts here focus on the adsorption kinetics to determine adhesion.

3.1 Introduction

We assume that the paradigm of adhesion (cf. Ch. 1, Fig. 1.1) can be divided into these three steps, namely:

(1) Approach to the surface, governed by an adsorption rate constant (cf. Equations 2.1 and 2.2-derivedwith certain assumptions as detailed in Section 2.1)

$$k_a = \frac{D}{\delta_a} \tag{3.1}$$

and

$$\delta_a = \int_{l_0}^{\infty} \left[\exp\left(\frac{\Delta G_{123}(z)}{k_B T} \right) - 1 \right] dz \tag{3.2}$$

where k_a is the adsorption rate coefficient; D is the coefficient of the bacterium; δ_a is the adsorption distance in the z direction, which is perpendicular to the adsorption surface; $\Delta G_{123}(z)$ is interfacial energy. The integral is taken from infinity down to the distance of closest approach l_0.

Because the assumption of a large Peclet number is not application to our experimental conditions, strictly speaking we cannot use Equation (3.2), hence we approximate k_a using a heuristic approach (cf. Equation (3.6)), multiplying the diffusive contribution D/δ_d, where δ_d is the diffusion boundary layers thickness, by a Boltzmann factor $\exp(-\Delta G_a/k_B T)$, giving

$$k_a \approx \frac{D}{\delta_d} \exp\left(\frac{-\Delta G_a}{k_B T} \right) \tag{3.3}$$

(2) Arrival: the bacterium falls into a deep potential well at a distance z_b from the surface.

(3) Postarrival: the cytoplasm of bacteria may secrete chemicals or biochemical after attaching to the substrate. The shape and surface composition of bacteria may change and this usually causes enhancement of adhesion.

In solution, the interaction free energy ΔG_{123} will increase or decrease when two particles or bacteria approach each other, or when the bacteria come near the surface. These two situations are quite similar. The net interfacial energy ΔG_{123} can be obtained by Equation (3.4) (see (van Oss, 2006)):

$$\Delta G_{123} = \Delta G_{13} + \Delta G_{22} - \Delta G_{12} - \Delta G_{23} \tag{3.4}$$

where ΔG_{23}, ΔG_{12} and ΔG_{13} are the interaction free energies between bacteria and medium, medium and substrate, and substrate and bacteria respectively, and ΔG_{22} is the cohesive energy of the medium (e.g., water). How the binary ΔG quantities are defined from the surface tension data (e.g. Table 2.1) is described in section 3.4.

Much metrology, more or less quantitative, has been merely concerned with counting the number of bacteria present at solid/liquid interfaces (e.g., (Harris *et al.*, 2004)). Much more information about the overall process can be obtained if it is possible to obtain high resolution kinetic data on the arrival, residence and departure of the bacteria. Appropriate metrology techniques will be described in Chapter 4.

3.2 The rate of accumulation of objects at the surface (dM/dt)

In the case of the perfect sink (pure diffusion):

$$\frac{dM}{dt} = c_b \left(\frac{D}{t}\right)^{1/2} \tag{3.5}$$

where M is the mass of the objects, c_b is the bulk concentration and D is the diffusion coefficient of the object. When the liquid in which the object is dissolved or suspended flows over the surface, deposition occurs via convective diffusion:

$$\frac{dM}{dt} = c_b \left(\frac{D}{\delta_d} \right) \tag{3.6}$$

where δ_d is the thickness of the diffusion boundary layer (typically 10-100 nm), i.e., that distance from the surface at which transport by diffusion and by convection are equally fast; it depends on the actual geometry of the flow (Levich, 1962).
Note that:

- Careful investigation of adsorption kinetics is an extremely powerful and sensitive method for probing the energetic profile in the vicinity of an adsorbing surface.
- Bacterium: has a highly heterogeneous surface, nevertheless adsorption is rather precisely characterized by dM/dt and may display very rich behavior when approaching the substratum.
- An adsorption energy barrier E_a can be introduced via the chemical rate coefficient for adsorption k_a:

$$k_a = \tilde{a}\, \delta\, \upsilon \exp(-E_a/k_B T) \tag{3.7}$$

where $\tilde{a}$ is an orientation factor (the fraction of bacteria which approach the surface in an orientation which permits adsorption) and will be unity for a uniform, spherical colloidal object. δ is an appropriate length. υ is an appropriate attempt frequency. Compare this with equation (3.3).

We now relax the perfect sink assumption by introducing the available area function ϕ. It is equal to $(1-\theta)$ in the case of discrete, independent sites equal in size to or bigger than the adsorbing particles (Langmuir's condition), applicable to gas molecules adsorbing to a metal in high vacuum. Furthermore, we have the energy barrier E_a, which has the effect of introducing a rate coefficient for adsorption k_a: Hence instead of equation (3.6), we have

$$\frac{dM}{dt} = k_a c_s \phi \tag{3.8}$$

Because the adsorbent surface is no longer a perfect sink, the relevant bulk concentration of dissolved particles is $c_s < c_b$, where c_s is the particle concentration right above the interface and can be derived by summing fluxes to and from a thin layer

$$V\frac{dc_s}{dt} = S(c_b - c_s)\frac{D}{\delta_d} - Sk_a c_s \phi \qquad (3.9)$$

where V is unit volume and S is unit surface. By letting the left hand side go to zero, we can derive

$$c_s = c_b\left(\frac{k_a \phi\, \delta_d}{D} + 1\right) \qquad (3.10)$$

for substitution into equation (3.8).

3.3 The available area function

Bacteria are typically regular spheres or spherocylinders a few hundred nanometres to a few micrometres in diameter. It may be assumed that upon arrival at the surface, they can at most form a monolayer. The biofilm formation that may ultimately ensue of course involves a complex multilayered structure, but it goes beyond the scope of this work. The aim here is essentially to determine the form of the function ϕ in Equation (3.8).

Since we are not considering multilayer formation, the bacteria must be arranged in nonoverlapping fashion in a plane immediately above the surface. This implies that the centre of an arriving bacterium of radius r (we shall initially restrict ourselves to spheres) must remain at the distance of at least 2r from the centre of any previously arrived bacterium (the circle of radius 2r centred on the previously arrived bacterium encloses the exclusion zone associated with that bacterium), see Figure 3.1. In other words, defining θ = ba, where a (= πr^2 in the case of spheres) is the area occupied by the bacterium on the surface, as the fractional occupation of the surface, we have ϕ =1 − 4θ. However, the factor 4 can only be valid at the very beginning of addition of bacteria to the surface; as soon as it becomes moderately occupied, exclusion zones will overlap and the factor will overestimate the exclusion; hence additional terms proportional to θ^2, θ^3,... must be added (Schaaf and Talbot, 1989). This is known as the random sequential addition (RSA) model. The constants of proportionality depend on the aspect ratio for the spherocylinders (Ricci *et al.*, 1992; Viot *et al.*, 1992).

The RSA model also delivers the value θ_J of the surface coverage θ at which ϕ becomes zero and hence no further addition is possible, called the jamming limit.

For spheres, $\theta_J \sim 0.54$ (Schaaf and Talbot, 1989); the value of this constant depends on the aspect ratio for spherocylinders and (Ricci *et al.*, 1992; Viot *et al.*, 1992) (See Table 3.1). The aspect ratio is defined as the ratio of the long axis to the short axis.

Table 3.1 Jamming limits for different aspect ratios of spherocylinders (Viot *et al.*, 1992).

Aspect ratio	Jamming Limit (θ_J)
1	0.54
1.25	0.56
1.75	0.58
3	0.56
4	0.55
6	0.52
10	0.48
15	0.44

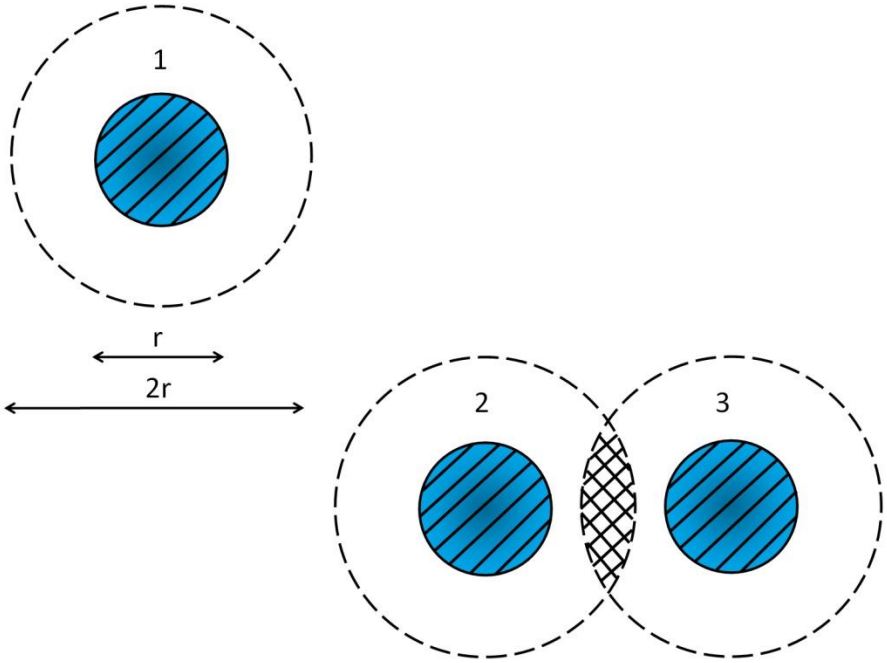

Figure 3.1 Diagram of an RSA process. Disk 1 (hatched) creates an exclusion zone around itself, whose border is marked by the dashed ring. No bacterium can be deposited with its centre within this zone. The exclusion zones of bacteria 2 and 3 overlap (crosshatched zone).

For practical use, accurate interpolation formulae are available valid over the entire range $0 \le \theta \le \theta_J$, of which an example is (Schaaf and Talbot, 1989):

$$\phi=(1-\frac{\theta}{\theta_J})^3\left[1-0.8120\frac{\theta}{\theta_J}+0.4258(\frac{\theta}{\theta_J})^2+0.0716(\frac{\theta}{\theta_J})^3\right] \quad (3.11)$$

3.4 Predicting interfacial interactions from surface tension data

Assuming that the properties of the bacterial surface are uniform, the interaction energy with a planar adsorbent surface can be readily calculated from knowledge of the surface energies of the bacteria (see Table 2.1) and the adsorbent.

A convenient mesoscopic formalism is based on Young's law, as extended by Girifalco, Good and van Oss (van Oss, 2006). This allows the calculation of the interfacial tension between bacterium and substratum in the presence of a liquid medium. Dupré-like equations are then used to calculate the interfacial energy from the interfacial tension (van Oss, 2006; Cacace *et al.*, 1997).

The interfacial energy can be decomposed into the Lifshitz-van der Waals (LW), electron donor-acceptor (da) (Lewis acid-base) and electrostatic (el) (Coulombic) interactions. Whereas the short range Lifshitz-van der Waals interactions are attractive, the other two interactions can be either repulsive or attractive. In the presence of appreciable concentrations ($\sim$ 0.1 M, i.e. physiological concentrations) of salt, the electrostatic interactions are strongly shielded (e.g. (Cacace *et al.*, 1997)), and the electron donor-acceptor interactions will typically account for about 90% of the total interaction.

The Lifshitz-van der Waals force arises through correlations between the electrons of the atoms of adjacent materials. It is therefore generally attractive, and is weak and short-range, the potential decaying as $1/z^2$. Denoting $\Delta G^{(LW)\|}$ as the interaction between two infinite planes, the interaction between an infinite plane (representing the planar substratum) and the sphere of radius r (representing the bacterium) – see Figure 3.2 and making use of the Derjaguin approximation – is (van Oss, 2006)[3]:

[2] The potential initially decays rapidly in capanian with exp(-z), but has a very long tail. Hence, at intermediate range, the exoententailly decaying function is actually more significant.
[3] The prefactor is different for a cylinder (rod-shaped bacterium).

$$\Delta G_{123}^{(LW)}(z) = 2\,\pi\, l_0^2\, \Delta G_{123}^{(LW)||}\, \frac{r}{z} \qquad (3.12)$$

where l_0 is the so-called distance of closest approach, equal to about 1.6 ångström units, beyond which the Born repulsion between electron clouds on the atoms of the two materials prevents approach (cf. Fig. 2.1).

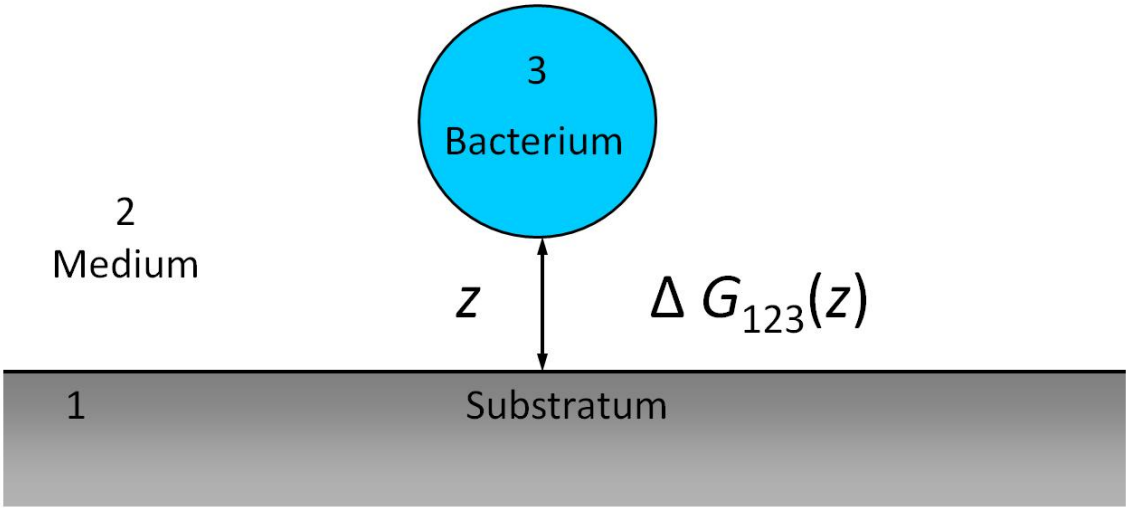

Figure 3.2 The interaction free energy between a bacterium (label 3) and a substratum (label 1) in the presence of a medium (label 2).

The electron donor-acceptor force is due to the interaction between Lewis acids and bases in the adjacent materials. Its most common manifestation in biological systems is the hydrogen bond. Electron donors in one material will repel electron donors in the opposing material, but attract electron acceptors. Hence, the net interaction force can be either attractive or repulsive. It is strong and long-range[4], and the potential decays exponentially according to (van Oss, 2006):

$$\Delta G_{123}^{(da)} = 2\,\pi\,\chi\,\Delta G_{123}^{(da)||} \exp\left(\frac{l_0 - z}{\chi}\right) r \qquad (3.13)$$

where χ is the characteristic decay length for the da interactions, which is one of the least well-determined parameters in intermolecular science. Unlike the Debye length

[4] See footnote 2 (p. 22).

discussed below, no convenient expression showing its dependence on characteristic parameters of the medium is presently available. χ seems to be at least 1 nm and may well be longer under typical biomedical conditions.

The electrostatic force is the Coulomb force between electrostatic charges created at the surfaces of the materials typically by the ionization of certain elements, or the protonation of certain chemical groups, modulated by the presence of dissolved ions, which is taken into account via the Debye length $1/\kappa$, defined by:

$$\kappa = e\left(\frac{c_{ion}}{\varepsilon\varepsilon_0 kT}\right)^{1/2} \tag{3.14}$$

where ε is the relative dielectric constant of medium 2, for a 1:1 electrolyte such as KCl. The electrostatic interaction potential is given by (e.g., (van Oss, 2006) :

$$\Delta G_{123}^{(el)} = 4\pi\epsilon_0\epsilon\psi_1\psi_3 \ln[1+\exp(-kz)]r \tag{3.15}$$

where the ψ are the electrostatic surface potentials. These can readily be determined using Healy and White's surface ionizable group model (Healy and White, 1978). For monoprotic acidic or basic groups with a dissociation constant K present at a density N_s on a surface, we have

$$pH=pK-\frac{y}{2.303} \pm \log_{10}\left(\frac{\pm\Gamma}{\sinh(y/2)}-1\right) \tag{3.16}$$

(taking plus signs for a (Brønsted) basic and minus signs for an acidic surface), where y = $\psi e/(k_B T)$ is the dimensionless surface potential, and Γ is a dimensionless parameter defined by $\Gamma = N_s\kappa/(4c_{ion})$; for an amphoteric surface with isolectric point pH_0 (e.g., a metal oxide), we have the expression:

$$\frac{\sinh(y/2)}{\Gamma} = \frac{\delta \sinh \xi}{1+\delta \cosh \xi} \tag{3.17}$$

where $\delta = 2 \times 10^{-\Delta pK/2}$, where $\Delta pK=pK_- - pK_+$ and $\xi = 2.303\Delta pH - y$, where $\Delta pH=pH_0-pH$.

Depending to the surface potential and its sign, the immediate vicinity of the surface may be enriched or depleted in protons, resulting in a surface pH different from the bulk value, and given by

$$pH_s = pH + \frac{y}{2.303} \tag{3.18}$$

In the presence of moderate to high ionic strength liquids between interacting materials, the electrostatic interaction potential is weak and long-range. It can be either attractive or repulsive. Typically, in calculations the net surface charge is taken (mean field approach).

As a result of the difference between bulk and surface pH, the surface potential ψ_3 of the bacterium might change as it nears the surface, changing the value of $\Delta G_{123}^{(el)}$. It can be either attractive or repulsive, but individual charges are supposed to be laterally smeared out and the net surface charges are used to calculate $\Delta G_{123}^{(el)}$. This is valid at low ionic strength when $1/\kappa$ is large, and in the presence of moderate to high ion concentrations the electrostatic interaction potential is anyway weak (amounting to 5–10% of $\Delta G_{123}^{(da)}$).

From the above it is apparent that to estimate the interaction potential between a surface and a bacterium, it is necessary to know the surface tension components for the adsorbent substratum (label 1), the bacterium (label 3) and the intervening fluid (label 2), which will typically be some kind of aqueous solution containing salts and small osmolytes such as glucose (Johnson and Harvey, 1937). Note in particular that we need:

a. The Hamaker constant A_H for calculating the LW interaction potential, using the relation $\Delta G^{(LW)} = -A_H\, r/(6z)$. If A_H is not available $\Delta G^{(LW)}$ can of course be calculated from the LW component of the surface tension.
b. The dativită (electron donor potential, or Lewis basicity), most conveniently expressed as the surface tension component $\gamma^{\ominus}$.
c. The recettività (electron acceptor potential, or Lewis acidity), most conveniently expressed as the surface tension component $\gamma^{\oplus}$.
d. The mean net electrostatic surface potential.

Dupré-like laws are then used to compute the pairwise interaction potentials between infinite planar surfaces required in (3.12) and (3.13), that is (van Oss, 2006):

$$\Delta G_{12}^{(LW)||} = -2\left(\gamma_1^{(LW)}\gamma_2^{(LW)}\right)^{1/2} \tag{3.19}$$

and

$$\Delta G_{12}^{(da)||} = -2\left[\left(\gamma_2^{\oplus}\gamma_1^{\ominus}\right)^{1/2}+\left(\gamma_1^{\oplus}\gamma_2^{\ominus}\right)^{1/2}\right] \tag{3.20}$$

The same equations, mutatis mutandis, are used to compute ΔG_{13} and ΔG_{23}. The final step is to compute the overall interaction between protein and biomaterial in the presence of solvent (cf. Equation (3.4)).

$$\Delta G_{123}^{(total)||} = \Delta G_{22}^{(total)||} + \Delta G_{13}^{(total)||} - \Delta G_{12}^{(total)||} - \Delta G_{23}^{(total)||} \tag{3.21}$$

Once the interfacial energy between infinite parallel planar surfaces has been obtained, it is straightforward to calculate the interaction energy between an infinite plane of the adsorbent and a spherical object (the bacterium) using Equations (3.12), (3.13) and (3.15). The sum of these expressions is then integrated to yield the interaction length (Equation (3.2)) and hence the rate constant for arrival.
The actual energy of adhesion, $\Delta G_{123}^{(total)}$ at $z = z_b$ corresponds to the depth of the well in Figure 3.2. If the medium 2 is excluded (e.g. as adhesion tightens), then $\Delta G_{13}^{(total)}$ should be computed instead.

In the case of heterogeneous surfaces, the obvious first approach is simply to take the arithmetically weighted mean of all the different components (the Cassie-Baxter law). This can reasonably be expected to give correct predictions of the interfacial potential when the characteristic scale of the substratum heterogeneity is much smaller or much larger than that of the bacterium. On the other hand, if the length scale of substratum heterogeneity is commensurate with that of bacterial surface heterogeneity, the actual interfacial potential may differ considerably from the mean prediction, since patches of dativită on the substratum could match complementary patches of recettività on the bacterium, and so forth. This forms the basis of my Hypothesis 4.

3.5 Electrostatic forces via electrokinetic phenomena

Although, as has been pointed out earlier, under physiological conditions the electrostatic component of the interfacial energy is typically rather minor (of the order of 10% of the total), under certain circumstances (for example, the adhesion of bacterium to the internal surfaces of potable water distribution networks) the ionic strength is very low, and hence the electrostatic forces will be more prominent (cf. (Ramsden and Máté, 1998)). In this case, the electric charge density on the surface of the bacterium can be deduced from measuring the velocity of bacteria in an electric field (particle electrophoresis) (e.g. (Torimura *et al.*, 1999; Pelletier *et al.*, 1997; Bellon-Fontaine *et al.*, 1996)), see also section 2.4.

3.5.1 Estimated interfacial energies

Table 3.2 gives the surface tension parameters for commonly encountered metal oxides and liquids of practical importance. For an example of prediction, we take the mean of the two determinations of *Streptococcus thermophilous* B (Table 2.1), namely $\gamma^{(LW)}$ = 37, $\gamma^{\oplus}$ = 0.3 and $\gamma^{\ominus}$ = 60 mJ/m^2. Table 3.3 gives the results of applying Equations (3.19), (3.20) and (3.21) to this data. Electrostatic interactions are neglected, as is appropriate for a physiological solution (approximately 150 mM NaCl). This estimate yields the signs and magnitudes of the energies between infinite planar surfaces.

Table 3.2 Surface tension parameters (in mJ/m^2) for common metal oxides and liquids.

Substance	$\gamma^{(LW)}$	$\gamma^{\oplus}$	$\gamma^{\ominus}$	Ref.
Alumina	36.4	0.0	4.5	[d]
Silica	39	0.8	41	[e]
Titania	43	0.6	46	[e]
Zirconia	35	1.3	3.6	[e]
Water	22	25.5	25.5	[e]
Ethanol	19	0.0	68	[e]
Cellulose	44	1.6	17	[e]
Water/Ethanol	20.5	12.7	46.7	[d]

[d] Determined in this work.

[e] (van Oss, 2006).

Table 3.3 Interfacial interaction energies $\Delta G_{123}^{|\,|}$ (in mJ/m^2) between infinite planes of *Streptococcus thermophilous* B (Gram positive) and two common metal oxides in pure water and a 50%-50% ethanol-water mixture, neglecting electrostatic interactions.

	Water	Ethanol-water
Silica	30.3	-3.1
Zirconia	-10.7	-29.8

In other words, *Streptococcus thermophilous B* will be repelled from silica in water, but attracted to zirconia; the addition of ethanol will make the bacterium weakly attracted to the silica, and will enhance the attraction to zirconia. It is a corollary of this result that there will be an ethanol fraction at which the silica-*S. thermorohilous B* interaction will be precisely zero.

Another example of interfacial interaction energies is for *Staphylococci epidermidis* NCTC 100892 (Gram positive) (Table 3.4). From the comparison with Table 3.3, the affinities to two metal oxides in pure water and a 50%-50% ethanol-water mixture are only quantitatively different, that is, *Staphylococci epidermidis* NCTC 100892 should be less strongly repelled from silica in water than *Streptococcus thermophilous B*, but otherwise this pattern of interactions is similar. We presume that different types of binding agents are present on the surface of different bacteria, which have different binding affinities (Neu, 1996; Otto *et al.*, 1999; Grossman *et al.*, 2004), in accordance with Hypothesis 1.

Table 3.4 Interfacial interaction energies $\Delta G_{123}^{|\,|}$ (in mJ/m^2) of *Staphylococci epidermidis* NCTC 100892 (Gram positive) determined from Equations (3.19), (3.20) and (3.21).

	Water	Ethanol-water
Silica	22.0	-2.1
Zirconia	-2.1	-11.9

Here is another example with a similar pattern. Interfacial interaction energies of *Streptococci sanguis* CR311VAR3 (Gram positive) shown in Table 3.5.

Table 3.5 Interfacial interaction energies $\Delta G_{123}^{||}$ (in mJ/m^2) of *Streptococci sanguis* CR311VAR3.

	Water	Ethanol-water
Silica	28.7	-2.9
Zirconia	-10.6	-27.9

Some other bacteria are given in the following Tables 3.6 to 3.7.

Table 3.6 Interfacial interaction energies $\Delta G_{123}^{||}$ (in mJ/m^2) of *Actinobacillus actinomycetemcomitans* HG1099 (Gram-negative).

	Water	Ethanol-water
Silica	-32	-40.1
Zirconia	-59	-52.2

Now we see strong attraction of *Actinobacillus actinomycetemcomitans* HG1099 to silica in water, as well as to zirconia.

Table 3.7 Interfacial interaction energies $\Delta G_{123}^{||}$ (in mJ/m^2) of *Serratia marcescens* RZ37 (Gram-negative).

	Water	Ethanol-water
Silica	-14.7	16.6
Zirconia	96.7	142.2

Serratia marcescens RZ37 is *only* attractive to silica in water and strongly repulsive from everything else.

Table 3.8 Interfacial interaction energies $\Delta G_{123}^{||}$ (in mJ/m^2) of *Serratia marcescens* RZ30 (Gram-negative).

	Water	Ethanol-water
Silica	18.7	-2.4
Zirconia	-7.8	-14.7

Despite apparent closeness to strain RZ37, its behaviour is rather like that of S. *thermophilous B*.

3.5.2 Calculation of adsorption energies

For more precise calculations, the bacteria could considered to be uniform spheres interacting with a uniform planar surface (see Figure 3.2), Equations (3.12) and (3.13) (Derjaguin approximation) integrated from $z = \infty$ to z_0. However,the bacteria are mostly not uniform spheres, making the value of this precision doubtful.

3.6 Conclusions

My second hypothesis is that we can deduce bacterial interfacial energies from the adsorption kinetics (Hypothesis 2). It follows that we need an accurate method to measure the kinetics experimentally with the requisite precision. The next Chapter 4 considers this.

Chapter 4 New Ways of Measuring Bacterial Adhesion

4.1 Principle of chemical sensing

The process of sensing includes three main steps: input preparation, surface reaction and signal collection. The purpose of the sensor is to understand and interpret the sample and surrounding situations. It can sense heat, pressure, light, sound in physical sensing; gas, liquid, solid in chemical sensing; DNA, protein, bacteria in biological sensing. Advanced micro- and nanosensors are smaller, faster, smarter, cheaper, etc. then their macro brothers. The capture layer concentrates (captures, see Fig. 4.1) analyte from the sample. Its presence is converted into an electrical, optical, etc, and output by the transducer.

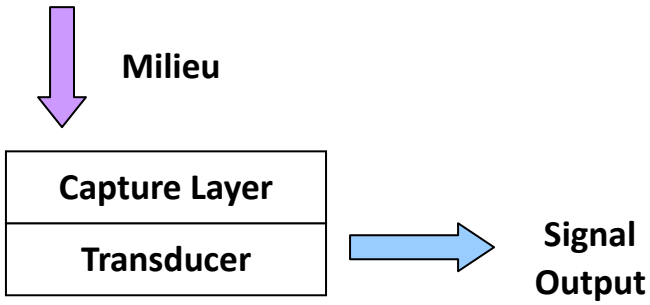

Figure 4.1 Principle of chemical sensing.

To create a synthetic surface capable of interacting with selected bacteria whose presence is then sensed is an important part of this research.

In the first stage of this work, a variety of pure oxides with different surface free energy parameters were investigated as capture layers (Chapter 6). Finally, nanotextured surface were developed (Chapter 9). In parallel, a practical model for qualifying bacterial adhesion was developed. Mostly, optical waveguide lightmode spectroscopy (OWLS) has been used to monitor capture *in situ*. The rest of this chapter focuses on the transducer function.

4.2 Principle of waveguide chemical sensing

Many techniques are available for measuring the presence of micro- and nano- objects at a surface (Ramsden, 1994) and one of the most important areas of interest among biosensors is the optical biosensor. However, among of the most informative and versatile methods are those using the evanescent field of total internally reflected light to sense particle on the surface. Not only they are the most sensitive, with mass resolution ± 1 ng/cm^2 or better at present but they can offer a straightforward understanding of density profile perpendicular to the sensing surface and thus enable the determination of the mass of the adsorption or number of the adsorbed particles. Among these evanescent field-based methods, optical waveguide lightmode spectroscopy (OWLS) is the most attractive and powerful technique in the field of optical particle sensing.

The basic principle of the reflection of light at the boundary of two transparent dielectrics F (waveguide film) and C (cover) with refractive indices n_F and n_C is encapsulated by Snell's law:

$$n_F \sin \alpha_F = n_C \sin \alpha_C \qquad (4.1)$$

where n_F and n_C are the refractive indices of F and C respectively and α_F and α_C are the angles of incidence and transmission respectively to the normal of the boundary surface. For $n_F > n_C$, a beam of light propagating in the dielectric layer F with an angle α_F to the normal of the dielectric-interface is refracted at the interface with an angle of α_C to the normal of the interface. This is called external reflection. However, if n_F is bigger enough than n_C (for example $\sin\alpha_C = 1$), then $\sin\alpha_F = n_F/n_C$, which means that a ray with an incident angle bigger then this particular α_F will be totally reflected back to F. If a planar dielectric material F is surrounded by two layers, Support and Cover, of which both the refractive indices are smaller than that of the film F, the light is confined between the boundaries with S and C and propagates as a zigzag wave within the film as shown in Figure 4.2

In Figure 4.2, an optical waveguide composed of an optical glass support S with thickness typically 0.5 mm (i.e. thick enough to be mechanically strong) and a high refractive index waveguiding layer F in a few hundred nanometers thick, which gives the highest sensitivity that can be attained with thin waveguides and the cover C that normally is the liquid containing with sample particles. The light can be successfully

propagated by total internal reflection at the F, S and F, C interfaces. The reflectivity will change when particles are adsorbed at the F, C interface. The evanescent field is represented by the penetration distance Δz of the beam beyond the confines of F and decays exponentially with a chatacteristic length of typically 200-300 nm for the glass-water interface. Modes propagate with discrete phase velocities which depend on the mode number and the polarization, and not only on the refractive indices of S, F but also of the cover C and adlayer A, and the thicknesses of F and A (Ramsden, 1993). The electromagnetic field distributions of various guided modes in an optical waveguide are shown in Figure 4.3.

Depending on the optical parameters of the waveguiding film only certain modes can propagate in the layer. This is at least the zeroth order mode with two different polarizations, the transverse electric (TE) and the transverse magnetic (TM) waves. These have respectively either their electric or their magnetic component perpendicular to the reflection plane.

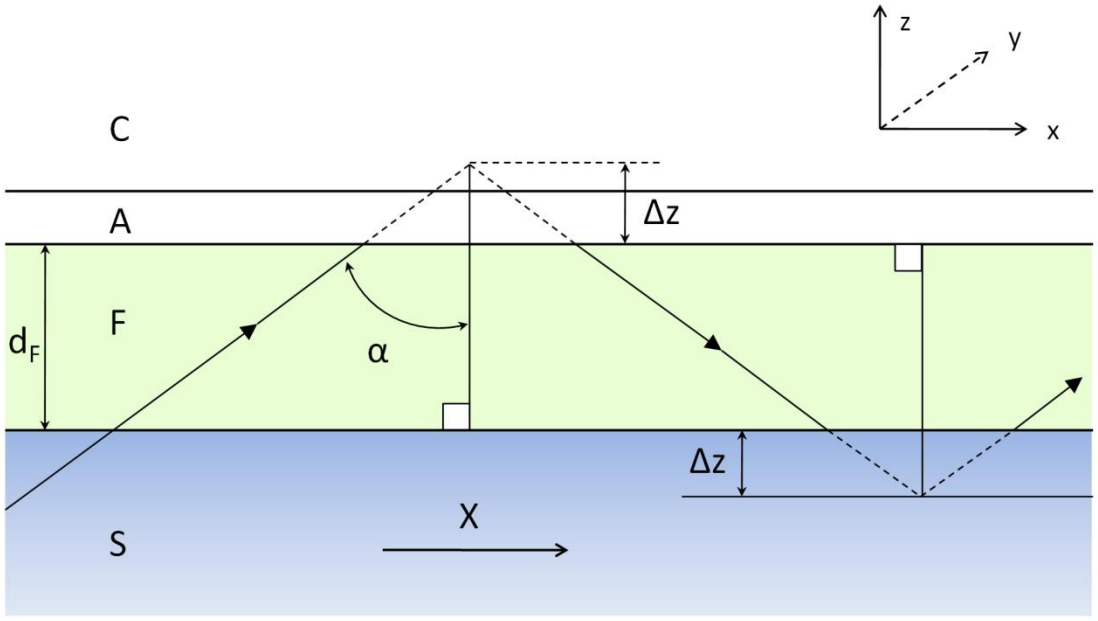

Figure 4.2 An optical waveguide. C: cover medium; A: adlayer of captured sample; F: high refractive index waveguide film; S: glass supporting substrate; d_F: thickness of waveguide film F; α: angle of total internal reflexion; Δz: penetration depth and X: propagation direction of light.

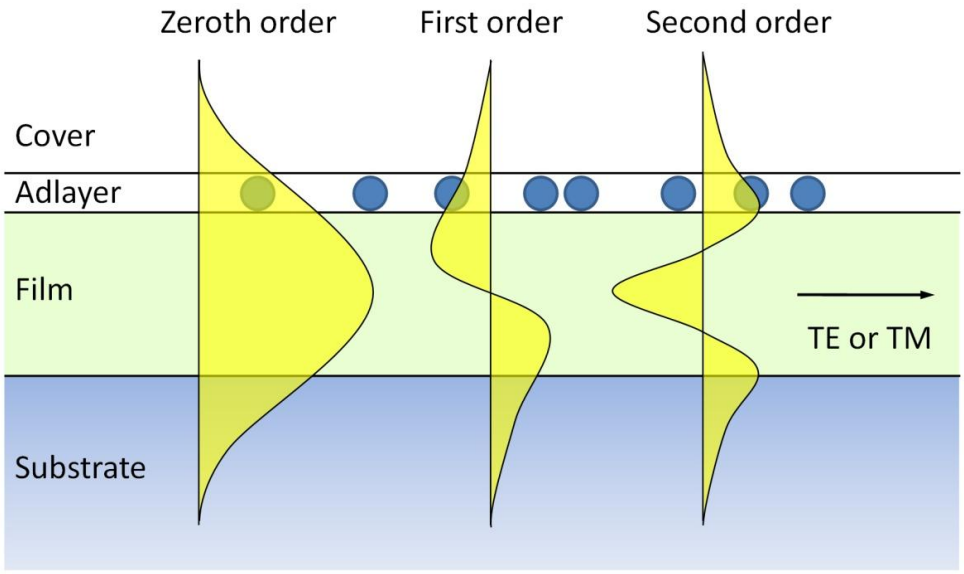

Figure 4.3 Electric field distribution of successive guided wave modes: the zeroth, first and second modes. Bacterial suspensions constitutes the cover, and the discs in the adlayer represent adsorbed bacteria; here the actual decay length of the evanescent fields is -λ/3 where λ is the (vacuum) wavelength of the guided light.

In order to couple an external beam into the waveguide for detecting bacteria, a grating is the most convenient way. One possible way to measure the effective refractive indices N(TE), N(TM), shown in Figure 4.4. The laser beam is coupled into the waveguide film. At a certain angle either the TE mode or the TM mode (zeroth mode) is excited and measured by a photodetector at the end of the waveguide. By matching the incident laser beam, with its wavelength λ, with a possible guided mode (kN) falling on the grating with incoupling angle α, one can immediately derive the effective refractive indices N(TE), N(TM) from the coupling angle using the coupling equation:

$$kN(n_F, d_F, n_S, n_C) = kn_{air} \sin\alpha + \frac{2\pi L}{\Lambda} \qquad (4.2)$$

where N is the effective refractive index = c / v_p, where v_p is phase velocity, α is a coupling angle; k is a free space wavenumber= 2π /λ; L is a diffraction order (0, ±1, 2, 3…) and Λ is a grating constant.

Whenever the diffracted external beam matches a possible guided mode kN (note that N depends on the refractive index of the layers (n_s, n_F, and n_C) and the thickness of F (d_F), propagation occurs, i.e. the light beam is coupled in and a peak is measured by a photodetector at the end of the waveguide.

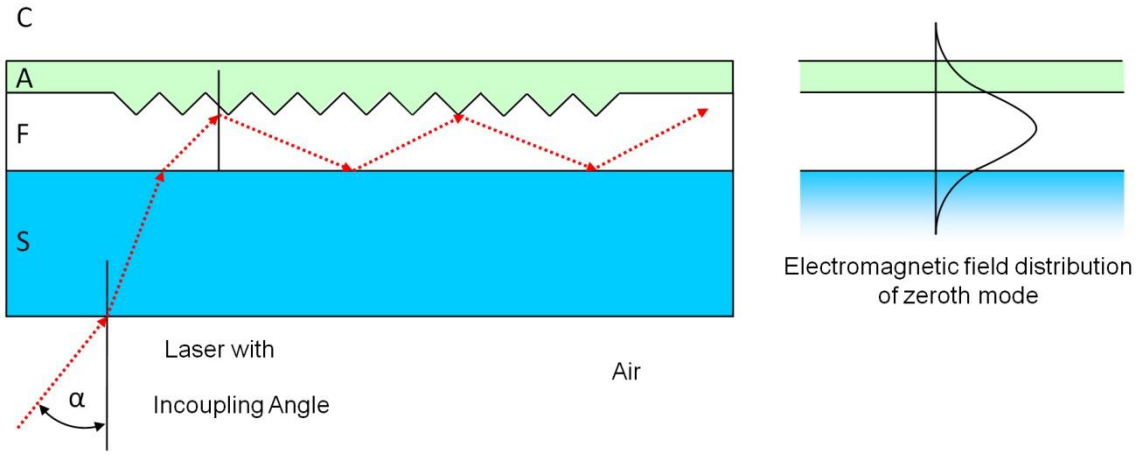

Figure 4.4 A diagram of the optical grating biosensor principle. The high refractive index layer (F) is supported on a substrate (S). The cover medium (liquid or air) is C. The red zig-zag represents a guided light beam and the part at the right hand side shows the evanescent fields (right) generated by total internal reflections at the F, A, C and F,S interfaces. The evanescent field interacts with capture layer A, which modifies the waveguide propagation constant and allowing cell shape and size, thin layer formation and dissolution, or more generally polarizability changes, to be monitored and analysed. Waveguide thickness d_F is typically 170 to 220 nm. Capture layer thickness d_A is typically less than 10 nm.

A mode is characterized by its effective refractive index (or mode index) which can be defined by the following equation

$$N=\frac{\beta}{k}=n_F \sin \alpha_F \qquad (4.3)$$

where β is the propagation constant (the wave component parallel to the waveguide), and k(=2π/λ) is the free space wavenumber. If no adlayer is adsorbed on the surface of the waveguide, then the measured effective refractive indices obey the following three-layer mode equation (Tiefenthaler and Lukosz, 1989) which can be used to calculate the parameters of the system, i.e. determine n_F and d_F in the case of the zeroth order modes) from the measured incoupling angles:

$$\pi m = \frac{2\pi}{\lambda}\sqrt{n_F^2-N^2}\,d_F - \tan^{-1}\left[\left(\frac{n_F}{n_S}\right)^{2\rho}\sqrt{\frac{N^2-n_S^2}{n_F^2-N^2}}\right] - \tan^{-1}\left[\left(\frac{n_F}{n_C}\right)^{2\rho}\sqrt{\frac{N^2-n_C^2}{n_F^2-N^2}}\right] \tag{4.4}$$

where ρ=1, $N=N_{TM}$ for TM mode; ρ=0, $N=N_{TE}$ for TE mode and m is the mode (in the case of zeroth order mode, m=0). When only these two modes are propagating in the film and n_C, n_S are known, then by measuring N(TE) and N(TM), the optogeometrical parameters, n_F and d_A, of the waveguiding film can hence be determined. If a thin optically isotropic adlayer (d_A « λ) is formed on the surface, then it leads to the four-layer mode equations (Tiefenthaler and Lukosz, 1989),

$$\pi m = \frac{2\pi}{\lambda}\sqrt{n_F^2-N^2}\left\{d_F+d_A\frac{n_A^2-n_C^2}{n_F^2-n_C^2}\left[\frac{\left(\frac{N}{n_C}\right)^2+\left(\frac{N}{n_A}\right)^2-1}{\left(\frac{N}{n_C}\right)^2+\left(\frac{N}{n_F}\right)^2-1}\right]^{\rho}\right\} \tag{4.5}$$

$$- \tan^{-1}\left[\left(\frac{n_F}{n_F}\right)^{2\rho}\sqrt{\frac{N^2-n_S^2}{n_F^2-N^2}}\right] - \tan^{-1}\left[\left(\frac{n_F}{n_C}\right)^{2\rho}\sqrt{\frac{N^2-n_C^2}{n_F^2-N^2}}\right]$$

where, as before, ρ=0 and 1 for the TE and TM modes respectively. If n_C, n_S, n_F and d_F are known, by solving these equations simultaneously to the parameters characterizing the adlayer d_A and n_A can be determined when N(TE) and N(TM) are measured, i.e., the adlayer parameters are calculated explicitly from the linearized 4-layer model (Ramsden, 1993), assuming the opticgeometrical parameters of the waveguide film (n_F and $d_{F)}$, the refractive indices of the cover (n_C) and the substrate (n_S), λ and mode number (m=0) are known. Equations for practical use are:

$$n_A=\left[\frac{\frac{FM(N(TM))}{A(N(TM))}-d_F}{\frac{FE(N(TE))}{A(N(TE))}-d_F}\left(\frac{1}{n_C^2}+\frac{1}{n_F^2}-\frac{1}{N(TM)^2}\right)-\frac{1}{n_C^2}+\frac{1}{N(TM)^2}\right]^{-1/2} \tag{4.6}$$

and

$$d_A=\left[\frac{FE(N(TE))}{A(N(TE))}-d_F\right]\left(\frac{n_F^2-n_C^2}{n_A^2-n_C^2}\right) \tag{4.7}$$

where

$$A(N)=\frac{2\pi}{\lambda}\sqrt{n_F^2-N^2}\ ; \tag{4.8}$$

$$FE(N)=\tan^{-1}\left[\sqrt{\frac{N^2-n_S^2}{n_F^2-N^2}}\right]+\tan^{-1}\left[\sqrt{\frac{N^2-n_C^2}{n_F^2-N^2}}\right]\ ; \tag{4.9}$$

and

$$FM(N)=\tan^{-1}\left(\frac{n_F^2}{n_S^2}\sqrt{\frac{N^2-n_S^2}{n_F^2-N^2}}\right)+\tan^{-1}\left(\frac{n_F^2}{n_C^2}\sqrt{\frac{N^2-n_C^2}{n_F^2-N^2}}\right) \tag{4.10}$$

It must be emphasized that the effective refractive indices N of an optical waveguide are a function not only of the materials of the waveguide properties, but also its environment (Tiefenthaler and Lukosz, 1989; Ramsden, 1993; Tien, 1977).

Table 4.1 summarizes the contributions to the uncertainty of the effective refractive index caused by the environment and mechanical properties of the apparatus used to measure α. During the measurement, the refractive index of the air will increase/decrease if the room temperature decreases or increases. The uncertainty of effective refractive index ΔN is therefore ± 1∼2 × 10^{-6}, note that all the contribution are of comparable magnitude.

Table 4.1 Contributions to the uncertainty of effective refractive index N in an input grating coupler (Ramsden, 1997).

Parameter	Typical value	Uncertainty	Physical origin
n_{air}	1.0002673	10^{-7}	Temperature fluctuations (±1°C)
α	0.09 rad	1.25x10^{-6} rad	Goniometer (mechanical instability)
λ	632.816 nm	0.001 nm	Laser mode jumping
Λ	416.147 nm	0.001 nm	Grating lateral thermal movement

4.3 Theory: analysis of results

4.3.1 Calculation of the number of adsorbed bacteria

The raw data from the OWLS measurement consist of sequential values of effective refractive index. Bacteria are somewhat too big to fulfill the conditions enabling us to make the uniform thin film approximation (UTFA) (Mann *et al.*, 1997) in order to calculate b. We could possibly correct the values determined from the UTFA, but since the correction requires parameters we do not have, we prefer to use a different procedure.

The number of adsorbed bacteria b is, to a good approximation, linearly proportional to the effective refractive index N(t). However, the constant of proportionality depends on the thickness and the refractive index of the waveguide prior to adsorption. To allow for this, we define a normalized effective refractive index:

$$\tilde{N}(t)=\frac{N(t)-N_0}{N_0} \tag{4.11}$$

where N_0 is the effective refractive index prior to adsorption. We therefore assume that b (the number of bacteria adsorbed on the surface) is proportional to $\tilde{N}$.

Provided the adsorption is quasi-irreversible, b will saturate at the jamming limit. Hence,

$$b_{sat}=\frac{\theta_J}{a} \tag{4.12}$$

where a is the area occupied by one bacterium (determined from micrographs).
This Equation (4.12) provides us with the means to calibrate $\tilde{N}(t)$, i.e.

$$\frac{\tilde{N}(t)}{\tilde{N}_{sat}}=\frac{b(t)}{b_{sat}} \tag{4.13}$$

The waveguides were examined in an optical microscope before and after exposure to the bacteria to verify (i) the cleanliness of the starting slide, and (ii) to check the precision of the calculation of b.

Chapter 5 Experimental Methods

5.1 Overview

The general approach was to use coated planar optical waveguides as adsorbing substrata for the bacteria when a fresh bacterial suspension was brought in contact with a waveguide, and to determine the kinetics of adsorption and the quantity adsorbed via continuous measurement of the effective refractive indices (phase velocities) of the zeroth order transverse magnetic (TM) and/or the transverse electric (TE) guided modes.

This chapter is organized as follows:
5.2 Culture and storage of bacteria
5.3 Viability
5.4 Resuspension
5.3 Estimation of concentration of bacteria in suspension
5.4 Determination of size of bacteria
5.5 Optical waveguide sensor
5.6 Waveguide cleaning process
5.7 Optical Waveguide Lightmode Spectroscopy (OWLS)
5.8 The propensity for *Escherichia coli* to adhere on gratings
5.9 Surface design by sputtering method (Future work)

5.2 Culture and storage of bacteria

The bacteria used for this work were *Escherichia coli* (strain JM83, a K12 derivative) and *Lactobacillus plantarum*[5]. These two were chosen as they are common nonpathogenic strains widely used for research, which makes them good representatives for investigating bacterial adsorption. Culture was carried out in the microbiology lab in Cranfield Health in Silsoe under Dr. Sarah Morgan's instructions. The materials for plate culture are general microbiological laboratory reagents including 10 g tryptone, 5 g NaCl, 10 g yeast extract. The materials were suspended into 1 L of distilled water to make a Luria broth (LB), then autoclaved at 120 ^{o}C. After cooling, 15 g of agar was added to the LB for making the bed on Petri dishes. The standard procedures for bacterial growth are follows:

[5] Provided by Dr. Sarah Morgan in Cranfield Health in Cranfield University.

(1) Take an agar plate and label it with the bacteria details with name and the condition of environment.
(2) Take inoculation loop and heat until red to remove any contaminants from loop.
(3) Let the loop cool to room temperature and use it to take a small quantity of culture from the frozen stock.
(4) Streak one quarter of the plate with bacteria.
(5) Flame the loop again as above and let it cool down again.
(6) Rotate the plate one quarter and streak from the end of the first part.
(7) Repeat step 5 and 6 until the plate is treated.
(8) Incubate the plate at 37 °C for 24 hours and during this time, colonies develop.

After 24 hours incubation, a fresh and single colony of *E.coli* was grown and ready either for an adsorption experiment (see next paragraph) or stored in the freezer at -80 ^{o}C.

A live sample of *E. coli* was cultured in 100 ml Luria broth (LB) overnight for approx. 18 hours at 37 ^{o}C. *Lactobacillus plantarum* was cultured in 100 ml MRS broth overnight at 30 ^{o}C. After liquid culture, each of the samples were centrifuged at 1300 rpm for 10 min at 4 ^{o}C to pellet the bacteria. After removal of the supernatant, pellets were resuspended in cold phosphate-buffered saline (PBS) and centrifuged as above. This was a wash step to remove traces of the liquid broth, which may interfere with the surface in the adsorption measurement. After supernatant removal, the pellets were resuspended in cold aqueous buffer, either PBS or Z (HEPES) buffer. They were then stored at 4 ^{o}C before use.

5.3 Viability

Where necessary, the viability of the bacteria was checked by spread plating technique. The materials for plate culture are general microbiological laboratory reagents including 10 g tryptone, 5 g NaCl, 10 g yeast extract. The materials were suspended into 1 L of distilled water to make a Luria broth (LB), then autoclaved at 120 ^{o}C. After cooling, 15 g of agar was added to the LB for making beds in Petri dishes. Figure 5.1 shows the growth of *E. coli* on an agar plate and Figure 5.2 shows the viability test of *E.coli*.

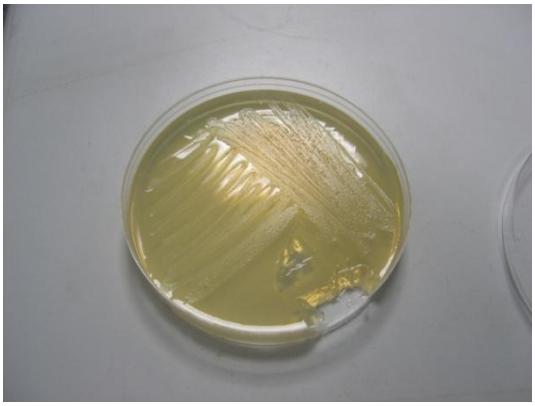

(a) After 1 hour

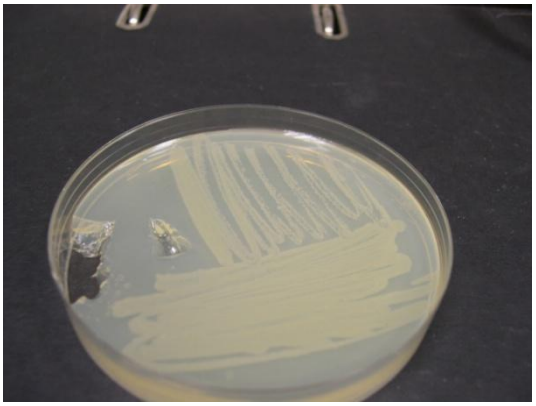

(b) After 10 hours

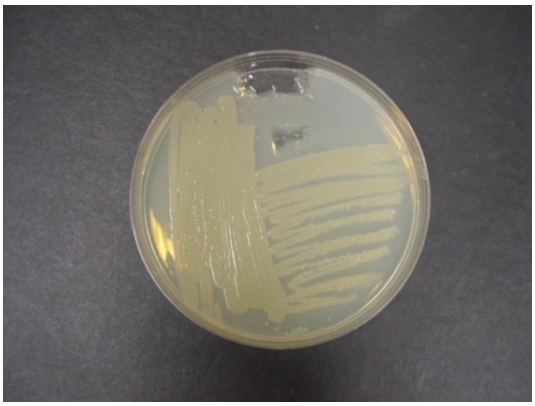

(c) After 15 hours

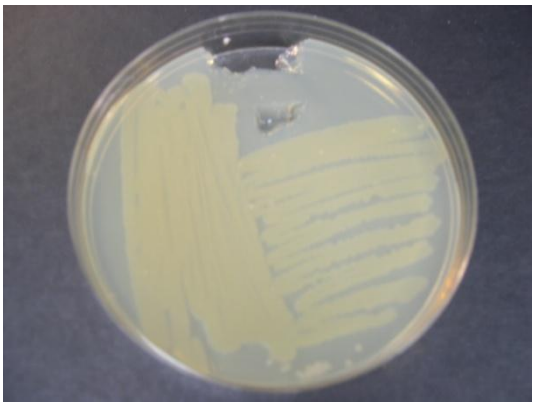

(d) After 24 hours

Figure 5.1 *E.coli* growth on agar.

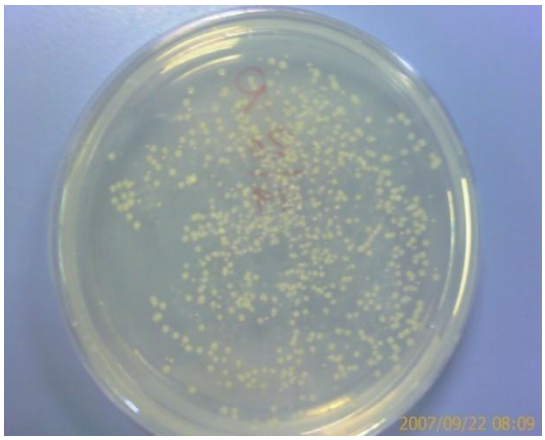

Figure 5.2 Viability test of *E.coli*.

5.4 Resuspension

Bacterial preparations were allowed to dry on a glass cover slip and examined in a Philips XL Series environmental scanning electron microscope (ESEM). A typical image is shown in Figure 5.3. Some of these preparations were coated with gold and examined in a Hitachi S-4200 scanning electron microscope (SEM). A typical image is shown in Figure 5.4. From these two figures it can be seen that the bacteria are actually quite polydisperse (variable in both size and shape). Figure 5.5 shows different magnifications and appearances.

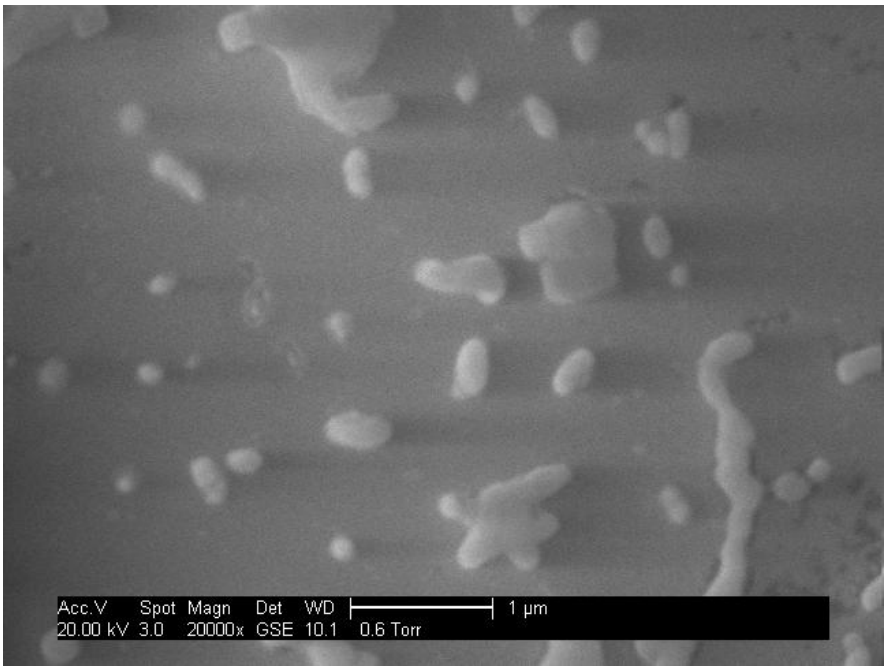

Figure 5.3 Typical ESEM image of *E. coli*.

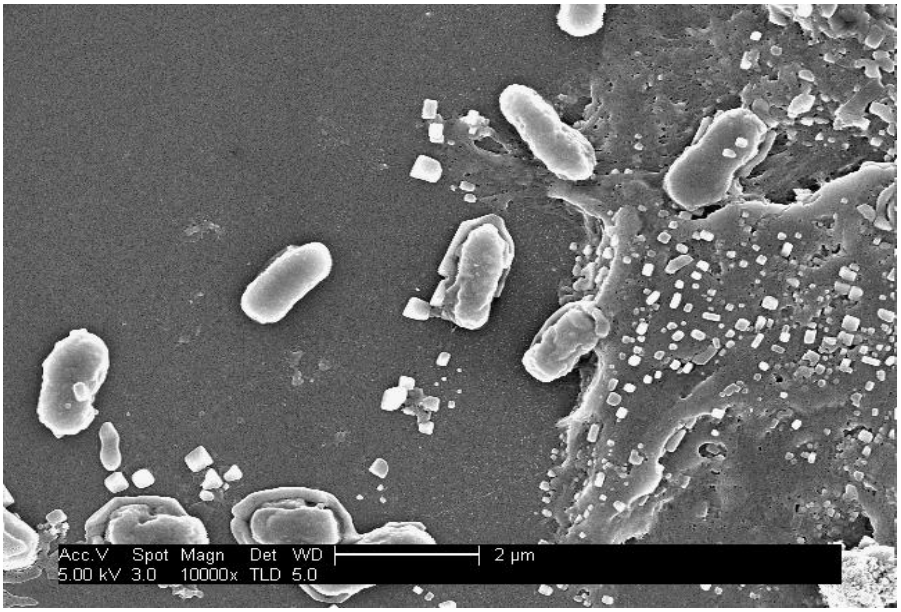

Figure 5.4 Typical SEM image of *E. coli* (gold-coated).

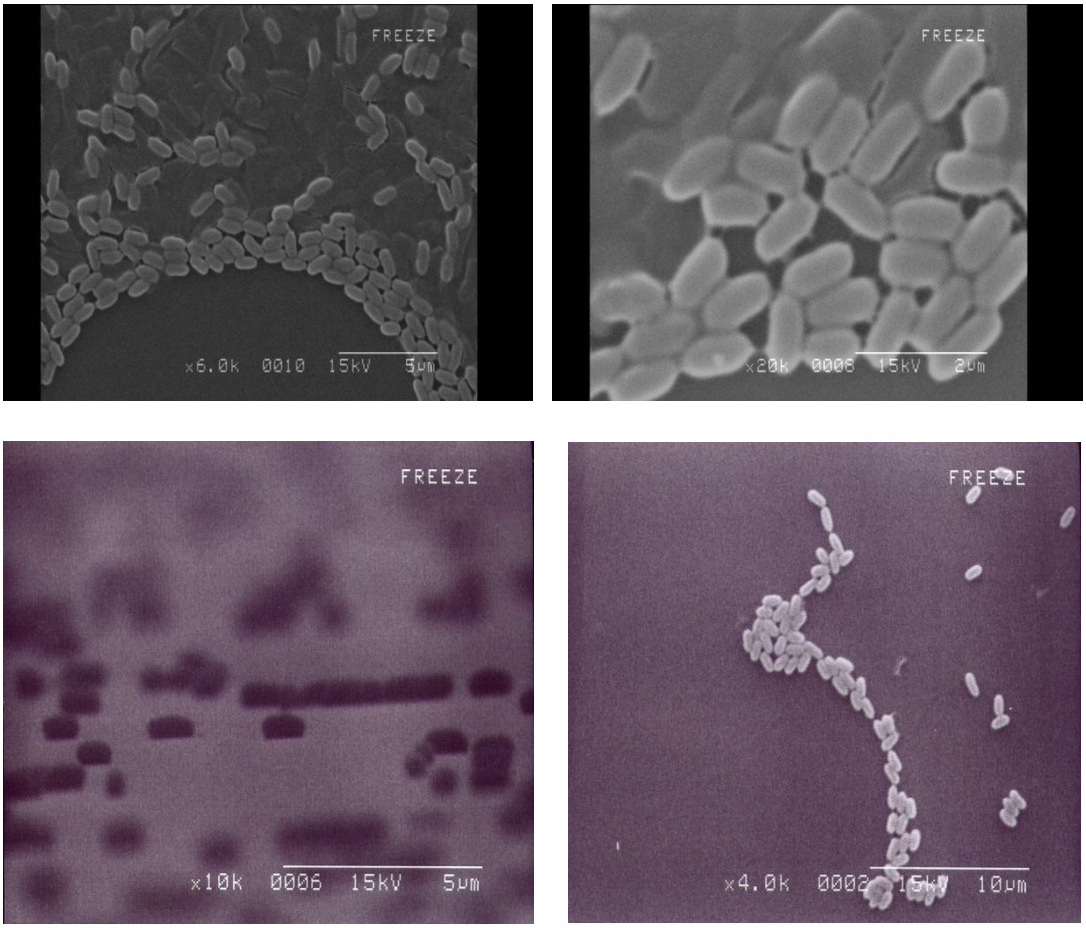

Figure 5.5 SEM images of *E. coli* (gold-coated).

5.5 Estimation of concentration of bacteria in suspension

The concentration c of bacteria in suspension was counted using a hemocytometer under an optical microscope. The hemocytometer (Figure 5.6) is a common device for counting cells or other microscopic particles in solution and provides a direct and visual approximation of cell concentrations in a specific volume. The hemocytometer was provided by Marienfeld (GmbH, Marienfeld, Germany, Neubauer-improved model). The bacterial suspension was diluted 10 to 100 times if the number of bacteria was too great to count.

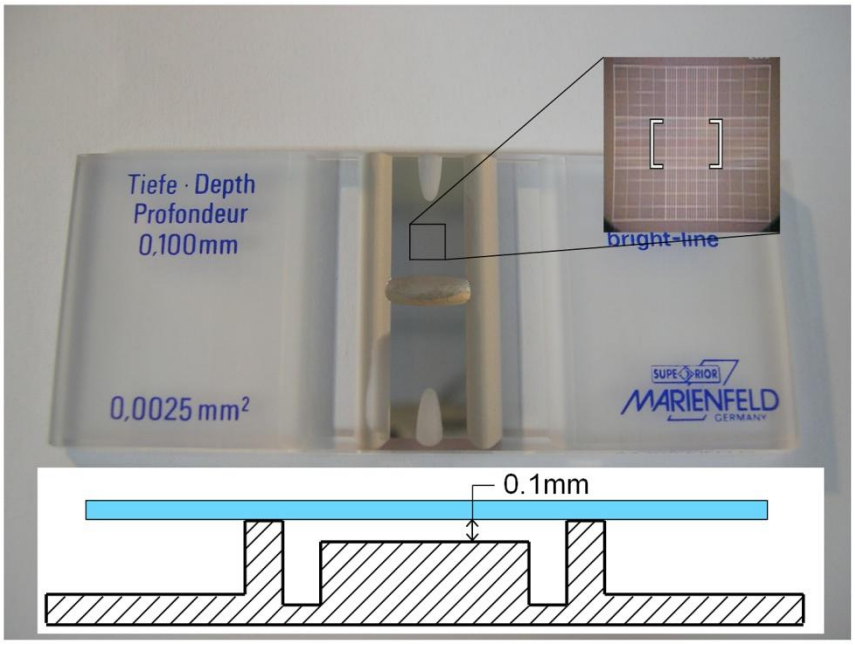

Figure 5.6 Hemocytometer.

The typical procedure was:

1. Collect 5 ml fresh samples from liquid cultured bacterial suspensions and dilute the concentration 10x with 50 ml PBS buffer solution.
2. Place a 50 µl drop of the diluted bacterial sample between the cover glass and the counting chamber on the hemocytometer.
3. Count the number of bacteria in five 0.2x 0.2 mm squares R_1 to R_5 (see Figure 5.7) and average.

Example: average numbers of *E. coli* per 0.04 mm^2 is 393, which means 9,825 *E. coli* in 1 mm^2. Because the thickness is 0.1 mm (see Figure 5.6), the number of *E.coli* in 1 ml in the original undiluted sample is 9.825 x 10^8 cells in buffer solution.

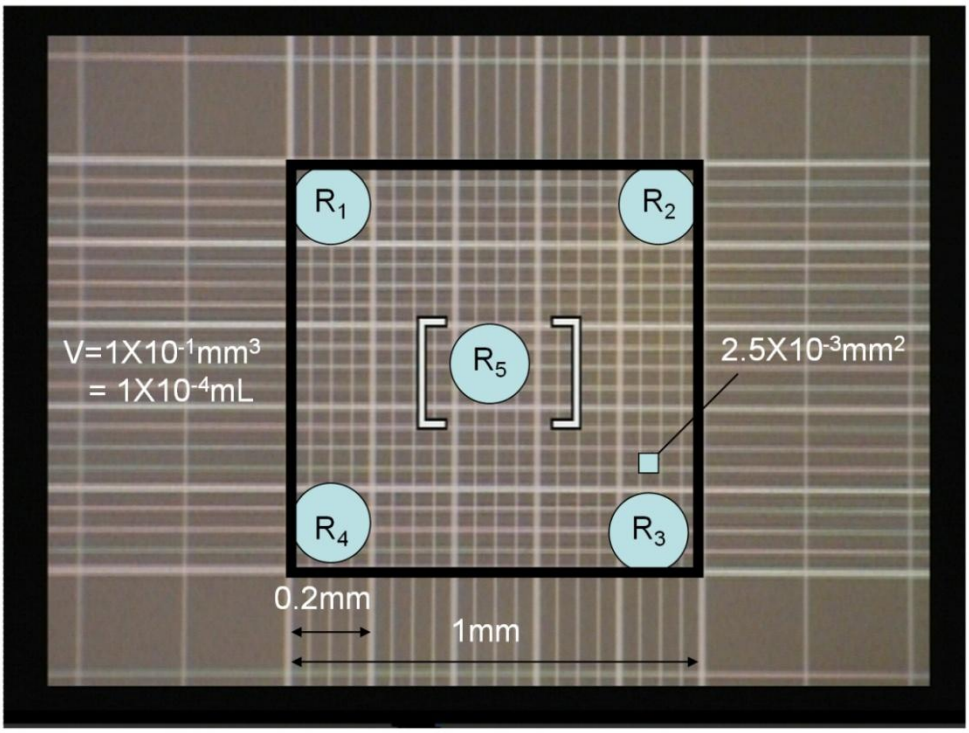

Figure 5.7 Hemocytometer grid.

5.6 Determination of the size of the bacteria

Usually colony size and morphology in many bacteria, including *E. coli* and *L. plantarum* can greatly vary from strain to strain in the same media. The outer aspect of a colony is not a good guide for identification. There is, however, we determined the size of bacteria using electron microscopy in this work for the consistency of the modeling adsorption kinetics.

5.6.1 Optical microscopy

Microscopic characterizations of bacterial suspensions were allowed to adsorb for 10 minutes on glass cover slips cleaned in the same way as the waveguides. The slides were examined in a Nikon 400X microscope (Figure 5.8) and Leica DM LB2 phase contrast microscope (Figure 5.9); the typical images are Figure 5.10 and Figure 5.11 respectively. For these preparations the bacterial stock solutions were diluted 100 times in buffer.

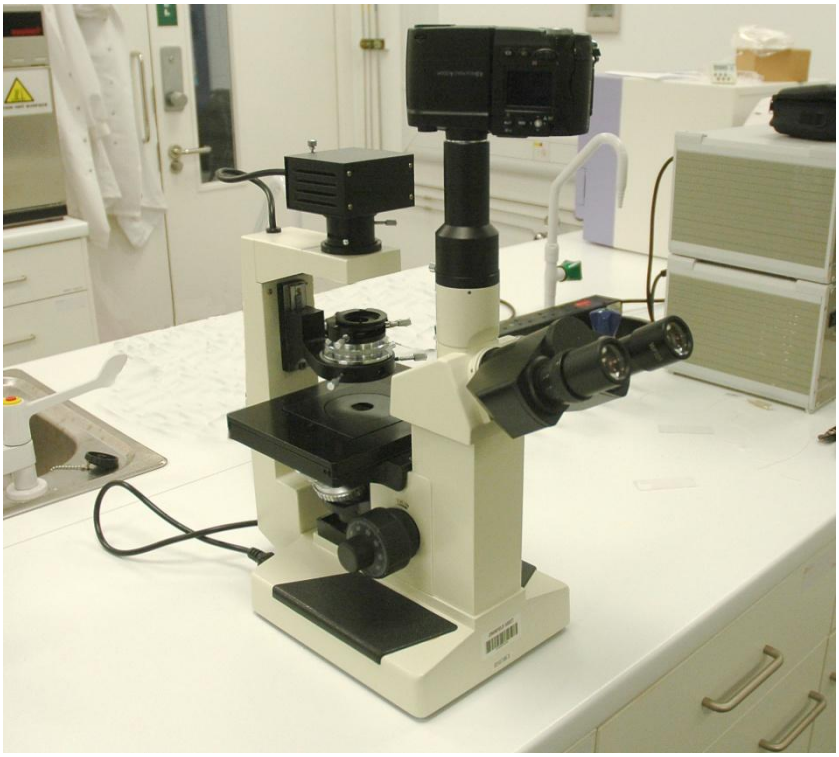

Figure 5.8 Nikon 400X microscope.

Figure 5.9 Leica DM LB2 phase contrast microscope.

Figure 5.10 Optical micrograph of *E. coli* adsorbed on a TiO_2 waveguide.

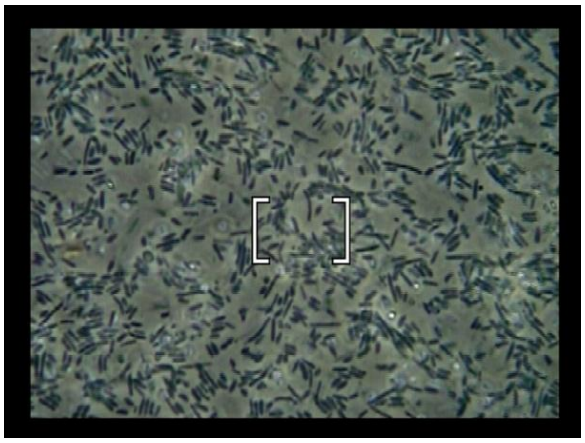

Figure 5.11 Phase contrast micrograph of cultivated *E. coli* in PBS.

5.6.2 Electron microscopy

This observation contrasts with the textbook characteristics of *E. coli* — a motile Gram-negative rod-shaped bacterium, 2 µm in diameter and 4 µm in length (Figure 5.12), and *Lactobacillus plantarum* - a non-motile Gram-positive rod-shaped bacterium, with a size of approximately 1 µm in diameter and 6 µm in length (Figure 5.13).

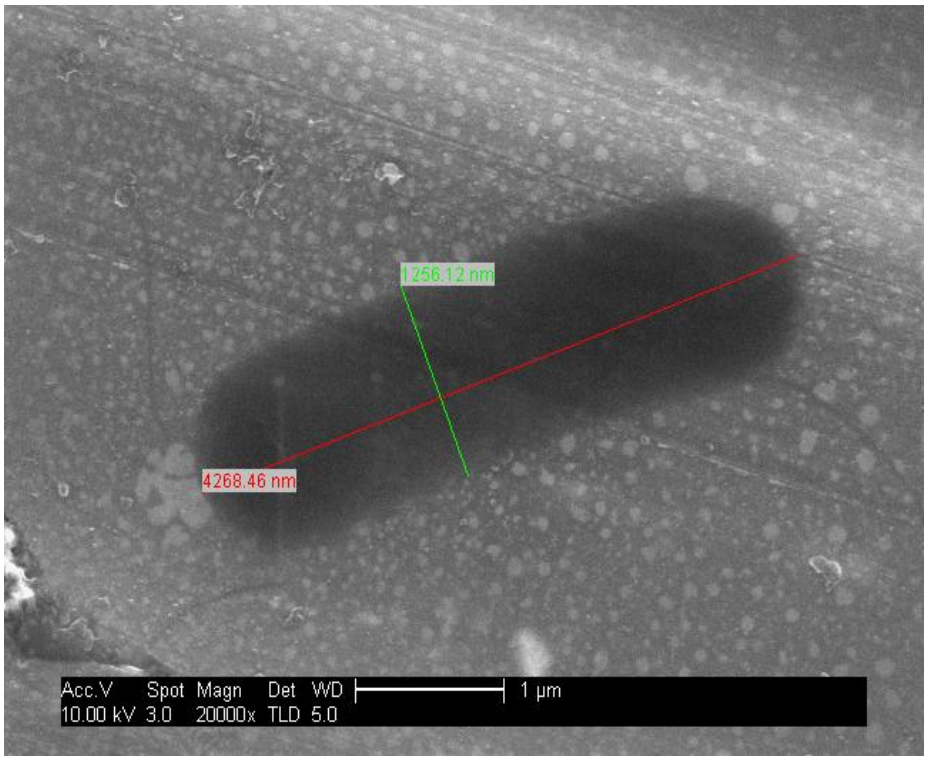

Figure 5.12 Representative SEM micrograph of *E.coli*.

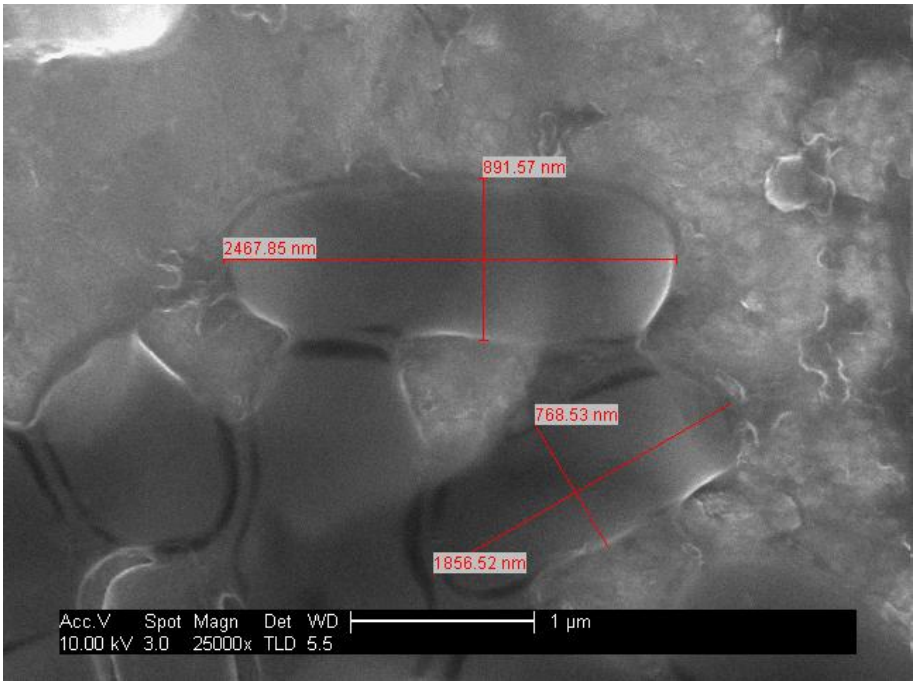

Figure 5.13 Representative SEM micrograph of *L. plantarum*.

5.6.3 Quantitation of size

The mean geometrical parameters of both bacteria are shown in Table 5.1. The size of each bacterium is different and varies from 50 to 100 nm in length and width. We assume that the diffusivity of bacterium is in homogeneous, isotropic, viscous media; hence, the diffusion coefficient D of the bacterium was determined from the Stokes-Einstein equation assuming the bacteria to be spherical:

$$D=\frac{k_B T_S}{6\pi r\eta} \tag{5.1}$$

where k_B is Boltzmann's constant ($k_B = 1.38\times10^{-23}$ J K^{-1}), T_S is the absolute temperature, r is the bacterial equivalent radius (i.e., the radius of the sphere equal to the radius of the disc with the same projected area as that of the (irregularly shaped) bacterium) and η is the viscosity of the medium (taken to be that of pure water (1.002×10^{-3} Ns/m^2 at 20 ^{o}C).

Table 5.1 Mean geometrical parameters of the bacteria.

Strain	Mean length/nm	Mean width/nm	Projected area $\bar{a}/\mu m^2$	Equivalent radius r/nm	Diffusivity D/m^2s^{-1} @20 ^{o}C
E. coli	4270±100	1256.12±100	5.02±0.01	1260 ±100	1.693×10^{-13}
Lactobacillus plantarum	2470±100	891.57±100	2.03±0.01	803 ±100	2.663×10^{-13}

This assumes that the evidently spherocylinderical bacteria adsorb with their long axis parallel to the substratum surface.

5.7 pH buffer solution

The buffer solutions for bacteria adsorption were PBS, Z1 and Z1150 buffer. The composition of the PBS was 0.14 M NaCl, 3 mM KCl and 0.01 M sodium phosphate buffer (pH 7.4), purchased in tablet form from Gibco (Paisley, Scotland). The Z1 buffer was made from 2.383 g of HEPES and 0.688 ml of 6 M KOH in 1 litre at 0.01 M (pH 7.4). The composition of Z1150 was Z1 with an additional 0.15 M NaCl.

5.8 Optical Waveguide Lightmode Spectroscopy (OWLS)

Optical waveguide lightmode spectroscopy (OWLS) is adequate for providing the high-accuracy kinetic data required with excellent time resolution. In this technique, the adsorbing surface (which should be ultra-smooth and planar) performs a dual role as both adsorbent and as an optical waveguide. The adsorbing surface is an optical waveguide, which can be coated with desired materials beforehand, and the spectrum of guided modes is measured by the grating coupler. The time resolution of the measurement depends on the particular experimental arrangement, see Chapter 4.

The optical waveguide is mounted on a goniometer, which is used for measuring the effective refractive indices N_{TE} and N_{TM} (Figure 5.15) while the biological samples flow through a cuvette of which the waveguide forms the floor. As the goniometer rotates with respect to the fixed laser beam, successive discrete modes (TM_0, TE_0, etc.) are coupled into the waveguide and received at the photodetector (Ramsden *et al.*, 1995).

The adsorption results presented in this thesis were obtained with the integrated optical scanner IOS-1. This is a commercially available instrument produced by the company Artificial Sensing Instruments (ASI, Zürich, Switzerland). Here the most basic model was used which consists of four main parts (Figure 5.14). The main part contains the measuring head with the sensor chip and detector photodiodes, preamplifiers, goniometer with the stepping motor for varying incoupling angle α, and the laser light source (see Figure 5.15). The second part is a PC-compatible computer with an A/D converter board. All the measurements are controlled by the computer. The third part is a power supply unit PSU 1-3 for the sensor system; this unit also contains a main signal amplifier. The fourth part is a peristaltic pump (Gilson Miniplus 3, Gilson Medical Electronics, Villiers-le-Bel, France) (see Figure 5.16); this is connected to the flow cell (cuvette) (see Figure 5.17).

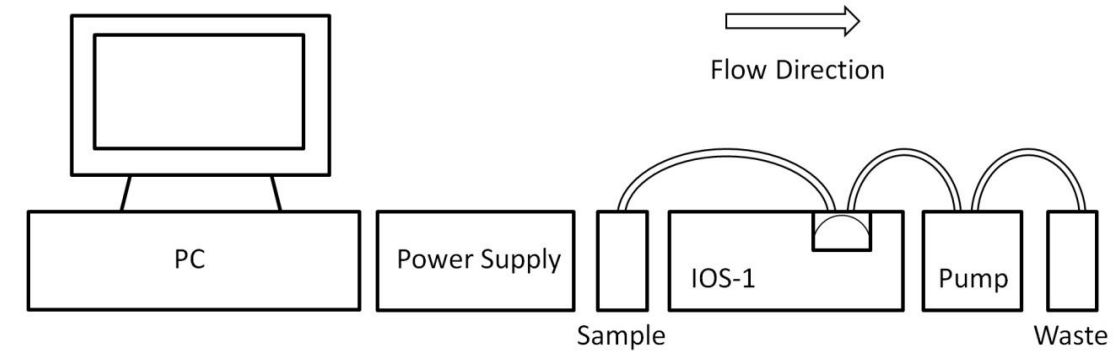

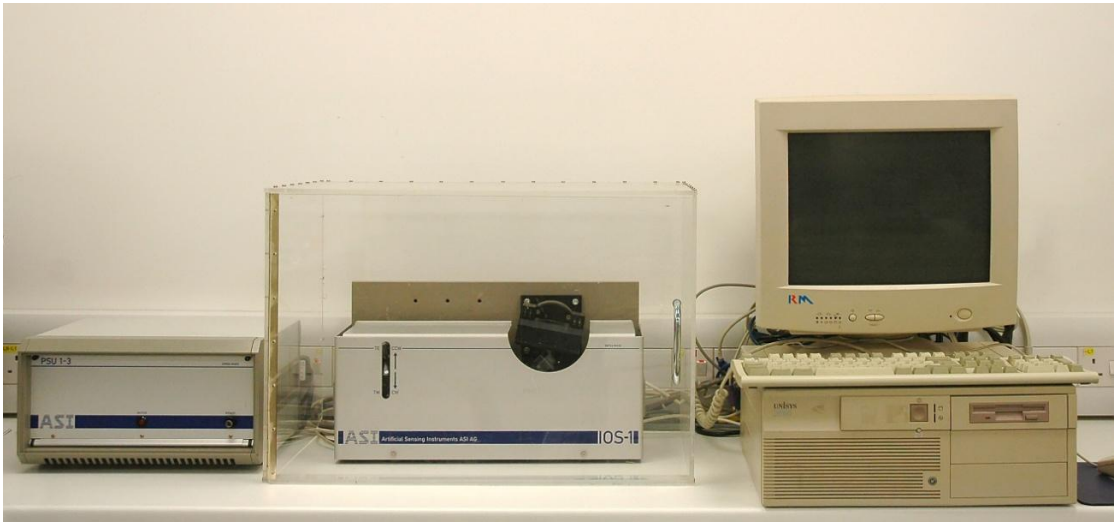

Figure 5.14 Integrated Optical Sensor (IOS-1), made by ASI.

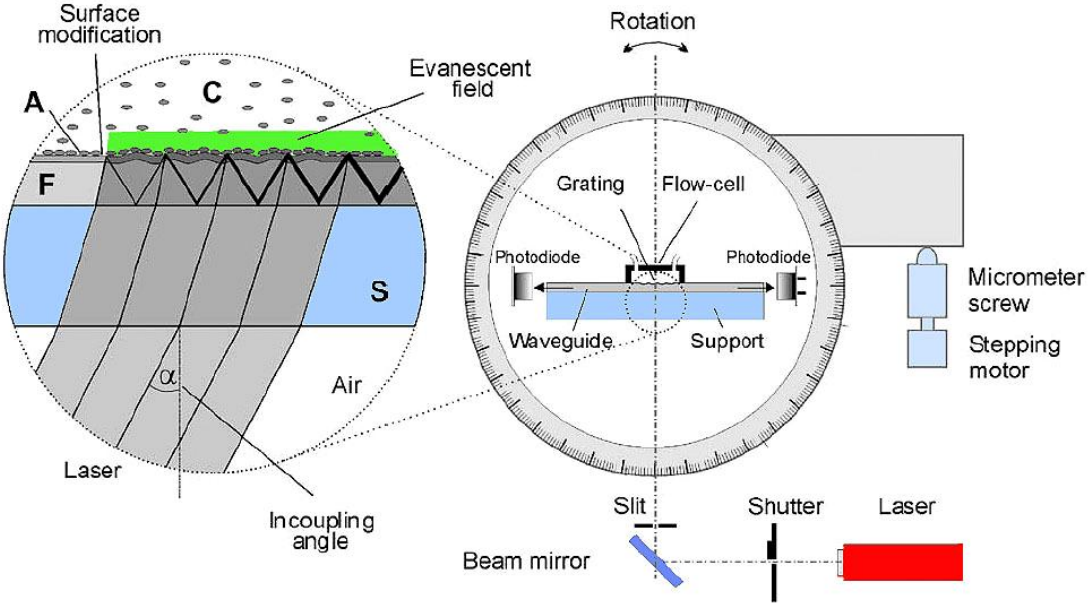

Figure 5.15 Goniometer (Vörös.J. *et al.*, 2002).

Figure 5.16 Gilson Minpuls 3 peristaltic pump.

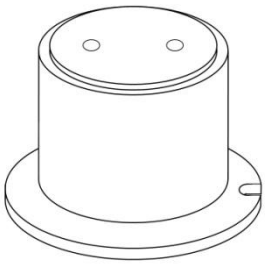

Figure 5.17 Flow cell (cuvette), diameter is 10 mm.

In this work, all the experiments were carried out at room temperature. To minimize temperature fluctuations during measurements, the main part was covered with a Perspex box. The flow cell was cylindrical and made from passivated aluminium. It was sealed to the chip with a Kalrez O-ring. The diameter was 1 cm and the total volume was 34 µl. The cuvette was clamped and sealed to the surface of the sensor chip with the help of a screw.

Inlet and outlet tubes of the flow cell were made of Teflon and had an inner diameter of 0.3 mm. The peristaltic pump was placed after the cuvette, which means that the solutions are sucked rather than pumped through the cell. This avoids contamination from the soft rubber tubing of the pump but sometimes leads to air bubble formation inside the flow cell. The tube between the sample solution holder and the cuvette was 20 cm long, which the total volume of solution in tube is 14 µl.

5.8.1 Optical waveguide grating coupler sensor chip (OW2400)

An optical waveguide grating coupler sensor chip is shown in Figure 5.18, it is the key element of the optical waveguide sensor and is used to sense the adsorption of the cells. For exact and reliable measurements, the waveguide chips need high specification characterics, for example the thickness and the refractive index of the waveguiding layer, the fine periodicity of the grating, etc. The chip can be divided into three layers: optical glass substrate, thin waveguide layer with fine optical grating, and cover medium. There is a resonance angle, at which a linearly polarized laser (He-Ne) is coupled via the grating into waveguide layer (see Chapter 4). This incoupling angle will change if there is some adsorption of cells on the waveguide surface.

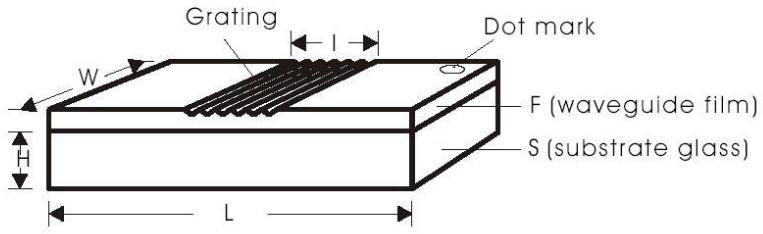

Figure 5.18 Waveguide grating coupler sensor chip (Made by MicroVacuum Ltd).

Sensor chips (Figure 5.18) for the IOS-1 instrument consist of a glass support S and a waveguiding film F resting on the top of S. The dimension of the chip is 48 mm long, 16 mm wide and 0.6 mm thick. The grating is 2 mm wide and has a depth of about 15 nm (details are in Table 5.2). The thickness of F is typically in the range of 170-220 nm and produced by pyrolyzed sol-gel dip coating (ASI 2400, made by Microvacuum Ltd., Budapest, Hungary). The incoupling grating was made by an embossing method. During embossing, the substrate with the gel film bends under the applied force produced by pneumatic cylinder and touches the master grating with 2400 lines/mm periodicity, the sol-gel material on the substrate fills the grooves of the master grating and a replica is formed in the sol-gel film.

Table 5.2 Physical and optical parameters of the sensor chip.

Sensor Chip	Characterization
Substrate Glass Slide (L × W × H)	48 mm × 16 mm × 0.55 mm refractive index (n_S)=1.53
Surface Relief Structure	depth≈ 5~15 nm
Grating Periodicity	2400 lines/mm
Grating Area Dimensions	length (l) ≈ 2 mm width (w)=16 mm
Waveguide Material (Sol-Gel)	$Si_xTi_{(1-x)}O_2$, where x=0.75±0.05
Waveguide Film	refractive index (n_F)=1.77±0.03 thickness (d_F)=170-220 nm

Different surfaces. Physical vapour deposition (PVD) was used to coat them with a thin (10–20 nm) layer of silica, titania alumina or zirconia.

5.9 Waveguide cleaning process

The surface properties of the chips are of great importance when doing any surface adsorption experiments or chemical modification of the chip surface. Unfortunately, the surface properties of the chip can vary quite a lot (e.g. due to contaminations) even when the chips come from the same product line. Although the chips were planned originally to be disposable, in practice they must be regenerated, not only because of their current relatively high price at present, but also due to the uniqueness of the chips, i.e. to produce reliable results, the same chips should be used in a series of experiments. This is only possible when the cleaning method used to regenerate the chips does not modify the surface properties of the sensors. Brand new chips may also be strongly contaminated (e.g. from the atmosphere or the package box) and should not be used directly.

A numbers of methods have been reported to clean the sensor chips in a reproducible ways:

(1) 30 minutes in Caro's acid (permonosulphuric acid, H_2SO_5; (Kurrat *et al.*, 1994));

(2) 10 minutes in an ultrasonic bath containing 10% Contrad 90® (Technosa SA, Lausanne, Switzerland) and then 1 minute in chromic acid (Nellen and Lukosz, 1990; Nellen and Lukosz, 1991);

(3) Washing with undiluted Deconex®(Borer Chemie AG, Switzerland) and then 5 minutes sonication in 10 % solution of Deconex® (Clerc and Lukosz, 1997). Between the different cleaning steps, the chips were always extensively rinsed in distilled water;

(4) We use standard planar optical waveguide sensor chip (ASI2400) obtained from MicroVacuum (Budapest). Prior to use, the waveguides were cleaned by immersing in chromic acid for 3 minutes and then very briefly dipped in potassium hydroxide (KOH) immediately afterwards to minimize the damage to grating. Then the waveguides were sonicated with deionized water at room temperature, changing the water frequently during sonication. Finally they were dried with filtered nitrogen and treated with O_2 plasma at 20 mW for 3 minutes. The waveguides were kept in deionized water for at least 30 minutes before measurement.

(5) A very effective method is cleaning in an oxygen plasma: 2 minutes removes any organic contamination from the surface, especially if some preliminary cleaning (washing with ethanol) is also carried out. After plasma treatment the surface is rather hydrophilic with a low contact angle (Chien *et al.*, 2005). These freshly cleaned surfaces are so reactive that after one hour in air they will be contaminated. To avoid this, one can only use freshly cleaned chips or must keep the cleaned chips in pure water or buffer solution.

(6) Prior to use, the waveguides were cleaned by agitated immersion in a 1% solution of COBAS Integra cleaner (Roche) at room temperature (25 ^{o}C), and equilibrated in PBS or Z1150 until a stable baseline was achieved.

For my experiments, the above cleaning process (4) was combined with oxygen plasma treatment (5).Procedure (6)was used between members of a series of consecutive experiments. A considerable inconvenience is the baseline drift of the chips, which means a slow change in N(TE) and N(TM) whenever a chip is placed in contact with a new cover medium C. The changes may last for tens of minutes to tens of hours so pre-soaking the waveguide chips in the buffer before measurement is needed to get the saturated baseline. Previous work shown that it is possible to reduce the N(TE) and N(TM) drift to $1.6 \times 10^{-8} s^{-1}$ and a slightly bigger drift could be acceptable (Csúcs and Ramsden, 1998b). With Kurrat's ASI-eval program[6], it is possible to extrapolate and subtract the baseline drift from the measured curves.

5.10 Adsorption experiments

The waveguides were sealed to a cylindrical flow-through cuvette such that they formed the floor of the cuvette. The assembled cuvette was mounted in an IOS-1 integrated optical scanner (Artificial Sensing Instruments, Zürich). The bacterial suspension was pumped through the cuvette using a Gilson Minpuls 3 peristaltic pump at a flow rate F of 10 µl/s. After a steady condition was reached, flow was switched back to pure PBS or Z1150 without bacteria. The effective refractive indices N of the zeroth transverse magnetic (TM_0) and transverse electric (TE_0) modes at a wavelength λ = 632.814 nm were determined by continuously scanning the incoupling angles.

Choice of concentration of bacteria. It was found that diluting the original liquid cultures 100x gave conveniently measurable kinetics.

[6] Evaluation program written by Dr. Roger Kurrat for OWLS results, based on Equation (4.4).

An outline of the procedure is given in Figure 5.19 and the details are described in Figure 5.20.

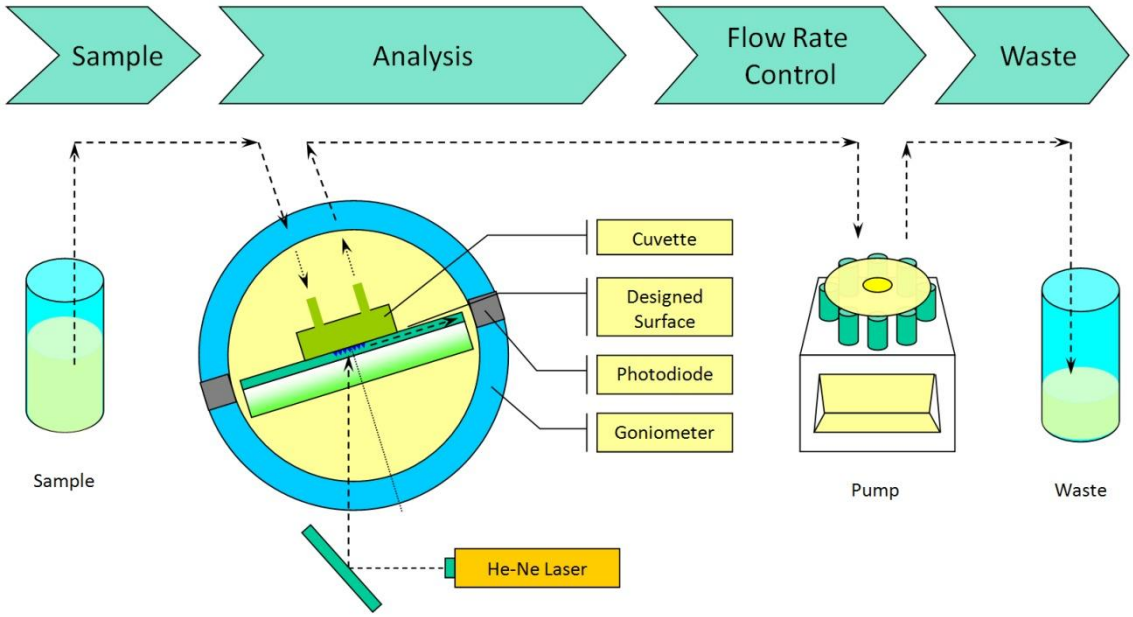

Figure 5.19 Outline of adsorption kinetics measurement procedure.

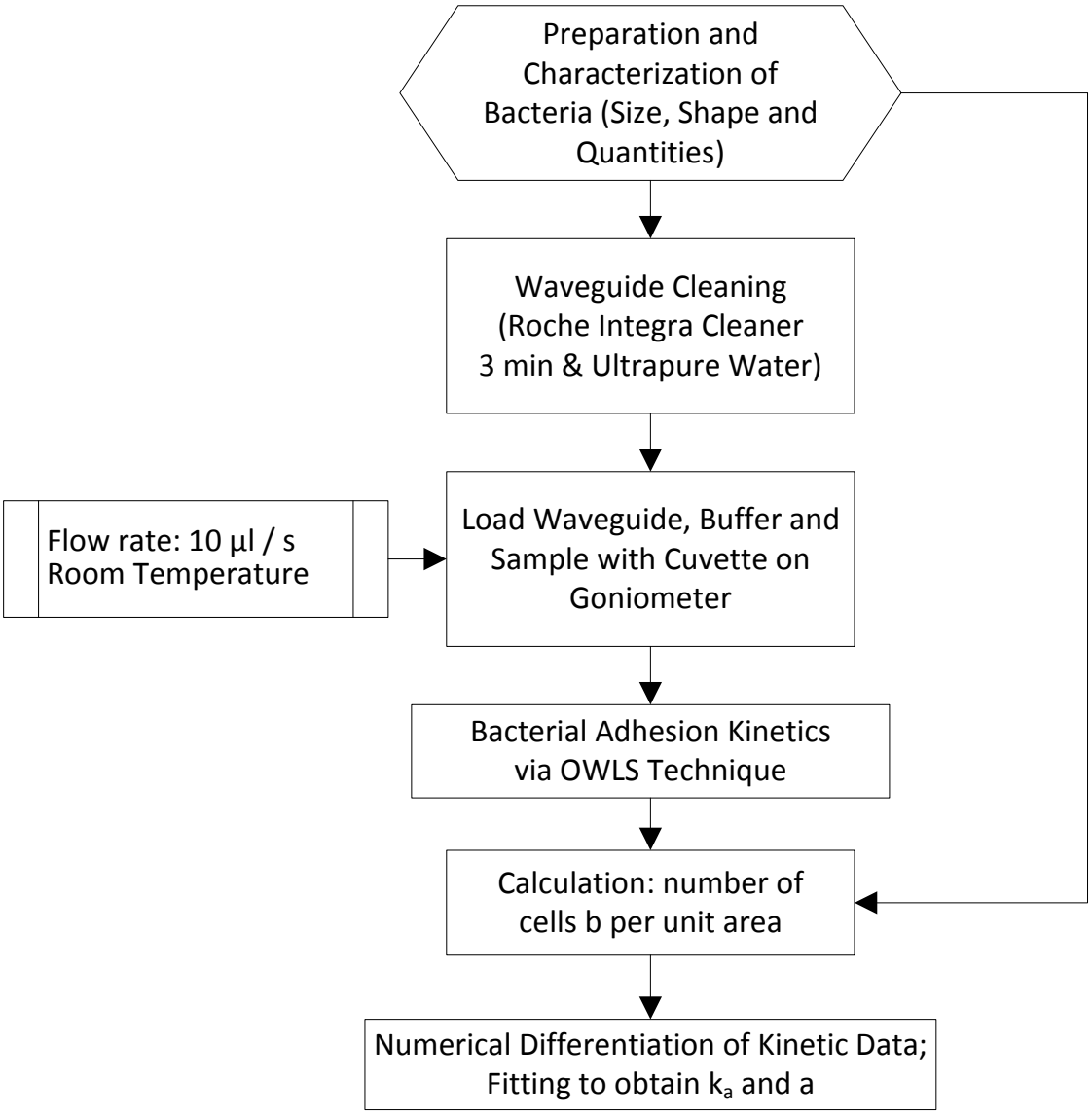

Figure 5.20 Standard procedures (experimental flow chart).

5.11 The propensity for *Escherichia coli* to adhere to gratings

Since the use of the grating coupler inevitably implies that deposition takes place on the grating (albeit a shallow one), it was of interest to investigate the influence of the grating on bacterial adsorption.

5.11.1. Grating Fabrication

In this work, two types of grating (U grooved and V grooved) were applied to a common polymer biomaterial PMMA, the dimension of the substrate 10 mm x 10 mm x 3 mm. The specific gravity of PMMA is 2.1 g cm^{-1} and the melting point is 170 ^{o}C.

The fabrication technique of the nanostructure is the hot embossing method. The die material is silver-nickel alloy, and is commercially available (a part of the dies used to emboss DVD ROMs). The dimensions of the U groove were 400 nm in width and 200 nm in depth (Figure 5.21) and the V groove had the same width of 200 nm but was only 50 nm in depth (Figure 5.22).

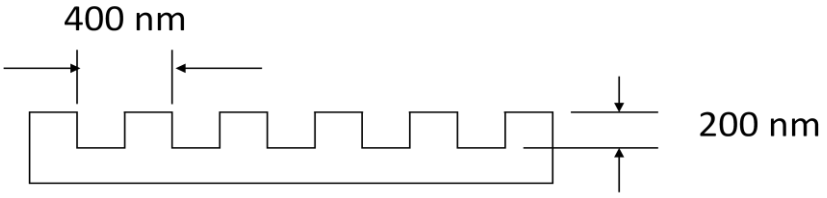

Figure 5.21 U-grooved structure.

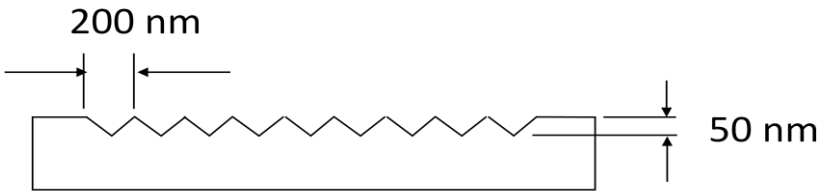

Figure 5.22 V-grooved structure.

The schematic diagram of hot embossing is shown in Figure 5.23. During the experiments, the optimized condition for making fine grating on PMMA is a 400 kg load at 150 ^{o}C for 90 seconds. After applying the U-grooved and V-grooved gratings on PMMA, the substrates were sterilized in an autoclave at 121 ^{o}C for 30 minutes and then put into a flask containing a suspension culture of *E.coli* at 37 ^{o}C for 24 hours after cooling.

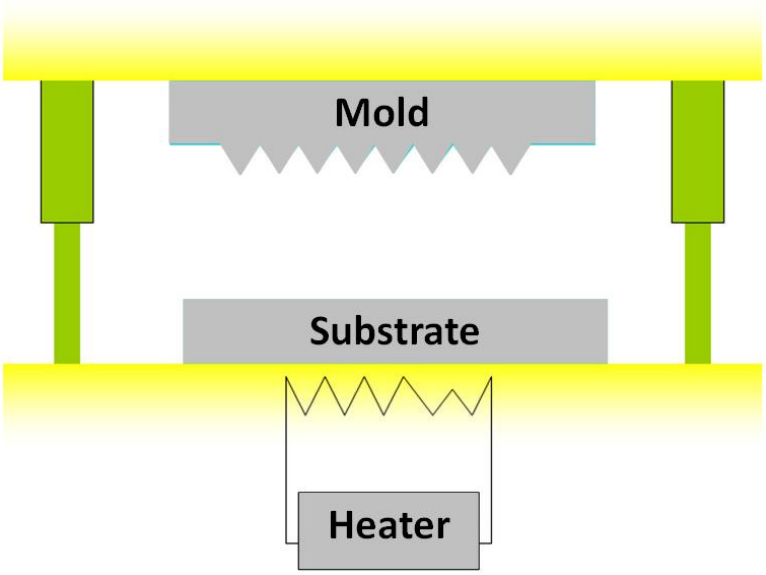

Figure 5.23 Schematic diagram of hot embossing.

5.11.2 Fabrication results

The structure of U-grooves and V-grooves on PMMA were investigated by scanning electronic microscopy (Figure 5.24). The results of atomic force microscopy (AFM) are shown in Figures 5.25 and 5.26. Grating shapes are satisfactory and can be changed by grating die redesign.

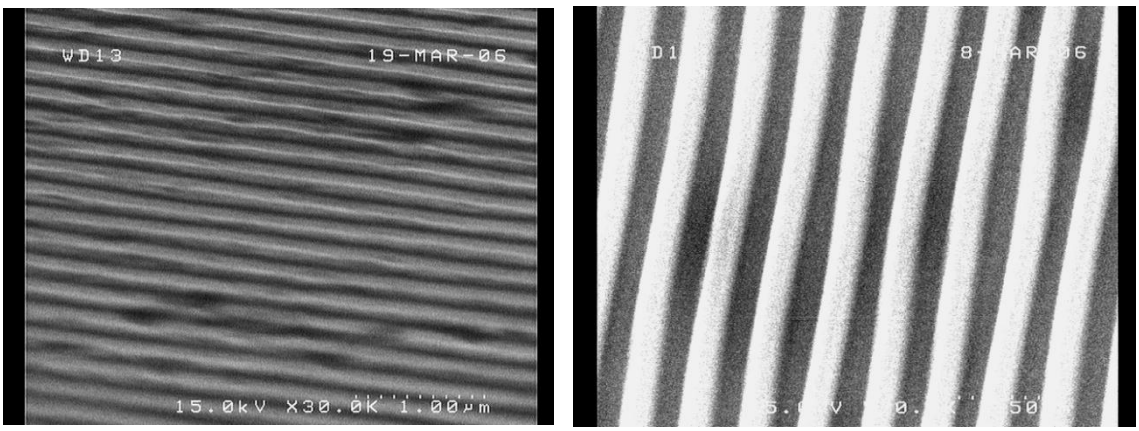

Figure 5.24 SEM images of V-grooved grating (Left) and U-grooved (Right) on PMMA.

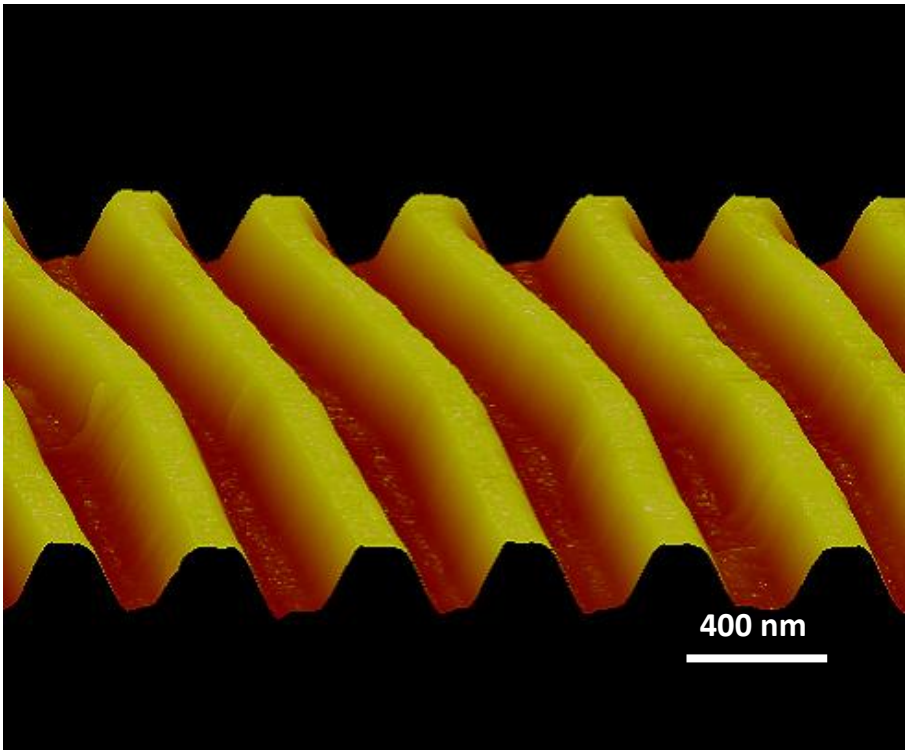

Figure 5.25 AFM image of U-grooved grating on PMMA.

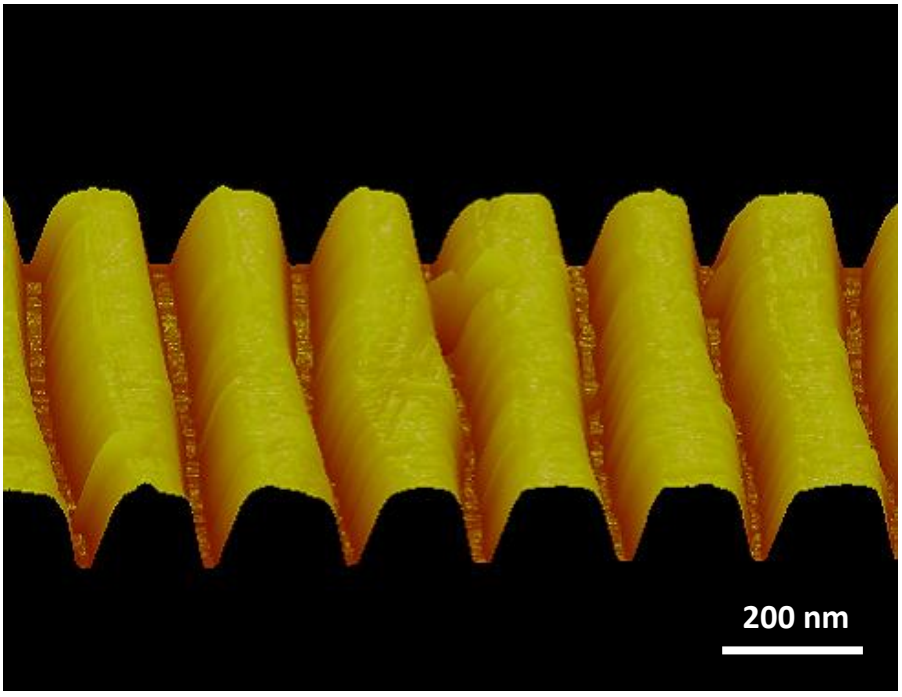

Figure 5.26 AFM image of V-grooved grating on PMMA.

5.11.3 Adhesion results

In order to investigate the affinity of ungrooved PMMA to *E.coli* for comparison, we also simply placed the ungrooved PMMA into an agitated *E.coli* suspension for 24 hours at 37 ^{o}C and rinsed with pure water. Figure 5.27 shows the SEM results. Although pure PMMA is fairly hydrophobic (water contact angle is 53 ^{o}C), nevertheless only very few *E.coli* cells randomly attached to the ungrooved PMMA (Right). Note that PMMA is well known as a biocompatible material for contact lenses and intraocular devices (Alava *et al.*, 2005; Bertoluzza *et al.*, 1991).

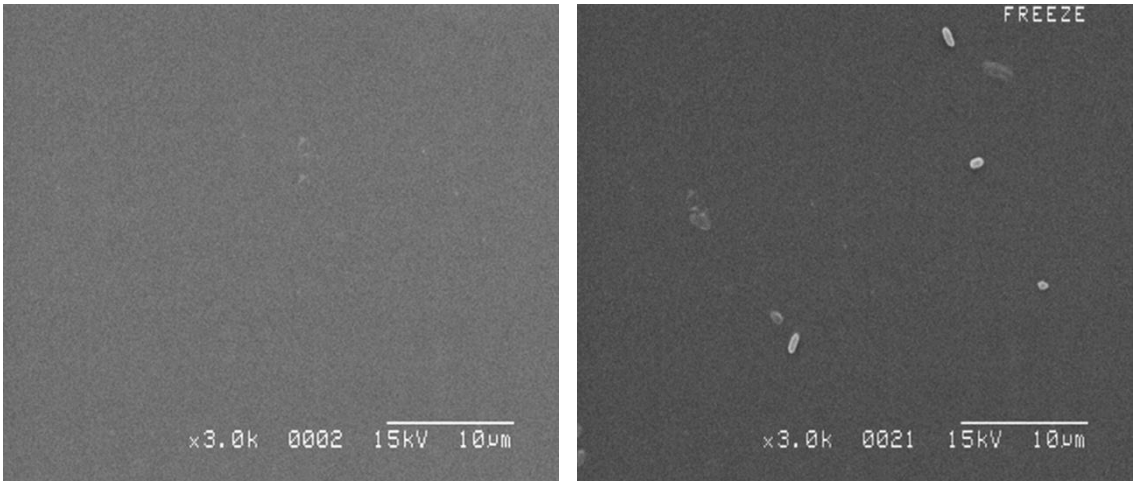

Figure 5.27 SEM image of ungrooved PMMA before (Left) and after (Right) placing in an *E. coli* suspension culture.

The modulated surfaces made by the hot embossing method into U and V grooves have been shown in Section 5.8.2 and the results of the U-grooved and V-grooved modified structures of PMMA placed in an agitated *E.coli* suspension are shown in Figure 5.28. The U-grooved and V-grooved modified structures of PMMA were kept in an agitated *E.coli* culture suspension for 24 hours at 37 ^{o}C. The SEM results show that both modified surfaces are more attractive than a smooth PMMA surface. The results also show that a V-grooved surface has less attraction than a U-grooved surface. This could be due to the higher aspect ratio of U-grooved PMMA: the grooves dominate the attachment and the orientation of *E.coli* (Curtis and Wilkinson, 1997; Curtis and Wilkinson, 2001; Edwards and Rutenberg, 2001; Curtis, 2004) and give the benefit of preventing the accumulation of bacteria. On the other hand, the V-grooved structure

shows no cell agglomeration and alignment effect, this will allow that bacteria to more easily congregate together and results in biofilm formation afterwards (Fux *et al.*, 2005; van Houdt and Michiels, 2005; Diaz *et al.*, 2007).

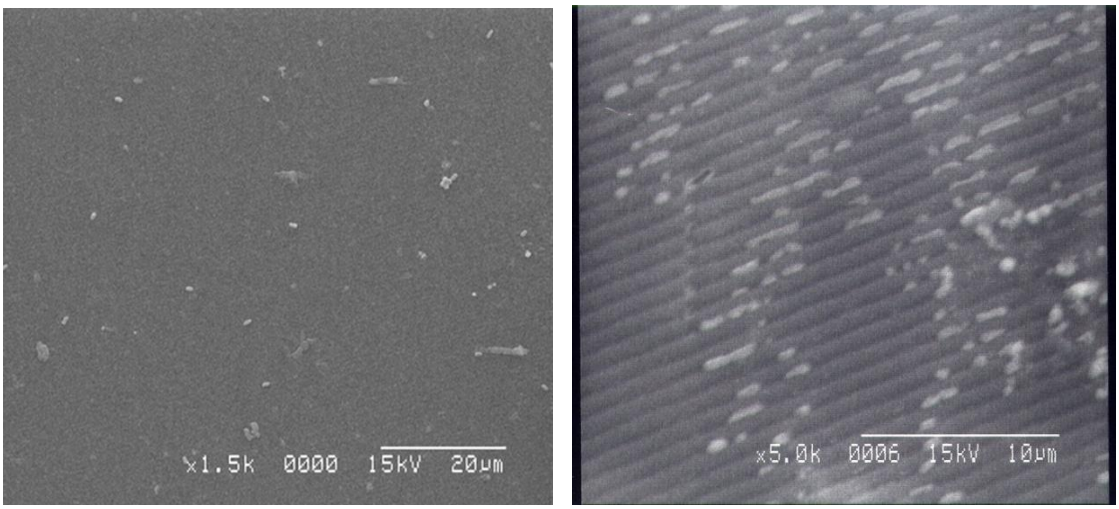

Figure 5.28 After *E. coli* suspension culturing and drying at room temperature. V-grooved (Left) and U-grooved (Right).

5.11.4 Conclusions

The surfaces with a nanostructured grating raise the adhesion surface area for *E.coli* and the alignments of bacteria is demonstrated on SEM images and indicate that a nanostructured substratum can control the adhesion behaviour of *E. coli* cells, rather than the surface chemical properties of the substratum material in this study. This is in contradiction to the earlier work of (Magnani *et al.*, 2003; Wong *et al.*, 2004). *E. coli* cells were found to be aligned along the nanogrooved surface with a higher aspect ratio, which is not beneficial for the further aggregation and growth of *E. coli* cells due to the 1-D confinement effect. However for some applications this may be advantageous.

In summary, designed surfaces made by the hot embossing method (U and V grooves) have been demonstrated here. Surfaces with low aspect ratio give rise to random adhesion of *E.coli*, and surface with high aspect ratio give rise to the alignment and orientation of bacteria along the grooves.

Note that these gratings are much deeper than the optical waveguide grating couplers.

Chapter 6 Bacteria Interacting With Smooth Pure Substrata

Figure 6.1 shows the results from a typical adsorption/desorption experiment. Adsorption approaches saturation, apparently asymptotically. Upon flooding with buffer solution at the same flow rate, some bacteria were desorbed (in this case). Note that our bacterial suspensions (original liquid culture) were aliquotted into small Eppendorf tubes and kept at -20 ^{o}C until required. The procedure for 100x dilution was to put 0.5 ml of the original suspension from an Eppendorf tube into 49.5 ml of buffer solution with a pipette. 50x dilution was made by adding 1 ml of the original suspension from an Eppendorf tube to 49 ml buffer solution and 200x dilution was made by adding 0.25 ml of the original suspension from an Eppendorf tube to 49.75 ml buffer solution.

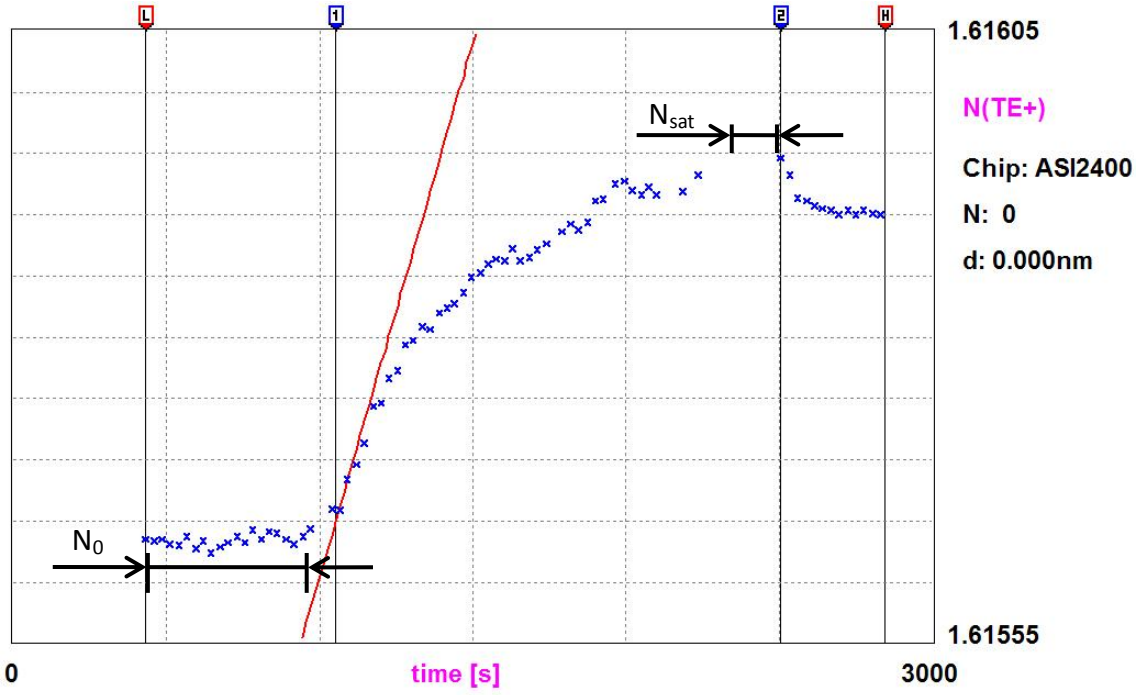

Fig 6.1 The results from a typical adsorption/desorption experiment for *E. coli*. Concentration c_b = 1.04 x 10^8 cells/ml (100X dilution), adsorbing on zirconia in Z1. The temporal limits of the curve segments used to calculate N_0 and N_{sat} are shown. Marker 1 indicates the start of bacterial flow and marker 2 indicates its end (after which the cuvette is flooded with buffer). [Experimental code: 080304-5]

The rest of this chapter is organized as follows.

First, we describe the standard drill used to analyze the results, applicable to all the data. Then we present the actual data that comprise the measurements of the two bacterial strains, *Escherichia coli* and *Lactobacillus plantarum*, (their salient surface properties are summarized in Table 6.1 and 6.2) adsorbing on alumina, silica, titania and zirconia, in the presence of different aqueous media of differing ionic strengths.

Table 6.1 The salient surface properties of the bacterial strains.

Strain	$\gamma^{(LW)}$	$\gamma^{\oplus}$	$\gamma^{\ominus}$	Note
E. coli K12	35.1	2.2	38.5	[c]
E. coli O8K(A)28	36	2.1	27.4	[a]
E. coli Hu734	37.2	1.5	52.8	[b]
E. coli O2K2	36.4	2.9	14.9	[a]
E. coli O2K7	34.3	1.5	47.4	[a]
E. coli O157K-	31.6	3.1	50.3	[a]
L. plantarum	39.3	1.3	28.1	[c]
L. plantarum RC6	40.3	0.3	54.4	[a]
L. plantarum RC20	38.3	2.4	1.8	[a]

[a] (van der Mei *et al.*, 1998)

[b] (Reid *et al.*, 1996)

[c] In the absence of measurements of our strains, the expedient of simply averaging all available data for closely related strains has been adopted.

Table 6.2 Aqueous buffer media at 25 ^{o}C (cf. Section 5.4).

Medium	Buffer	Salt	pH	Note
Z1	10 mM Hepes	0	7.4	[a]
Z1150	10 mM Hepes	150 mM NaCl	7.2	[b]
PBS	10 mM Phosphate	140 mM NaCl	7.4	[c]

[a]:(Good *et al.*, 1966)

[b]:(Cacace *et al.*, 1997)

[c]: GIBCO® PBS Tablets Cat. No. 18912-014.

6.1 Data treatment

The raw data (N(t), for TE or TM) were first examined for the stability of the baseline (prior to addition of bacteria). If there was a uniform drift, it was extrapolated and subtracted from the measured points. If it had a progressively diminishing slope, it was assumed to approach stability logarithmically, and a logarithmic function was fitted to the baseline, which was extrapolated and subtracted from the rest of the curve.

The corrected (where it was necessary) data were then transformed according to Equations (4.11 to 4.13). From Equations (4.12) and (4.13), we get

$$b(t)=\frac{\tilde{N}(t)}{\tilde{N}_{sat}}\cdot\frac{\theta_J}{\bar{a}} \tag{6.1}$$

using areas from Table 5.1 and θ_J = 0.54 (Table 3.1)---note that this value applies to aspect ratios of both one and about 3---we get the number of bacteria adsorbed on the surface of waveguide. In other words, we assume that b_{sat} corresponds to the jamming limit. Figure 6.2 shows the data of Figure 6.1 transformed to a plot of number of bacteria adsorbed at the surface vs. time.

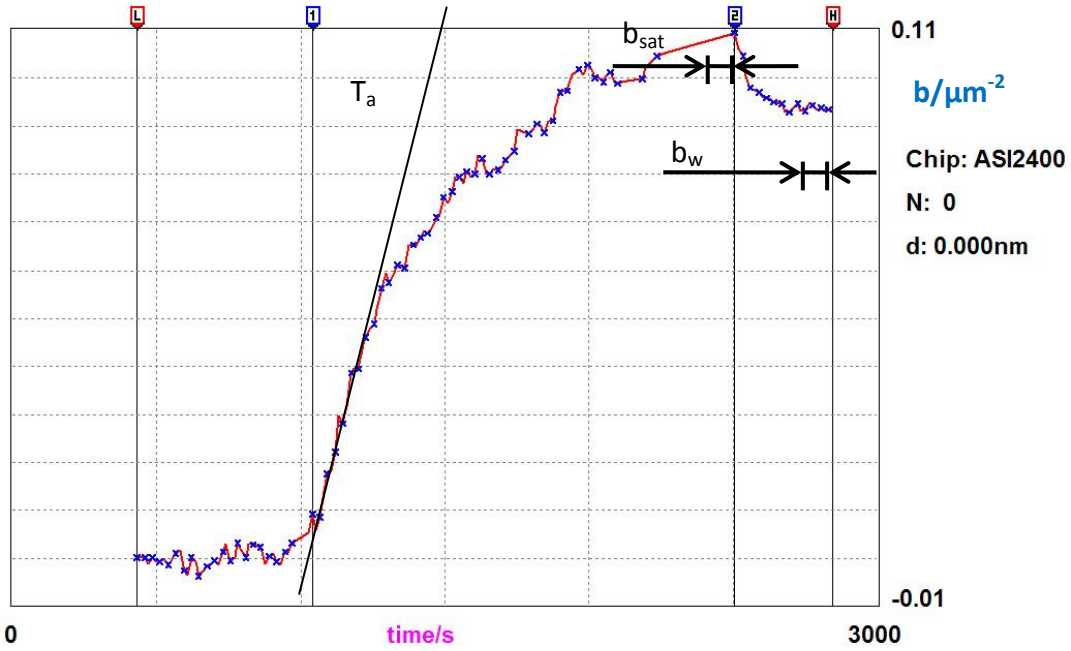

Figure 6.2 Data of Fig 6.1 transformed to yield b(t). The temporal limits of the curve segments used to calculate b_{sat} and b_w are shown. Marker 1 indicates the start of bacterial flow and marker 2 indicates its end (after which the cuvette is flooded with buffer). The initial tangent is labelled T_a.

b_{sat} is the saturation value and b_w is the number of adsorbed bacteria remaining on the surface after flooding with buffer. We use the ratio b_w/b_{sat} as a measure of the irreversibility of the adsorption.

6.2 Data analysis

From the discussion of adsorption in Section 3.1, we now give the canonical equation for addition to a surface, specifically for bacteria, as (cf. Equation (3.8)):

$$\frac{db}{dt} = k_a c_s \phi(a,b) \tag{6.2}$$

where k_a is the rate coefficient for adsorption, c_s is defined as the (approximately) stationary concentration of particles in a layer directly above the surface, given by Equation (3.8), and the available area function ϕ depends on b and a, the area occupied by one bacterium.

Since the precision of the determination of the bacterial concentration is not very great, we approximate c_s as equal to c_b in Equation (6.2).

Equation (6.1) implies that we can estimate k_a from the initial slope of the b(t) curve when ϕ is still practically equal to 1 (tangent T_a in Figure 6.2). i.e., $(db/dt)_{t->0} = k_a c_b$. From Equation (3.3), we then estimate ΔG_a :

$$\Delta G_a \approx - k_B T \ln\left(\frac{k_a \delta_a}{D}\right) \tag{6.3}$$

where k_B is the Boltzmann constant ($1.38X10^{-23}$ J/K). The diffusion coefficient D was determined using the Stokes-Einstein Equation (see Equation (5.1)). I assume δ_a is equal to the equivalent radius r of the bacterium.

By numerical differentiation, the b(t) data were transformed into db/dt and plotted against b. This enabled Equation (6.2) to be fitted directly. A convenient expression for ϕ, alternative to Equation (3.11), is (Schaaf and Talbot, 1989):

$$\phi=(1-\chi)^3/(1+f_1\chi+f_2\chi^2+f_3\chi^3) \tag{6.4}$$

where $\chi = \theta/\theta_J$, θ = ba, and the constants f_1 , f_2 and f_3 are -0.8120, 0.2336 and 0.00845 respectively (Schaaf and Talbot, 1989).

If Equation (6.2) with ϕ given by Equation (6.4) was a good fit to the data, bacterial deposition was considered to follow RSA, and the parameters k_a and a were determined as fitting parameters. It is clear that a plot of db/dt vs mass of bacteria (*E.coli*), as shown in Figure 6.3, is reasonably well fitted by a random sequential adsorption process.

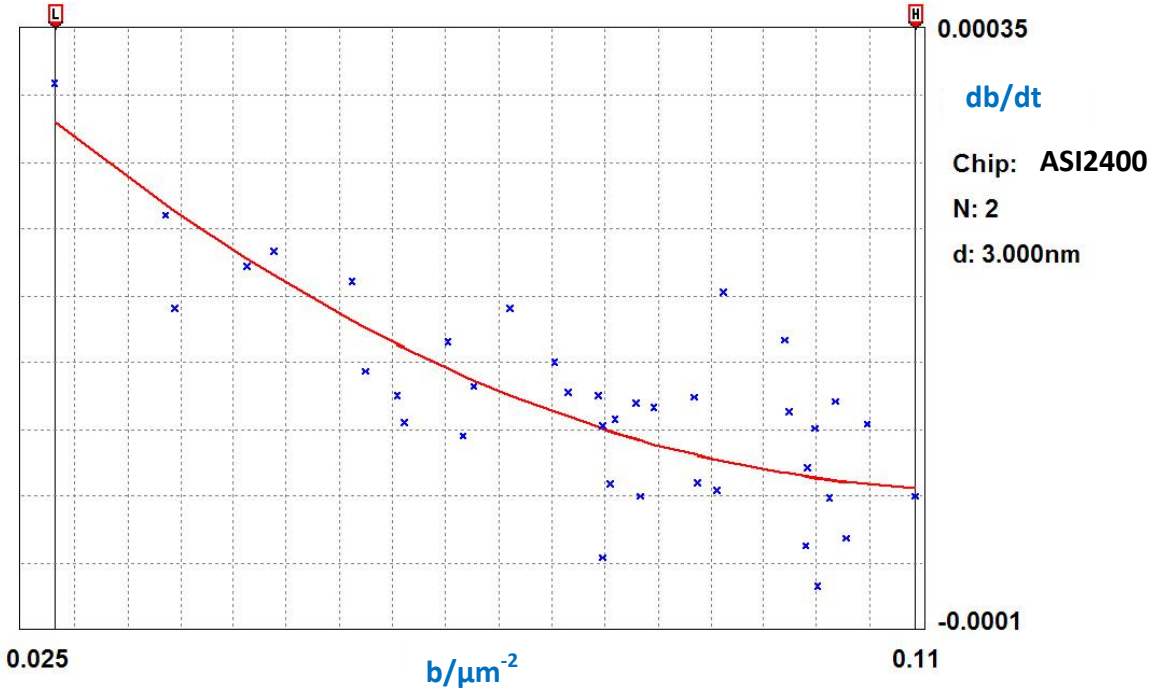

Figure 6.3 Data of Figure 6.2 (between the markers 1 & 2) transformed to the time derivative of absorbed number and plotted against adsorbed number and the fitting curve.

Desorption. In same case, desorption of bacteria from the surface takes place.
The simple desorption equation is:

$$\frac{db}{dt} = - k_d b \tag{6.5}$$

where k_d is the rate coefficient for departure, implying that b(t) decreases exponentially. By integrating it, we get

$$b(t)=b_{sat}\exp(-k_d t) \tag{6.6}$$

Hence, a plot of b vs time enables k_d to be determined Two examples are shown in Figures 6.4 and 6.5. The departure of the (usually small) desorbable fraction follows reasonably pure exponential kinetics. Given the stability of the post-flooding plateau b_w, it is possible that the departing bacteria have slightly different surface properties from their congeners. However, I considered it sufficient to note the fraction desorbed (see Section 6.3.3).

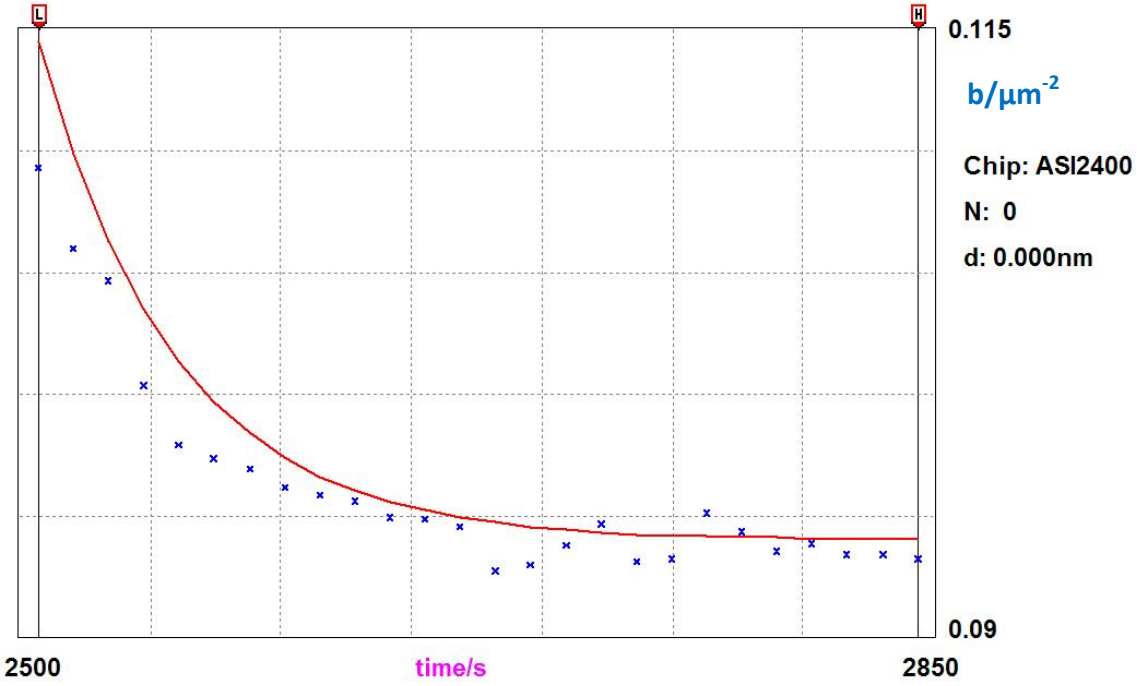

Figure 6.4 Plot of b vs time of *E.coli*, fitting $b(t)=b_w+(b_{sat}-b_w)\exp(-k_d t)$ with b_w and k_d as fitting parameters. b_w is 0.093 μm^{-2} and k_d is 0.019 s^{-1}.

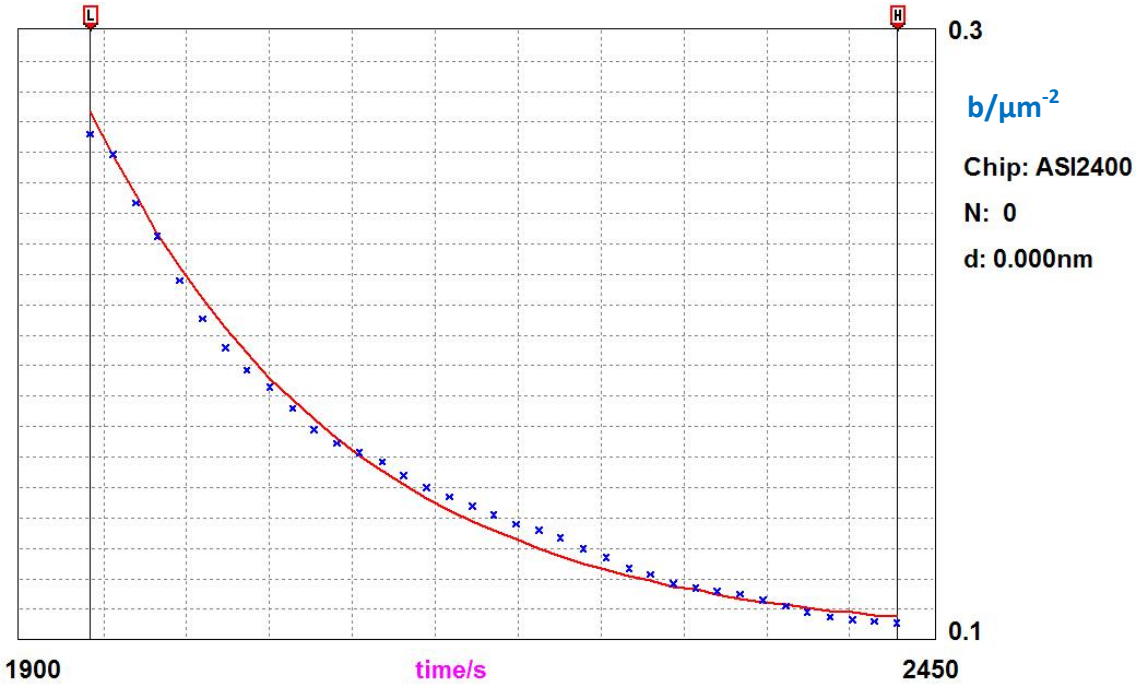

Figure 6.5 Plot of b vs time of *L.plantarum*, fitting $b(t)=b_w+(b_{sat}-b_w)\exp(-k_d t)$ with b_w and k_d as fitting parameters. b_w is 0.10 μm^{-2} and k_d is 0.0065 s^{-1}.

6.3 Data

6.3.1 Qualitative summary of the main features

Nearly all adsorption is following the random sequential adsorption model, only in a few cases (*E.coli* on Al_2O_3 in PBS, very markedly; *L. plantarum* on ZrO_2 in PBS, *E.coli* on SiO_2 in Z1150) follow the generalized ballistic deposition (GBD) model (Csúcs and Ramsden, 1998a), see details in Section 6.4.5.

Reversibility. In many cases the adsorption was irrversible with respect to dilution with bacteria-free medium; in some cases an appreciable fraction could be removed.

Reproducibility. Acceptable given the intrinsic variability of a growth culture. My general strategy was to assess whether the results from many experiments under diverse condictions (substrata, media) fit into an interpretable framework, rather than repeat a single experiment 20 times. I postulate that where different batch gave a different result, the bacterium was in a different state due to a difference in its life-history (Hypothesis 6).

6.3.2 Compendium of results

First I present another result of bacterial adsorption from the strain *L.plantarum*.

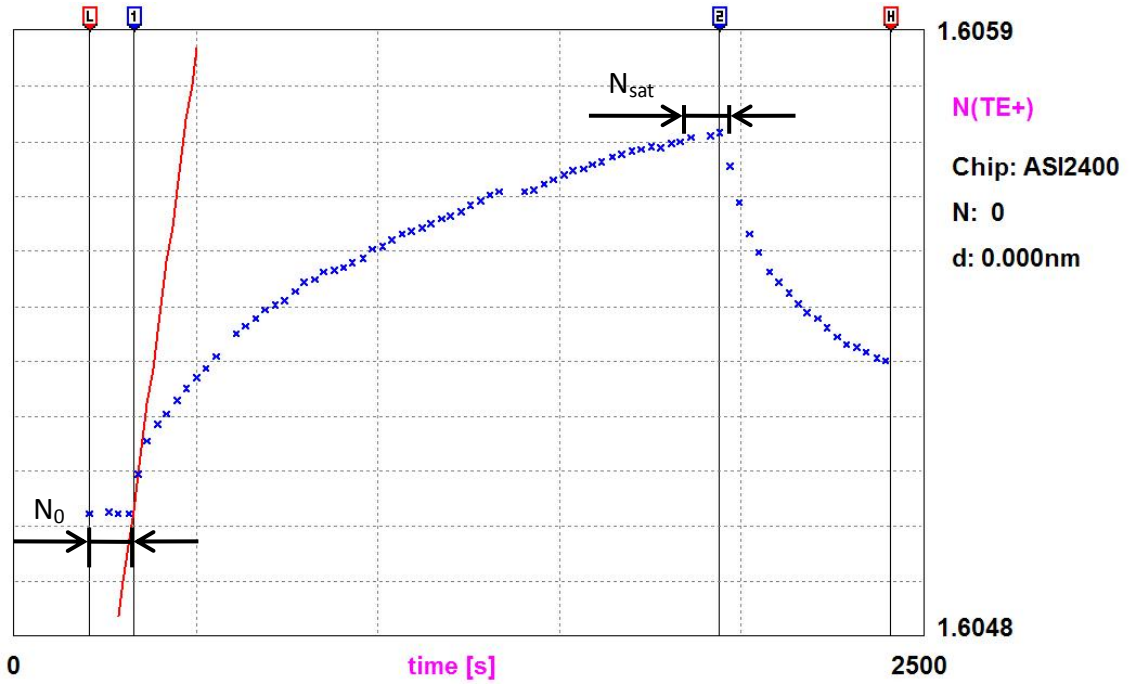

Fig 6.6 The results from a typical adsorption/desorption experiment for *L. plantarum*. Concentration c_b = 4.22 x 10 ^{6} cells/ml (100X dilution), adsorbing on silica in PBS. Curve segments used to calculate N_0 and N_{sat} are shown. Marker 1 indicates the start of bacterial flow and marker 2 indicates its end (after which the cuvette is flooded with buffer). [Experimental code: LPS100]

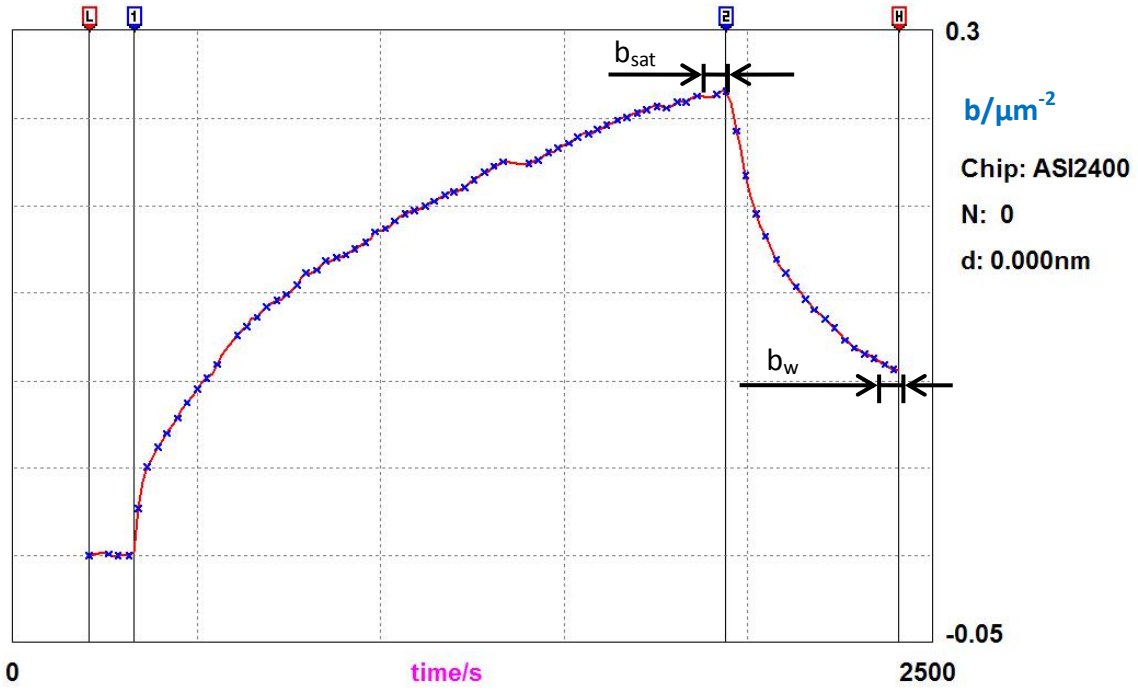

Figure 6.7 Data of Fig 6.6 transformed to yield b(t). The temporal limits of the curve segments used to calculate b_{sat} and b_w are shown. Marker 1 indicates the start of bacterial flow and marker 2 indicates its end (after which the cuvette is flooded with buffer).

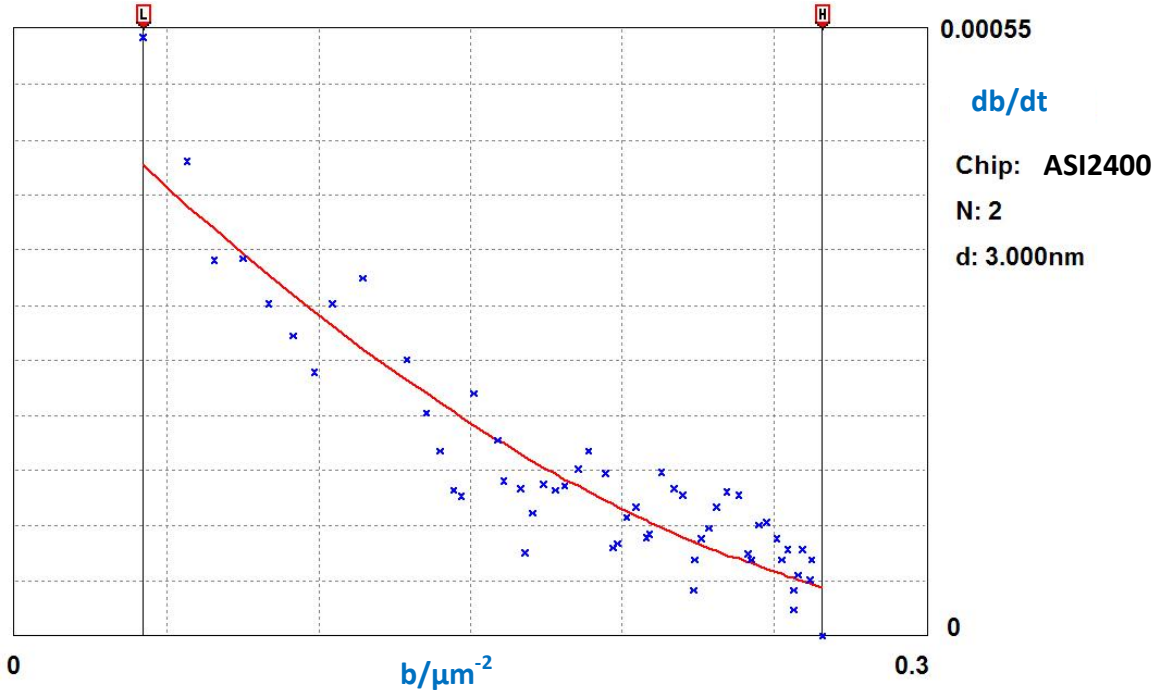

Figure 6.8 Data of Figure 6.7 (between the markers 1 & 2) transformed to the time derivative of absorbed number and plotted against adsorbed number and the fitting curve.

The following figures are results from different bacteria including both *E. coli* and *L. plantarum* in PBS, HEPES (Z1) and HEPES with salt (Z1150) buffer solutions on silica, titania, zirconia and alumina.

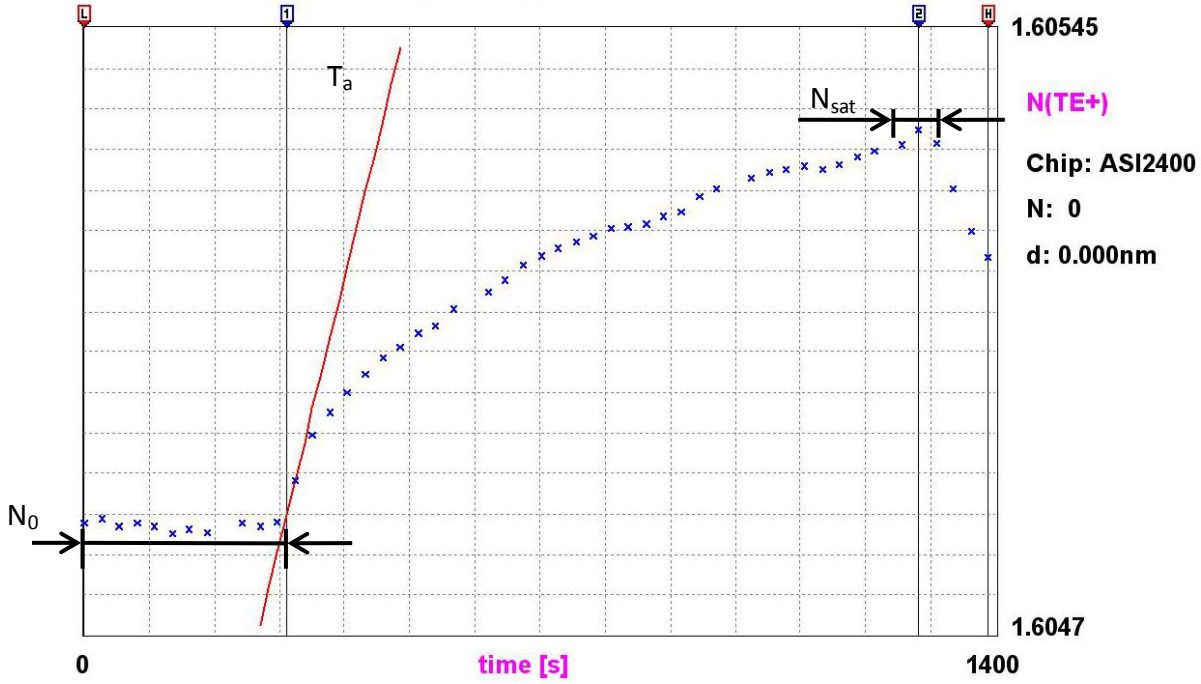

Figure 6.9 N-t diagram of *E.coli* in PBS on silica. [Experimental code: EPS100]

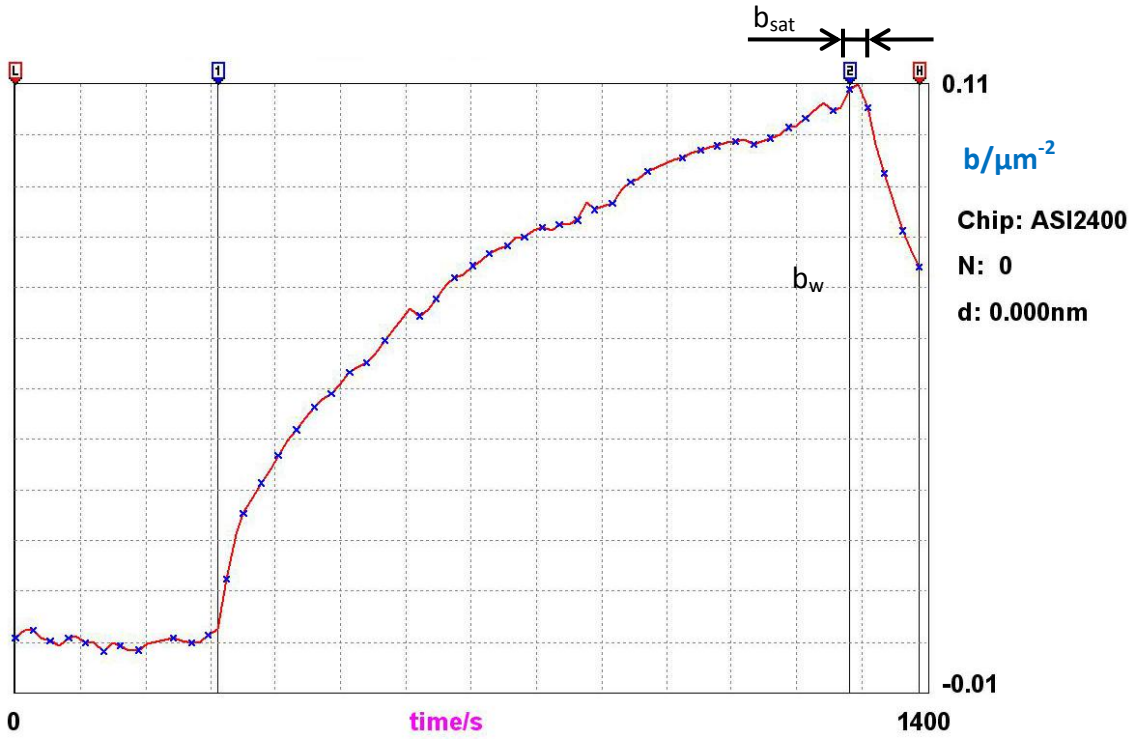

Figure 6.10 b-t diagram of *E.coli* in PBS on silica. b_w was established by extrapolation.

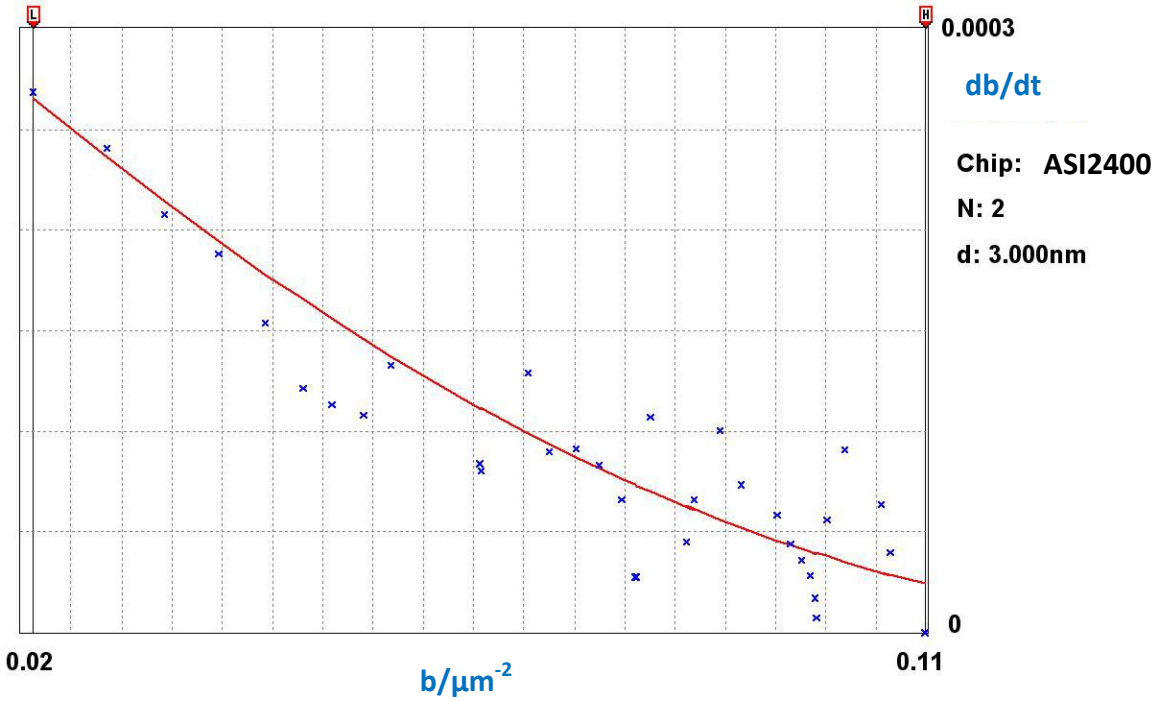

Figure 6.11 RSA Fitting of db/dt vs. b of *E.coli* in PBS on silica.

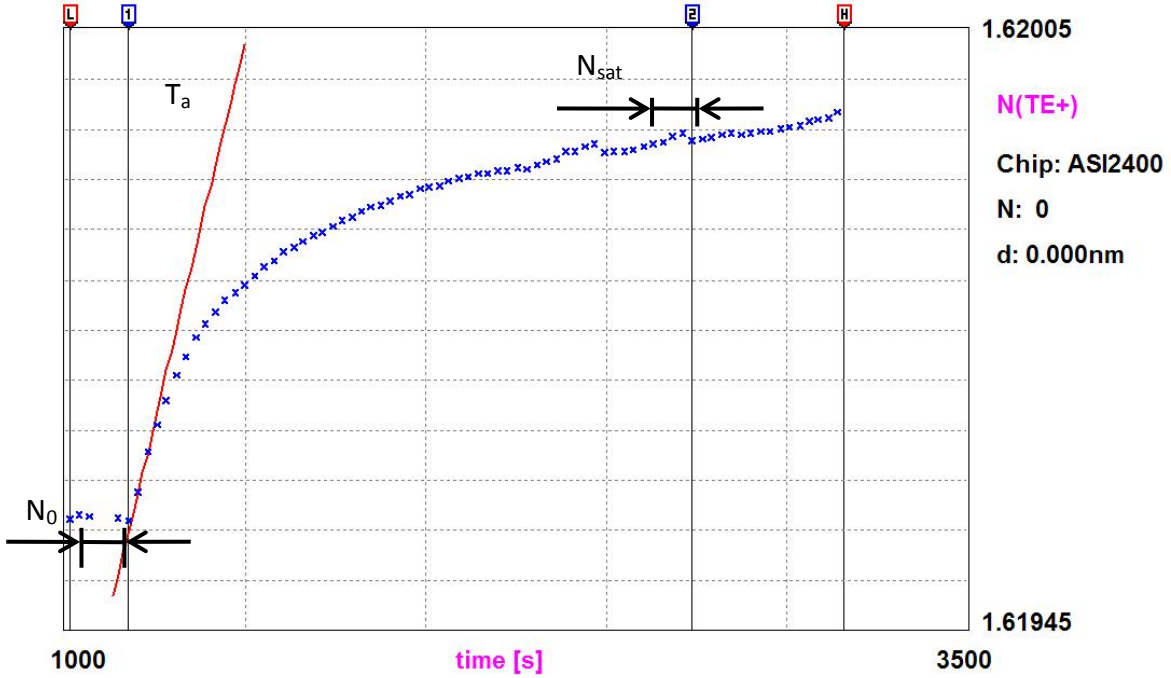

Figure 6.12 N-t diagram of *E.coli* in PBS on zirconia. [Experimental code: 090304-6]

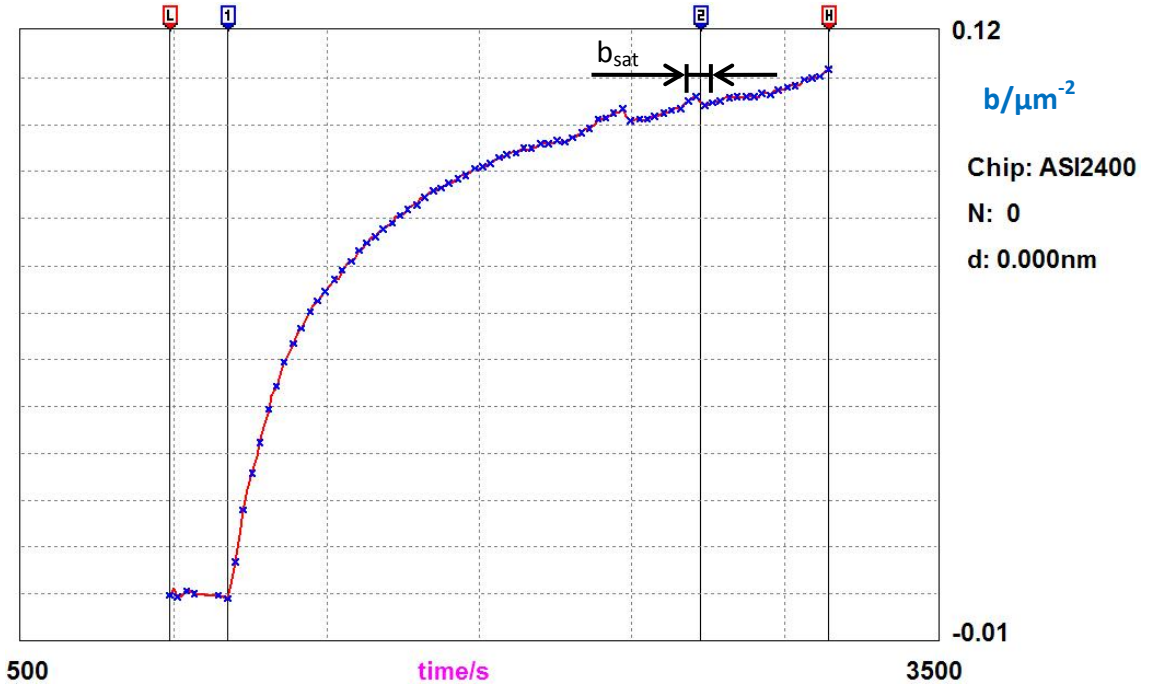

Figure 6.13 b-t diagram of *E.coli* in PBS on zirconia. $b_w = b_{sat}$.

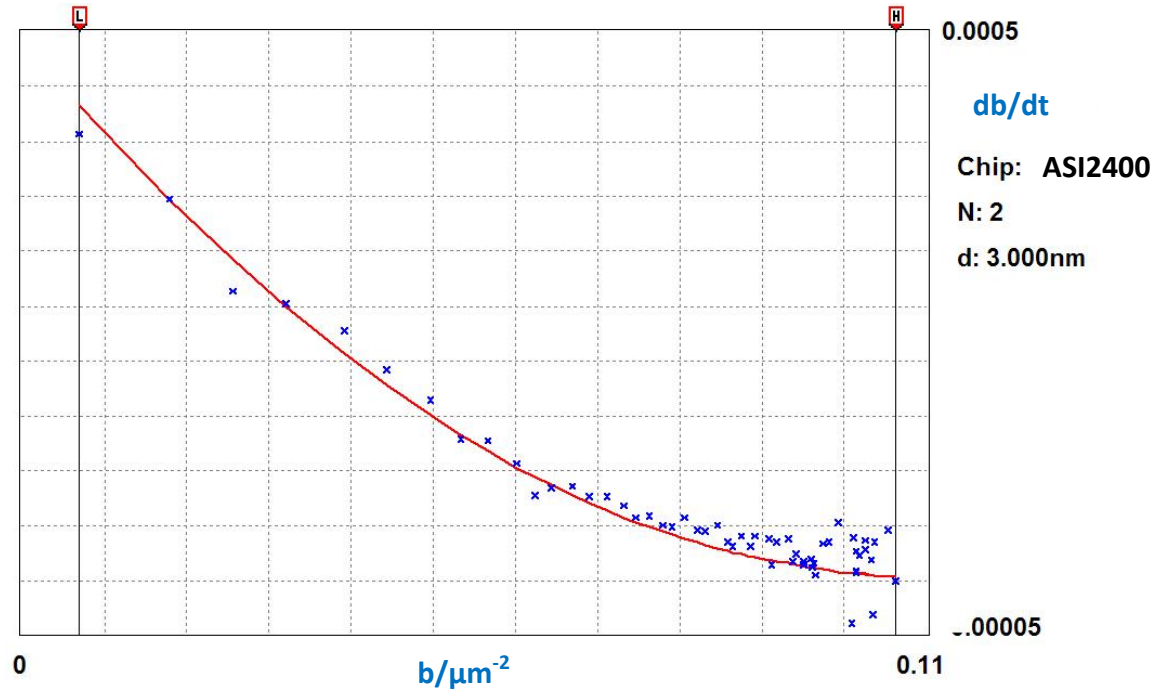

Figure 6.14 RSA Fitting of db/dt vs. b of *E.coli* in PBS on zirconia.

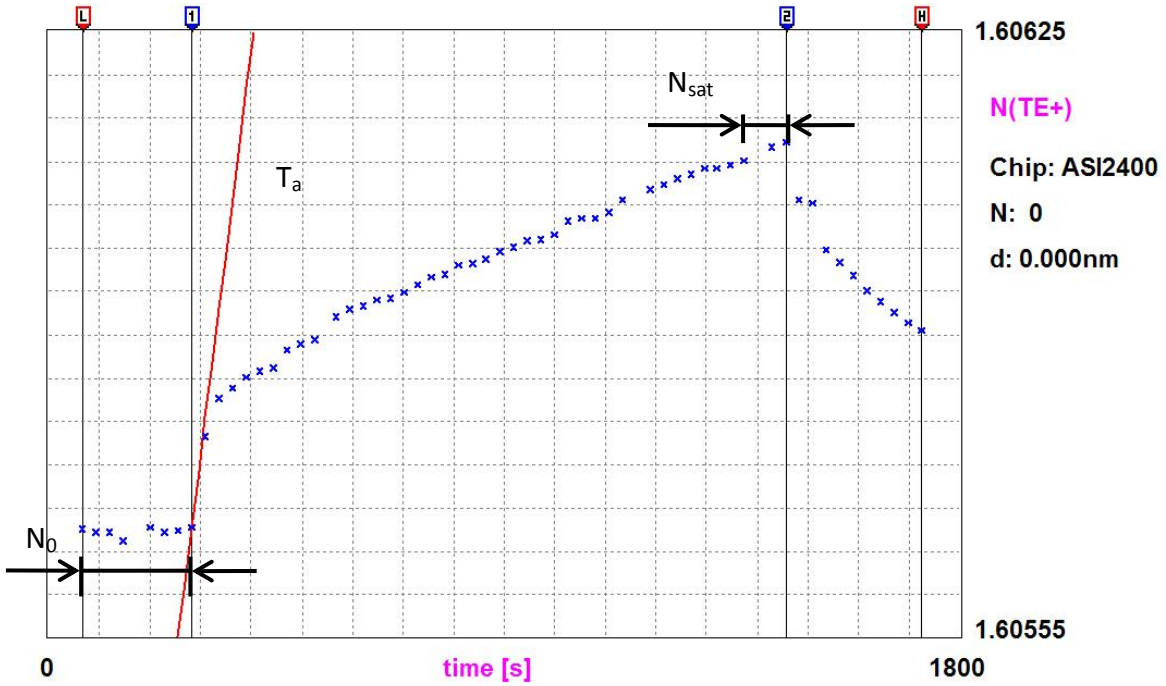

Figure 6.15 N-t diagram of *E.coli* in Z1150 on silica. [Experimental code: EZS100]

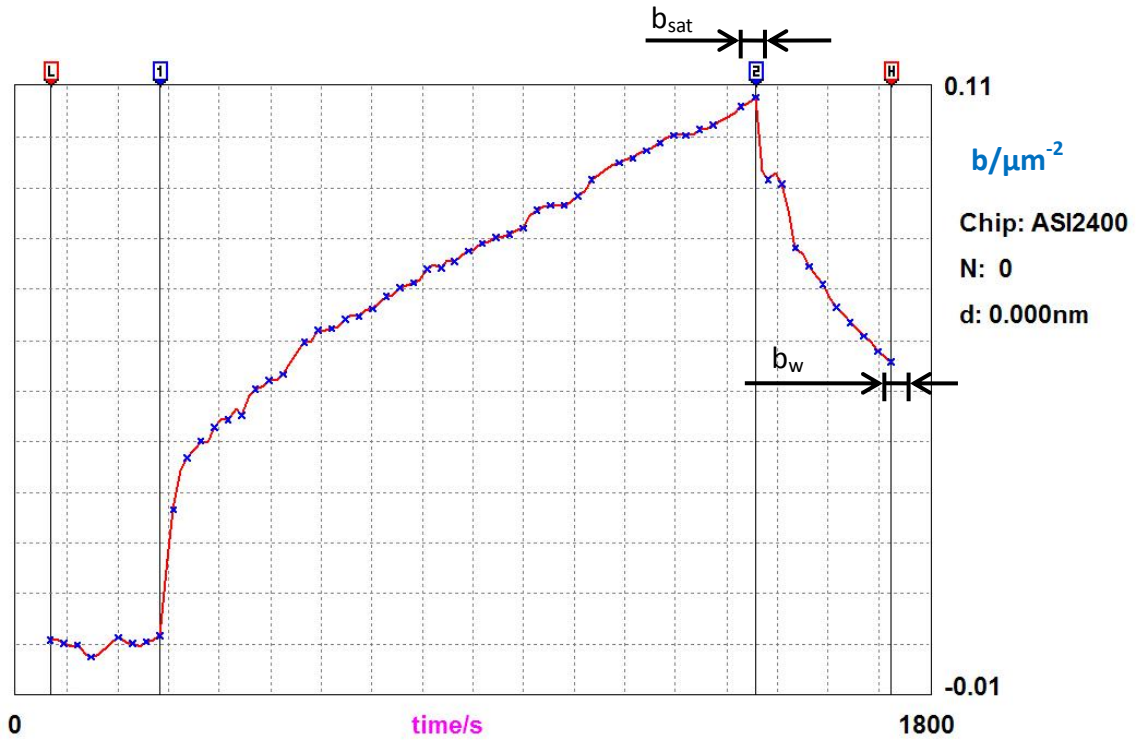

Figure 6.16 b-t diagram of *E.coli* in Z1150 on silica.

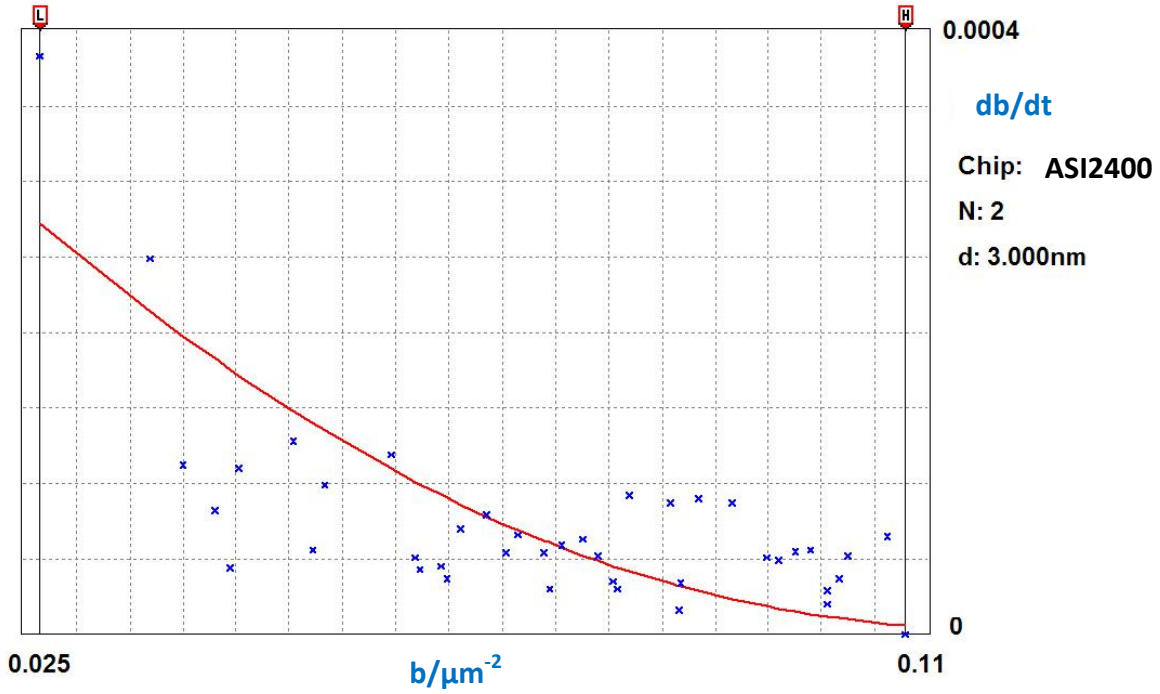

Figure 6.17 RSA Fitting of db/dt vs. b of *E.coli* in Z1150 on silica.

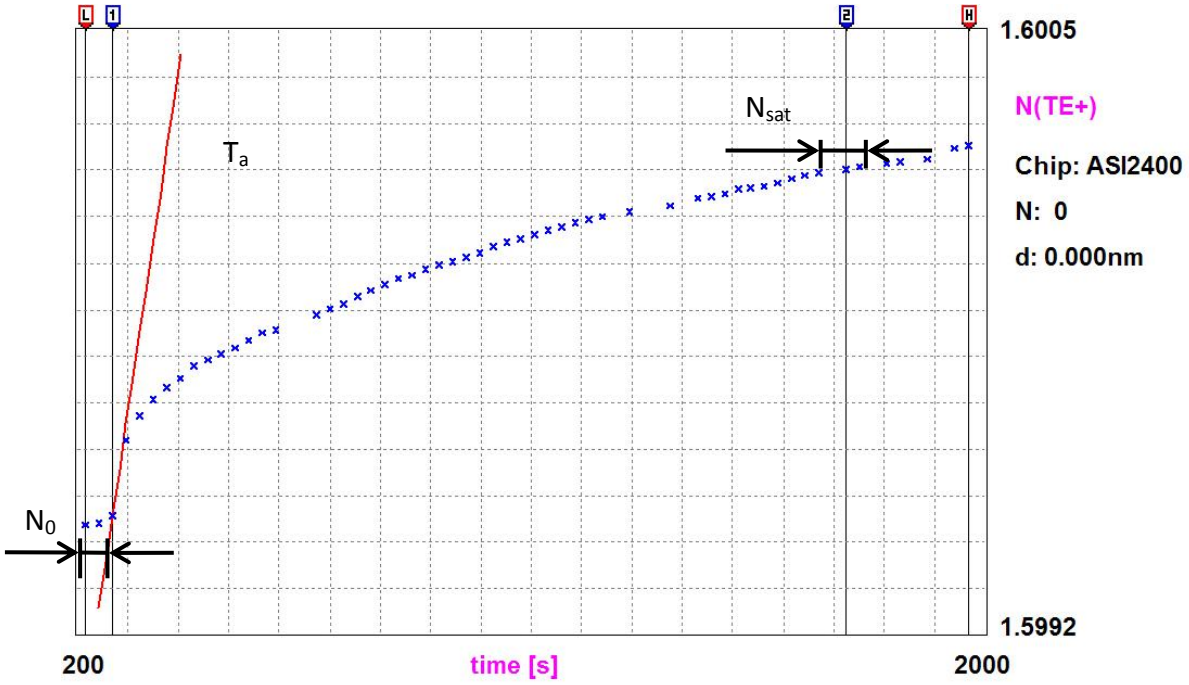

Figure 6.18 N-t diagram of *L. plantarum* in PBS on titania. [Experimental code: LPT100]

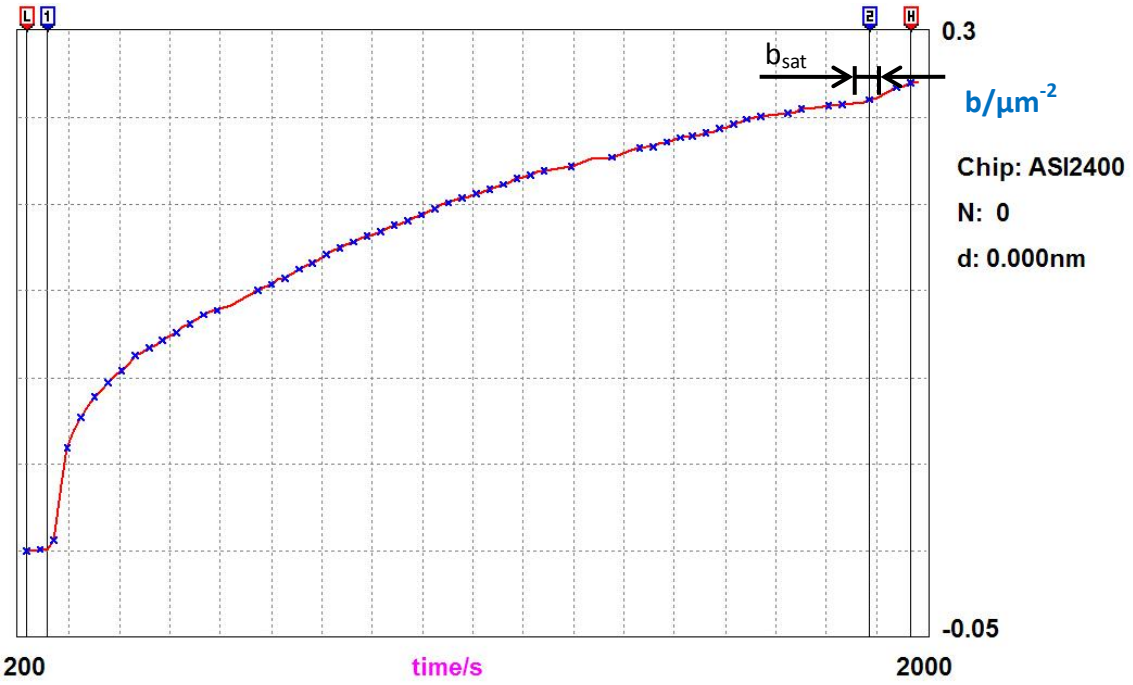

Figure 6.19 b-t diagram of *L. plantarum* in PBS on titania. $b_w = b_{sat}$.

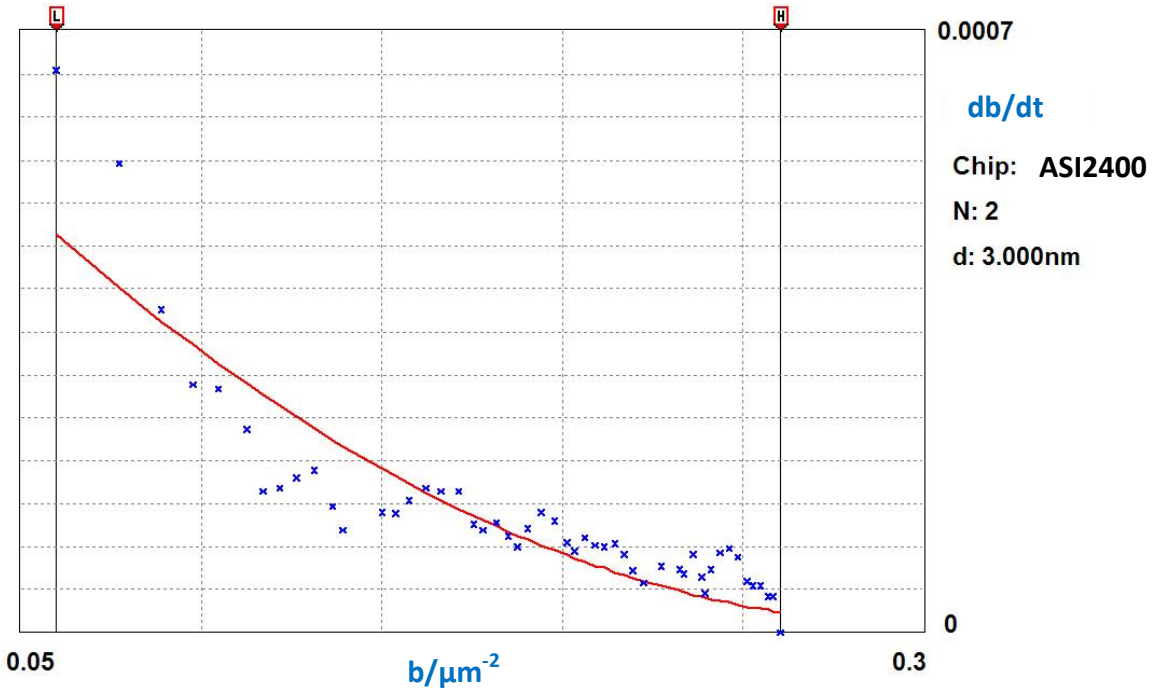

Figure 6.20 RSA Fitting of db/dt vs. b of *L. plantarum* in PBS on titania.

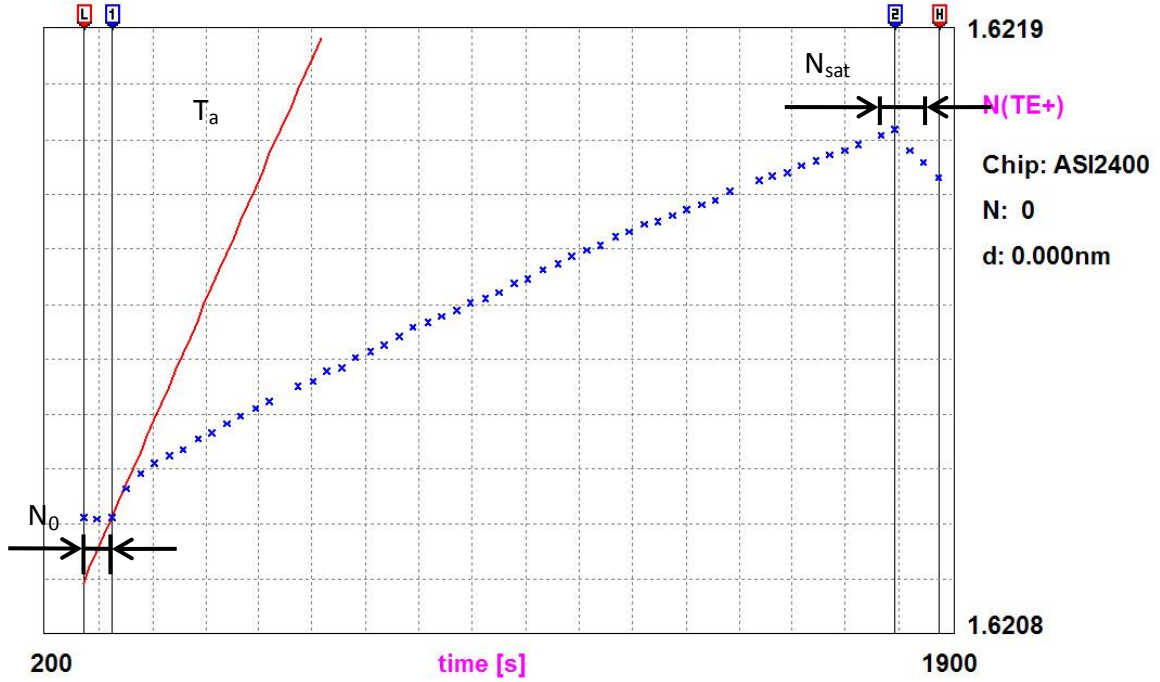

Figure 6.21 N-t diagram of *L. plantarum* in PBS on zirconia. [Experimental code: LPZ100]

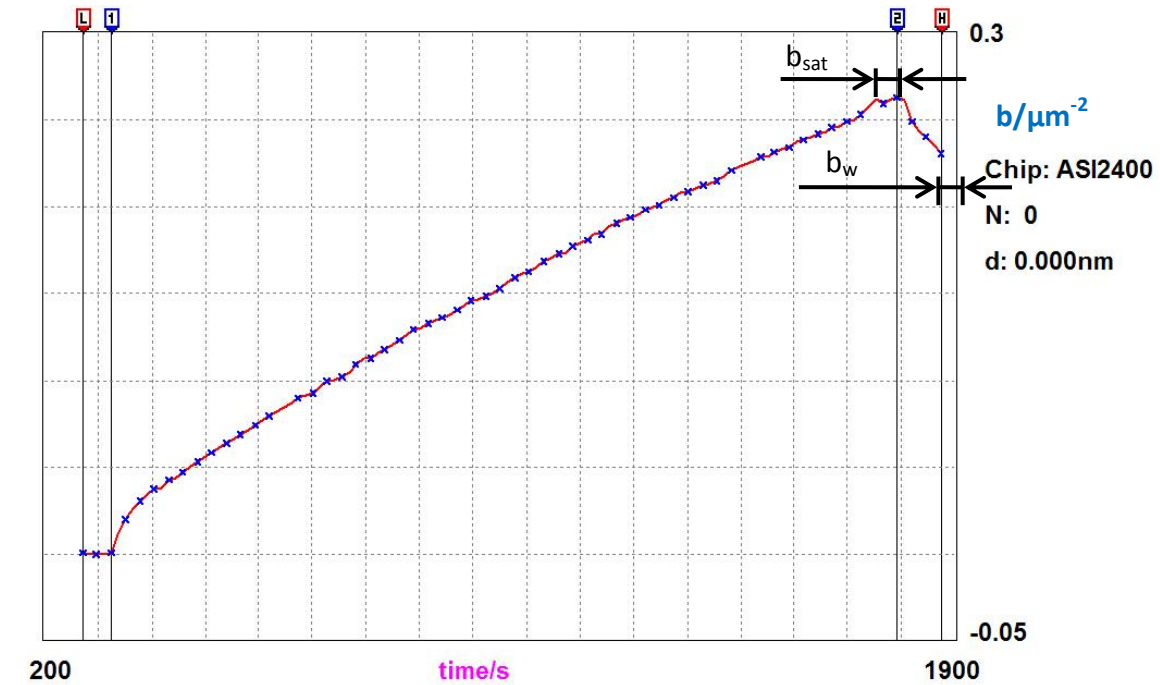

Figure 6.22 b-t diagram of . *plantarum* in PBS on zirconia. Clearly not pure RSA.

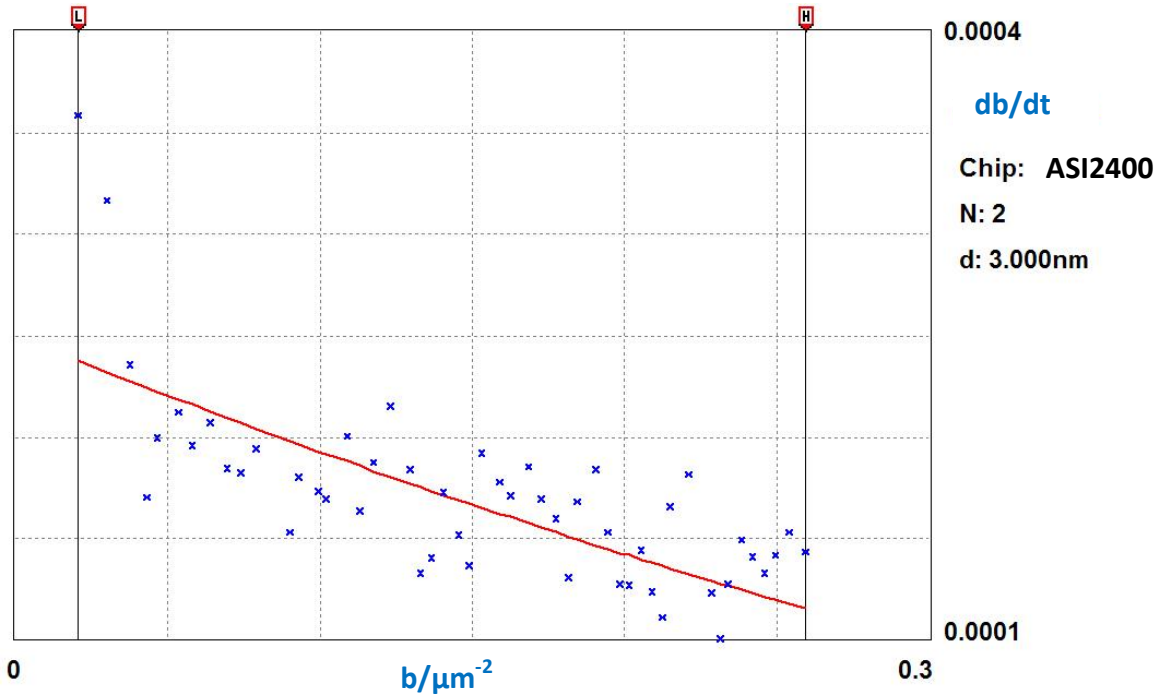

Figure 6.23 RSA Fitting of db/dt vs. b of *L. plantarum* in PBS on zirconia.

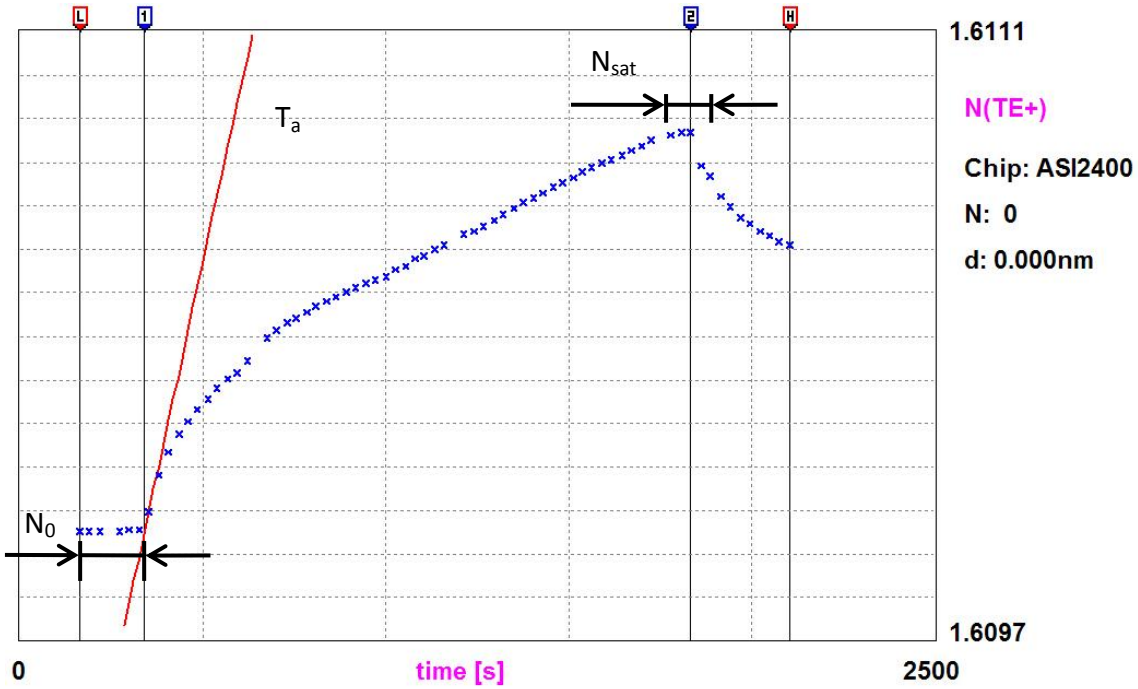

Figure 6.24 N-t diagram of *L. plantarum* in Z1150 on silica. [Experimental code: LZS100]

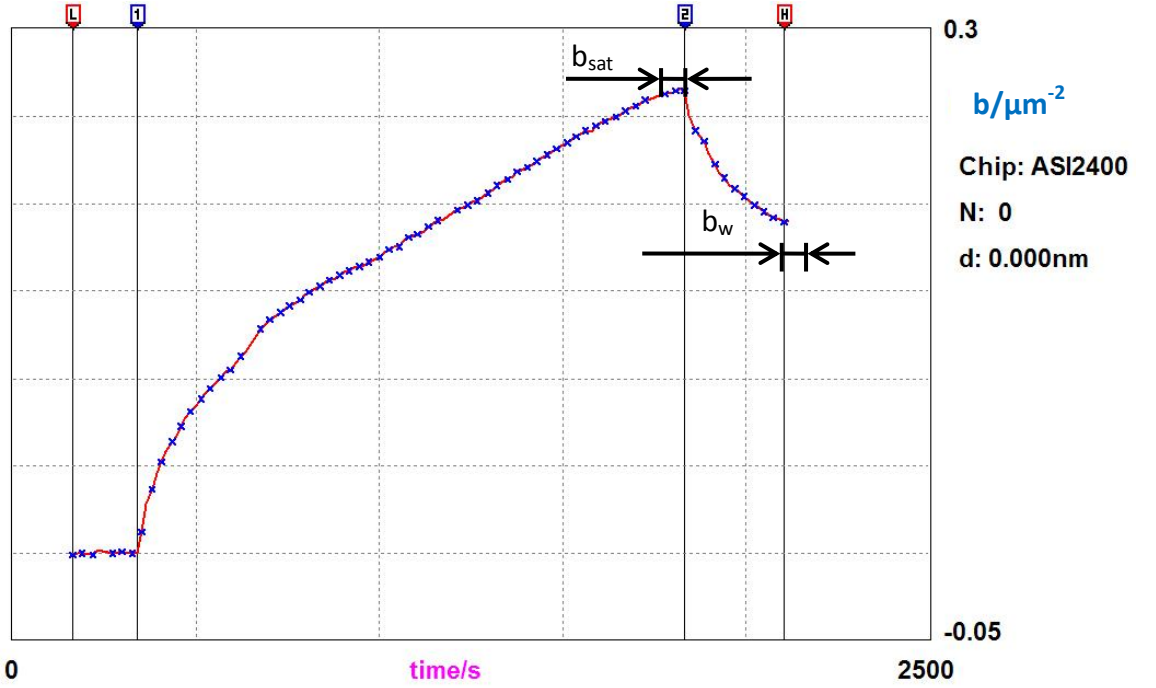

Figure 6.25 b-t diagram of *L. plantarum* in Z1150 on silica.

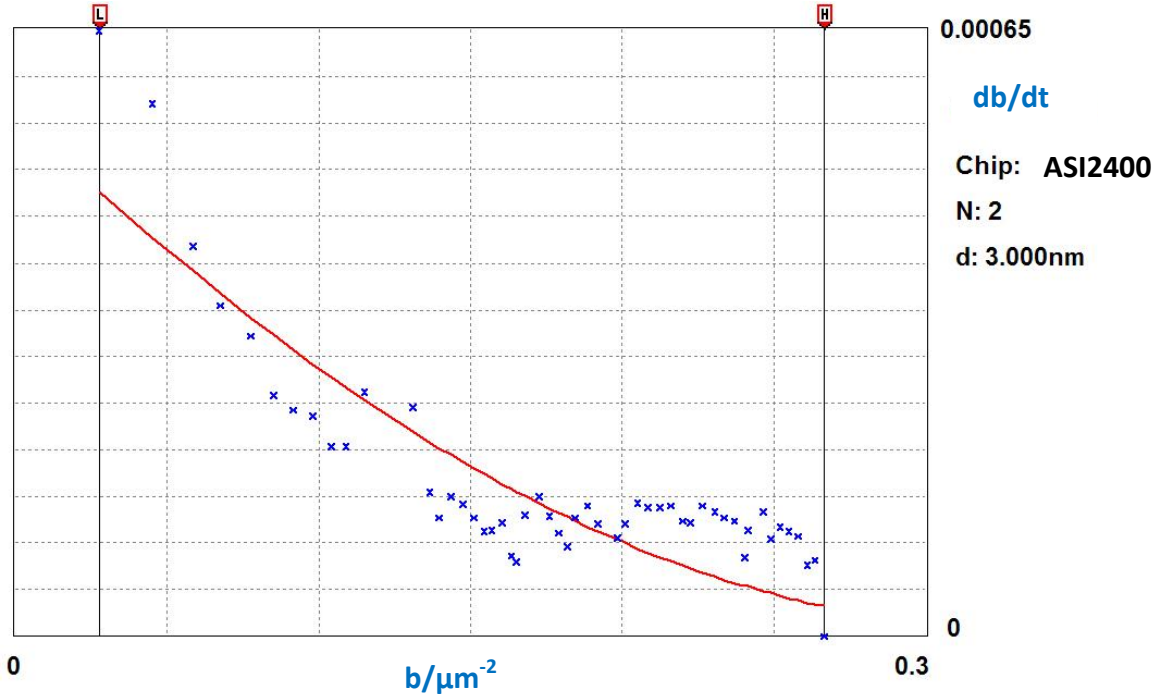

Figure 6.26 RSA Fitting of db/dt vs. b of *L. plantarum* in Z1150 on silica.

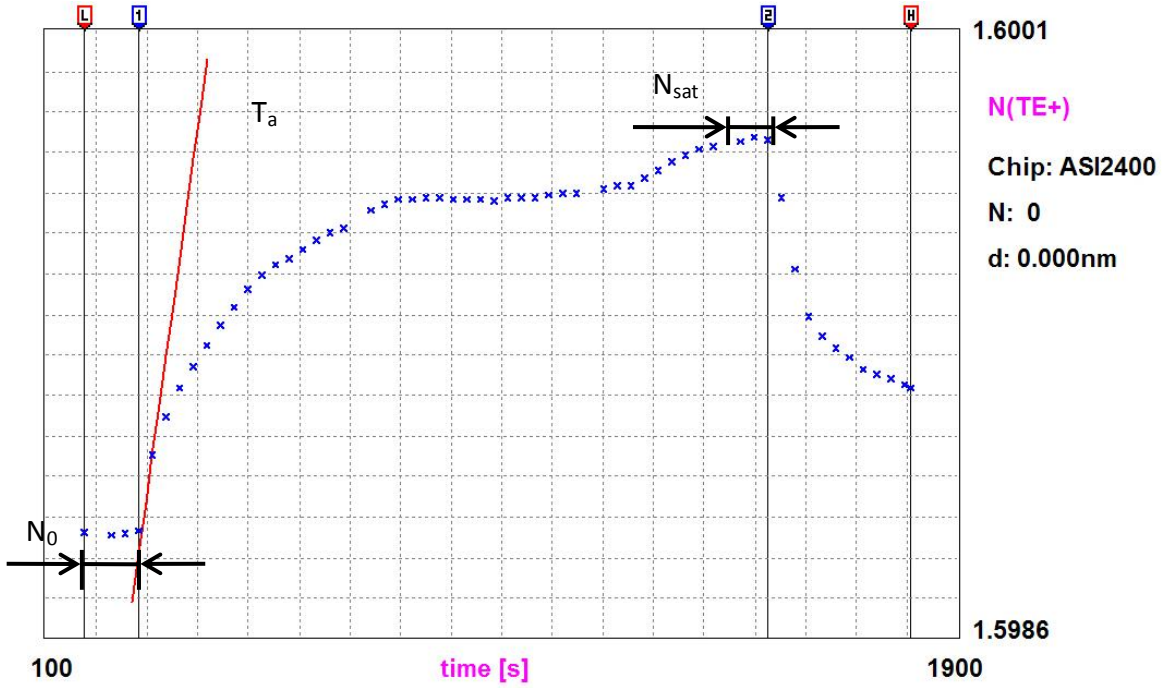

Figure 6.27 N-t diagram of *L. plantarum* in Z1150 on titania.
[Experimental code: LZT100]

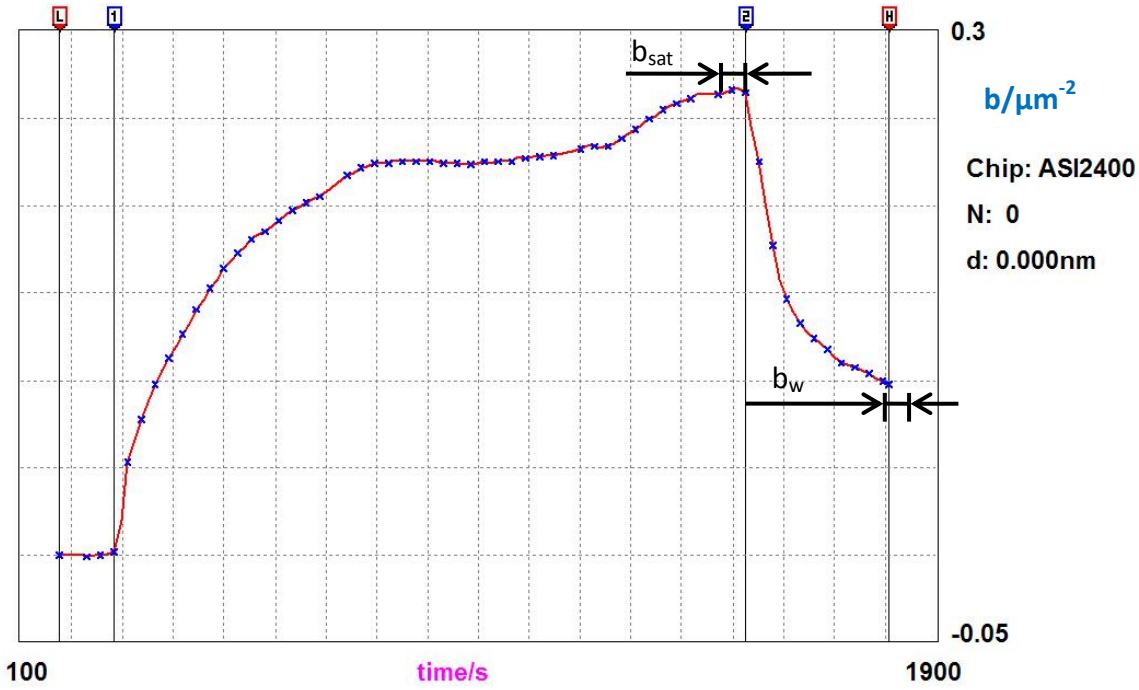

Figure 6.28 b-t diagram of *L. plantarum* in Z1150 on titania.

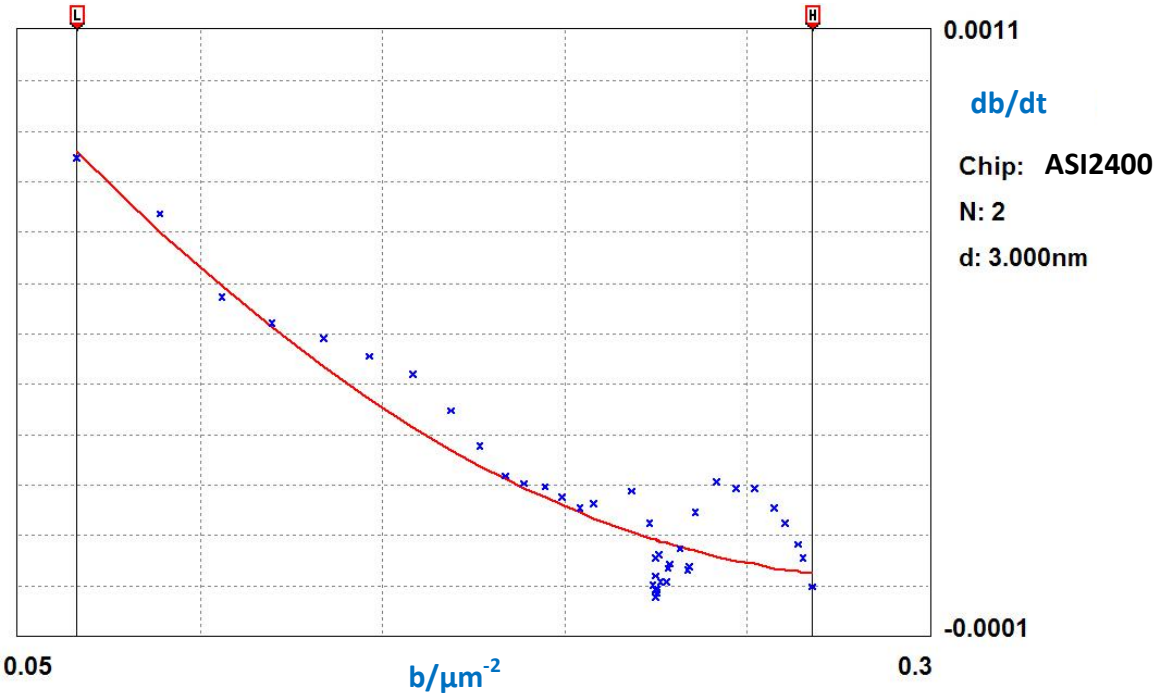

Figure 6.29 RSA Fitting of db/dt vs. b of *L. plantarum* in Z1150 on titania.

To a first approximation, we ascribe no special signifance to the erratic behaviour near saturation.

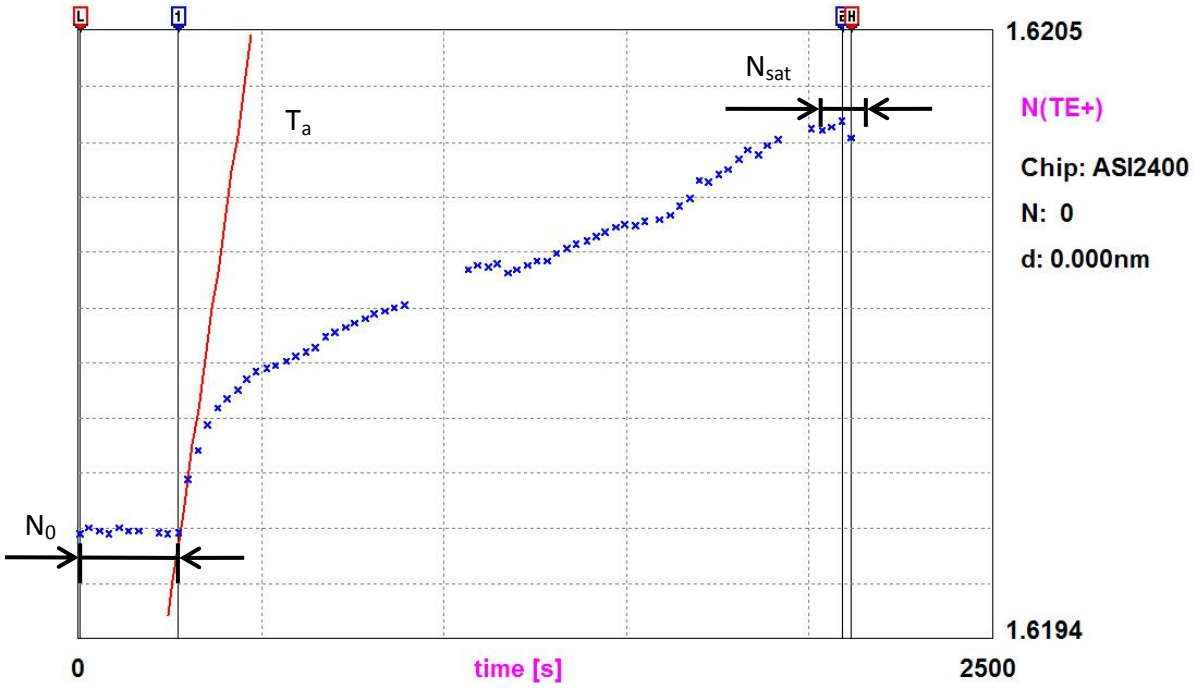

Figure 6.30 N-t diagram of *L. plantarum* in Z1150 on zirconia. [Experimental code: LZZ100]

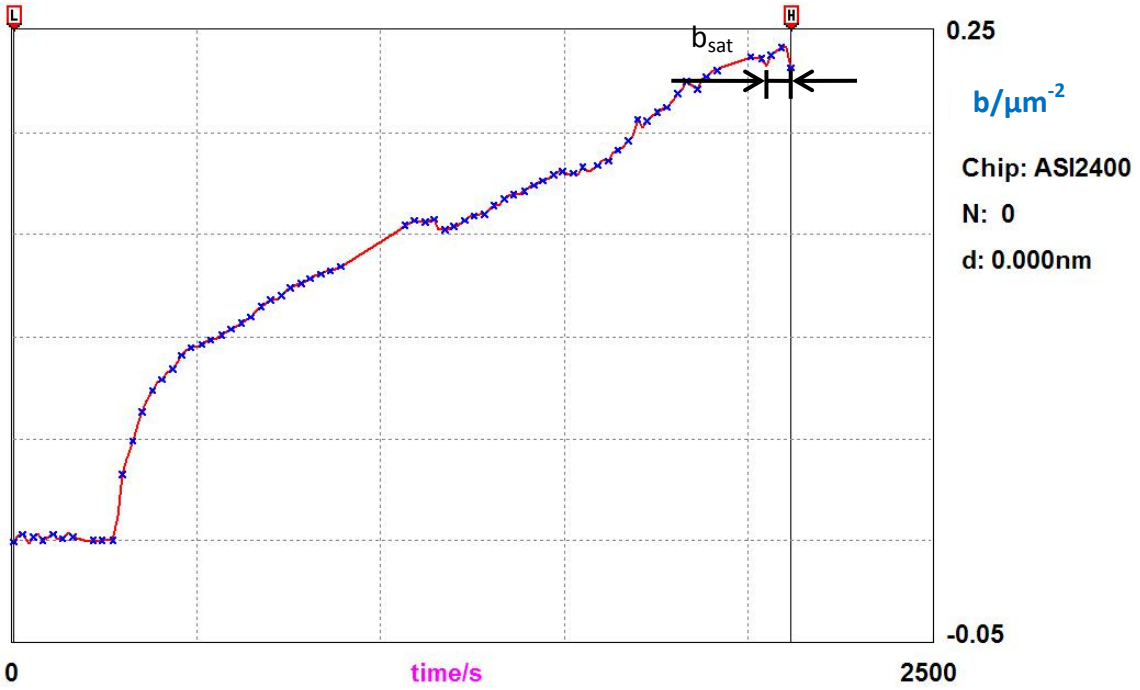

Figure 6.31 b-t diagram of *L. plantarum* in Z1150 on zirconia. $b_w = b_{sat}$.

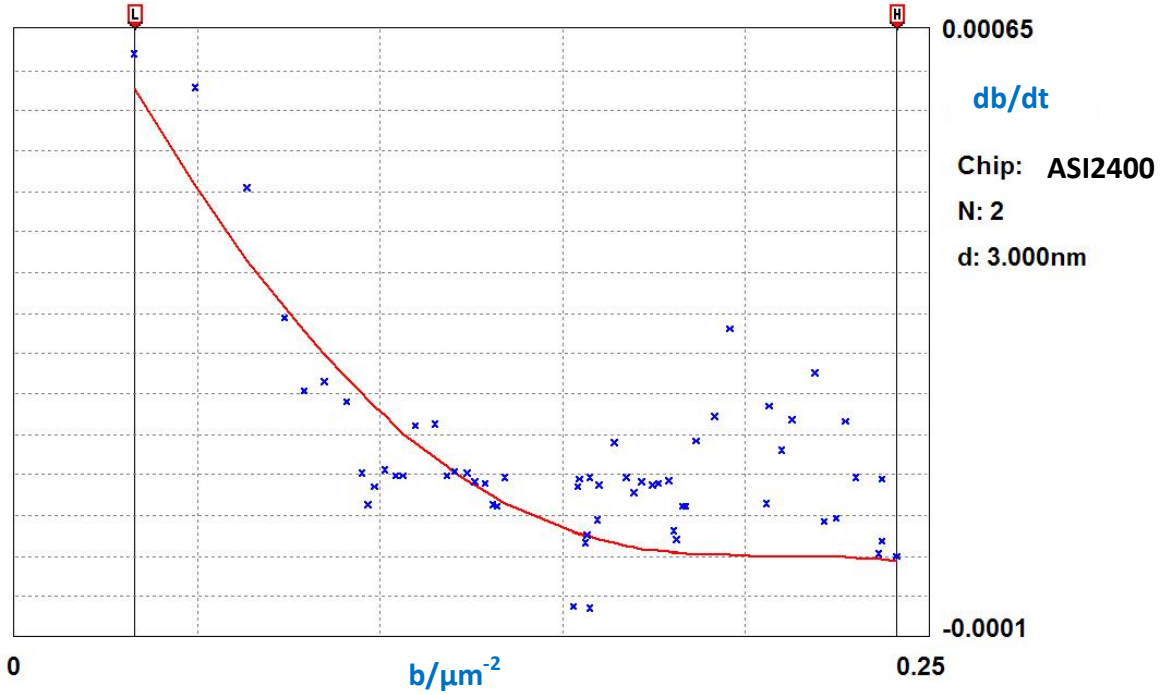

Figure 6.32 RSA Fitting of db/dt vs. b of *L. plantarum* in Z1150 on zirconia.

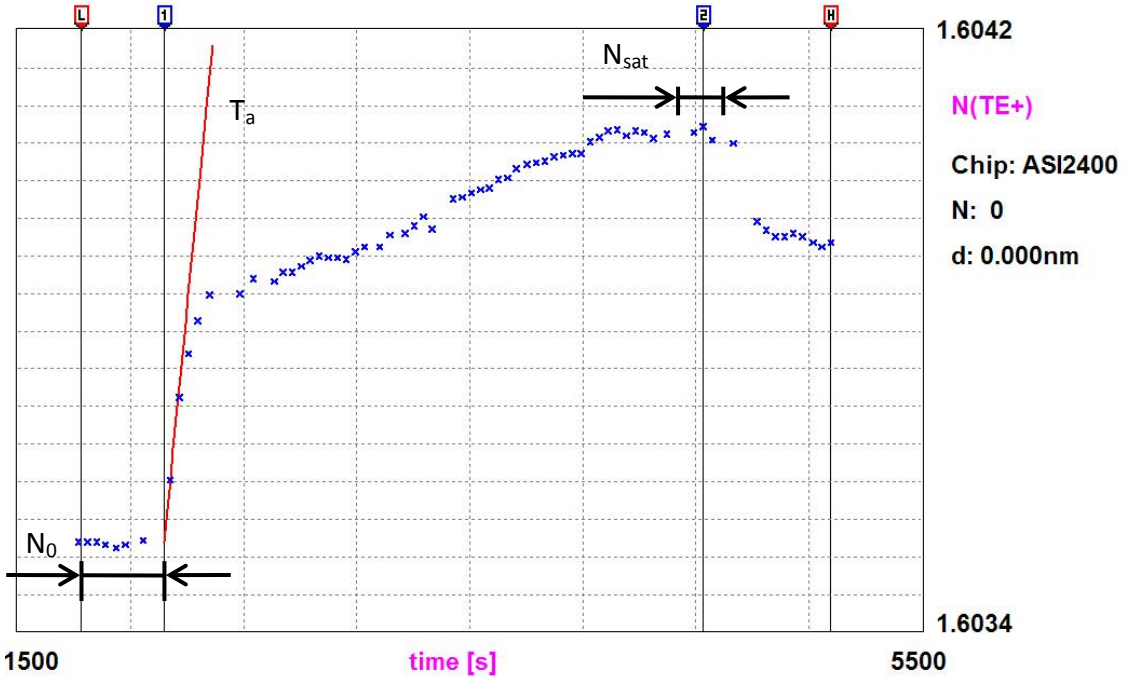

Figure 6.33 N-t diagram of *E.coli* in PBS on titania. [Experimental code: 090304-3]

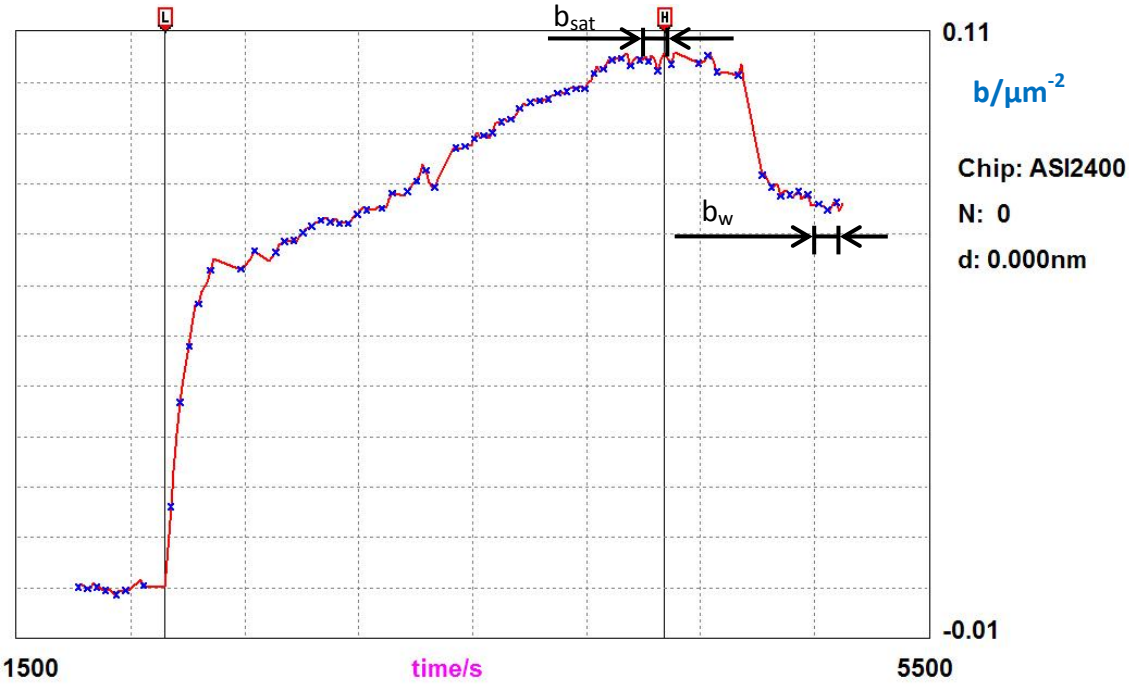

Figure 6.34 b-t diagram of *E.coli* in PBS on titania.

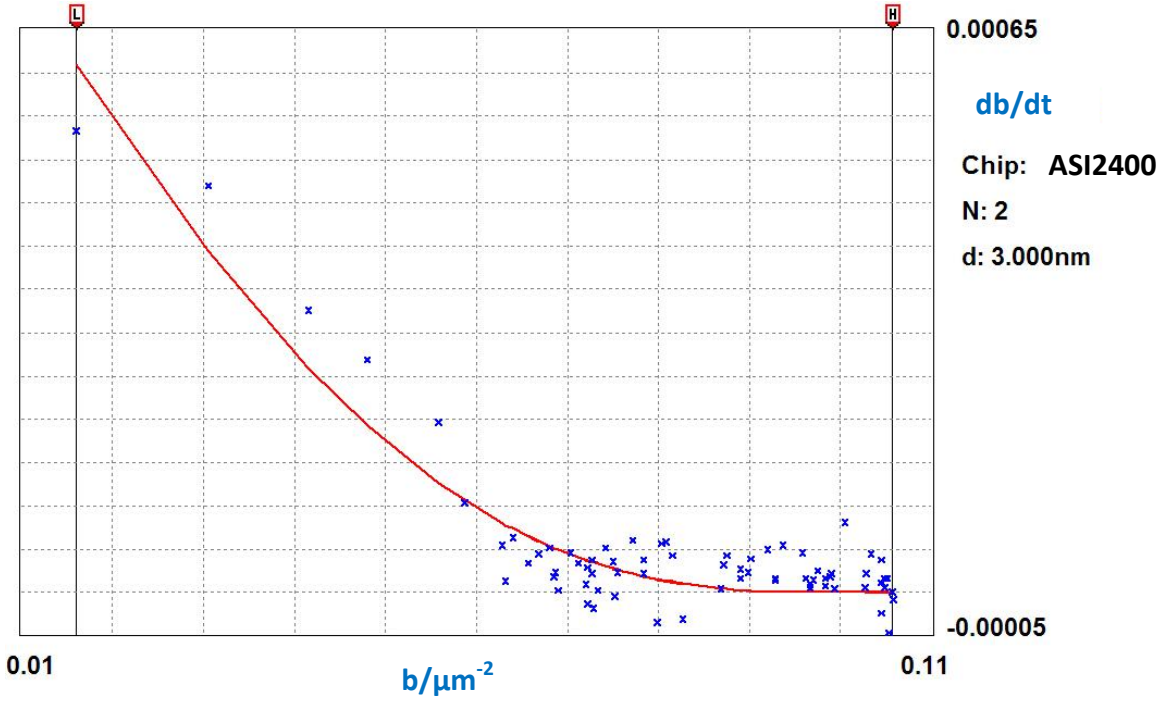

Figure 6.35 RSA Fitting of db/dt vs. b of *E.coli* in PBS on titania.

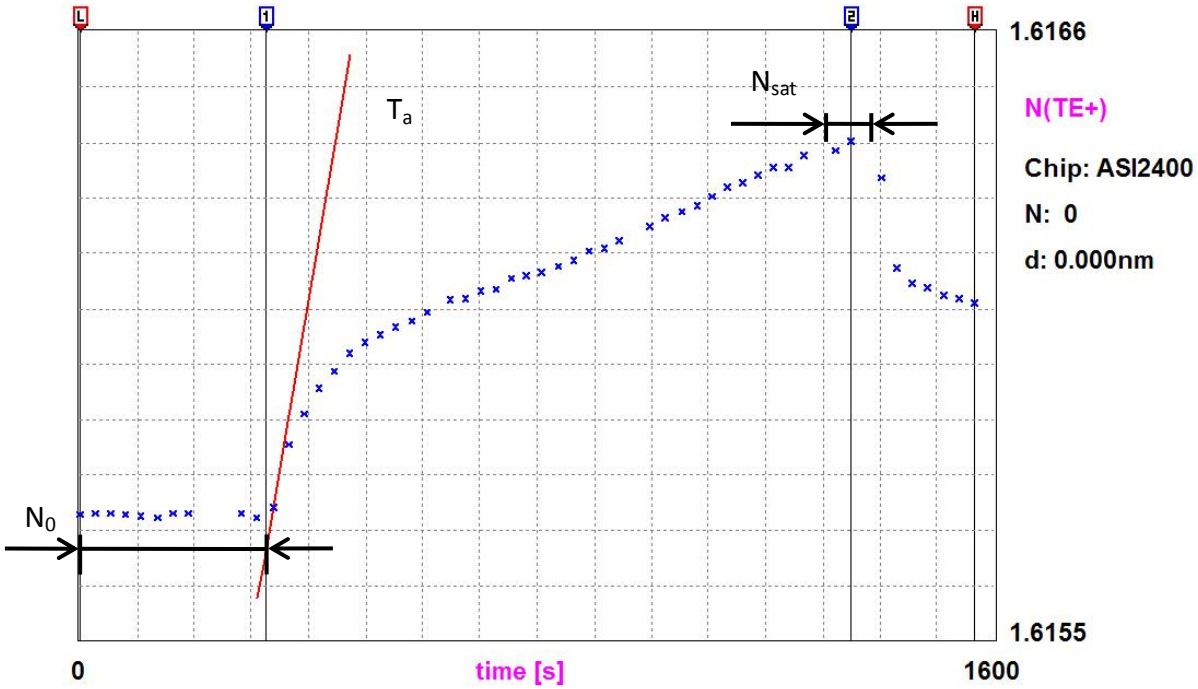

Figure 6.36 N-t diagram of *E.coli* in Z1150 on zirconia. [Experimental code: EZZ100]

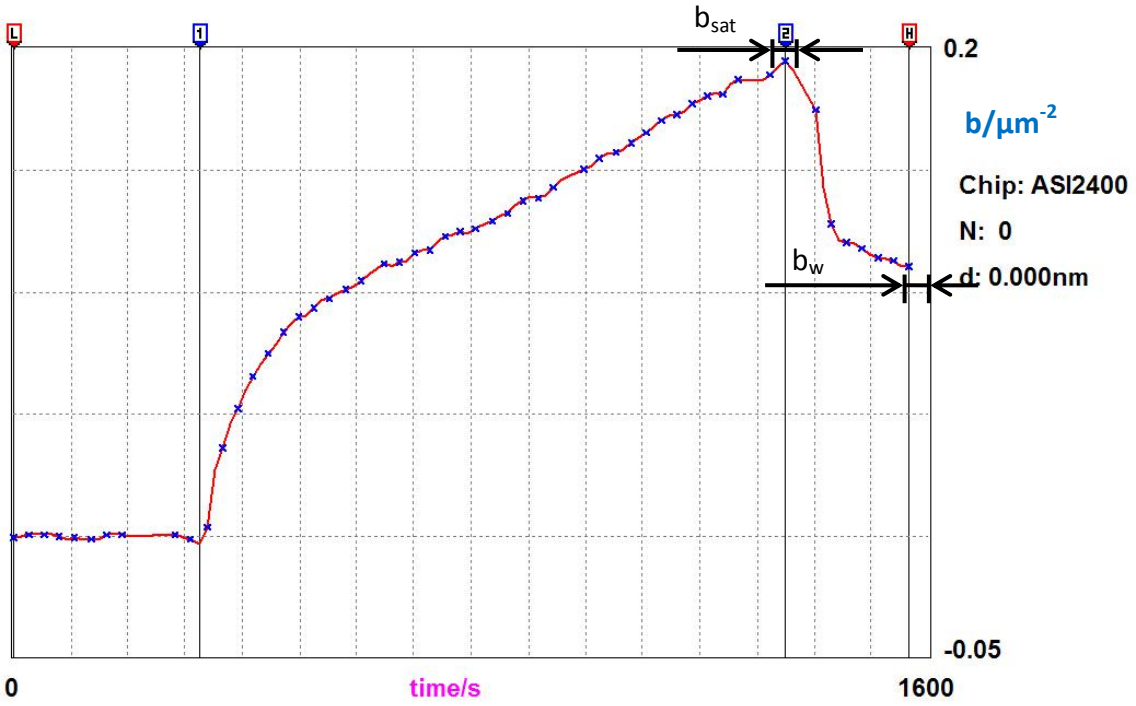

Figure 6.37 b-t diagram of *E.coli* in Z1150 on zirconia.

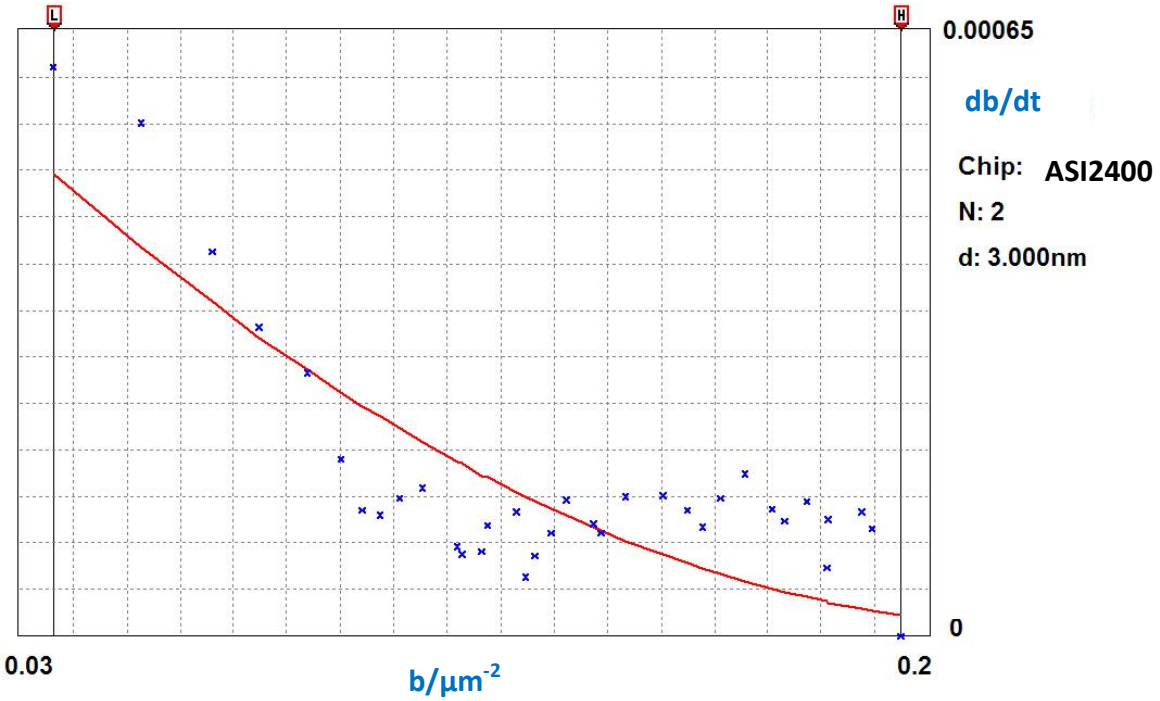

Figure 6.38 RSA Fitting of db/dt vs. b of *E.coli* in Z1150 on zirconia.

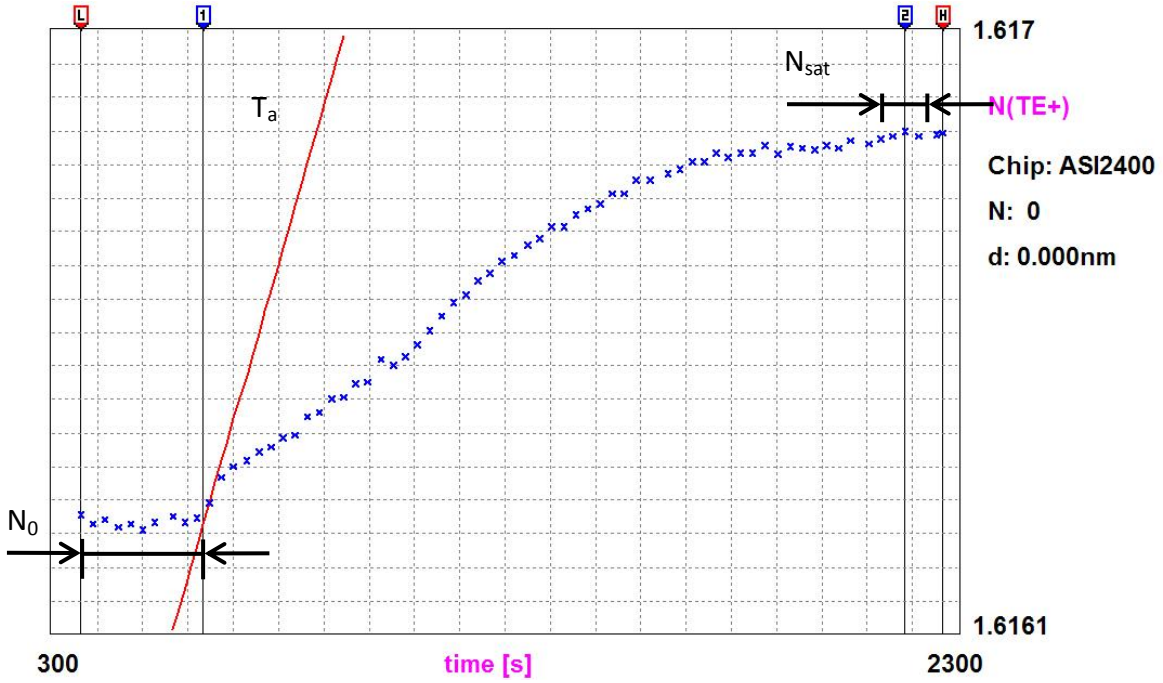

Figure 6.39 N-t diagram of *E.coli* in PBS on alumina. [Experimental code: ALE100X1]

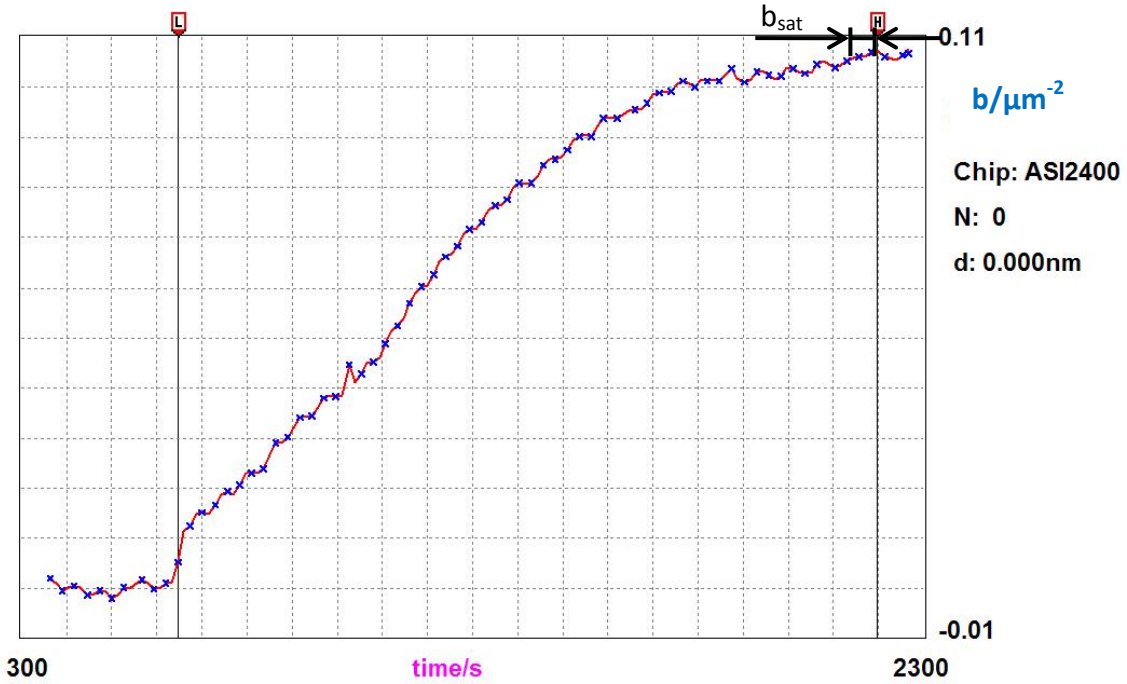

Figure 6.40 b-t diagram of *E.coli* in PBS on alumina. Clearly not pure RSA.

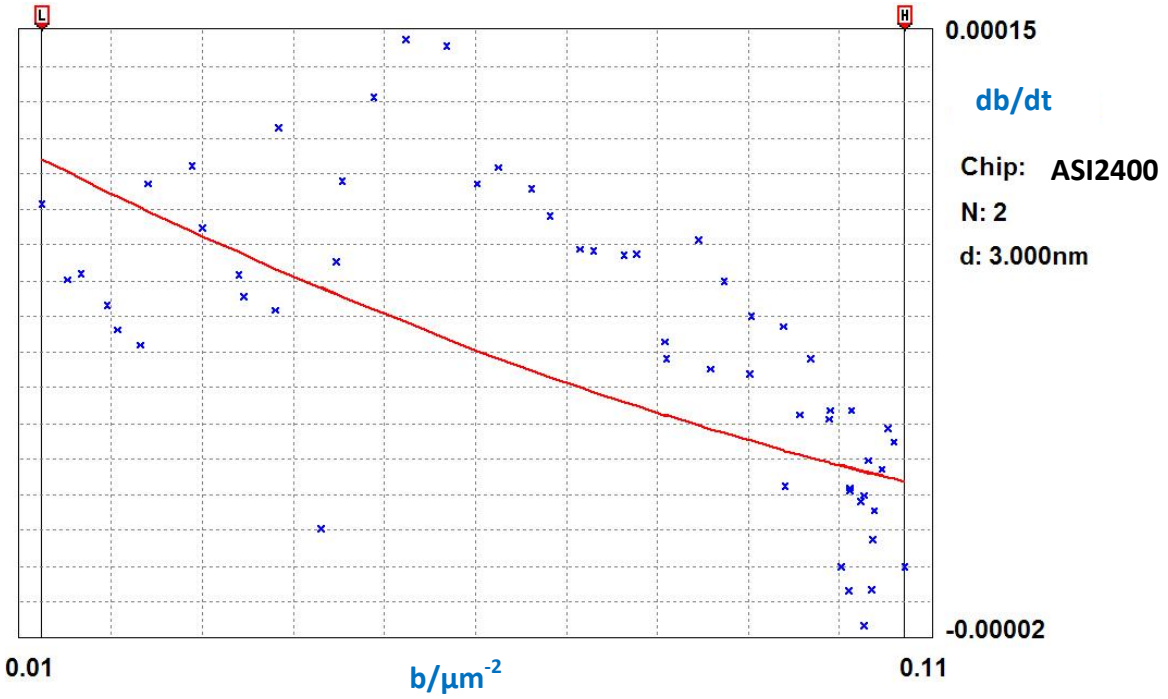

Figure 6.41 RSA Fitting of db/dt vs. b of *E.coli* in PBS on alumina.

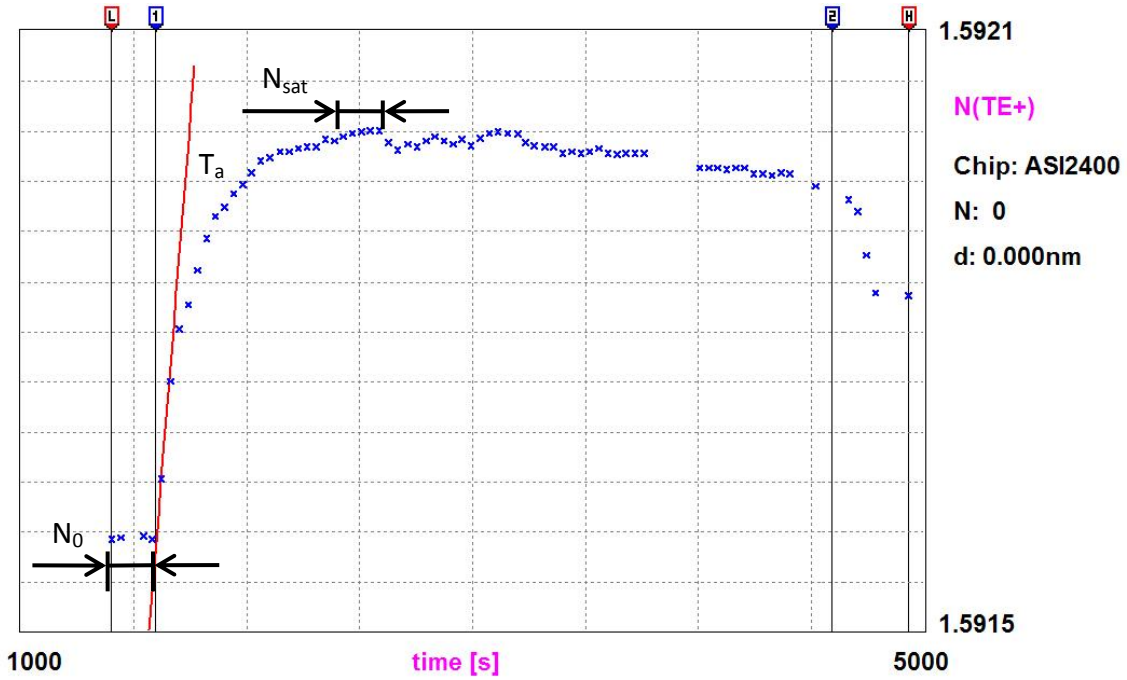

Figure 6.42 N-t diagram of 50x dilution *E.coli* in PBS on silica [Experimental code: R0-1].

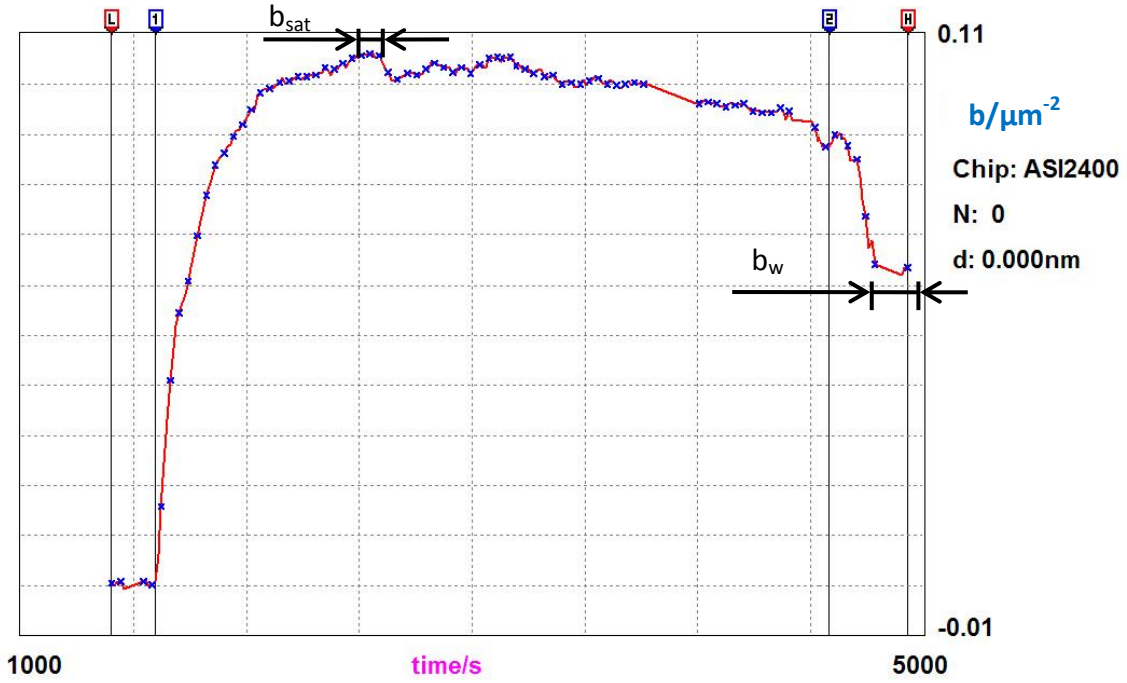

Figure 6.43 b-t diagram of 50x dilution *E.coli* in PBS on silica. Unusual desorption behaviour.

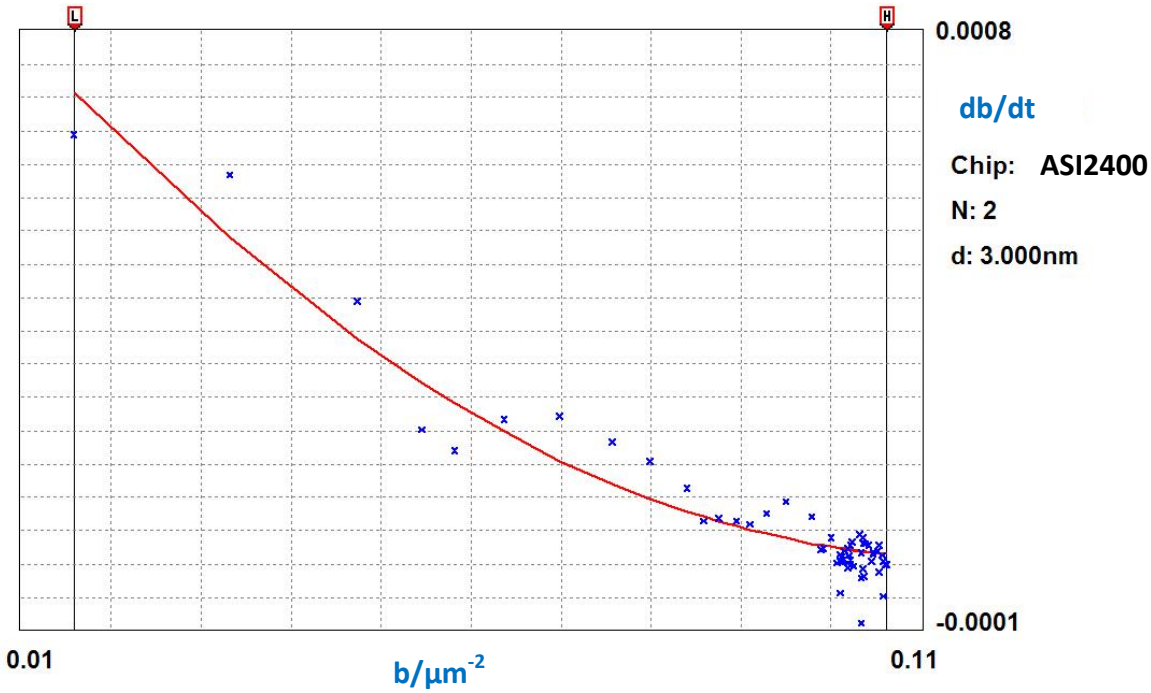

Figure 6.44 RSA Fitting of db/dt vs. b of 50x dilution *E.coli* in PBS on silica.

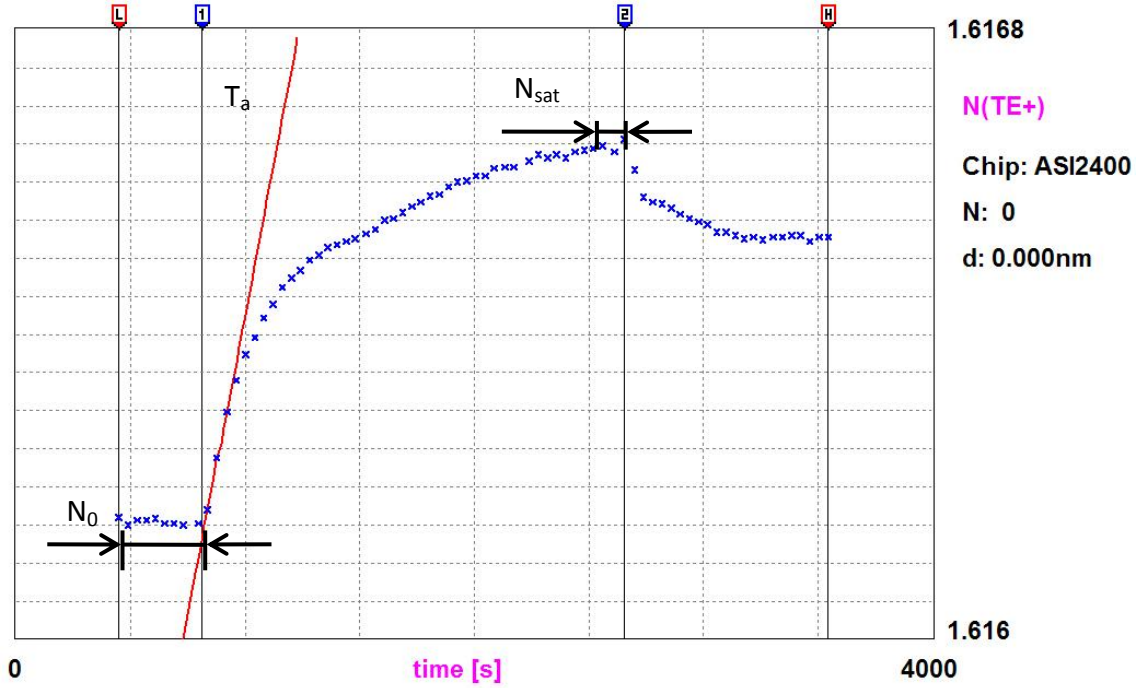

Figure 6.45 N-t diagram of 50x dilution *E.coli* in PBS on zirconia [Experimental code: R0-2].

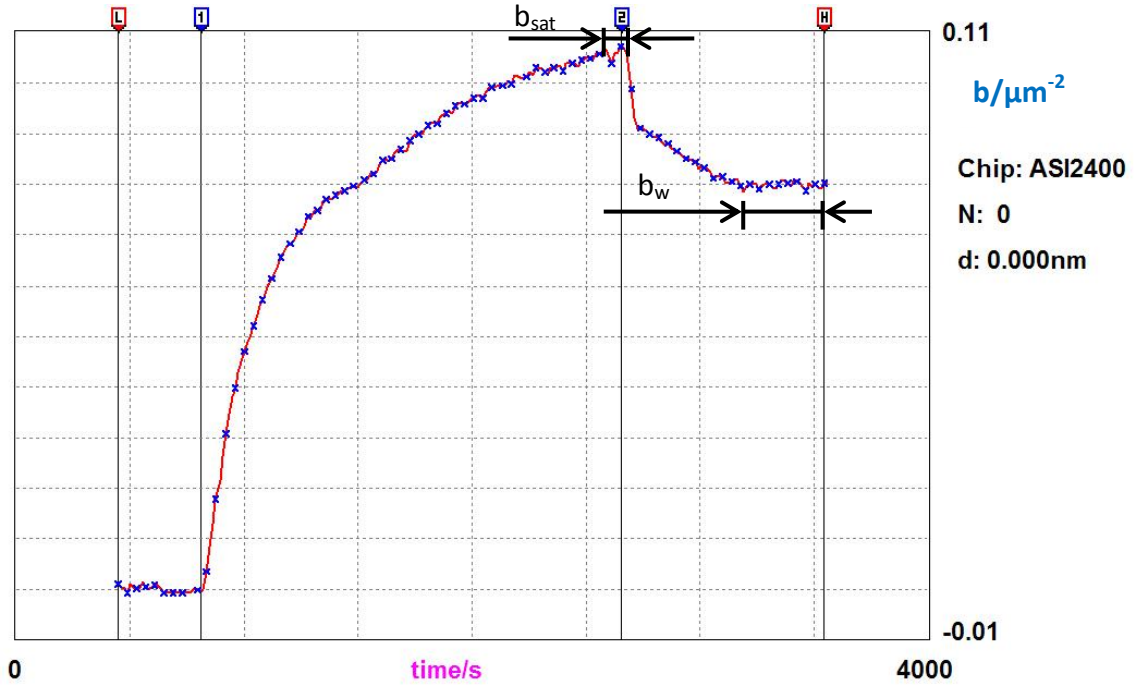

Figure 6.46 b-t diagram of 50x dilution *E.coli* in PBS on zirconia.

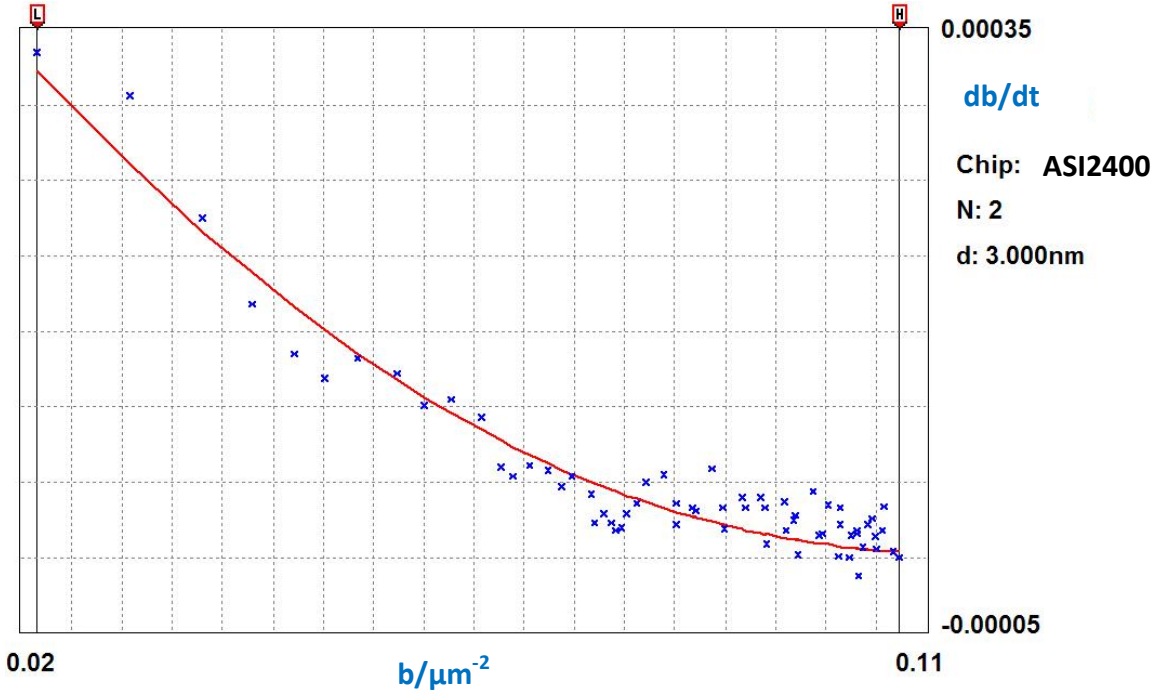

Figure 6.475 RSA Fitting of db/dt vs. b of 50x dilution *E.coli* in PBS on zirconia.

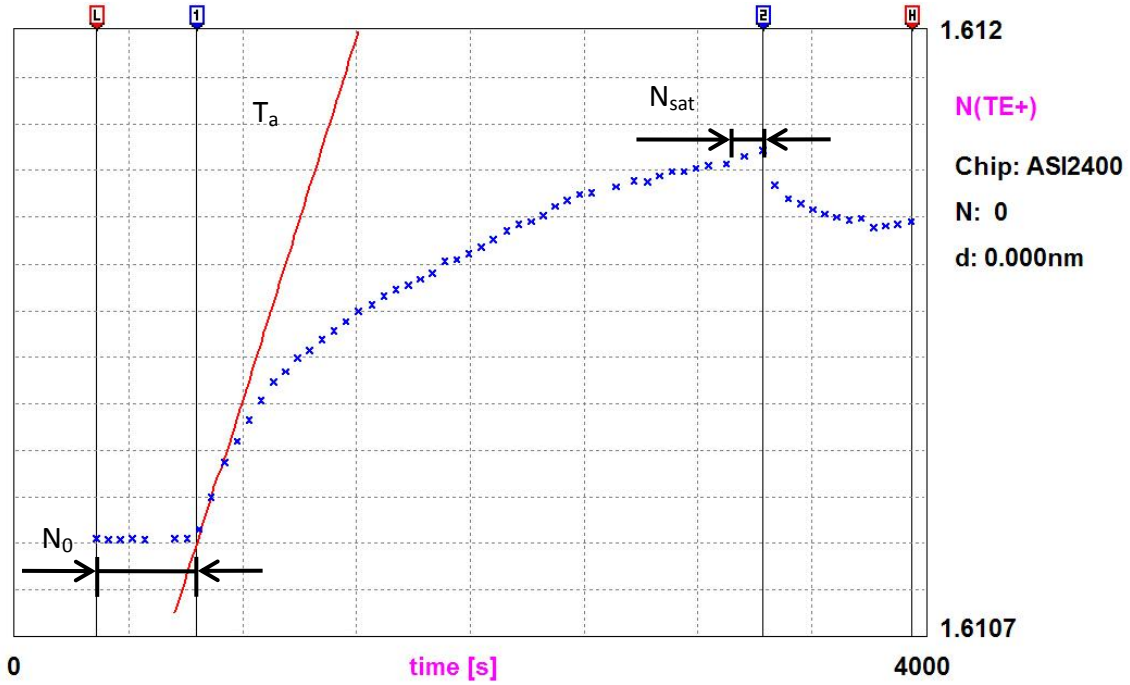

Figure 6.48 N-t diagram of 50x dilution *E.coli* in PBS on titania [Experimental code: R0-3].

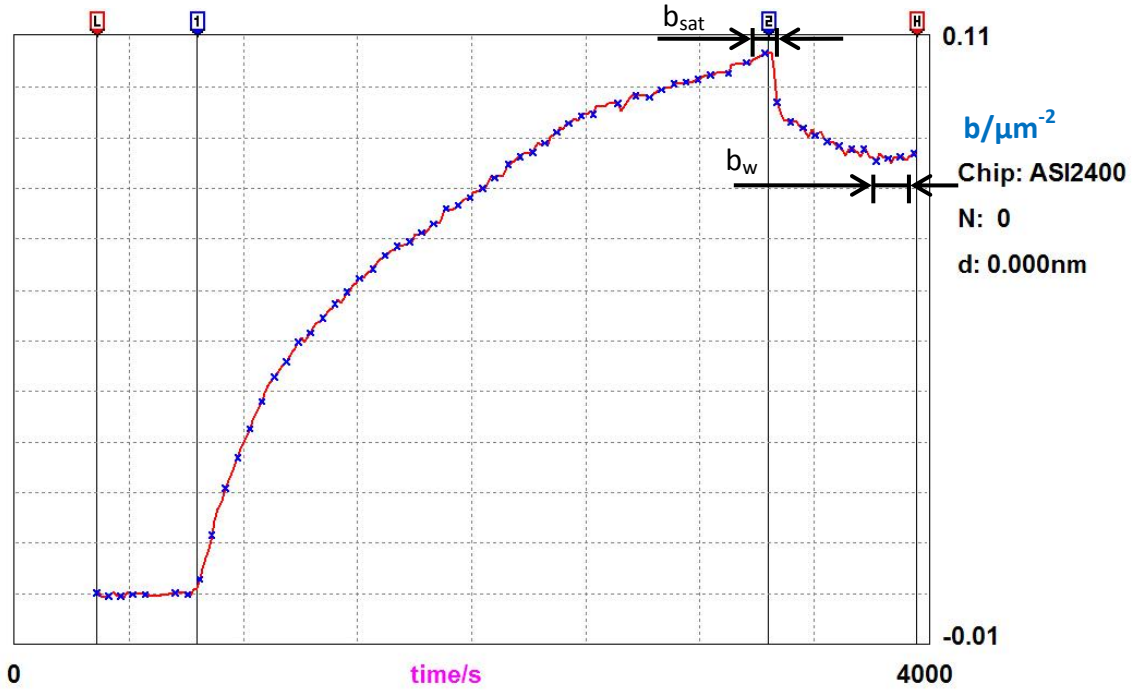

Figure 6.49 b-t diagram of 50x dilution *E.coli* in PBS on titania.

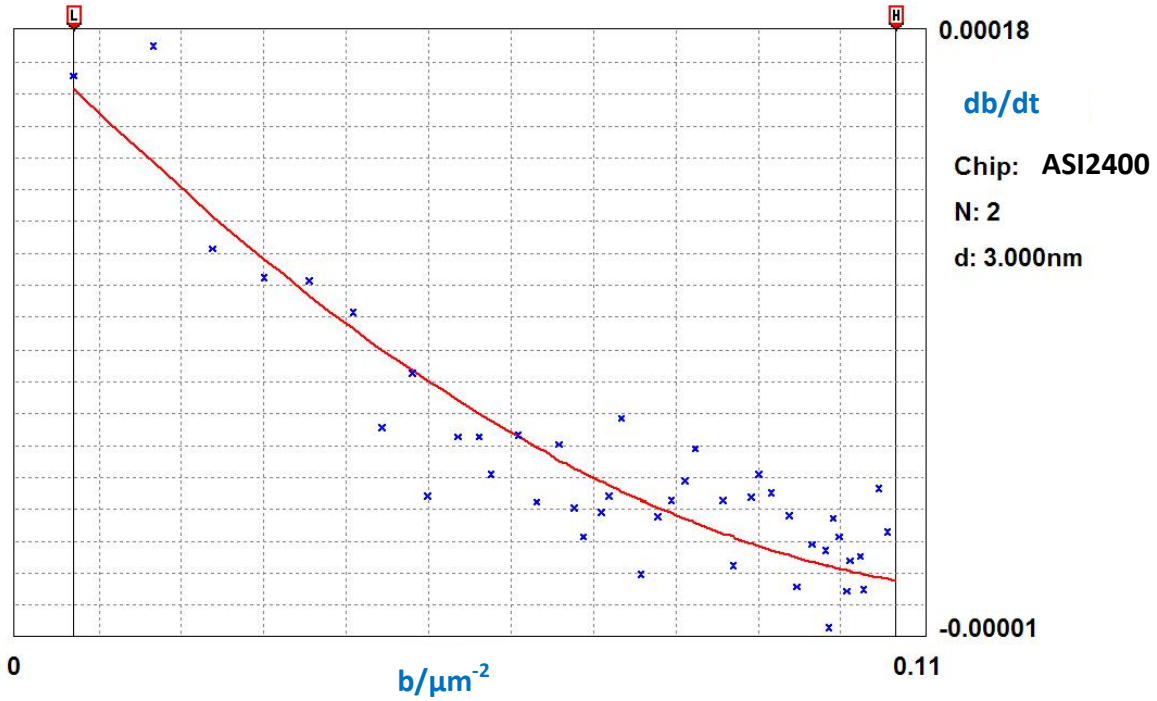

Figure 6.50 RSA Fitting of db/dt vs. b of 50x dilution *E.coli* in PBS on titania.

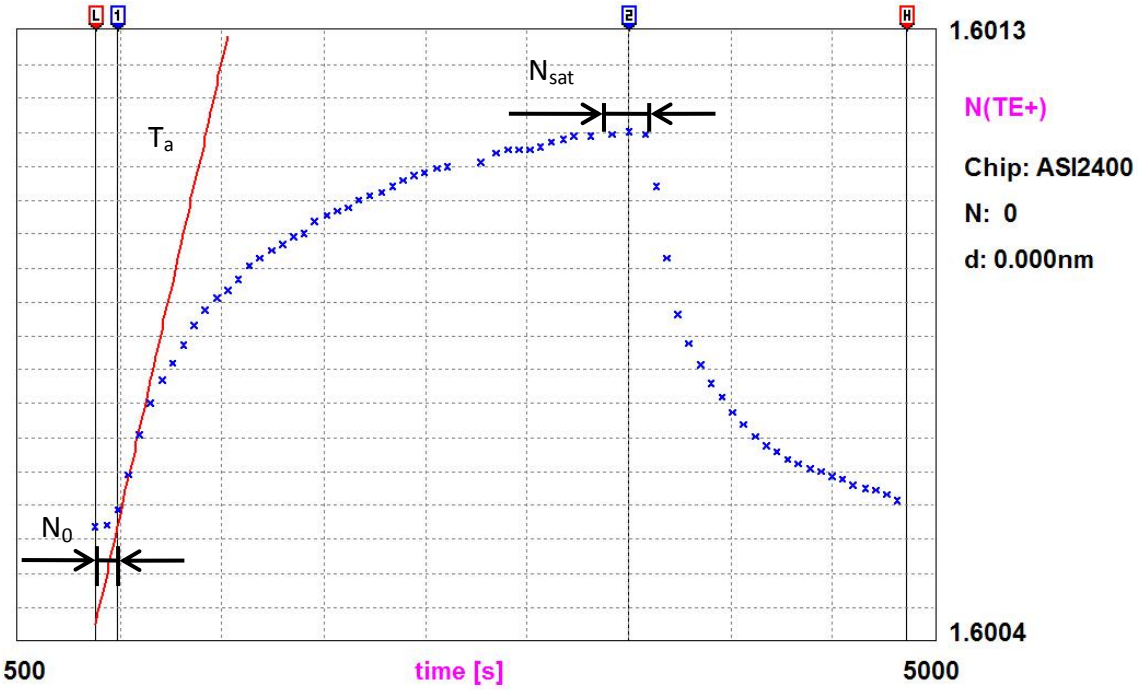

Figure 6.51 N-t diagram of 200x dilution *E.coli* in PBS on silica.

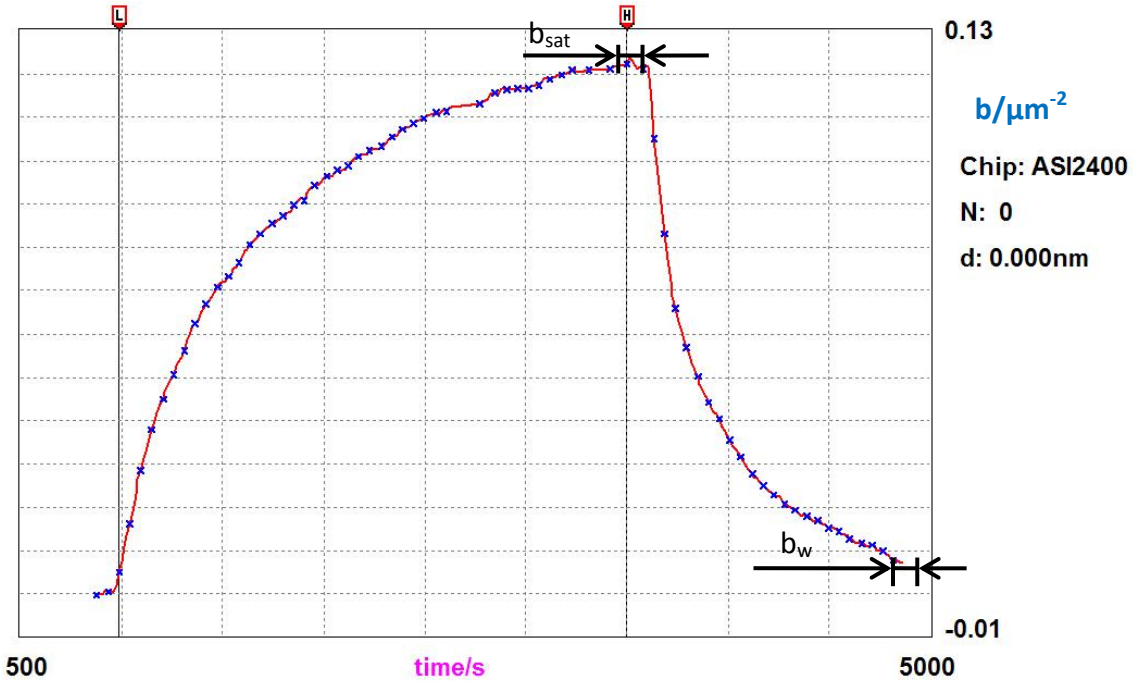

[Experimental code: R0-7].

Figure 6.52 b-t diagram of 200x dilution *E.coli* in PBS on silica.

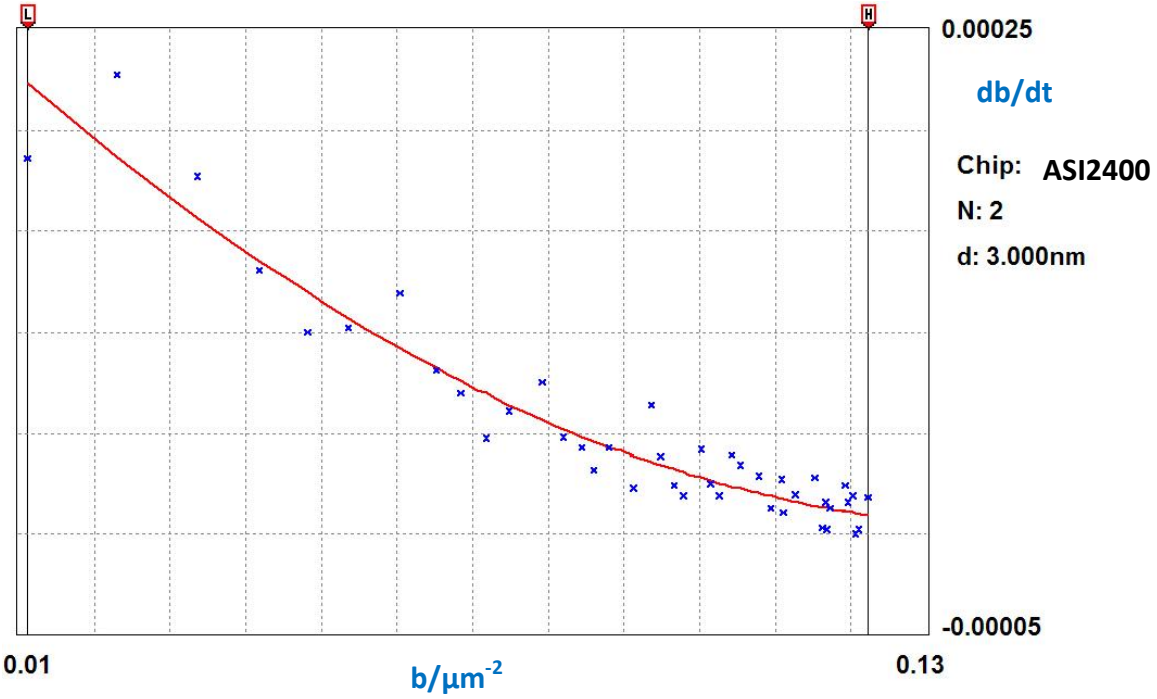

Figure 6.53 RSA Fitting of db/dt vs. b of 200x dilution *E.coli* in PBS on silica.

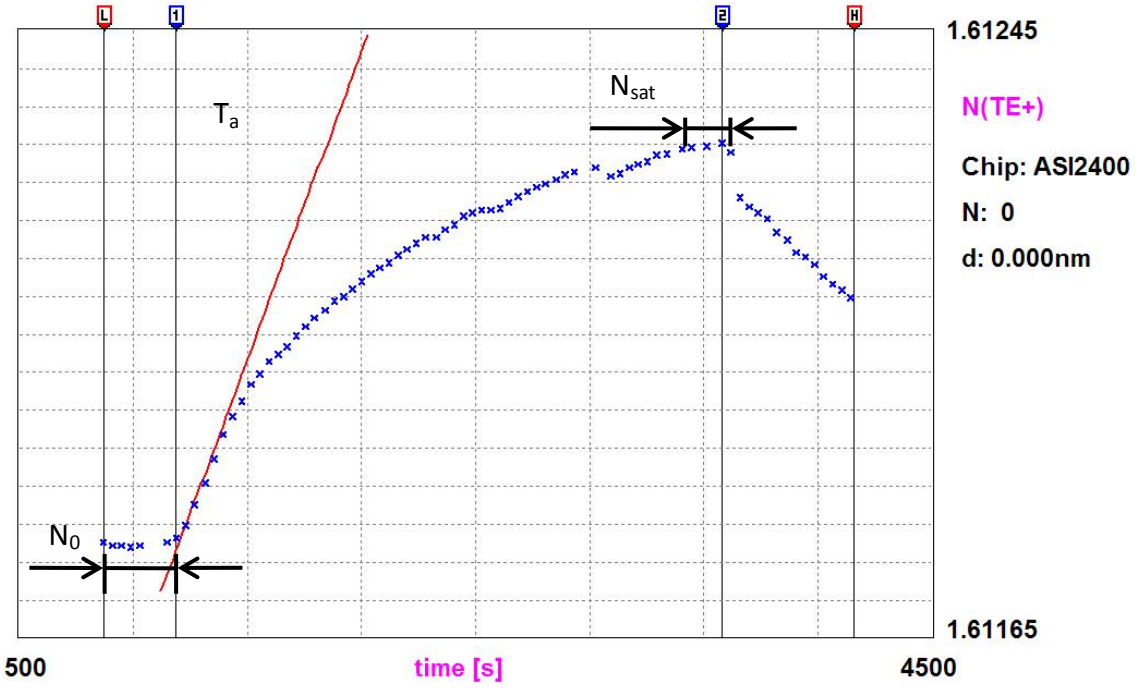

Figure 6.54 N-t diagram of 200x dilution *E.coli* in PBS on zirconia [Experimental code: R0-8].

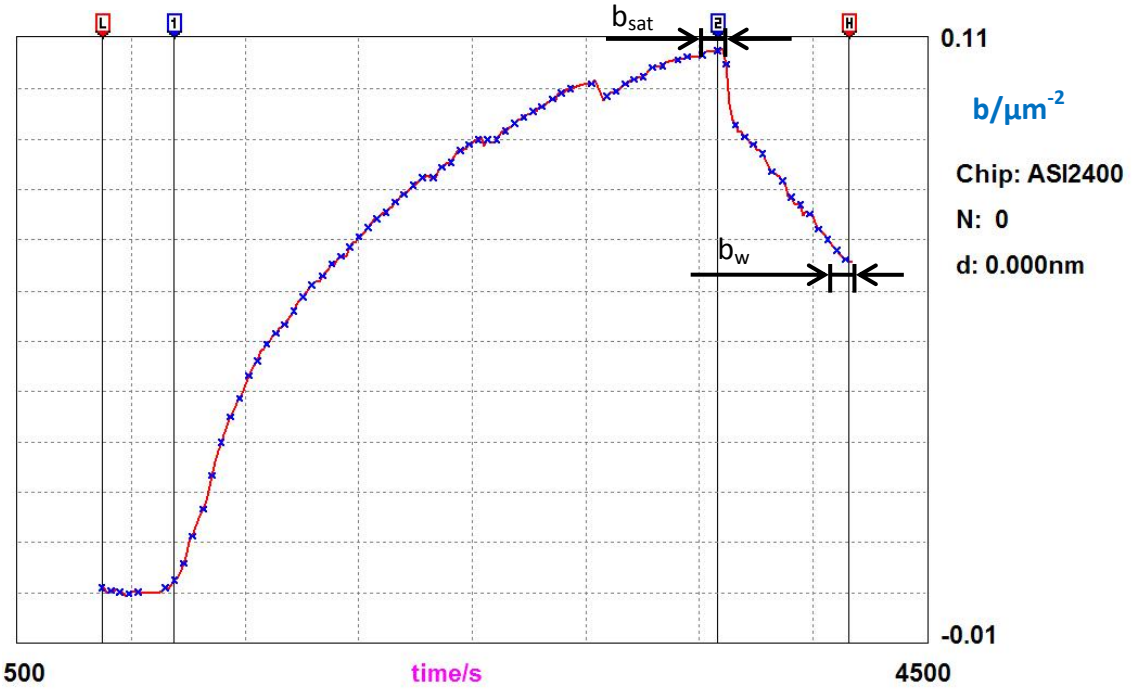

Figure 6.55 b-t diagram of 200x dilution *E.coli* in PBS on zirconia.

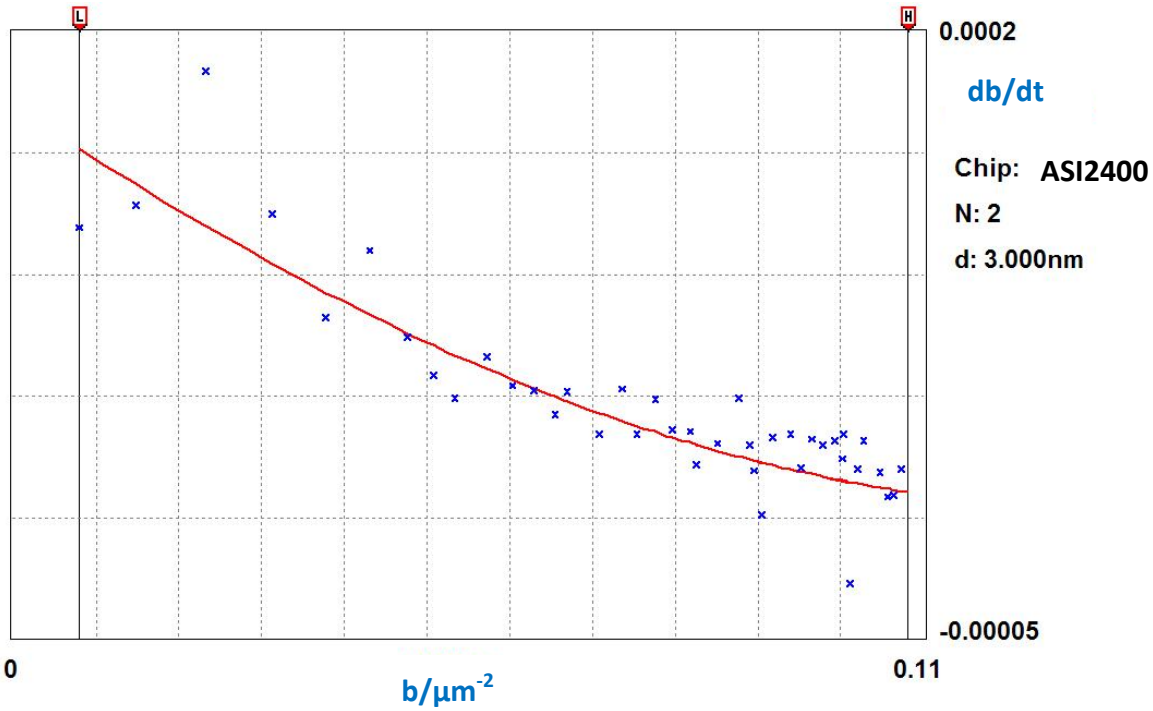

Figure 6.56 RSA Fitting of $d\theta/dt$ vs. θ of 200x dilution *E.coli* in PBS on zirconia.

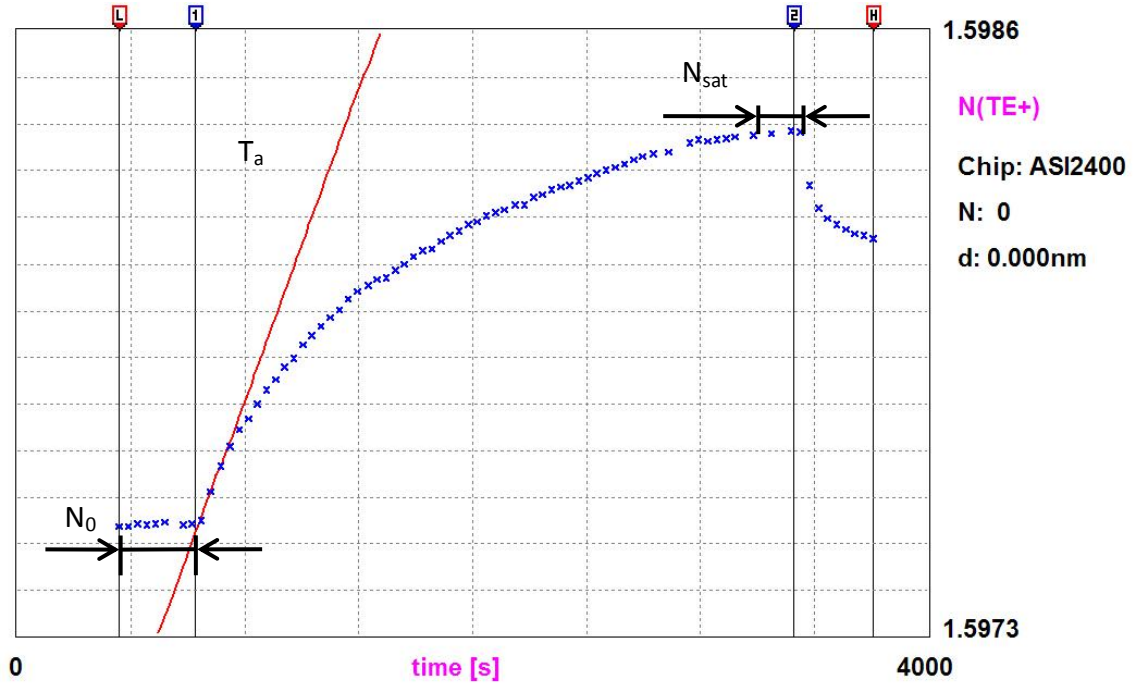

Figure 6.57 N-t diagram of 200x dilution *E.coli* in PBS on titania [Experimental code: R0-9].

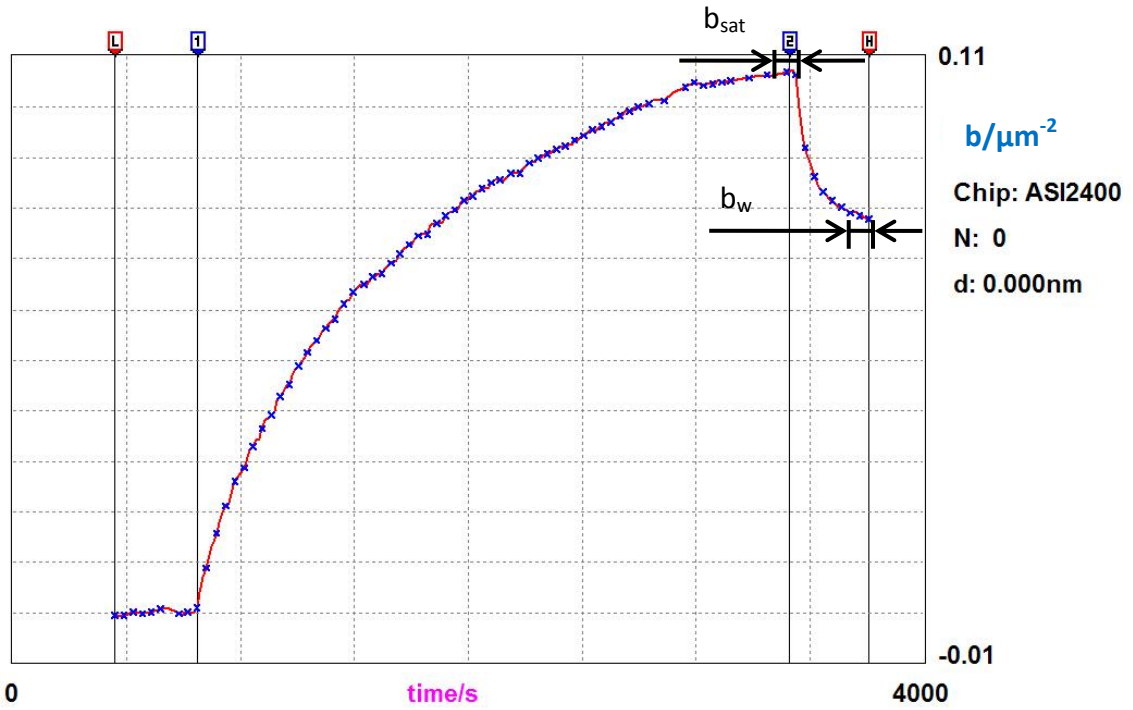

Figure 6.58 b-t diagram of 200x dilution *E.coli* in PBS on titania.

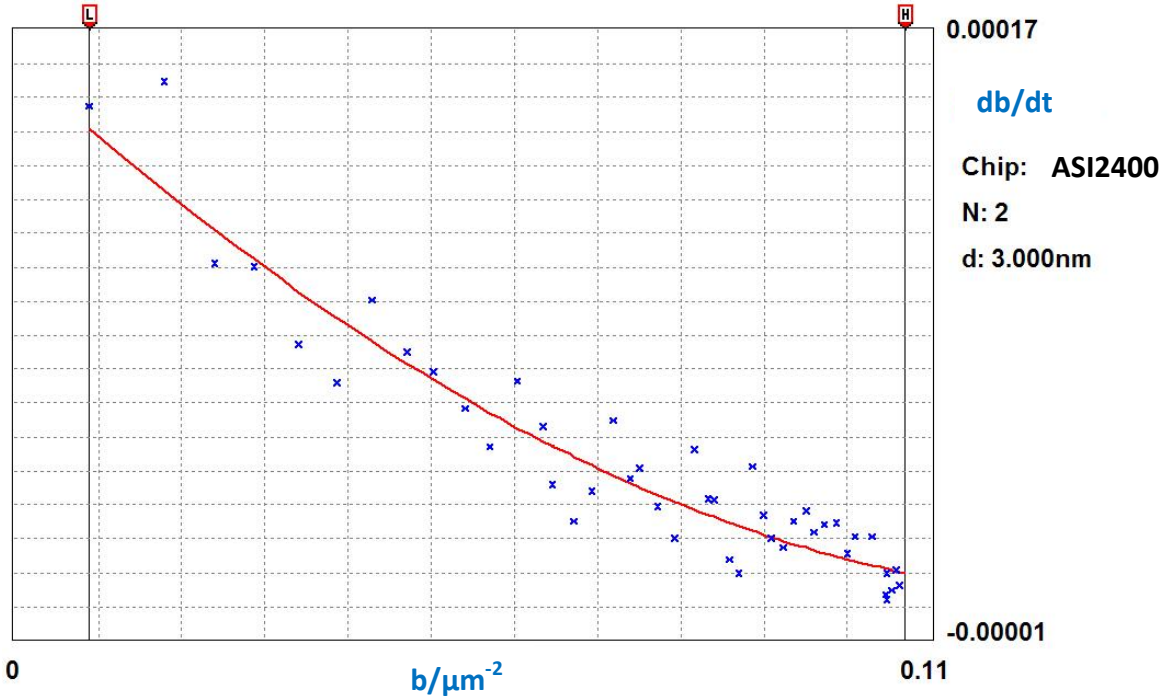

Figure 6.59 RSA Fitting of db/dt vs. b of 200x dilution *E.coli* in PBS on titania.

6.3.3 Tabular summary

Fitting results yielding kinetic parameters for random sequential bacterial adsorption derived from previous equations and figures are tabulated in this section. Here is the summary of how each term is obtained:

b_{sat} is read from the b versus t curve where the adsorption of bacteria reaches saturation.

b_w is the number of bacteria remaining adsorbed on the surface after flooding (washing) with buffer, also read from the b versus t curve.

k_a and a respectively are the kinetic rate coefficient of adsorption and the area occupied by one bacterium and both are derived from fitting Equation (6.2) (p. 67).

Interfacial energy ΔG_a is derived from k_a using Equation (6.3) (p. 68) and the interfacial energy $\Delta G_{123}^{|\,|(exp)}$ is estimated as ΔG_a / a and compared with calculated from the independently obtained surface tensions (Table 6.12, p 106).
The bacterial concentration was (100x dilution) 1.56×10^{-7} cells/ml.

Table 6.3 Kinetic parameters for random sequential bacterial adsorption for *E.coli* in PBS.

Parameter	Al_2O_3	SiO_2	TiO_2	ZrO_2	unit	Typical Uncertainty
b_{sat}	0.105	0.11	0.105	0.105	μm^{-2}	±0.005
b_w/b_{sat}	100 %	<50 %	70 %	100 %	–	±5-10 %
k_a	0.08[(a)]	0.23	0.6	0.46	μm/s	±0.01
a	2.54[(a)]	3.22	5.3	4.26	μm^2	±0.05
ΔG_a	1.76[(a)]	-2.2	-6.2	-5.1	10^{-18} mJ	$\pm 1x10^{-20}$
$\Delta G_{123}^{\|\|(exp)}$	6.9[(a)]	-6.8	-11.6	-11.7	10^{-7} mJ/m^2	$\pm 5x10^{-8}$

(a) Generalized Ballistic Deposition.

Table 6.4 Kinetic parameters for random sequential bacterial adsorption for *E.coli* in Z1.

Parameter	TiO_2	ZrO_2	unit	Typical Uncertainty
b_{sat}	0.105	0.11	μm^{-2}	±0.005
b_w/b_{sat}	–[(b)]	90%	–	±5-10 %
k_a	0.59	0.46	μm/s	±0.01
a	2.76	4.05	μm^2	±0.05
ΔG_a	-6.1	-5.1	10^{-18}mJ	$\pm 1x10^{-20}$
$\Delta G_{123}^{\|\|(exp)}$	-22.1	-12.6	10^{-7} mJ/m^2	$\pm 5x10^{-8}$

(b) ''–'' means no experimental data available.

Table 6.5 Kinetic parameters for random sequential bacterial adsorption for *E.coli* in Z1150.

Parameter	SiO_2	ZrO_2	unit	Typical Uncertainty
b_{sat}	0.108	0.19	μm^{-2}	±0.005
b_w/b_{sat}	50%	60%	–	±5-10 %
k_a	0.42[(c)]	0.44	μm/s	±0.01
a	4.06[(c)]	2.04	μm^2	±0.05
ΔG_a	-4.66[(c)]	-4.86	10^{-18}mJ	$\pm 1x10^{-20}$
$\Delta G_{123}^{\|\|(exp)}$	-11.4[(c)]	-23.8	10^{-7} mJ/m^2	$\pm 5x10^{-8}$

(c) Assuming pure RSA, GBD may have fitted better.

Table 6.6 Kinetic parameters for random sequential bacterial adsorption for *L.plantarum* in PBS.

Parameter	SiO_2	TiO_2	ZrO_2	unit	Typical Uncertainty
b_{sat}	0.27	0.26	0.26	μm^{-2}	±0.005
b_w/b_{sat}	60%	100%	80%	–	±5-10 %
k_a	1.279	1.71	0.58[(d)]	μm/s	±0.01
a	1.285	1.52	0.59[(d)]	μm^2	±0.05
ΔG_a	-5.66	-6.85	-2.45[(d)]	10^{-18}mJ	$\pm 1x10^{-20}$
$\Delta G_{123}^{\|\|(exp)}$	-44	-45.1	-43.1[(d)]	10^{-7} mJ/m^2	$\pm 5x10^{-8}$

(d) Generalized Ballistic Deposition.

Table 6.7 Kinetic parameters for random sequential bacterial adsorption for *L.plantarum* in Z1150.

Parameter	SiO_2	TiO_2	ZrO_2	unit	Typical Uncertainty
b_{sat}	0.26	0.27	0.24	μm^{-2}	±0.005
b_w/b_{sat}	70%	45%	60%	–	±5-10 %
k_a	1.29	3.3	2.1	μm/s	±0.01
a	1.37	1.59	2.57	μm^2	±0.05
ΔG_a	-5.7	-9.5	-7.7	10^{-18}mJ	$\pm 1x10^{-20}$
$\Delta G_{123}^{\|\|(exp)}$	-41.6	-59.7	-29.9	10^{-7} mJ/m^2	$\pm 5x10^{-8}$

We also present the different dilution (50x and 200x dilution from original concentration) of *E.coli* suspensions for the comparison in Table 6.8 and 6.9.

Table 6.8 Kinetic parameters for random sequential bacterial adsorption for twice concentrated (50X dilution from original concentration) *E.coli* in PBS.

Parameter	SiO_2	TiO_2	ZrO_2	unit	Typical Uncertainty
b_{sat}	0.105	0.108	0.108	μm^{-2}	±0.005
b_w/b_{sat}	60%	90%	80%	–	±5-10 %
k_a	0.599	0.114	0.312	μm/s	±0.01
a	4.05	3.61	4.24	μm^2	±0.05
ΔG_a	-6.08	6.44	-3.43	10^{-18}mJ	$\pm 1x10^{-20}$
$\Delta G_{123}^{\|\|(exp)}$	-15.0	17.8	-8.1	10^{-7} mJ/m^2	$\pm 5x10^{-8}$

Table 6.9 Kinetic parameters for random sequential bacterial adsorption for twice diluted (200X dilution from original concentration) *E.coli* in PBS.

Parameter	SiO_2	TiO_2	ZrO_2	unit	Typical Uncertainty
b_{sat}	0.122	0.108	0.108	μm^{-2}	±0.005
b_w/b_{sat}	5%	75%	60%	–	±5-10 %
k_a	0.166	0.102	0.108	μm/s	±0.01
a	3.2	3.3	3.3	μm^2	±0.05
ΔG_a	-8.53	1.12	8.76	10^{-18}mJ	$\pm 1x10^{-20}$
$\Delta G_{123}^{\|\|(exp)}$	-26.7	3.4	26.5	10^{-7} mJ/m^2	$\pm 5x10^{-8}$

6.4 Discussion

My Hypothesis 3 is that RSA describes bacterial adsorption. In this case, not only should the kinetics follow the characteristic RSA law, but if the adsorption is irreversible then a should equal ā irrespective of the surface.

6.4.1 Comparison of a with ā

According to Equation (4.12), the area occupied by one bacterium at the jamming limit should be consistent with the projected area ā measured independently from microscopy (*E.coli* is 5.02 μm^2 and *L.plantarum* is 2.03 μm^2, see Table 5.1, p.49). However, according to my results, a depends on substratum and medium.

For *E.coli* and *L. plantarum* on titania, a ≈ ā, confirming titania's reputation as a highly biocompatible material (Ramsden, 2008). In many other cases a is smaller than ā (never larger). The possible reasons could be:

- Sample preparation for the electron microscopy distorts the size (Hillman, 2009).
- There is a distribution of sizes and different sizes have different interfacial energies.
- There is a distribution of orientations (bacteria are typically sphereocylinders or prolate ellipsoids ; ā assumes the bacteria are oriented with their long axis parallel to the substratum).

- The orientation of the prolate-ellipsoidal bacteria is substratum dependent.

The dependence on ionic strength (comparing Z1 with Z1150, see Table 6.10) => the effective radius of the bacterium is augmented by long range mutual electrostatic repulsion, which is shielded by salt.

Table 6.10 Summary results of area occupied by one bacterium (a/μm^2) in Z1 and Z1150 on ZrO_2.

Bacteria	Material	Z1	Z1150
E.coli	ZrO_2	4.05	2.04

The dependence on ion type (comparing Z1150 with PBS, see Table 6.11): on silica, the difference is not so great (slightly smaller in PBS for both *E.coli* and *L.plantarum*). On zirconia, there is a dramatic difference - *E.coli* is bigger in PBS, but *L.plantarum* is smaller. On silica, a is in good agreement with ā in PBS on TiO_2, but somewhat smaller on SiO_2. Note that phosphate is Kosmotropic (stablizing) (Cacace *et al.*, 1997).

Table 6.11 Summary results of area occupied by one bacterium (a/μm^2) in PBS and Z1150.

Bacteria	Material	PBS	Z1150
E.coli	SiO_2	3.22	4.06
	ZrO_2	4.26	2.04
L.plantarum	SiO_2	1.29	1.37
	TiO_2	1.52	1.59
	ZrO_2	0.59	2.57

6.4.2 Comparison of $\Delta G_{123}^{||(exp)} = \Delta G_a/a$ with predicted $\Delta G_{123}^{||}$

By using the data from Tables 6.1 to 6.7, the experimental free energy $\Delta G_{123}^{||(exp)}$ derived from the area (a) occupied by one bacterium is hugely different from the free energy $\Delta G_{123}^{||}$ derived from the surface tensions (see Table 6.12). This could be because the real contact area of one bacterium is only a tiny fraction - less than one millionth - of the projected area due to protrusions (Hypothesis 5). However, this may not be the only reason. Equation (6.3) implies that the bacteria follow Boltzmann statistics. Nevertheless, equilibration of the lumbering bacterium may be too slow compared with the characteristic duration of an individual adsorption process, i.e. ergodicity is broken, as in many biological processes (Ramsden, 2009).

We predict repulsive interaction for silica and titania, but attraction for zirconia and alumina. Experiment, however, shows attraction for all substrata (in PBS), although this does depend on the assumption of $\delta_a = r$ (Equation (6.3)).

Table 6.12 Predicted interfacial energy $\Delta G_{123}^{||}$(mJ/m^2) of *E.coli* and *L.plantarum*.

$\Delta G_{123}^{||}$ [(a)]	Al_2O_3	SiO_2	TiO_2	ZrO_2
E.coli	-12.5	15.4	17.8	-16.5
L.plantarum	-24.6	7.8	10	-26.6

(a) Calculated from Equations (3.19), (3.20) and (3.21) using the data from Table 6.1, assuming the medium is pure water.

6.4.3 Comparison of k_a with the hydrodynamic limit

The maximum flux to the surface is given by D/δ_d, where the diffusion boundary distance (δ_d) is calculated using (Ramsden, 1998)

$$\delta_d = 3\left(\frac{D}{K}\right)^{1/3}\left(\frac{KS_cA_c}{F_c}\right)^{1/2} \qquad (6.7)$$

where D is the diffusion coefficient; K is kinematic viscosity (assumed to be that of water, i.e. 9×10^{-3} cm^2/s); S_c is distance along the cuvette (3.5×10^{-3} mm for our cuvette); F_c is volumetric flow rate and A_c is a cross-sectional area (2.826 mm^2 for our cuvette).

So the mean diffusion boundary distance (δ_d) in this study is 0.513 µm for *E.coli* and 0.596 µm for *L. plantarum* in this study.

Hence D/δ_d =0.33 µm /s for *E.coli* and 0.44 µm/s for *L.plantarum*. In a few cases, we are adsorbing faster than this. This seems to be especially associated with negative ΔG^{II}_{123}.

6.4.4 Correlation between required area and interfacial energy

The more attractive the interfacial energy, the bigger the occupied area a (see Figure 6.60). Presumably if the interfacial interaction is highly repulsive, the bacterium will minimize interfacial area; e.g., by adsorbing with its long axis perpendicular to the plane of the substratum (see Figure 6.61).

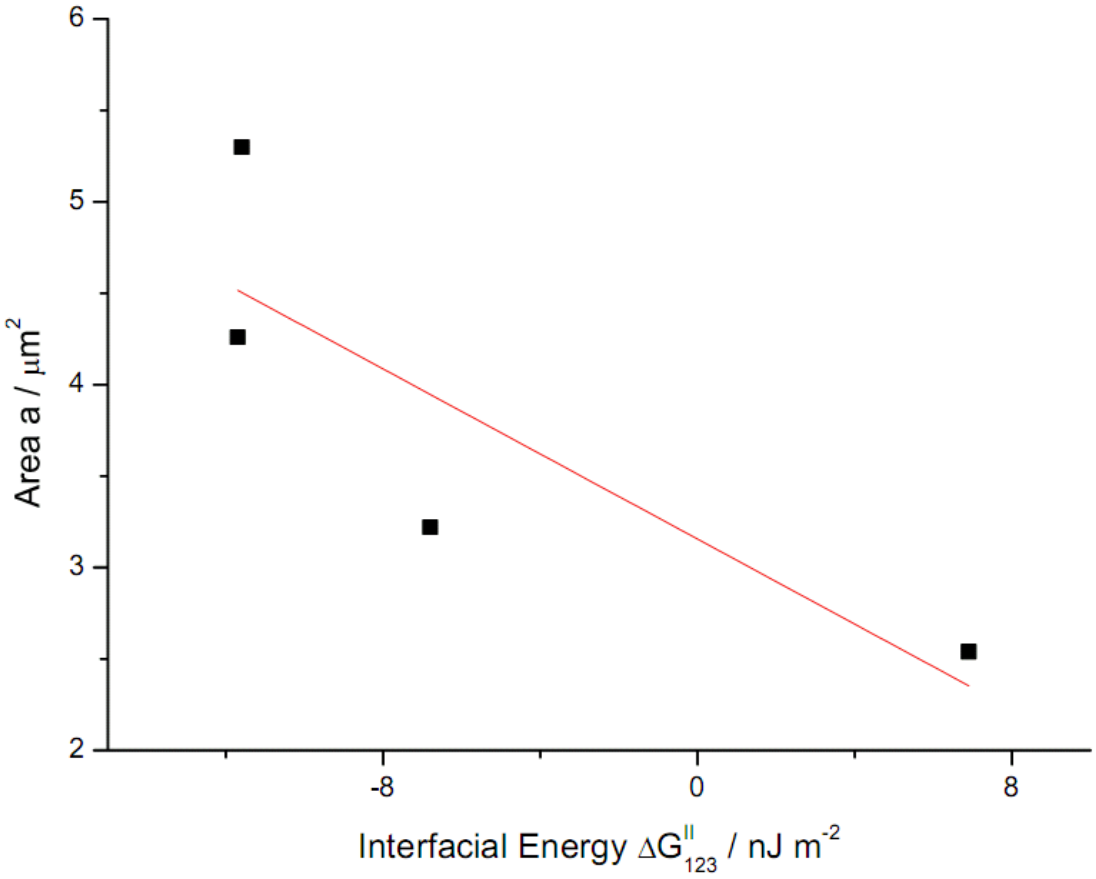

Figure 6.60 Correlation between a and ΔG^{II}_{123} of *E.coli* in PBS. The fitted line is y=-0.12(±0.05)x+3.2(±0.5).

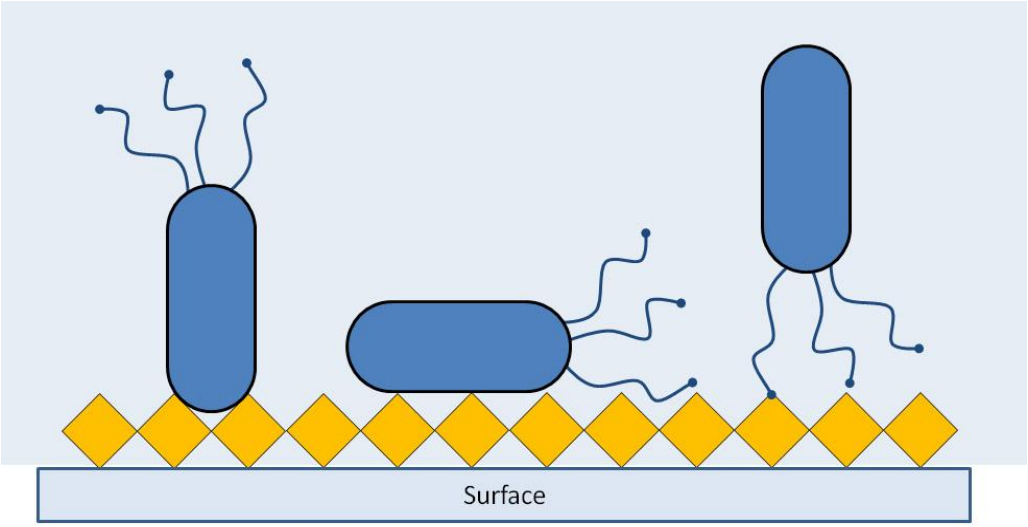

Figure 6.61 Schematic diagram of possible adsorbing orientations of bacteria on a surface.

6.4.5 Cases where RSA is inapplicable (GBD)

There are three cases (*E.coli* in PBS on alumina, *E.coli* in Z1150 on silica and *L.plantarum* in PBS on zirconia) is where pure RSA is inapplicable,instead we must use the generalized ballistic deposition (GBD) model (Csúcs and Ramsden, 1998a), which implies that the bacteria like to cluster on the surface. This might be because alumina may not be that attractive to *E.coli* further implying that area occupied area by one *E.coli* is small and the adsorption rate is slow (see Table 6.3). In the case of *E.coli* in Z1150 on silica (Figure 6.7), I assume pure RSA adsorption, nevertheless, GBD may have fitted better, because there was still area available for *E.coli* adsorbing on the surface. In the case of *L.plantarum* in PBS on zirconia, it is clear that it is not pure RSA (Figure 6.22), though *L.plantarum* has reached the jamming limit, the adsorption rate and occupied area are smaller than with silica and titania, this may be because *L.plantarum* was repeatedly arriving at and leaving the zirconia surface. However, this needs to be further investigated.

6.4.6 Effect of bulk bacterial concentration

The adsorption of *E.coli* in PBS was investigated at double and half the chosen standard concentration. The results (expressed in terms of the fitted parameters, comparing Tables 6.8 and 6.9 with 6.3) are not in perfect agreement, although none of these parameters should be concentration-dependent. However, the experiments were not perfectly comparable in so far as the bacteria had different ages.

Ideally every combination of bacterial strain/substratum/medium should be investigated with microbes over a broad range of concentrations. Although trivial for nonliving adsorbates, this presents many problems of sample stability (for example, bacterial behaviour is known to be sensitive to the proximity of congeners), hence we defer serious investigation of this aspect (see Chapter 11).

Chapter 7 Nanotextured Surfaces

The size of our bacteria is approximately 1-2 µm and surface features are likely to have a characteristic dimension of 10 nm or less. I found only a few data about surface features in the literature. The previous chapter presented the results of adhesion to chemically pure and morphologically smooth substrata. I hypothesize that if chemical and topographical features at least approximately match those of the bacterium surface, adhesion could be enhanced (or diminished) (Hypothesis 4).

In order to make a proper comparison between featureless and feature-containing surfaces, they should be made from the same materials. (Aggarwal *et al.*, 2009) make such a comparison for a protein. I have only been able to take some first steps in this direction. The systems investigated are the following:

1. PMMA and ePTFE;
2. Mucin: a naturally nanostructured giant glycoprotein (Ch 8.).
3. Nanostructured self assembled films from complex organometallic compounds (Ch 9.).

The remainder of this chapter deals with the discussion of nanostructured surface on PMMA and ePTFE, integrated with scanning electronic microscopy.

7.1 *Escherichia coli* adsorption on surface-modified polymers

The control of bacterial attachment to the surface has gained much interest in recent years; especially following the development of nanotechnology. The mechanism of bacterial adhesion may involve sophisticated surface properties of bacteria and attached substrata, either chemical or physical (Wong *et al.*, 2004; Webster *et al.*, 2004). For example the surface roughness (Alava *et al.*, 2005), nanopatterned polymer surfaces (Satriano *et al.*, 2006), chemically microstructured surfaces (Magnani *et al.*, 2003), etc. may affect adhesion.

Here, we focus on the effect of superhydrophobicity on the adhesion of *E.coli* to surfaces. In general, there are two approaches to achieve superhydrophobic properties;

one is chemical, such as to synthesise C-F materials like Teflon, see early work of (Satyaprasad *et al.*, 2007), another approach is to produce nano/microstructured surface leading to the lotus effect. We are more interested in nano/microstructured surfaces. In recent years, there already are many publications showing various processes for the fabrication of superhydrophobic surface, the most frequently used method is to create regular or irregular rough surfaces by lithography or an etching process, followed by fluorine-based or organosilane-based coating for the further reduction of surface free energy (Nakajima *et al.*, 1999; Kessler and Theato, 2009; Wang and Wang, 2006; Jin *et al.*, 2007). Sol-gel processing and self-assembly is another popular process to produce superhydrophobicity relative to silica-based films (Tadanaga *et al.*, 1997; Coupe *et al.*, 2001; Shang *et al.*, 2005) . A few research results demonstrate the creation of a stable, superhydrophobic surface using a vertically aligned carbon nanotube forest together with a thin, conformal hydrophobic polytetrafluoroethylene (PTFE) coating on the surface of the nanotubes (Lau *et al.*, 2003).

As we have discussed the effect of different type of grating on *E.coli* attachment to PMMA in Section 5.8, this chapter shows the preliminary results about the effect of surface nanostructured with plasma treatment to the bacterial attachment.

7.1.1 Materials and methods

Bacteria. A single colony of *Escherichia coli* K12 (see Figure 7.1) was cultured on an agar plate and then suspended in a 0.1M PBS solution in 50 ml in the tube. After several washings by centrifugation, they were resuspended in PBS at concentration of 9.8×10^8 cells per ml.

Materials. Polymer material PMMA and ePTFE are both common biomaterials and used in this study. PMMA is commercially available and the dimension is 10 mm x 10 mm x 2 mm. The specific gravity of PMMA is 1.2 g cm^{-1} and melting point is 170 ^oC. Two types of nanostructure (U grooved and V grooved, see Section 5.8) were applied to PMMA followed by plasma surface modification. Another material for experiment is ePTFE and its dimension is 10 mm x 10 mm x 1 mm (see Figure 7.2). The melting point of ePTFE is 380 ^oC and average pore size is 1 µm. ePTFE was modified by plasma treatment only.

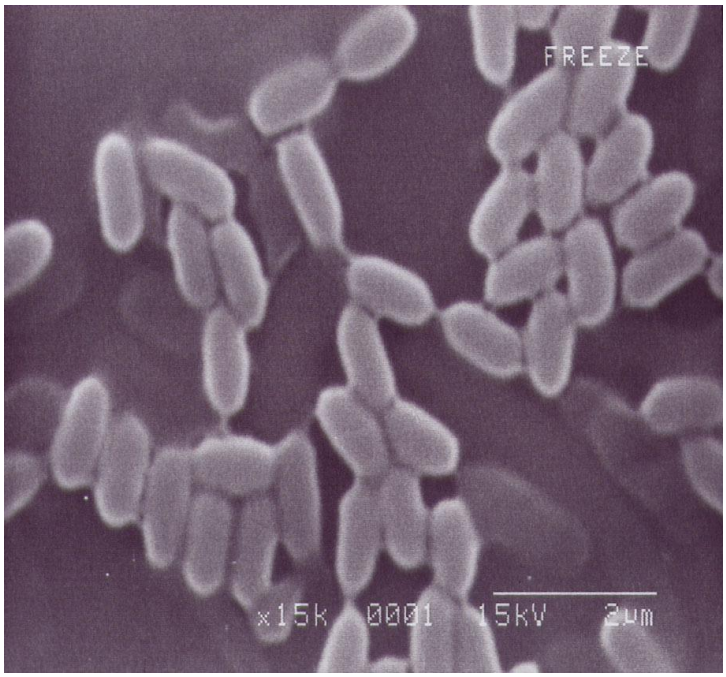

Figure 7.1 Scanning electronic microscopy image of *E.coli*.


Figure 7.2 Teflon material ePTFE, 10 mm x 10 mm x 1mm.

Groove embossing. The hot embossing method was used for the fabrication of nanogrooved surfaces as shown in Section 5.8. The optimized condition for making fine gratings on PMMA is a 400 kg load at 150 ^{o}C for 90 seconds. After applying the U-grooved and V-grooved gratings on PMMA, the sample was cleaned by ethanol and then modified by plasma modification treatment.

Plasma etching. Gas plasma surface treatment is an ideal technology for the surface modification of plastic, textile & film products while enabling hydrophilic and hydrophobic coatings. Our research concentrates on the plasma surface modification, the characteristics of modified surface (maybe by grafting, etching or sometimes deposition) depend on the process parameters such as plasma treatment time,

reaction gases, and ion energy (see Figure 7.3).

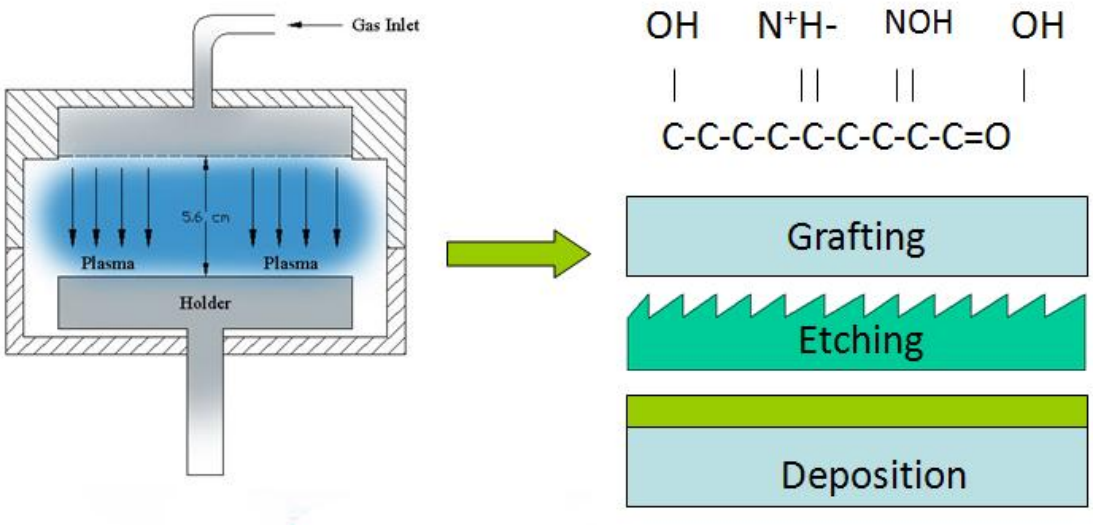

Figure 7.3 Schematic diagram of plasma surface modification on surface.

Both polymer materials were modified by plasma modification after cleaning with ethanol. Plasma treatment was carried out by a RF plasma etching system (Figure 7.4) with a maximum power of 600 W. The N_2 gas flow rate was in the range of 10 - 50 SCCM[7]. The working pressure was kept at 20 mTorr and plasma treatment duration was 1-20 min. After plasma modification, the substrates were put into a flask containing a suspension culture of *E.coli* at 37 ^{o}C for 24 hours.

The wettability of the modified PMMA and ePTFE substrates were evaluated by measuring the static contact angles with distilled water. The static contact angles were measured in air at room temperature using the sessile drop method and each drop was fixed at 50 µl. The contour of the droplet was projected onto a screen by visible light and the contact angles were measured on the images. Hitachi 4700 scanning electron microscope was used to characterise surface morphologies. Samples were coated with gold using a S150B Edwards Sputter Coater prior to their installation in the SEM. FTIR microscopy (Jasco FTIR-200) was employed to investigate the surface structure of ePTFE and PTFE plates after plasma treatment.

[7] Standard Cubic Centimeters per Minute.

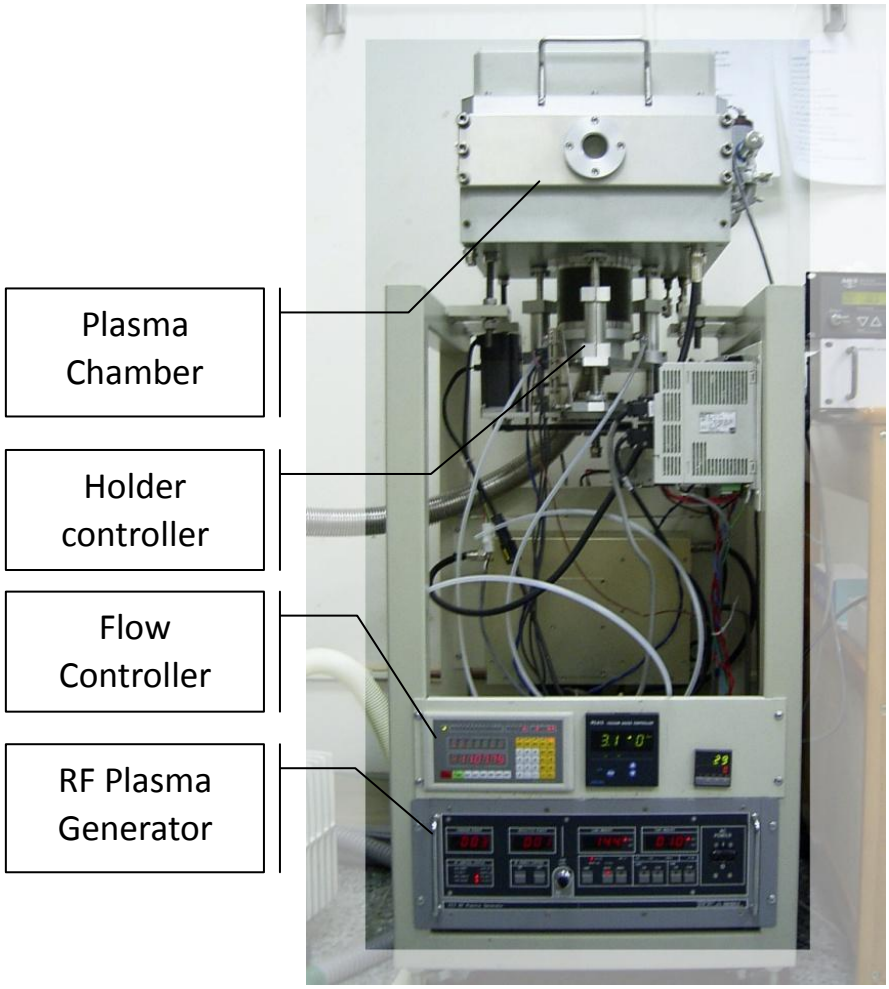

Figure 7.4 RF plasma etching system.

7.2 Results and discussion

The U-grooved and V-grooved structure on PMMA were prepared as described in Section 5.11 and after the grating structures were made, both were modified by plasma treatments. ePTFE only showed the results of plasma modifications because it is too soft to retain fine grooves on the surface. After plasma surface treatments, all samples were kept in agitated *E.coli* suspensions for 24 hours at 37 ^{o}C and rinsed with pure water afterwards. The results of FTIR were demonstrated for the comparison of functional group changes before and after plasma treatment.

PMMA. Figure 7.5 shows a SEM image of *E.coli* attached to an unmodified PMMA surface. It can be noticed that only a few bacteria sit on the surface due to its hydrophobicity (wetting angle is 53° before modification). Figure 7.6 shows the FTIR spectra of PMMA before plasma treatment.

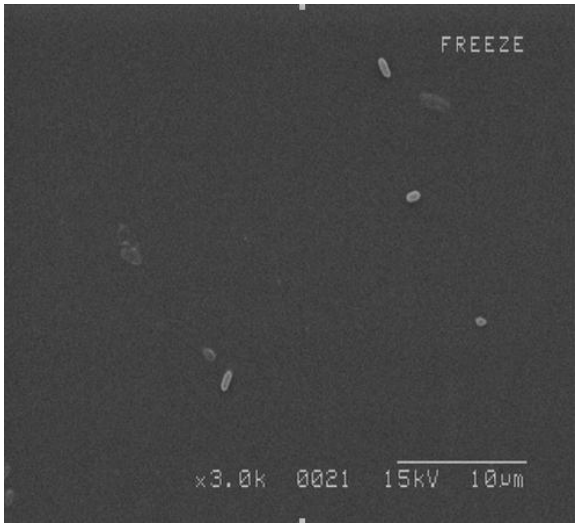

Figure 7.5 SEM image of bacterial attachment on unmodified PMMA (wetting angle is 53^{o}).

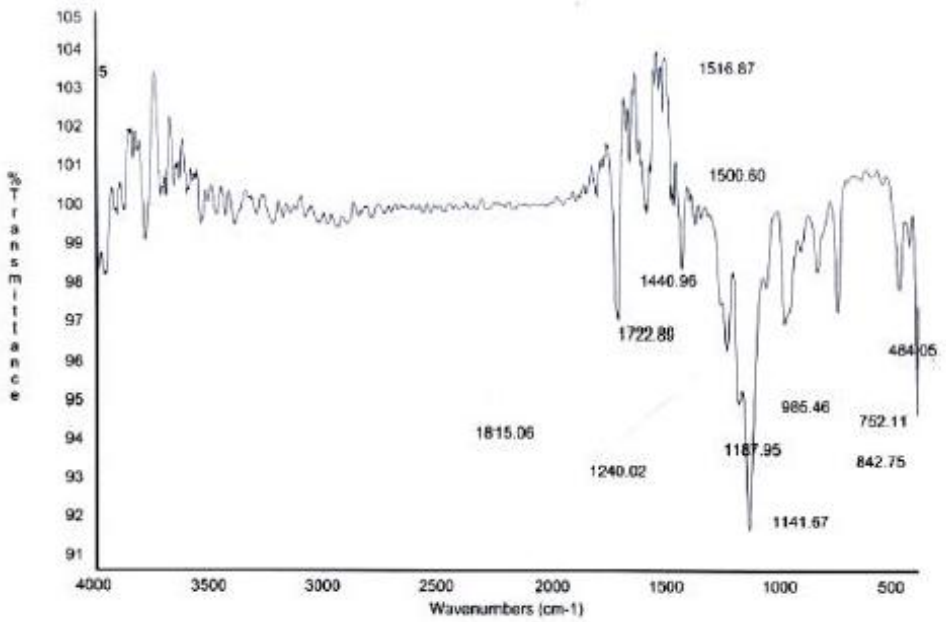

Figure 7.6 FTIR spectra of PMMA materials (without treatment).

***ePTFE*.** Figure 7.7 shows a SEM result of *E.coli* attachment on unmodified ePTFE surface. It also can be noticed that a few bacteria still sit on the surface, though it is well known as highly hydrophobic (wetting angle is 121° before modification), which should not impart high affinity to microbial adhesion. This may be because the porous structure facilitate bacterial residence. Figure 7.8 shows the FTIR spectra of ePTFE materials before treatment.

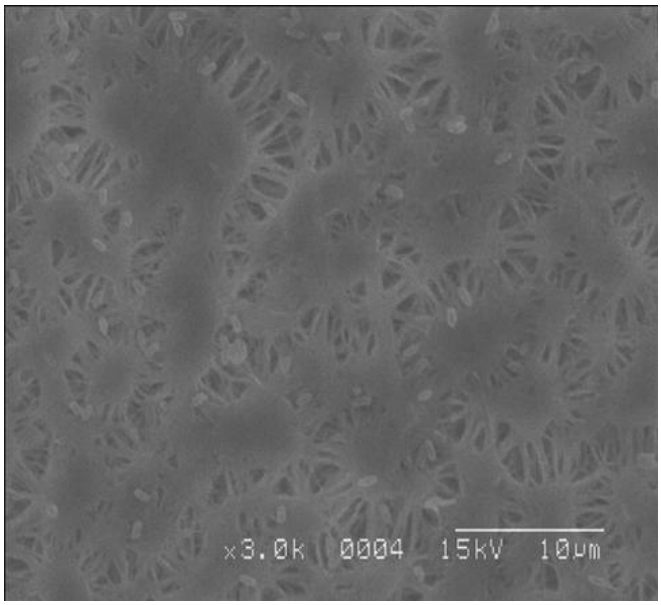

Figure 7.7 SEM image of bacterial attachment on unmodified ePTFE (wetting angle is 121^{o}).

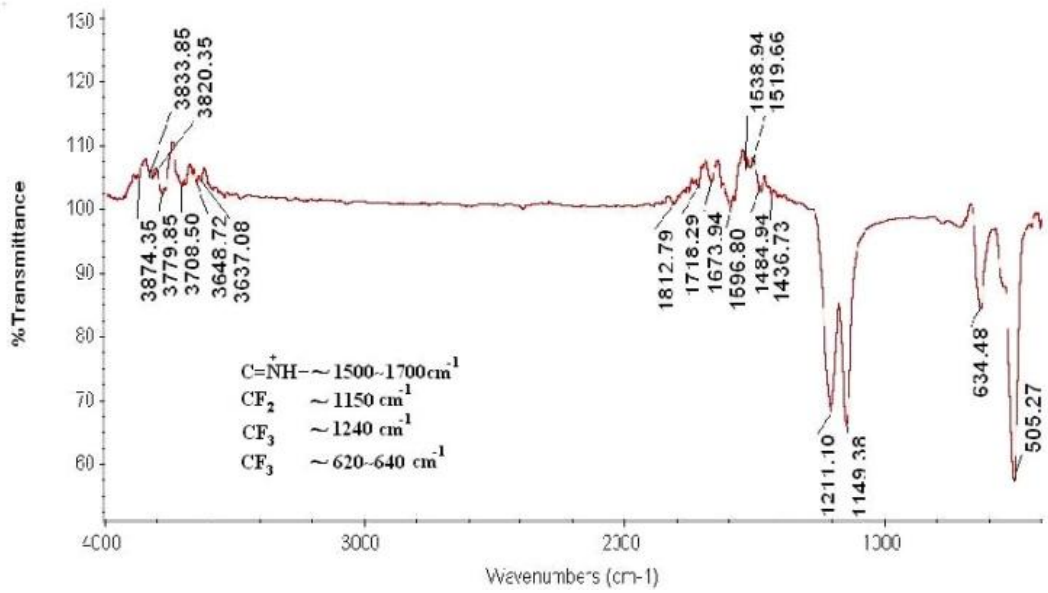

Figure 7.8 FTIR spectra of ePTFE materials (without treatment).

Figure 7.9 shows that the high aspect ratio U-grooved surface after N_2 plasma treatment has low affinity to *E.coli*. This seems to be due to the fact that the high aspect ratio grooves restrict the orientation of *E.coli*, hence do not allow the bacteria build up their society. However, Figure 7.10 shows the higher affinity of low aspect ratio (U-grooved) gratings to *E.coli*, this is not only because the lower aspect ratio gives more chance to allow the bacteria stay together and build up a society, which is essential to biofilm formation, but also plasma modification raises its hydrophilicity (wetting angle 10^{o}), which helps to increase affinity. Figure 7.11 shows that =NOH and $C=N^{+}H_{-}$ functional groups, which are the common hydrophilic functional groups, were discovered after N_2 plasma treatment.

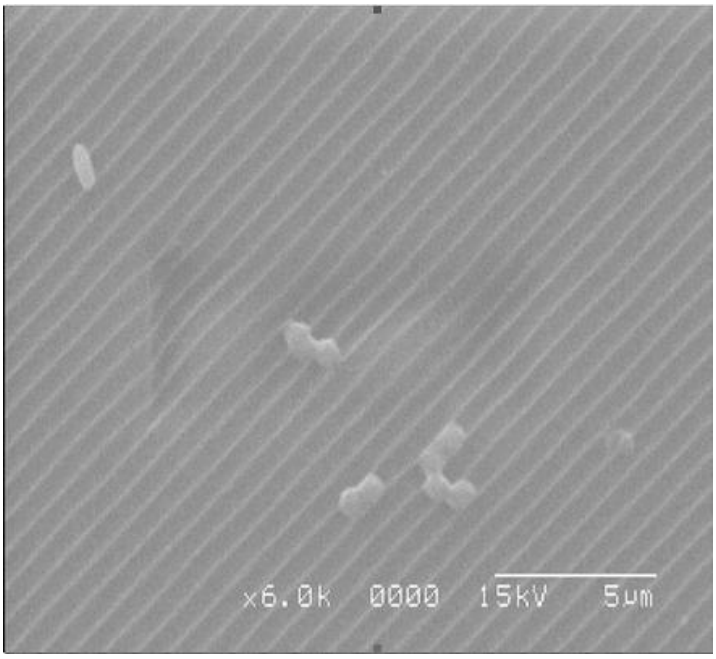

Figure 7.9 SEM image of bacterial attachment on N_2 plasma-modified PMMA material with higher aspect ratio U-grooves.

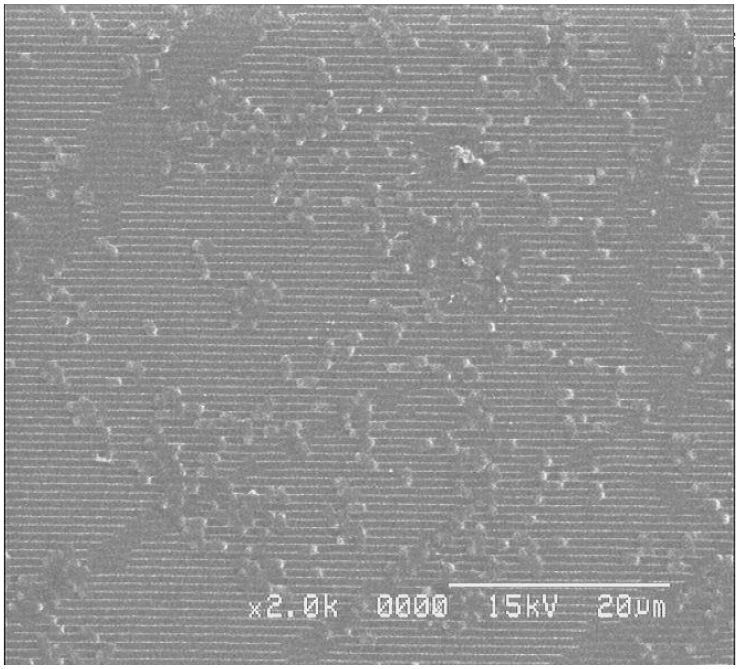

Figure 7.10 SEM image of *E.coil* attachments on N_2 plasma-modified PMMA material with lower aspect ratio U-grooves.

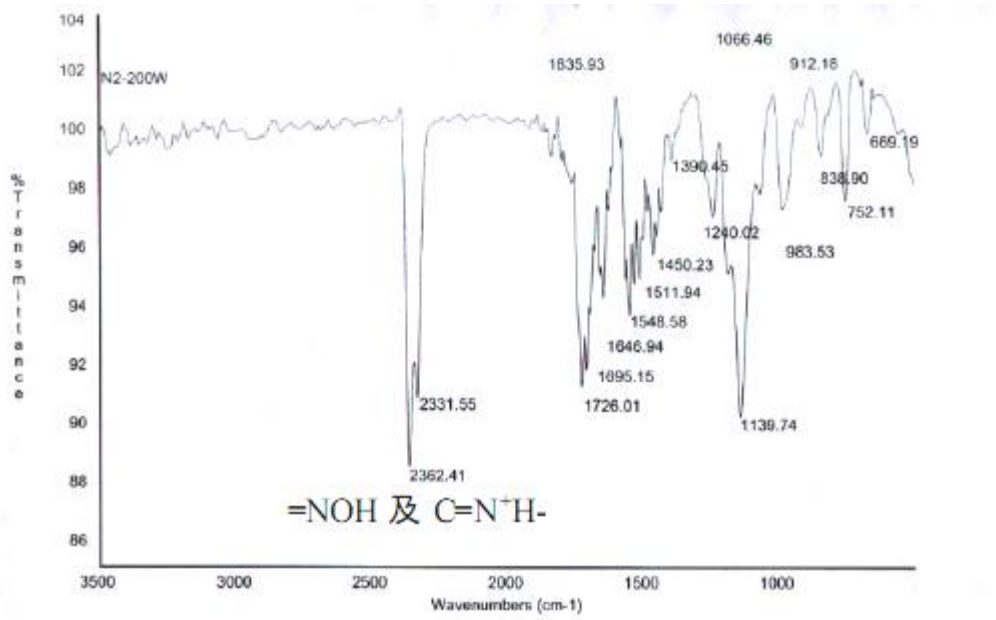

Figure 7.11 FTIR result of PMMA after 200 W N_2 plasma modification.

Furthermore, comparing the result of V-grooved PMMA in Figure 5.28 (Left, p. 63), N_2 plasma treatment increases the affinity of the surface to *E.coli*, shown in Figure 7.12, which should be due to the contribution of hydrophilic functional groups (see Figure 7.11).

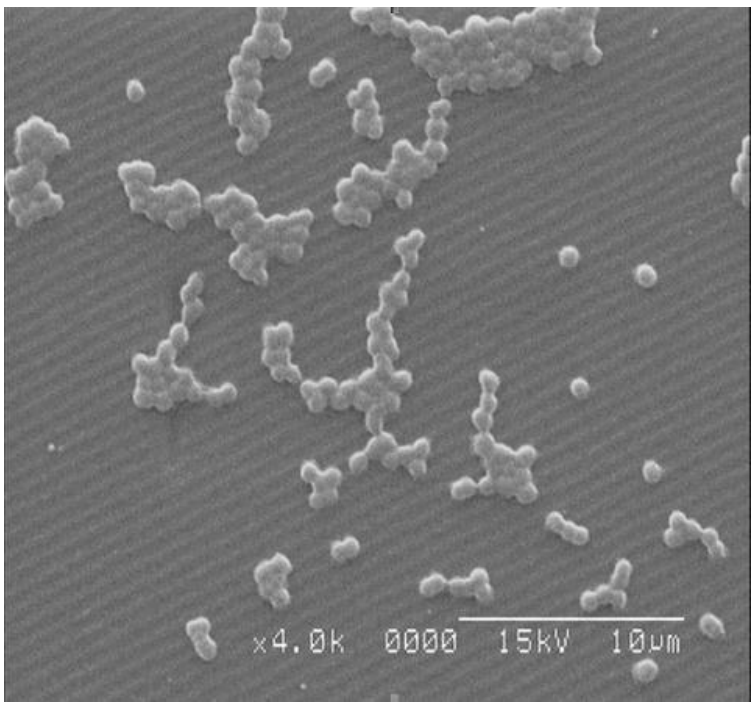

Figure 7.12 SEM image of bacterial attachment on N_2 plasma-modified PMMA material with V-grooves.

Figure 7.13 shows the result of bacterial attachment on N_2 plasma (500 W 20 sccm for 5 minutes)-modified ePTFE, nevertheless, the micrograph shows no *E.coli* attachment on the surface- presumably because the porous structure of ePTFE has been damaged by the plasma etching, which leads to a superhydrophobic surface (wetting angle is 151^{o}), and is unfavourable to *E.coli* adhesion (Lotus effect).

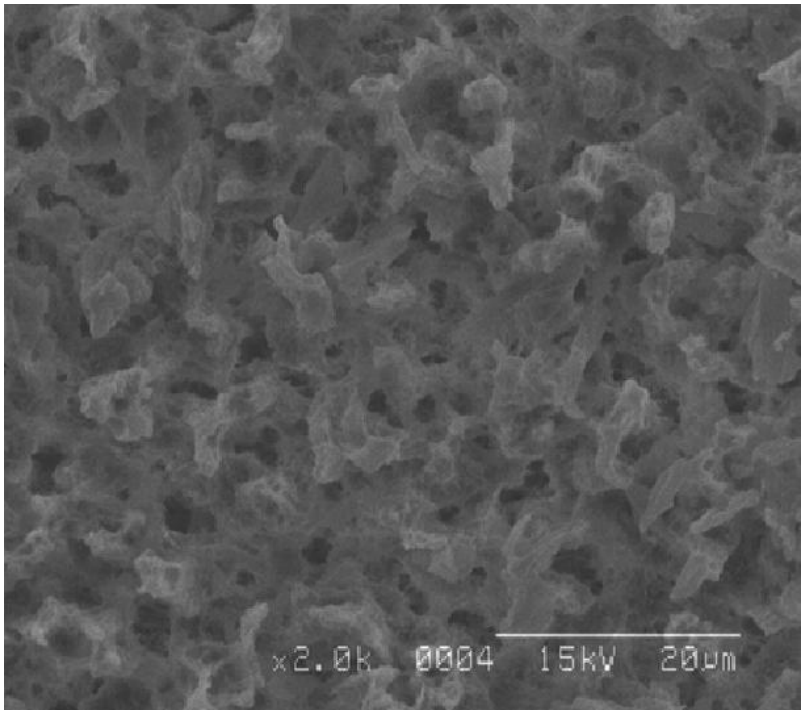

Figure 7.13 SEM of ePTFE after N_2 plasma treatment (500 W 20 sccm for 15 minutes).

7.3 Conclusion

The results indicated that a nanostructured surface dominates the adhesion behaviour of *E. coli* K-12 cells, rather than the surface chemical properties of materials. In the case of PMMA materials, the nanogrooved surface with a lower aspect ratio favors the attachment of *E. coli* K-12 cells on the surface. A thin layer of amino groups deposited on the nanogrooved surface of PMMA substrates can further improve the adhesion and growth of *E. coli* K-12 cells on the surface. However, *E. coli* K-12 cells were found to be aligned along the nanogrooved surface with a higher aspect ratio, which is not beneficial for the further aggregation and growth of *E. coli* K-12 cells due to the 1-D confinement effect. The ePTFE materials demonstrate superhydrophobic characteristics after N_2 plasma etching treatment due to the existence of needle-like structure on the surface, which obviously prevents the adhesion and growth of *E. coli* K-12 cells on ePTFE materials, even with hydrophilic functional groups on the surface.

The designed surfaces made by hot embossing into U and V grooves have been demonstrated here. The alignment of bacteria is demonstrated on SEM images. In addition, the needle-like nanostructures caused by plasma etching impart superhydrophobicity and may prevent the bacterial adhesion to the surface.

The ePTFE materials demonstrate superhydrophobic characteristics after N_2 plasma etching treatment due to the existence of needle-like structure on the surface, which obviously prevents the adhesion and growth of *E. coli* cells on ePTFE materials, even with hydrophilic functional groups on the surface.

In addition, the needle-like nanostructures caused by the plasma etching effect engender superhydrophobicity and may prevent bacterial adhesion.

Chapter 8 Interaction of bacteria with mucin layers

Epithelial surfaces, e.g. in the mouth, are lined with the giant glycoprotein mucin, which constitutes the first line of defence against bacteria. It is supposed to work by simply engulfing them. The self-assembly of mucin layers has been studied by others in the Ramsden group, and this provided a good opportunity to investigate molecularly microscopically (i.e., using OWLS) what happens when bacteria interact with a mucin layer. I prepared mucin coatings on a planar optical waveguide, and determined the kinetics of bacteria interacting with the coating and with mucin modified by the polyphenol EGCg, which has been recently found by another student in the group to profoundly affect the dynamical structure of the mucin layers.

8.1 Introduction

One of the most important functions of the ubiquitous proteoglycan mucin is the trapping and engulfment of bacteria invading the mucosae, such as the gastrointestinal tract. Mucin, abundantly secreted by goblet cells in a healthy organism, lines many of the internal surfaces of mammals etc., and is the first line of defence of the body against microbial invaders arriving at those surfaces (Slomiany *et al.*, 1996).

While this is well-known in traditional medico-physiological terms, details of the actual mechanism of trapping and involvement remain obscure. Indeed, it is only very recently that the structure and dynamics of the mucin layers themselves have been elucidated (McColl *et al.*, 2007; McColl *et al.*, 2008; Horváth *et al.*, 2008). Our purpose in this investigation is to give a more precise biophysico-chemical account of the process, revealing the underlying regularities. It is expected that this will be very useful in improving medical intervention in cases where the body is not able to eliminate the infection itself. It is also expected to help in designing artificial surfaces for trapping bacteria, with a variety of applications, including bacterial detection, in view.

The mucociliary system of the upper and lower respiratory tracts is a critical nonspecific pathway for the elimination of bacteria and other particulate matter (Bernstein and Reddy, 2000). The interaction between *Escherichia coli* and mucin has seen no previous studies, particularly on the kinetic interaction. Such information gained from these experiments would be of extreme importance in understanding the specific mechanisms of preventing colonization of bacteria to mucin.

8.2 Experimental details specific to this chapter

The experimental monitoring of bacterial adsorption/desorption to 0.1% mucin and to 0.1%mucin with 1% EGCg were carried out by OWLS.

8.2.1 Mucin

Pharmaceutical grade porcine gastric mucin was purchased from A/S Orthana Kemisk Fabrik, Kastrup, Denmark. The commercial preparation was extensively dialysed to remove all salts and other low molecular weight additives and finally lyophilized and stored for use as required. All solutions were freshly made up by dissolving weighed portions of the lyophilized material in Elga ultrapure (resistance 18.2 MΩ cm, filtered through 200 nm pores) water.

Mucins are cell surface and secreted glycoproteins characterized by high levels of O-linked glycosylation, often over 50% carbohydrate by weight, which is generally densely clustered in repeating units of 20 or so amino acid residues (termed tandem repeats) of protein sequence rich in serine, threonine and proline (Allen and Snary, 1972; Hanisch and Muller, 2000; Bansil and Turner, 2006).

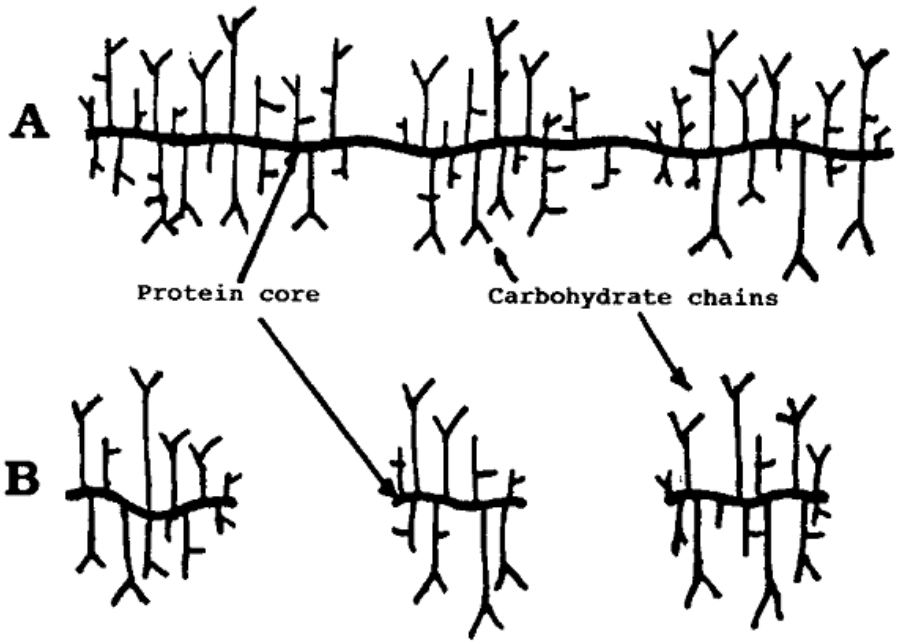

Structure 8.1 (A) high molecular weight (B) low molecular weight mucin (Slomiany *et al.*, 1996).

Table 8.1 Composition of mucin (Bromberg and Barr, 2000).

component	wt %	amino acid	(mol %)
total protein	22.8	aspartic acid	4.68
fucose	9.70	threonine	23.4
N-acetylglucosamine	16.9	serine	11.4
N-acetylgalactosamine	12.7	glutamic acid	5.75
galactose	22.6	proline	13.6
sialic acid	10.4	glycine	7.70
sulfate	4.90	alanine	9.93
		valine	4.98
		methionine	0.68
		isoleucine	1.93
		leucine	5.93
		tyrosine	0.78
		phenylalanine	1.52
		histidine	2.31
		lysine	2.23
		arginine	3.18

8.2.2 EGCg

Epigallocatechin-3-gallate (EGCg) (Structure 8.2) is one of the main catechins in green tea, which have been shown to be effective chemopreventive agents *in vitro* and in many *in vivo* animal models of induced carcinogenesis (Liao *et al.*, 1995; Liao *et al.*, 2001).

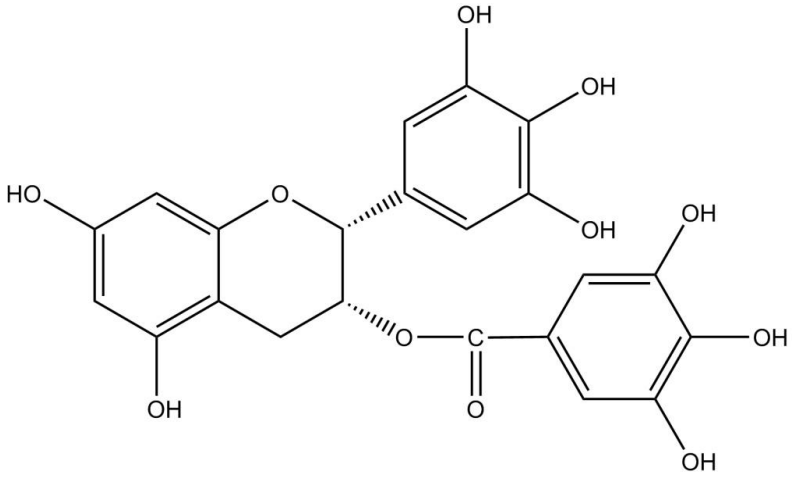

Structure 8.2 (-)Epigallocatechin-3-gallate (EGCg) (Yang and Wang, 1993). Note that the structure is copyed exactly as it appear in Yang and Wang, but the stereochemical indication seems to be incorrect.

8.2.3 Adsorption procedure

Deposition of mucin, and attachment of the bacteria to the mucin, was carried out on surfaces of the optical waveguides while measuring the zeroth order TE and TM modes using an IOS-1 integrated optical scanner (Artificial Sensing Instruments, Zürich) (see details in Sections 5.5 and 5.7).

The flow through the cuvette was controlled by a custom-built precision syringe pusher (Figure 8.1) (KFKI, Budapest, Hungary). The typical procedure was to ensure that the substrate was equilibrated with the covering medium (water for the mucin deposition phase), and then to flow the mucin solution through the cuvette until saturation monolayer coverage, known from previous work to be about 200 ng/cm^3.

The layer was then thoroughly rinsed in water to remove any weakly attached mucin and then the suspension of bacteria in water was flowed through the cuvette. After reaching or obviously approaching saturation of adsorption, flow reverted to pure water to remove adventitiously resident bacteria.

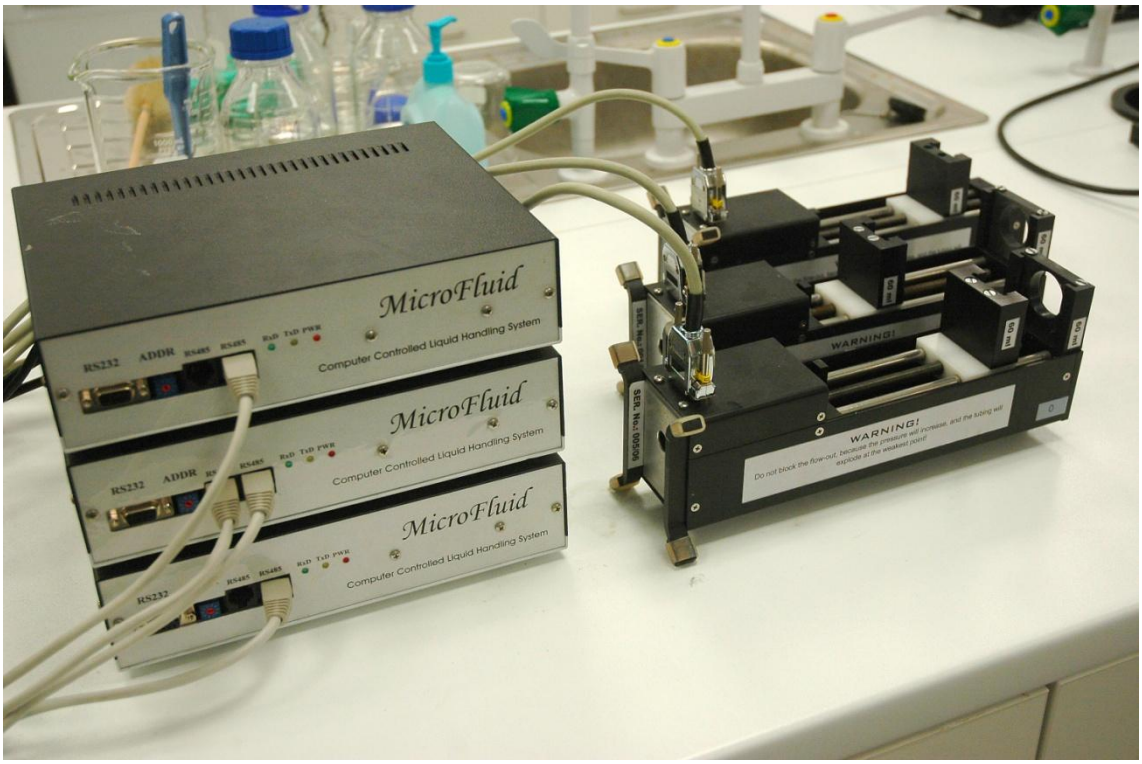

Figure 8.1 Custom-built precision syringe pusher: (left) controller; (right) syringe pusher.

8.3 Results

The results of adsorption of *E.coli* on a layer 1% mucin are shown in Figure 8.2.

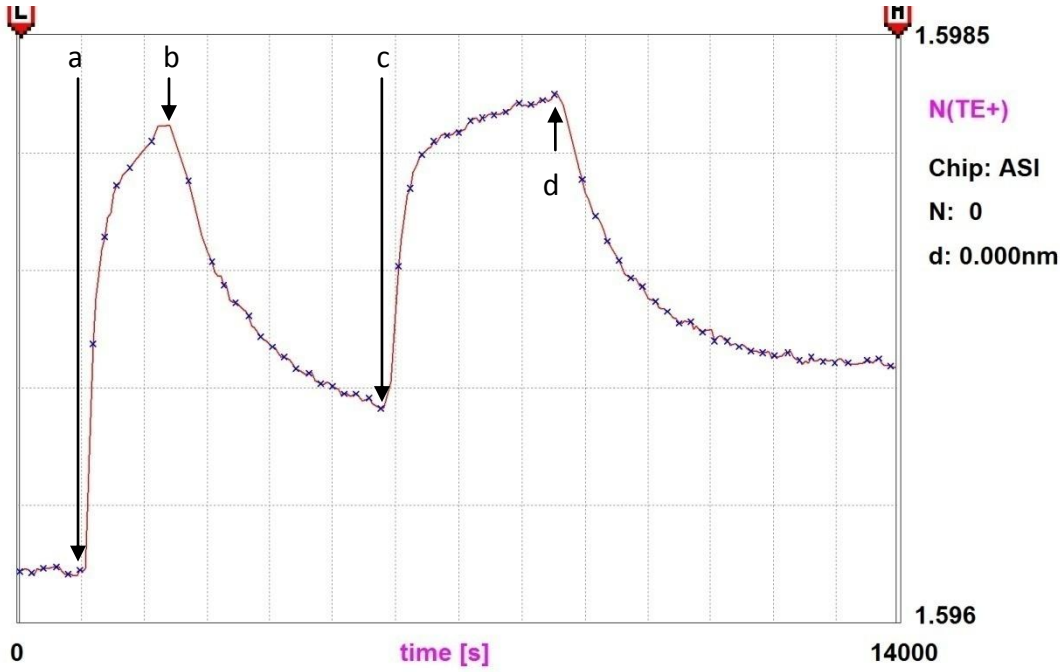

Figure 8.2 N-t diagram of 1%Mucin + *E. coli* in pure water. Marker a is at the start of 1% mucin adsorption on the waveguide; marker b is at the start of washing by water; marker c is at the *E.coli* adsorption start; marker d is the start of water washing again. [Experimental code: 201106].

The results of adsorption *E.coli* on 1% mucin/0.1% EGCg is shown in Figure 8.3.

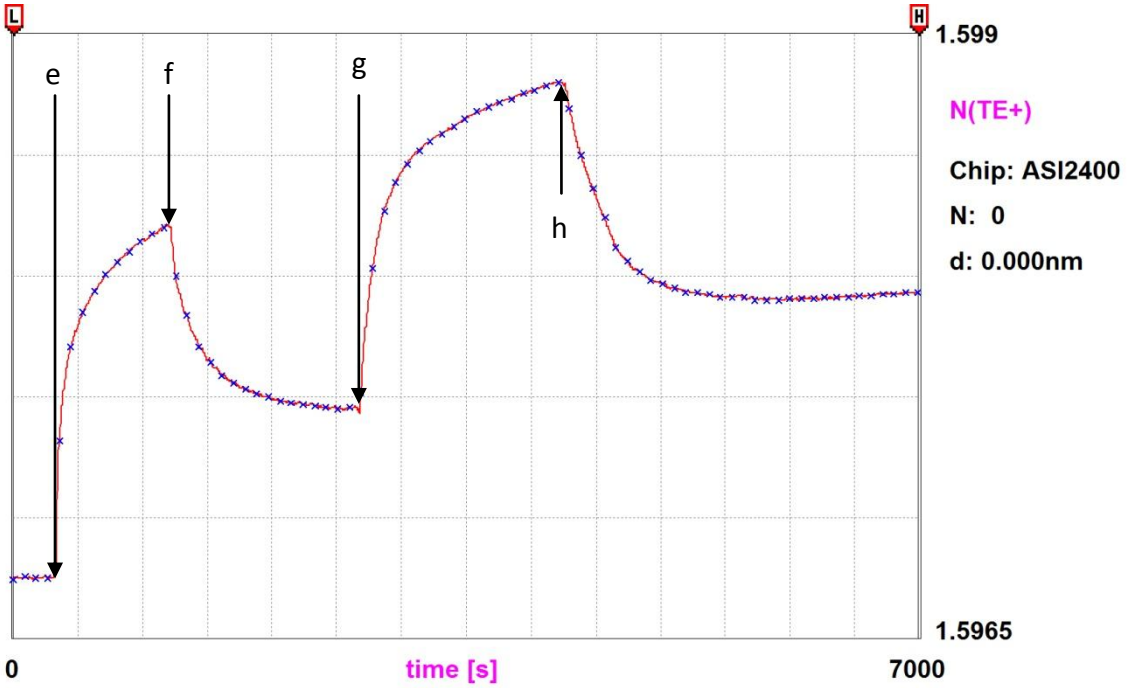

Figure 8.3 N-t diagram of 1%Mucin+0.1%EGCg+*Escherichia coli*. Marker e is at the start of 1% mucin/0.1% EGCg adsorption on the waveguide; marker f is at the start of washing by water; marker g is at the *E.coli* adsorption start; marker h is the start of water washing again. [Experimental code: 060207-1].

8.3.1 Qualitative survey

- Initial adsorption of bacteria is RSA, but prior admixture of EGCg makes a noticeable change.

- Adsorption is more reversible on mucin compared with uncoated oxides (e.g., zirconia, see Figure 6.1), but an appreciable residual deposit remains, $b_w/b_{sat} \approx 20\%$.

- Admixture of EGCg to the mucin makes the adsorption less reversible, $b_w/b_{sat} \approx 35\%$.

8.4 Discussion

Table 8.2 Surface tension parameters (in mJ/m^2) for mucin[(a)].

material	$\gamma^{(LW)}$	$\gamma^{\oplus}$	$\gamma^{\ominus}$
Mucin	27	0	60

(a) Estimated from similarly glycosylated molecules, see (van Oss, 2006).

Estimated interfacial energies are given in Table 8.3.

Table 8.3 Predicted interfacial energy $\Delta G_{123}^{||}$(mJ/m^2) of mucin and *E.coli*.

$\Delta G_{123}^{||}$	mucin	*E.coli*
SiO_2	34.5	15.4
mucin	–	29.6

Clearly mucin easily manages to overcome the large predicted repulsive barrier to silica. Perhaps this is not too surprising in view of its great conformational lability. This may also explain the attraction of E.coli to mucin, despite an even bigger repulsive barrier. The effect of EGCg on bacterial adsorption seems to be rather minor. That the desorption of E.coli from mucin with EGCg is less than from a pure mucin layer might be because of some chemical bonding to the bacterial surface. Note that EGCg has a strong antibacterial effect through causing damage to the lipid bilayer of the bacterial membrane (Ikigai *et al.*, 1993; Spina *et al.*, 2008). At present, we lack the specific chemical knowledge of the bacterial surface that would allow us to understand these results better.

Chapter 9 Complex Organometallic Compounds

The mucin/EGCg work shows the limitations of using natural nanotextured substrata. It is difficult to control the characteristics of the deposited film. In order to create nanosurfaces with better defined features, I explored the self-assembly of complex organometallic molecules (''nanoblocks'').

Large organometallic complexes are known from previous work to self-assemble into structured layers (Constable *et al.*, 1997). This provides a very convenient way of creating self-assembly nanotextured surface, with potentially, an almost limitless variety of chemistry and morphology. A visiting chemist, Dr Kaleem Khosa from the University of Faisalabad, provided novel organometallic molecules. We only investigated their self-assembly behaviour (adsorption/desorption kinetics) in this thesis. These compounds are not soluble in pure water, but in a suitable organic solvent such as dimethylsulfoxide (DMSO). Mixtures of DMSO and water can be used to achieve the deposition of stable layers. The ternary system organometallic complex/DMSO/water turned out to have a complex behaviour, which I was able to partly characterize and analyze.

The structure of this chapter is as follows:

9.1 Basic data for DMSO
9.2 Basic data for organometallic compounds
9.3 Experimental refractometry results for DMSO-water mixtures
9.4 Experimental refractometry results for DMSO-organometallic compounds mixtures and interpretation
9.5 Experimental results for organometallic compounds, self-assembly
9.6 Interpretation

9.1 Basic data for DMSO

Dimethyl sulfoxide (DMSO; Sigma Aldrich, U.K.), $(CH_3O)_2SO_2$, one of the strongest organic solvents, has been used as a solvent for water-insoluble substances applied to biological material, or as a radio- or cryoprotective agent for many years. It is also an effective solvent for a wide array of organic materials, including many polymers. DMSO also dissolves many inorganic salts, particularly transition metals nitrates, cyanides and dichromates. DMSO is miscible with water and most organic liquids. The structure of dimethyl sulfoxide (DMSO) is pyramidal with sulphur, oxygen and carbon atoms at the corners (Macgregor, 1967), as shown in Structure 9.1.

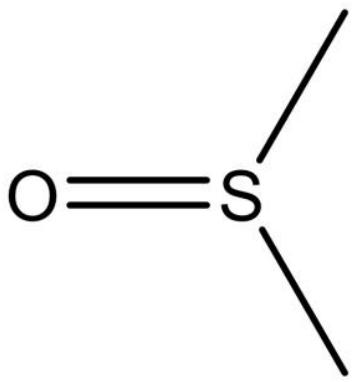

Structure 9.1 The structure of DMSO.

DMSO has special properties within the series of dipolar aprotic solvents. The methylsulfinyl carbanion is formed in reactions with bases. The dipolar aprotic solvent dimethyl sulfoxide is liquid over a wide range of temperatures, is a strong electron donor, and has a high polarity. It is therefore an excellent and selective solvent for many organic and even polymeric compounds, and can enter into Hydrogen-bonding and dipole-dipole association. The structure of dimethyl sulfoxide, with a oxygen atom and a sulfur atom, leads to good solvation of cations and poor solvation of anions. (Martin *et al.*, 1967; Constable *et al.*, 1997).

Dimethyl sulphoxide (DMSO) is an unusual solvent owing to its physicochemical properties. It has some properties similar to those of water with which it is fully

miscible, but it is a dipolar aprotic solvent which has a tendency to accept rather than to donate protons (Rammler and Zaffaroni, 1967). The hydrogen bonds which exist between DMSO and water are stronger than those existing between water molecules (Cowie and Toporowski, 1961).

Table 9.1 gives the surface tension parameter of DMSO from literature.

Table 9.1 Surface tension parameters (in mJ/m^2) for DMSO.

Substance	T/^oC	γ^{total}	$\gamma^{(LW)}$	γ^{AB}	$\gamma^{\oplus}$	$\gamma^{\ominus}$	Note
DMSO	20	44	36	8	0.5	39	[a]
DMSO	0	45.1	36.9	8.21	0.51	33.0	[b]

[a] (van Oss *et al.*, 1989)

[b] By extrapolations to 0^o and assuming that the ratios $\gamma^{(LW)}/\gamma^{AB}$ and $\gamma^{\oplus}/\gamma^{\ominus}$ valid at 20 ^oC remain unchanged (van Oss, 2006).

9.2 The Kaleem Khosa organometallic compounds

These organometallic compounds are Pd(II) complexes with organophosphines and dithiocarbamate derivatives of α-amino acids. The complexes of organophosphines and dithiocarbamates compounds are of great interest to the pharmacutical industry and analytical and organic chemistry due to their biological and catalytic properties (Bond and Martin, 1984; Alverdi *et al.*, 2004). In recently years, antitumor properties of dithiocarbamate and dithioester complexes of Pd(II) have been found in (Mital *et al.*, 1989) and (Faraglia *et al.*, 2001), and antibacterial effects (Shaheen *et al.*, 2007a). This provides a cue for characterizing and analyzing the self-assembly behaviour of these complex compounds, and investigate the kinetics of bacterial adsorption on them.

(1) FAR-1

One of the organometallic compounds in this work is **chloro-[(piperidine-1-dithiocarbamato) (triphenylphosphine)] - palladium(II)** (FAR-1) (Structure 9.2). It has been crystallized and XRD carried out (see Table 9.3).

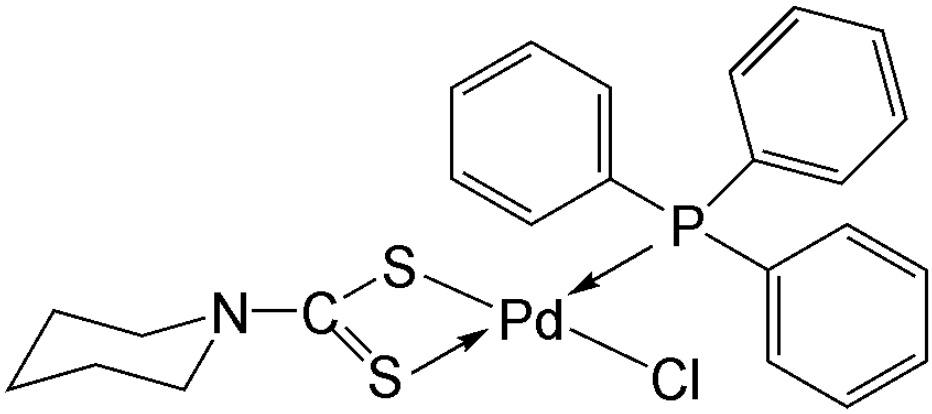

Structure 9.2 The structure of FAR-1 ($C_{24}H_{25}ClNPPdS_2$). Also see table 9.3 for details.

Table 9.2 Selected bond distances [Å] and bond angles [°] for compound FAR-1.

Bond Lengths		**Bond angles**	
C(1)-S(1)	1.735(6)	N(1)-C(1)-S(1)	124.3(4)
N(1)-C(1)	1.308(7)	N(1)-C(1)-S(2)	126.0(4)
C(1)-S(2)	1.715(6)	S(1)-C(1)-S(2)	109.8(3)
S(1)-Pd(1)	2.2874(14)	C(1)-S(1)-Pd(1)	88.43(19)
S(2)-Pd(1)	2.3506(14)	C(1)-S(2)-Pd(1)	86.86(19)
Pd(1)-S(1)#1	2.299(3)	P(1)-Pd(1)-S(2)	173.19(5)

Table 9.3 Crystal data and structure refinement for Compound-FAR-1[(a)].

Empirical formula	$C_{24}H_{25}ClNPPdS_2$
Formula weight	564.41
Temperature	571(2) K
Wavelength	0.71073 Å
Crystal system	orthorhombic
Space group	Pbcn (#60)
Unit cell dimensions	a = 13.7318(9) Å, α= 90°
	b = 20.7666(13) Å, β= 90°
	c = 18.4274(13) Å, γ = 90°
Volume	5254.8(6) $Å^3$
Density (calculated)	1.508 Mg/m^3
F(000)	2416
Crystal size	0.14 x 0.07 x 0.09 mm^3
Theta range for data collection	4.08 to 20.81°
Index ranges	-13<=h<=13,-20<=k<=20, -18<=l<=18
Reflections collected	19903
Independent reflections	2730 [R(int) = 0.0216]
Completeness to θ = 20.81°	99.2 %
Refinement method	Full-matrix least-squares on F^2
Data / restraints / parameters	2730 / 0 / 289
Goodness-of-fit on F^2	1.116
Final R indices [I>2σ (I)]	R_1 = 0.0317, wR_2 = 0.0887
R indices (all data)	R_1 = 0.0432, wR_2 = 0.1010
Largest diff. peak and hole	0.810 and -0.291 e $Å^{-3}$

(a) Data from Dr K. Khosa.

(2) FAR-A

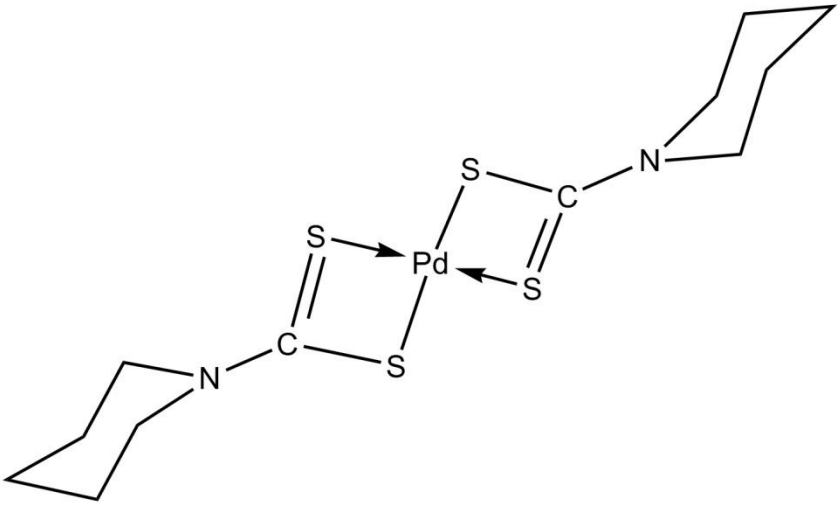

Structure 9.3 The structure of FAR-A(**$C_{12}H_{20}N_2S_4Pd$**), the molecular weight is 426.943.

(3) FAR-6

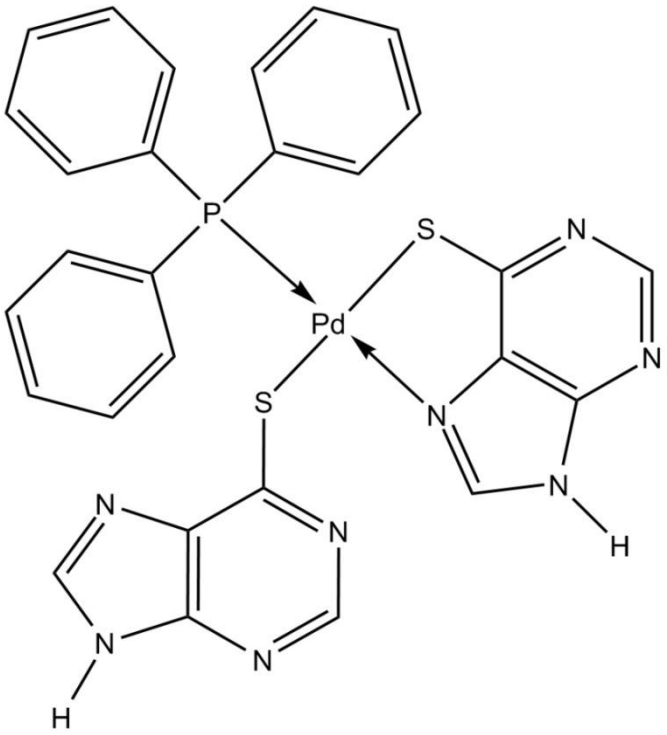

Structure 9.4 The structure of FAR-6 (**$C_{28}H_{21}N_8PS_2Pd$**), the molecular weight is 671.213.

(4) FAR-18

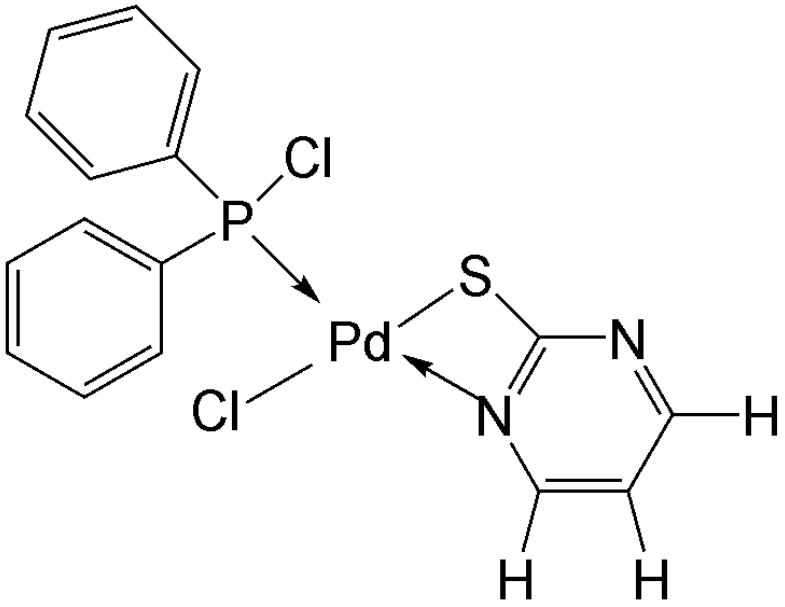

Structure 9.5 The structure of FAR-18 (**$C_{16}H_{13}N_2SPPdCl_2$**), the molecular weight is 473.632.

(5) FAR-41

FAR-41(**$C_{31}H_{37}NS_2PPdCl$**) was provided by Dr Kaleem and recrystallized from a mixture of dichloromethane and n-hexane.

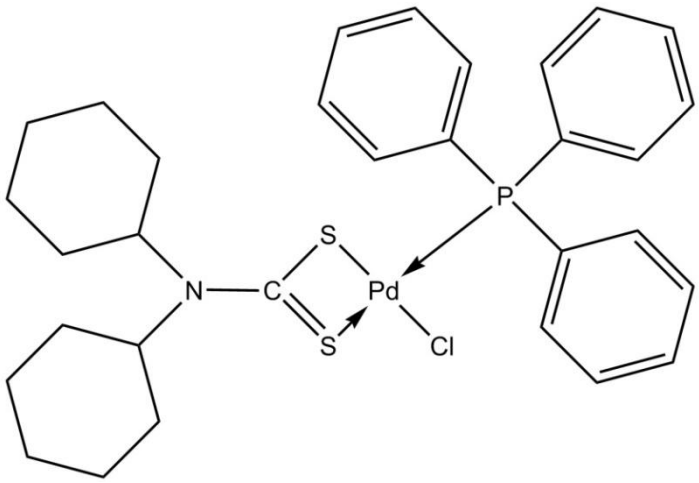

Structure 9.6 The Structure of FAR-41 (**$C_{31}H_{37}NS_2PPdCl$**), the molecular weight is

660.587. See Table 9.4

Table 9.4 Crystal data and structure refinement for compound FAR-41 (Shaheen *et al.*, 2007b).

Empirical formula	$C_{31}H_{37}NS_2PPdCl$
Formula weight	660.56
Temperature	293(2) K
Wavelength	0.71073 Å
Crystal system	Trigonal
Space group	$P3_1$
Unit cell dimensions	a = 16.262(1) Å,
	c = 10.198(1) Å,
Volume	2335.5(4) $Å^3$
Density (calculated)	1.409 Mg/m^3
F(000)	1020
Crystal size	0.1 x 0.1 x 0.1 mm^3
Theta range for data collection	4.25 to 26.37°
Index ranges	-20<=h<=20, -20<=k<=20, -12<=l<=12
Reflections collected	17684
Independent reflections	6340 [R(int) = 0.0590]
Completeness to θ = 25.31°	99.7 %
Adsorption correction	Analytical
Refinement method	Full-matrix least-squares on F^2
Data / restraints / parameters	6340 / 1 / 334
Goodness-of-fit on F^2	1.007
Final R indices [I>2σ (I)]	R_1 = 0.0400, wR_2 = 0.0708
R indices (all data)	R_1 = 0.0647, wR2 = 0.0774
Largest diff. peak and hole	0.470 and -0.270 e $Å^{-3}$

(6) FAR-42

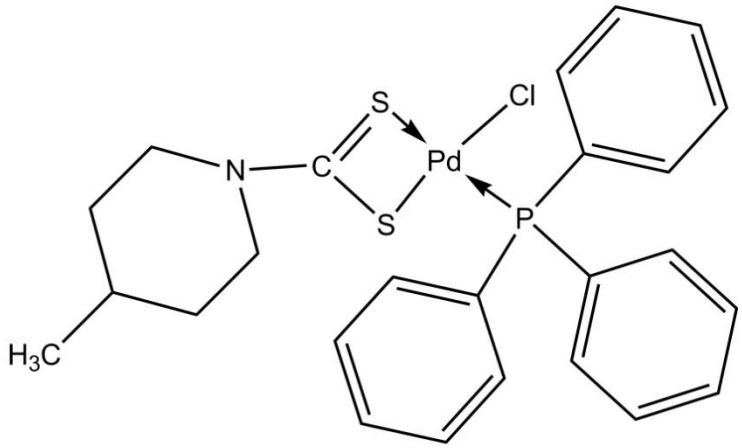

Structure 9.7 The structure of FAR-42 (**$C_{25}H_{27}NPS_2PdCl$**), the molecular weight is 578.444.

9.3 Experimental refractometry for DMSO-water mixtures

The refractive index of a few drops of each solution was measured using a Rudolph J357 refractometer (see Figure 9.1). As the refractive index of DMSO depends on the temperature and the water content, we have measured the refractive index of DMSO at different temperatures and water contents. Table 9.5 shows how the refractive index of DMSO decreases with the increase of temperature, due to its expansion (density decrease).

Figure 9.1 Rudolph J357 refractometer.

Table 9.5 Refractive index of DMSO (99.7%) at different temperatures.[(a)]

T/^{o}C	A	B	C	D
20	1.47619	1.47636	1.47583	1.47556
23	1.47362	1.47342	1.47326	1.47311
25	1.47113	1.47091	1.47080	1.47070
28	1.46879	1.46858	1.46851	1.46833
30	1.46730	1.46692	1.46670	1.46656

(a) Measurements A, B, C and D are repeats. Uncertainty is ± 0.0001.

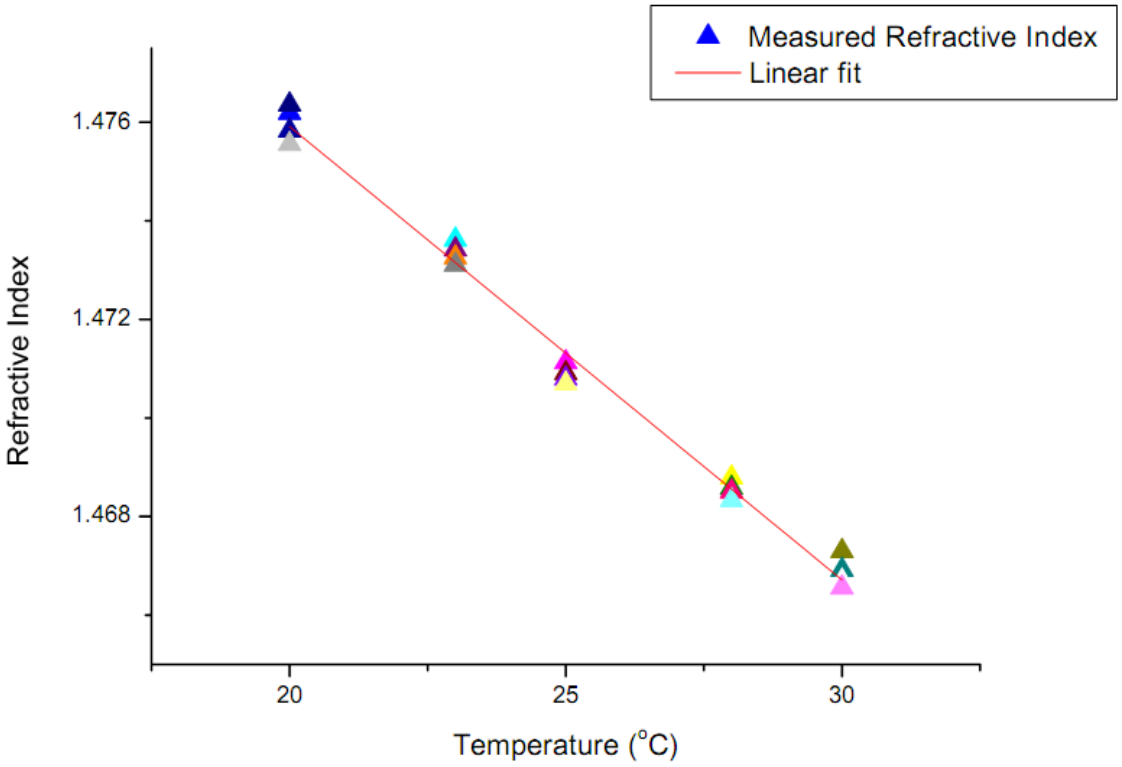

Figure 9.2 Refractive index of 99.7% DMSO (Table 9.1) plotted against temperature. The results somehow follow the linear equation $n = -9.2 \times 10^{-4} T + 1.4943$, where the error for slope and intercept are 2×10^{-5} and 5.4×10^{-4}.

Interestingly, the refractive index of DMSO-water mixtures is not linear with volume fraction, hinting at some nonideality, not surprising given the strong H-bonding between water and DMSO (see Section 9.1). The mixtures were made by separately preparing volumes of the constituents at room temperature (20 ^{o}C); e.g., for 20% water-DMSO, I prepared 20 mL water and 80 mL DMSO; and mixing them together. The mixture was then heated to 25 ^{o}C or 30 ^{o}C in refractormeter.

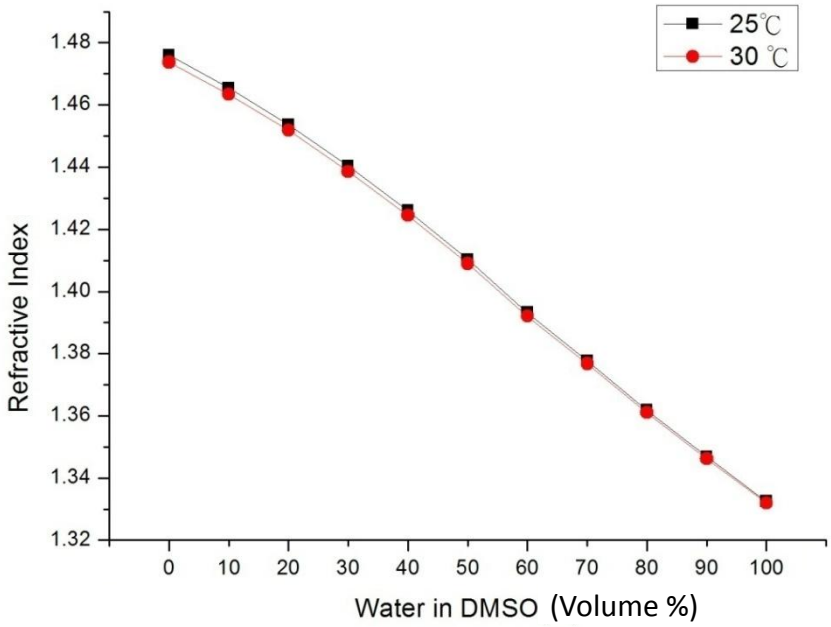

Figure 9.3 The effect of water on the refractive index of DMSO.

Hence, from measuring the refractive index at a given temperature, we can estimate the water content using Figure 9.3.

9.4 Experimental refractometry results for DMSO-organometallic compounds mixtures and Interpretation

The refractive index increments of organometallic compounds in DMSO at 28 ^{o}C were summarized in Table 9.6. Note that all the organometallic compounds are less polarizable than DMSO at this temperature. However this situation changes at 25 ^{o}C (see Table 9.7).

Table 9.6 Refractive Index of organometallic compounds and dn/dc at 200 µM (28.0 ^{o}C).

Compound	Refractive Index	dn/dc /cm^{3} mmol^{-1}
DMSO	1.47484	–
FAR-A	1.47473	-0.55
FAR-1	1.47452	-1.6
FAR-18	1.47481	-0.15
FAR-42	1.47477	-0.5
FAR-41	1.47480	-0.2
FAR-6	1.47462	-1.1

Table 9.7 The refractive index of different concentrations (2, 20 and 200μM) of FAR-A in DMSO.

	25 °C		30 °C	
	Measured	Means	Measured	Means
DMSO(99.9%)	1.47609 1.47590 1.47578 1.47565	1.47586	1.47398 1.47398 1.47388 1.47380	1.47391
FAR-A 200μM	1.47596 1.47596 1.47585 1.47572	1.47587	1.47384 1.47373 1.47369 1.47361	1.47372
FAR-A 20μM	1.47605 1.47601 1.47588 1.47573	1.47592	1.47384 1.47369 1.47357 1.47343	1.47363
FAR-A 2μM	1.47595 1.47577 1.47560 1.47545	1.47562	1.47386 1.47374 1.47367 1.47360	1.47368

For comparison, I attempted to calculate the refractive index of organometallic compounds from the molar refraction (R_M) using known tabulated atomic refractions (R_A), using:

$$R_M = \sum R_A \tag{9.1}$$

The refractive index can then be calculated from the Lorentz-Lorenz equation:

$$R_M = \frac{4\pi}{3} N_A H = \frac{n^2-1}{n^2+2} \frac{M}{\rho} \tag{9.2}$$

where M is the molar mass and ρ is the density, hence M/ρ is the molar volume V, n is

the refractive index, N_A is Avogadro's number and H is the polarization coefficient. Parameters M and ρ are from the X-ray crystallography data. (for example, for FAR-1 in Table 9.3).

As a check of molar volume, I used [Chembio] software (Figure 9.4) to estimate the molecular volume v as 2.24 nm^3. This is different from the value (5.23 nm^3) calculated from the unit cell (Table 9.3). However the molar volume M/ρ=564.41/1.508= 374 cm^3 (using calculated density 1.508 g/cm^3 in Table 9.3) whence v = V/N_A = 0.62 nm^3. So there is some uncertainty here.

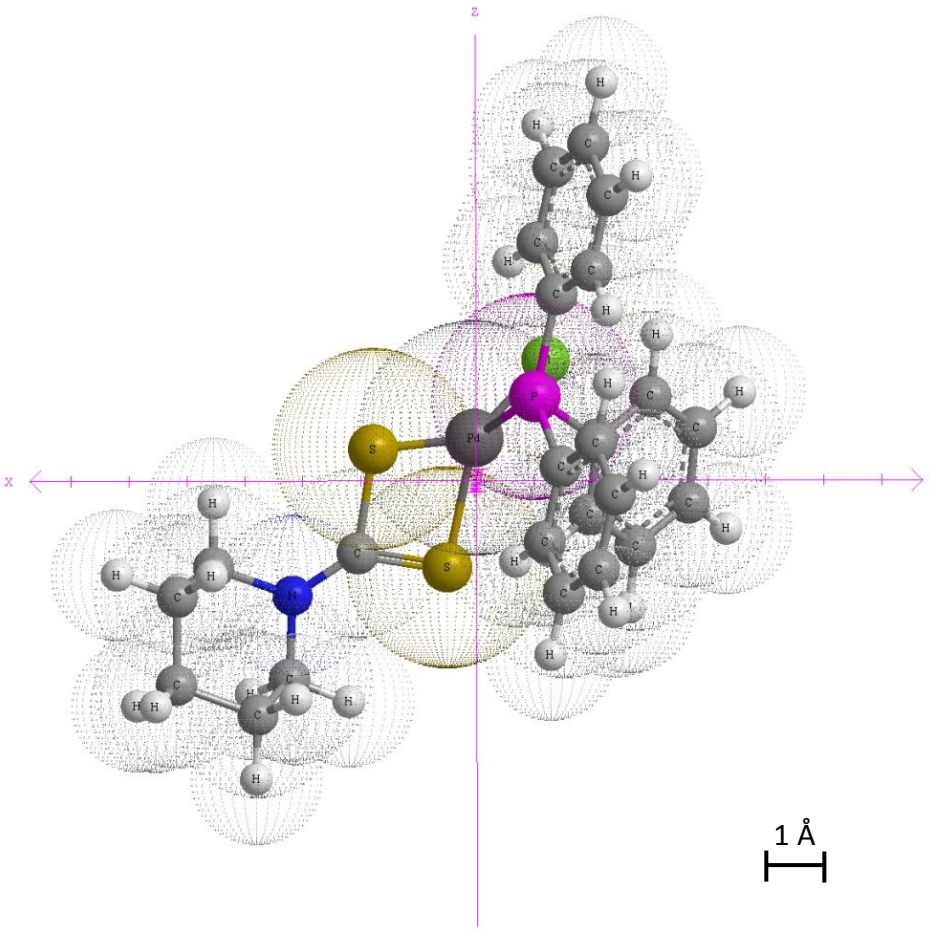

Figure 9.4 Representation of the molecule FAR-1 using [Chembio] software.

Example:

FAR-1 (see Structure 9.2):

From literatures in (Gladstone, 1896; Swientoslawski, 1920; Hammond and Lundberg, 1954; Sayre, 1964), we could summarize the bond refractions in Table 9.8.

Table 9.8 Refractions of bonds.

Bonds	Refraction
S	7.02
Pd	11.80
P	9.57
C-H	1.705
C-C	1.209
C=C	4.15
C-N	1.55
C-S	4.12
C=S	8.2
C-P	2.99
Pd-S	6.46
Pd-P	5.34
Pd-Cl	8.91

where,

$R_{C\text{-}S} = \frac{1}{4}R_C + \frac{1}{2}R_S$

$R_{C=S} = \frac{1}{2}R_C + R_S$

$R_{Pd\text{-}S} = \frac{1}{4}R_{Pd} + \frac{1}{2}R_S$

$R_{Pd\text{-}P} = \frac{1}{4}R_{Pd} + \frac{1}{4}R_P$

$R_{Pd\text{-}Cl} = \frac{1}{4}R_{Pd} + R_{Cl}$

$R_{C\text{-}S} = \frac{1}{4}R_C + \frac{1}{2}R_S$

From Equation (9.1), the total bond refractions of FAR-1 is

R_M = 10 $R_{C\text{-}H}$ + 4 $R_{C\text{-}C}$ + 3 $R_{C\text{-}N}$ + $R_{C\text{-}S}$ + $R_{C=S}$ + 2 $R_{Pd\text{-}S}$ + $R_{Pd\text{-}P}$ + $R_{Pd\text{-}Cl}$ + 3 (6 $R_{C\text{-}H}$ + 3 $R_{C\text{-}C}$ + 3 $R_{C=C}$) + 3 $R_{C\text{-}P}$ = 153.97 cm^3/mol.

Then from Equation (9.2) (using the three different estimates of v)

$$R_{FAR\text{-}1} = 153.97\ cm^3 = \frac{n^2-1}{n^2+2}\frac{565.4228\ g/mol}{2.24\ nm^3}$$

$$R_{FAR\text{-}1} = 153.97\ cm^3 = \frac{n^2-1}{n^2+2}\frac{565.4228\ g/mol}{5.23\ nm^3}$$

$$R_{FAR\text{-}1}=153.97\ cm^3=\frac{n^2-1}{n^2+2}\frac{565.4228\ g/mol}{0.62\ nm^3}$$

Hence, $n_{FAR\text{-}1}$ is 1.1815 (v=2.24 nm^3); 1.0746 (v=5.23 nm^3); 1.76595 (v=0.62 nm^3), of which only the last value is plausible. However, $n_{FAR\text{-}1}$ must be less than n_{DMSO} because dn/dc is < 0. Probably the true volume v is between 1 and 2 nm^3.

9.5 OWLS details

Self-assembly of organometallic compounds in DMSO on standard planar optical waveguides, was carried out using an IOS-1 integrated optical scanner (Artificial Sensing Instruments, Zürich) (see details in Sections 5.5 and 5.7). The typical procedure was to ensure that the substrate was equilibrated with the covering medium (DMSO for the organometallic compounds deposition), and then to flow the organometallic compounds solution through the cuvette until a steady state was reached.

The flow through the cuvette was controlled by a custom-built precision syringe pusher (see Figure 8.1) (KFKI, Budapest, Hungary) and the flow rate was 10 µl per second.

9.6 Experimental results for organometallic compounds' self-assembly

9.6.1 Explanation of methodology using the data from compound FAR-1

Figure 9.5 shows the raw data of N(TE) versus time. All the compounds investigated gave qualitatively similar results, characterized by the following striking features:

- an adlayer of organometallic compound builds up during exposure of the substratum

to the solution.

- the adlayers never seems to exceed one monolayer.

- the effective refractive index change during deposition is negative, as expected from the negative dn/dc values (Table 9.6).

- desorption is essentially complete, i.e. adsorption is wholly reversible. However, since the compound is insoluble in water, but DMSO and water are completely miscible, I expected that in DMSO-water mixture, an irreversible regime would be achievable at a certain fraction of water (see Section 9.8).

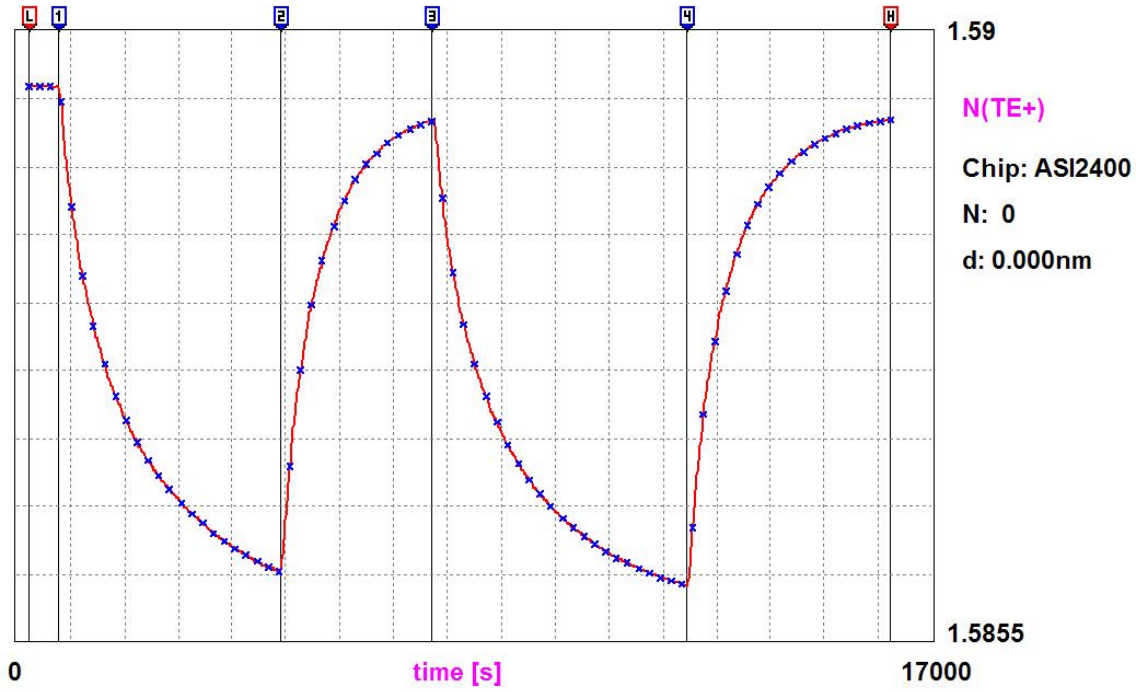

Figure 9.5 The N(TE) versus time raw data of FAR-1 at c_b = 0.2 mM in pure DMSO at T=30.9 ^{o}C. Marker 1 is at the start of FAR-1 adsorption on the waveguide; marker 2 is at the start of washing by DMSO; marker 3 is again the FAR-1 adsorption start; marker 4 is the start of buffer washing again. Note the good reproducibility of the repeated adsorptions and desorptions within this experiment. [Experimental code: NF1200B].

9.6.2 Calculation the number of adsorbed molecules

To calculate the kinetic parameters of an adsorption process, the number of molecules on the surface should be known. The mass of adsorbed particles per unit area (surface coverage) M is defined as

$$M=\int_0^{\infty}(c_s(z)-c_{bulk})\,dz \tag{9.3}$$

where c_s and c_{bulk} are the surface concentration and the bulk concentration of the bacteria respectively and z is the distance from the surface. Assuming that the molecular layer (adlayer) is compact and can be described by a mean concentration c_A and a mean thickness d_A and that $c_A >> c_{bulk}$, then Equation (9.3) reduces to

$$M=d_Ac_A \tag{9.4}$$

The refractive index n_A of the adsorbed layer is related linearly according to (Feijter *et al.*, 1978; Ball and Ramsden, 1997):

$$n_A=n_C+c_A\frac{dn}{dc} \tag{9.5}$$

where n_c is the refractive index of the covering buffer and dn/dc is the refractive index increment of the adsorbed molecule, which depends on its polariziblity. From Equation (9.4) and (9.5), by eliminating c_A, the mass (ng/cm^2) is determined from (Ball and Ramsden, 1997):

$$M=\frac{d_A(n_A-n_C)}{dn/dc} \tag{9.6}$$

where n_A and d_A are calculated as above, n_C and dn/dc are available from the literature or can be measured using a refractometer. From the above it can be seen that M can be calculated when the optogeometric parameters n_A and d_A of the adlayer are determined from N(TE) and N(TM) by solving Equation (4.6) and (4.7).

The standard four-layer mode equations reproduced in Appendix B, (Equations (B.1)-(B.8)) were used to determine n_A and d_A. The two four layer mode equations for

the zeroth TE and TM modes were solved simultaneously to yield thickness and refractive index of the adsorbed organometallic compound layer. However, since $n_A < n_C$, the thickness emerges artificially with a negative sign, which we ignore. These equations assume that the adlayer is isotropic. The thickness is plotted in Figure 9.6 and reaches a plateau of 2.2 nm, and the refractive index in Figure 9.7 which reaches a value of about 2.

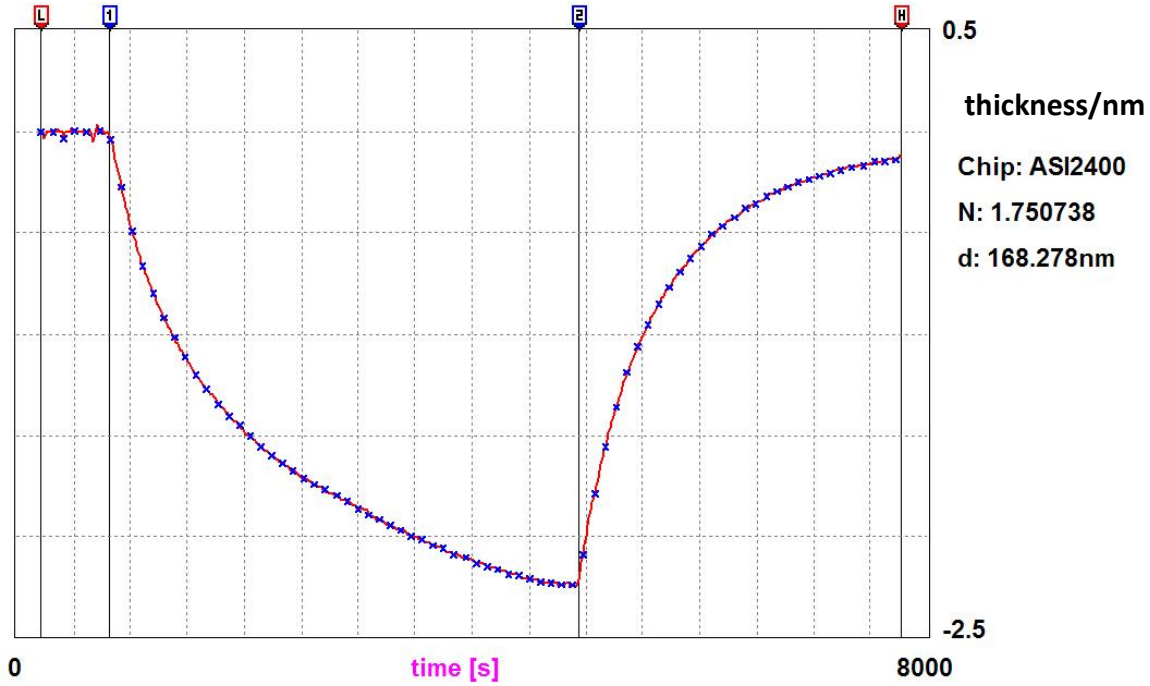

Figure 9.6 Thickness calculated from the plot shown in Figure 9.4 and the accompanying N_{TM} data. Marker 1 is at the start of FAR-1 adsorption on the waveguide; marker 2 is at the start of washing by DMSO. [Experimental code: NF1200B].

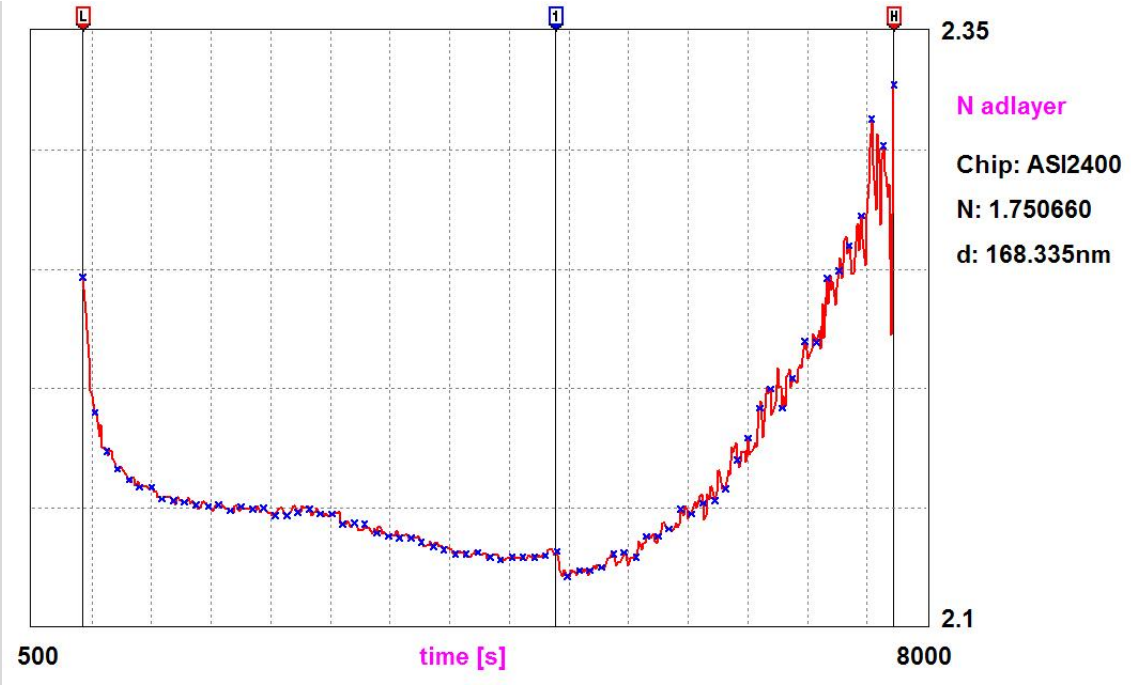

Figure 9.7 Refractive index of adlayer calculated from of the plot shown in Figure 9.5 and the accompanying N_{TM} data starting after marker L (at the start of FAR-1 adsorption on the waveguide) to omit the huge fluctuations at the beginning before a defined adlayer is formed; marker 1 is at the start of washing by DMSO. [Experimental code: NF1200B].

The quantity of the adsorbed organometallic compound adlayer was then computed from Equation (9.6). The results are shown in Figure 9.8.

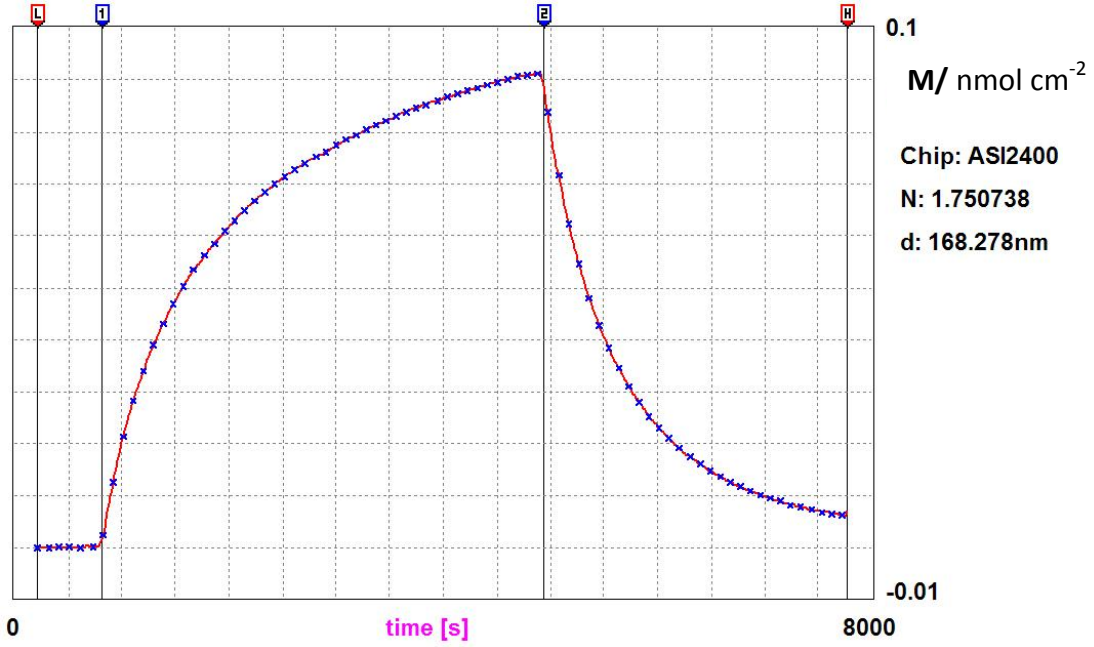

Figure 9.8 Calculated from the data shown in Figures 9.6 and 9.7. Marker 1 is at the start of FAR-1 adsorption on the waveguide; marker 2 is at the start of washing by DMSO. M_{plat}=0.009 nmol/cm^2.

The plateau of 0.09 nmol/cm^2 (Figure 9.8) corresponds to an area per molecule of 1.85 nm^2; together with our thickness of about 2.2 nm, this gives a molecular volume of about 4 nm^3, which lies between the X-ray diffraction and molecular model estimates.

This value of 1.85 nm^2 is in fact a slight overestimate because M_{plat} is depressed relative to the jamming limit because of the reversibility: $M_{sat}=\theta_J/(aN_A)$=0.12 nmol/cm^2, about 30% higher than the measured M_{plat}.

The data was numerically differentiated and plotted against M (Figure 9.9). Equation (3.8) and (3.11) were fitted to it, just as I did with the bacteria (see section 6.2), to obtain the parameters k_a and a, the area occupied per molecule. The excellence of the fit is a vindication of the applicability of RSA. We assume for simplicity that the jamming limit is that appropriate for spheres (θ_J=0.54). The fit yielded a=0.73 nm^2 / molecule. Given that the molecular volume is at least 2 nm^3 and is rather elongated (see Figure 9.4), this suggests that the molecule is depositing with its long axis parallel to the plane of the substratum.

Maximum surface number density, which is predicted to be θ_J / (a N_A), is equals 0.1 nmol/cm^2 in agreement with our results. This is a strong validation of our model.

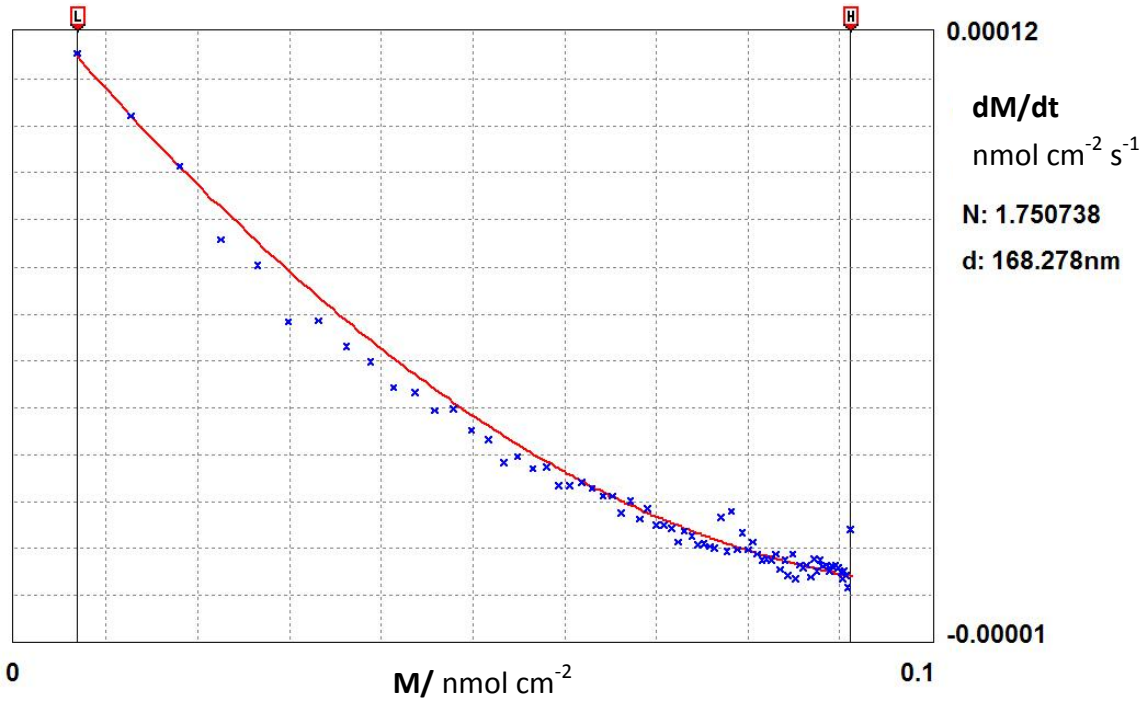

Figure 9.9 Numerically differentiated data from the adsorption part of Figure 9.8 plotted against M (with best fitting of Equation (6.4) A=8.1 and B=0.00013). $a=A\theta_J/N_A=0.73\ nm^2$. $k_a=B/c_b=6.5x10^{-7}$ cm/s.

Desorption. The canonical desorption equation is:

$$\frac{dM}{dt} = -k_d M \tag{9.7}$$

Integrating, we get

$$M(t)=M_{plat}\exp(-k_d t) \tag{9.8}$$

Hence, we plot ln($M(t)/M_{sat}$) vs time to obtain k_d. (see Figure 9.10).

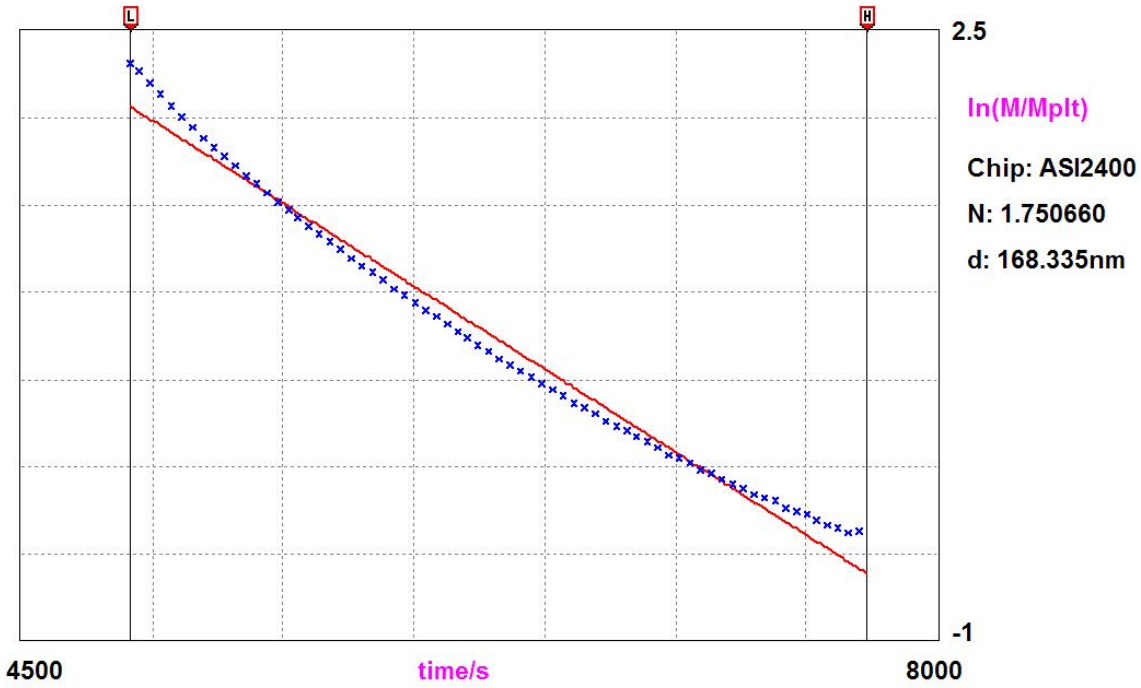

Figure 9.10 Plot of ln($M(t)/M_{sat}$) vs time(data from Figure 9.8 between marker 2 and H). Best fit is $k_d=9.5x10^{-4}$ s^{-1}.

The desorption is not, in fact, quite a pure exponential, which should be further investigated. Most likely rearrangements within the layer take place following initial desorption, giving rise to memory effects (Talbot, 1996). In other works, k_d in Equation (9.7) must be replaced by a time-dependent function. Evidently, the internal structure of the Kaleem Khosa compounds is sufficient complex to permit conformational rearrangement in the adsorbed state.

9.7 Experimental results – remaining compounds

The general appearance of the adsorption-desorption data from all the compounds tested was similar. We plotted dM/dt vs M for the adsorption to demonstrate RSA, and ln($M(t)/M_{plat}$) vs t to demonstrate memoryless desorption and summarize the fitting parameters in Table 9.9.

[FAR-1]

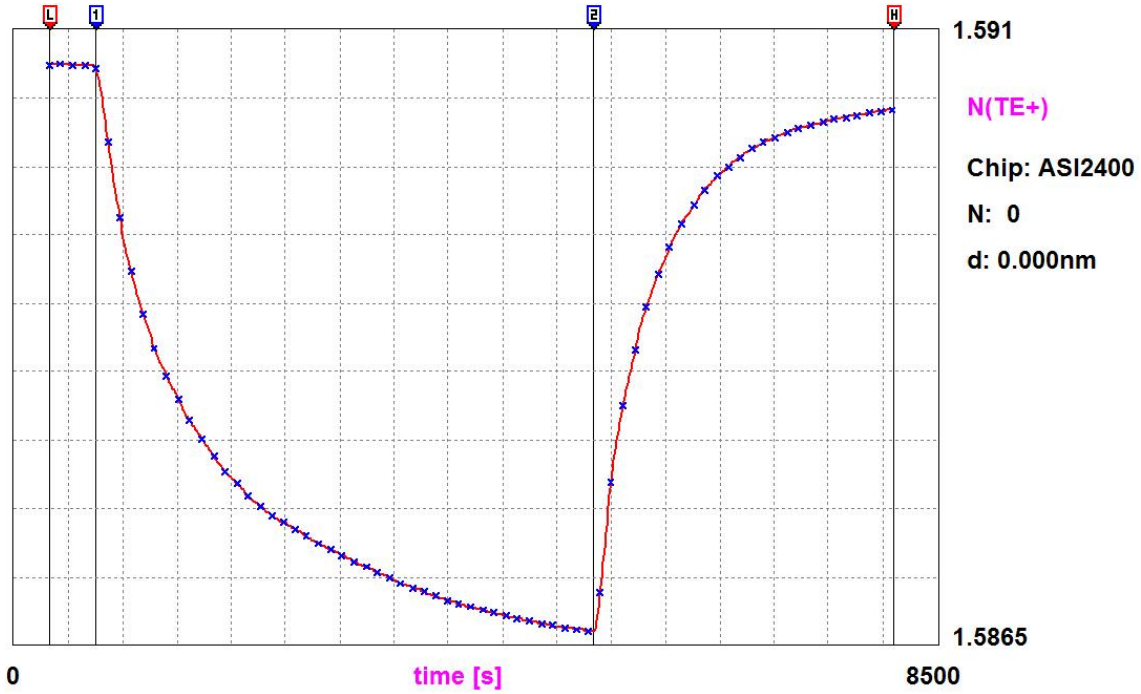

Figure 9.11 The N(TE) versus time raw data of FAR-A at c_b = 0.2 mM in pure DMSO at T=28.0 ^{o}C. Marker 1 is at the start of FAR-1 adsorption on the waveguide; marker 2 is at the start of washing by DMSO. [Experimental code: NFA200B].

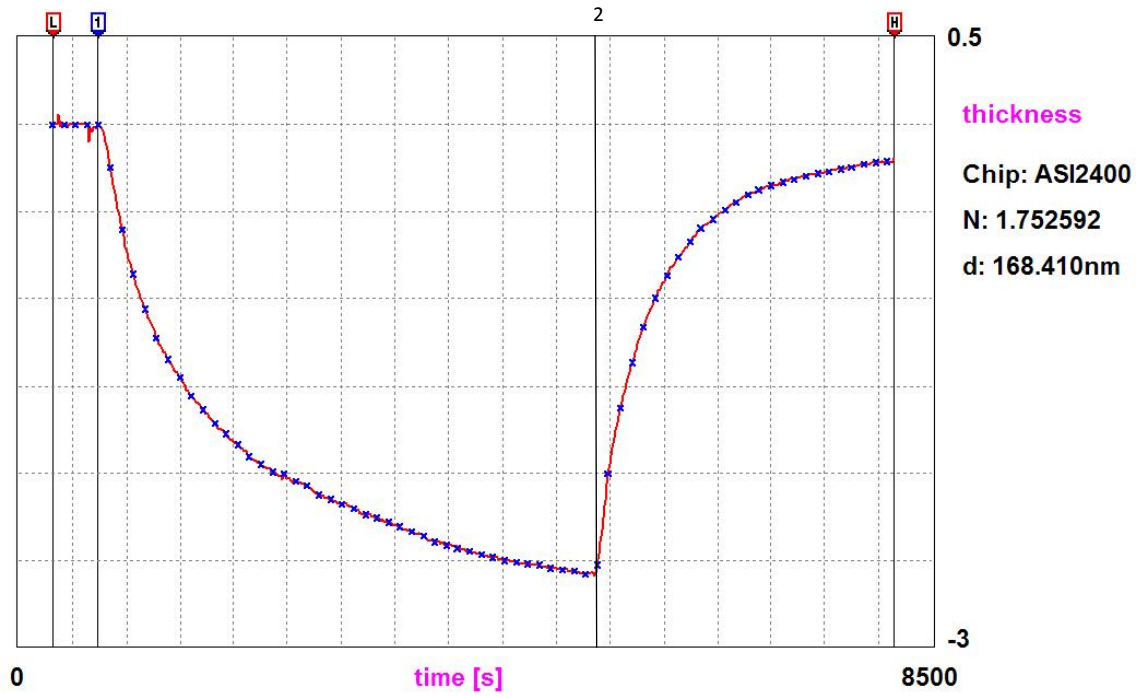

Figure 9.12 Thickness calculated from the plot shown in Figure 9.11 and the accompanying N_{TM} data. Marker 1 is at the start of FAR-A adsorption on the waveguide; marker 2 is at the start of washing by DMSO. [Experimental code: NFA200B].

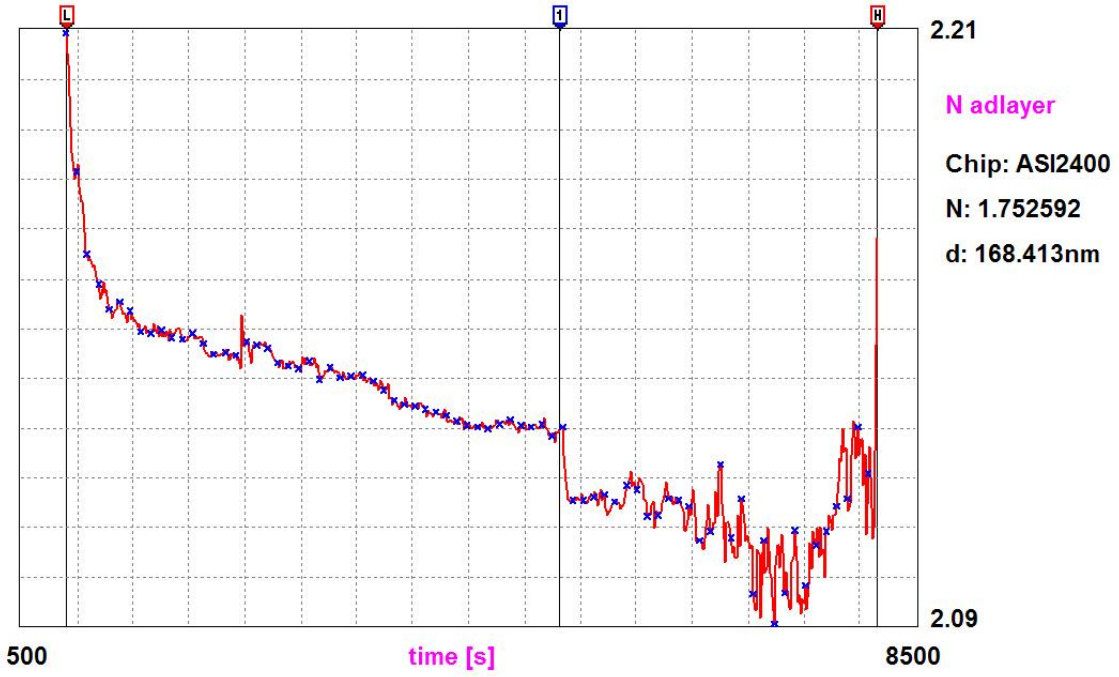

Figure 9.13 Refractive index of adlayer calculated from the plot shown in Figure 9.11 and the accompanying N_{TM} data. Marker L is at the start of FAR-A adsorption on the waveguide; marker 1 is at the start of washing by DMSO. [Experimental code: NFA200B]

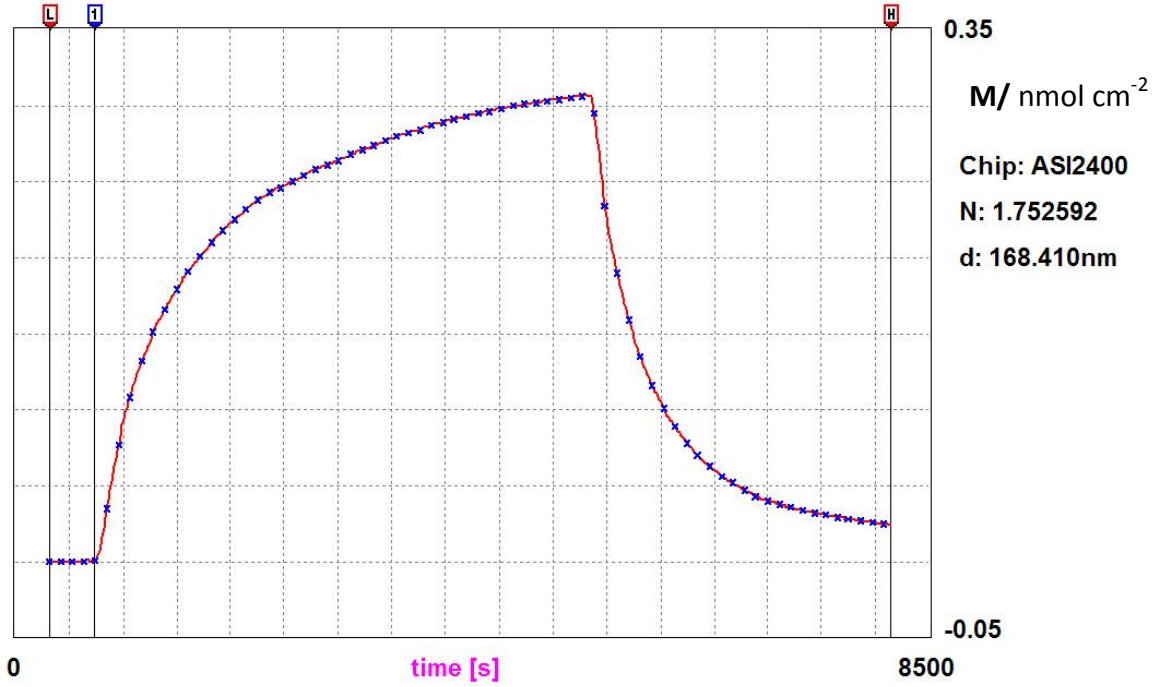

Figure 9.14 Calculated from the data shown in Figures 9.11 and 9.12. Marker 1 is at the start of FAR-A adsorption on the waveguide; marker 2 is at the start of washing by DMSO.

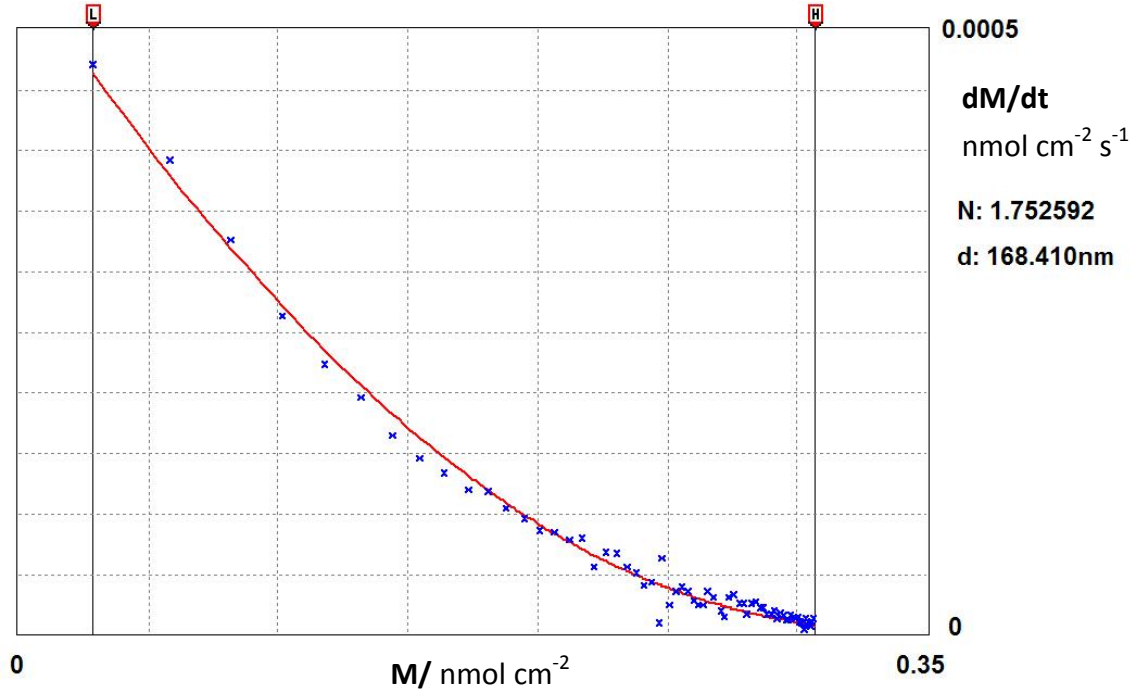

Figure 9.15 Numerically differentiated data from the adsorption part of Figure 9.11 plotted against M (with best fitting of Equation (6.4) A=2.61 and B=0.00055). by solving $A= a/\theta_J$ and $B=k_a c_b$, a is equal to 1.41 nm^2.

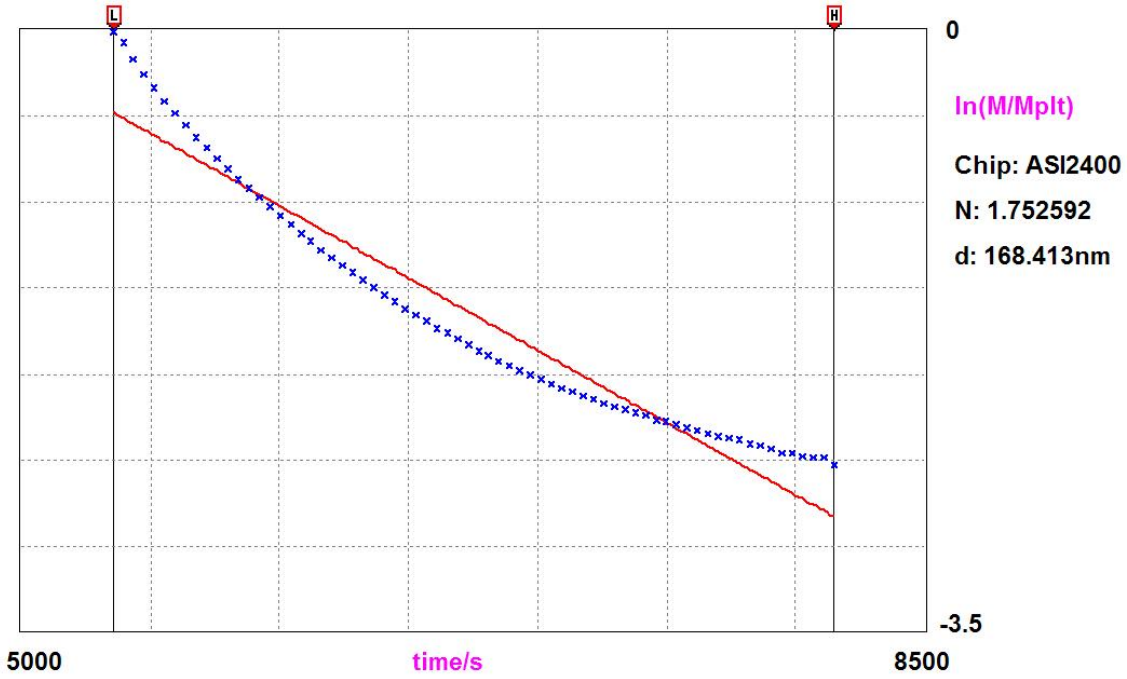

Figure 9.16 Plot of ln(M(t)/M_{sat}) vs time (data from Figure 9.11).

[FAR-18]

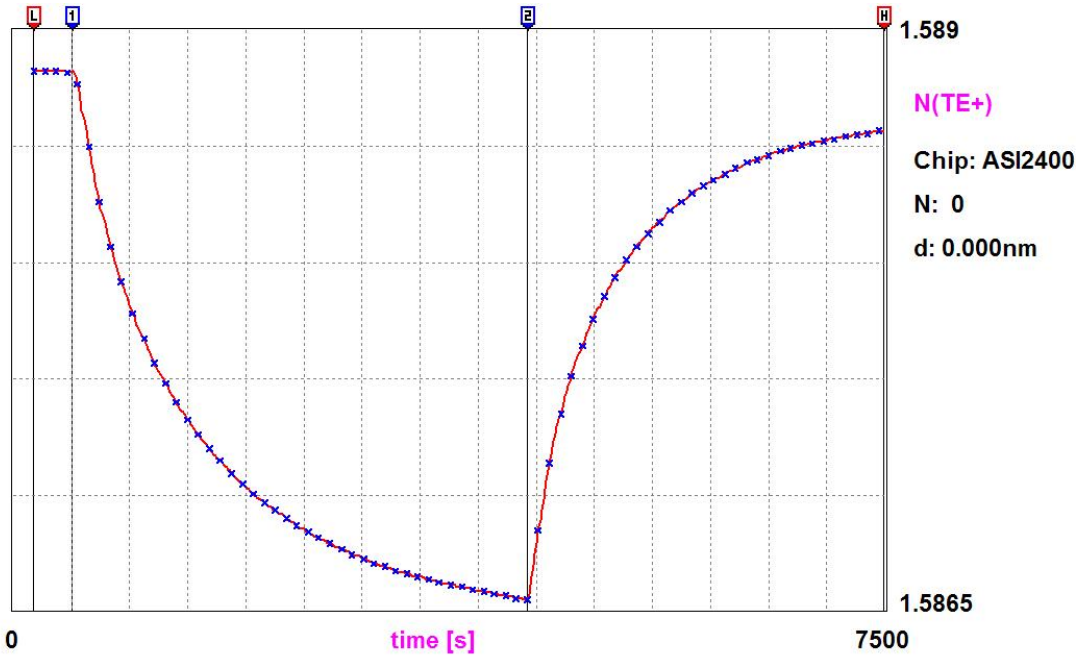

Figure 9.17 The N(TE) versus time raw data of FAR-18 at c_b = 0.2 mM in pure DMSO at T=28.5 ^{o}C. Marker 1 is at the start of FAR-1 adsorption on the waveguide; marker 2 is at the start of washing by DMSO. [Experimental code: NF18200B].

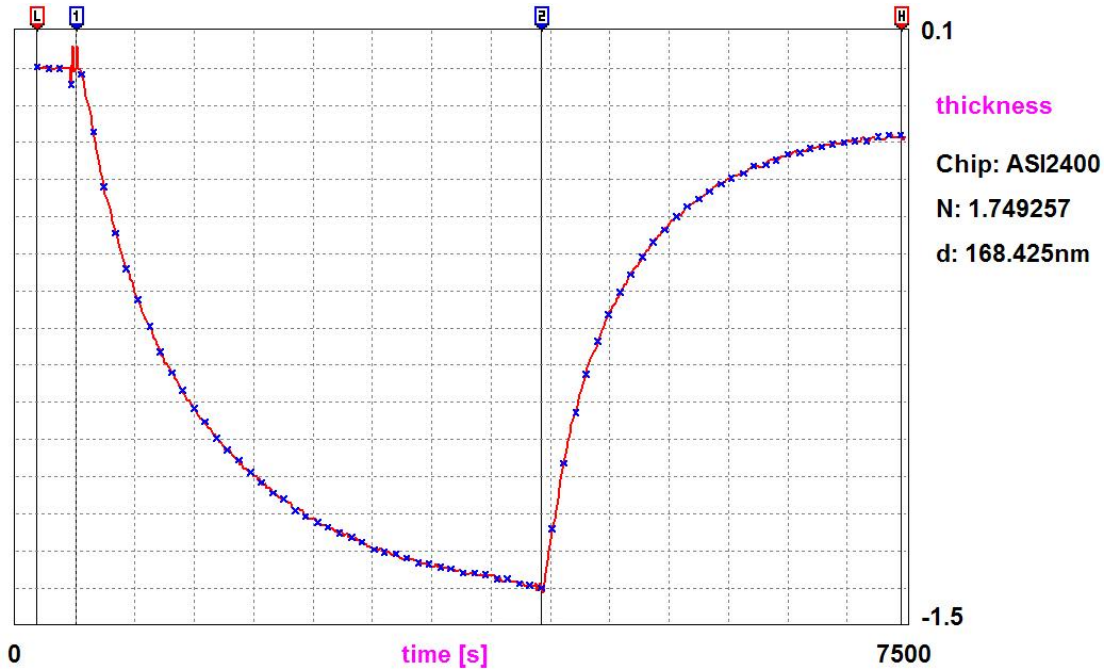

Figure 9.18 Thickness calculated from the plot shown in Figure 9.17 and the accompanying N_{TM} data. Marker 1 is at the start of FAR-18 adsorption on the waveguide; marker 2 is at the start of washing by DMSO. [Experimental code: NF18200B].

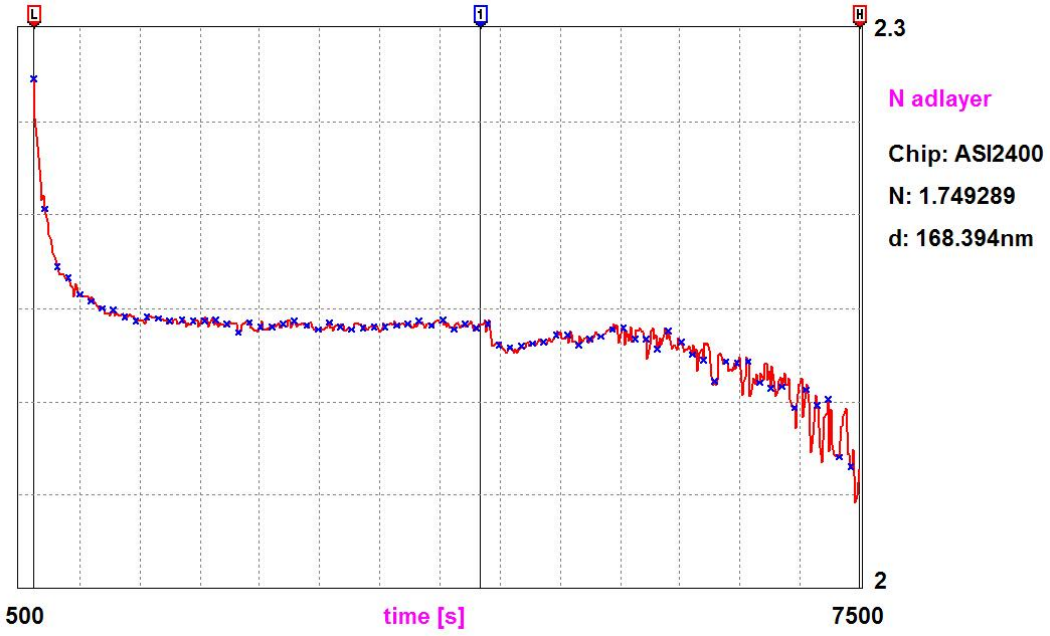

Figure 9.19 Refractive index of adlayer calculated from the plot shown in Figure 9.17 and the accompanying N_{TM} data. Marker L is at the start of FAR-18 adsorption on the waveguide; marker 1 is at the start of washing by DMSO. [Experimental code: NF18200B]

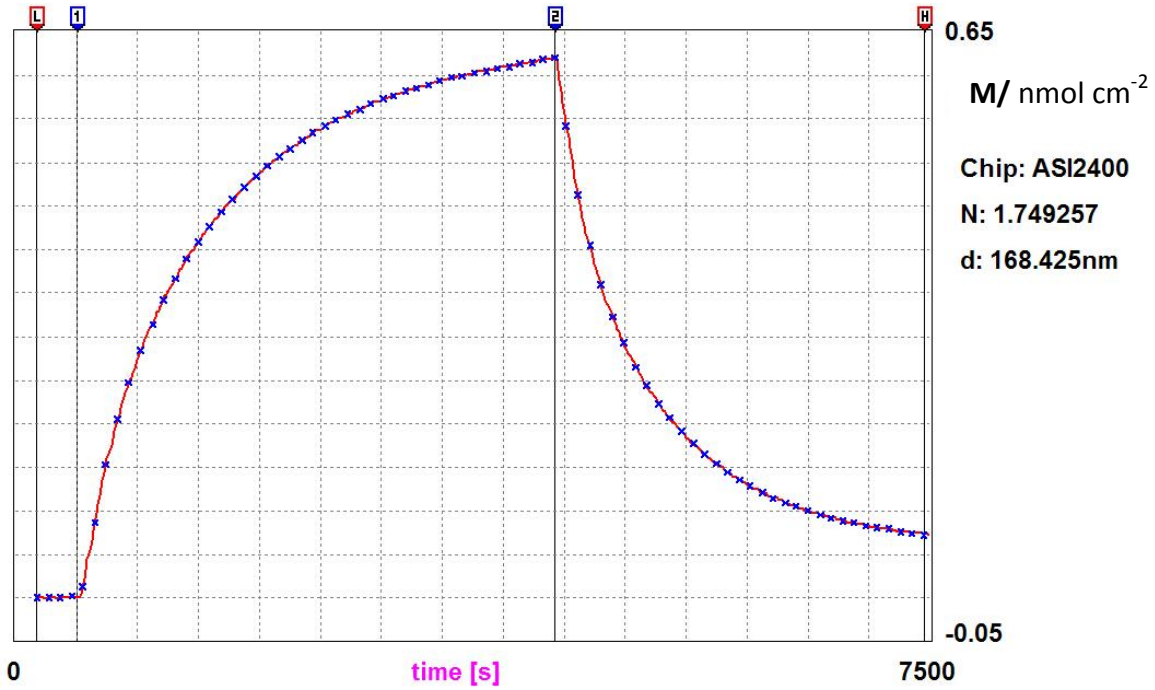

Figure 9.20 Calculated from the data shown in Figures 9.18 and 9.19. Marker 1 is at the start of FAR-18 adsorption on the waveguide; marker 2 is at the start of washing by DMSO.

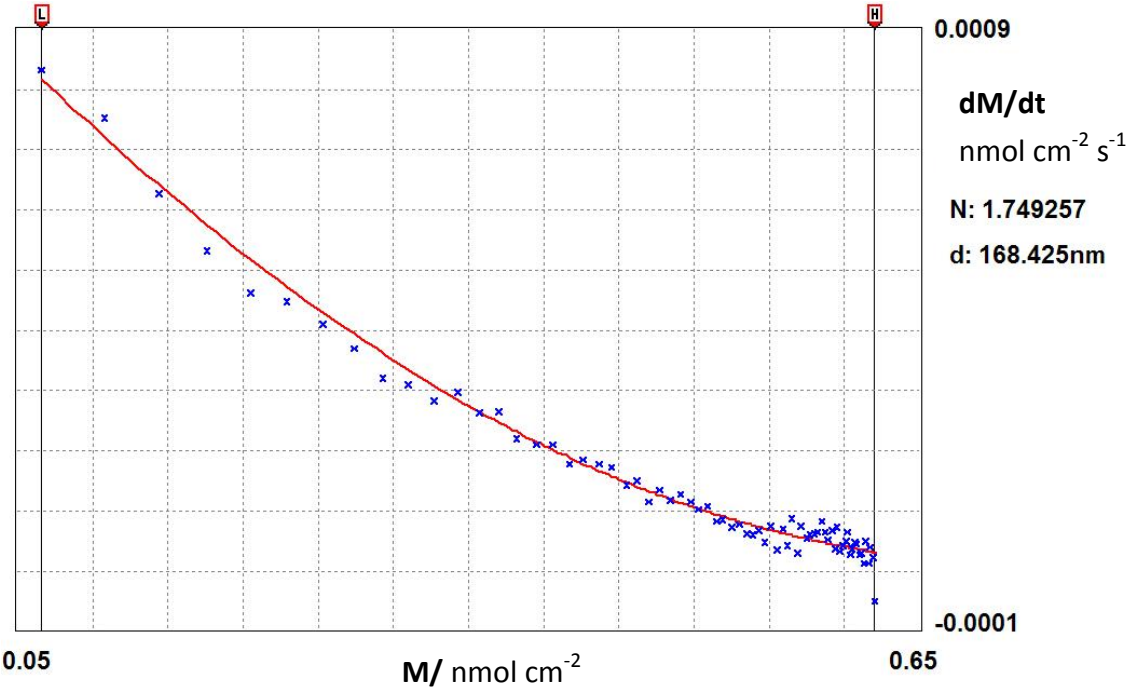

Figure 9.21 Numerically differentiated data from the adsorption part of Figure 9.17 plotted against M (with best fitting of Equation (6.4) A=1.19 and B=0.00098). by solving $A= a/\theta_J$ and $B=k_a c_b$, a is equal to 0.64 nm^2.

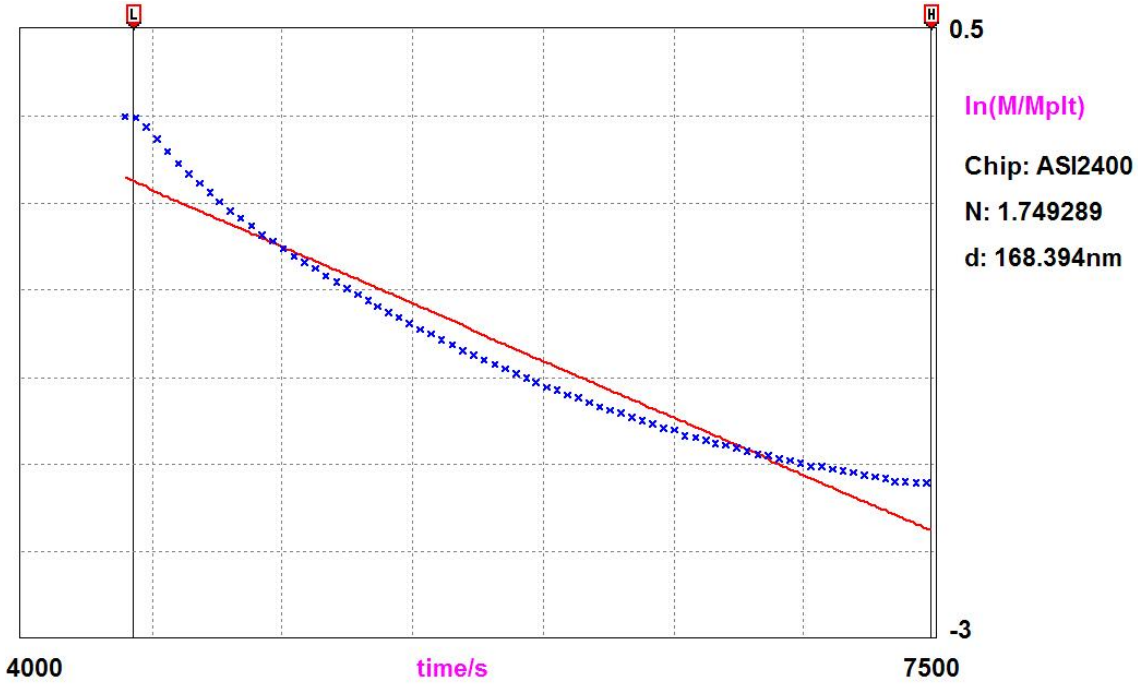

Figure 9.22 Plot of ln($M(t)/M_{sat}$) vs time(data from Figure 9.17).

[FAR-42]

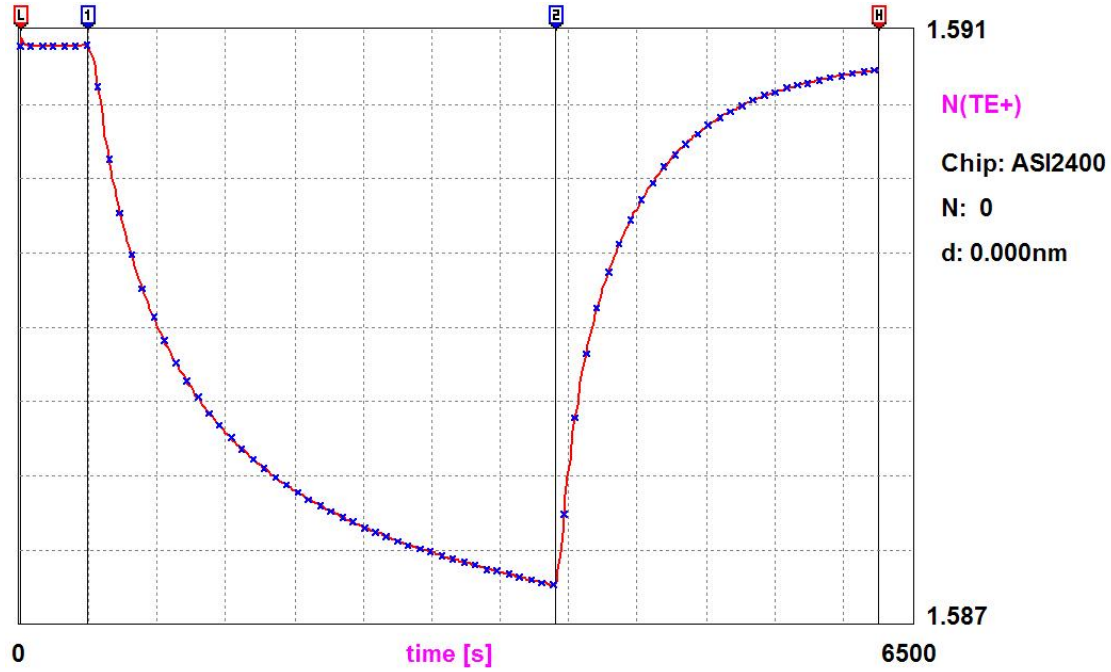

Figure 9.23 The N(TE) versus time raw data of FAR-42 at c_b = 0.2 mM in pure DMSO at T=27 ^{o}C. Marker 1 is at the start of FAR-1 adsorption on the waveguide; marker 2 is at the start of washing by DMSO. [Experimental code: NF4200B].

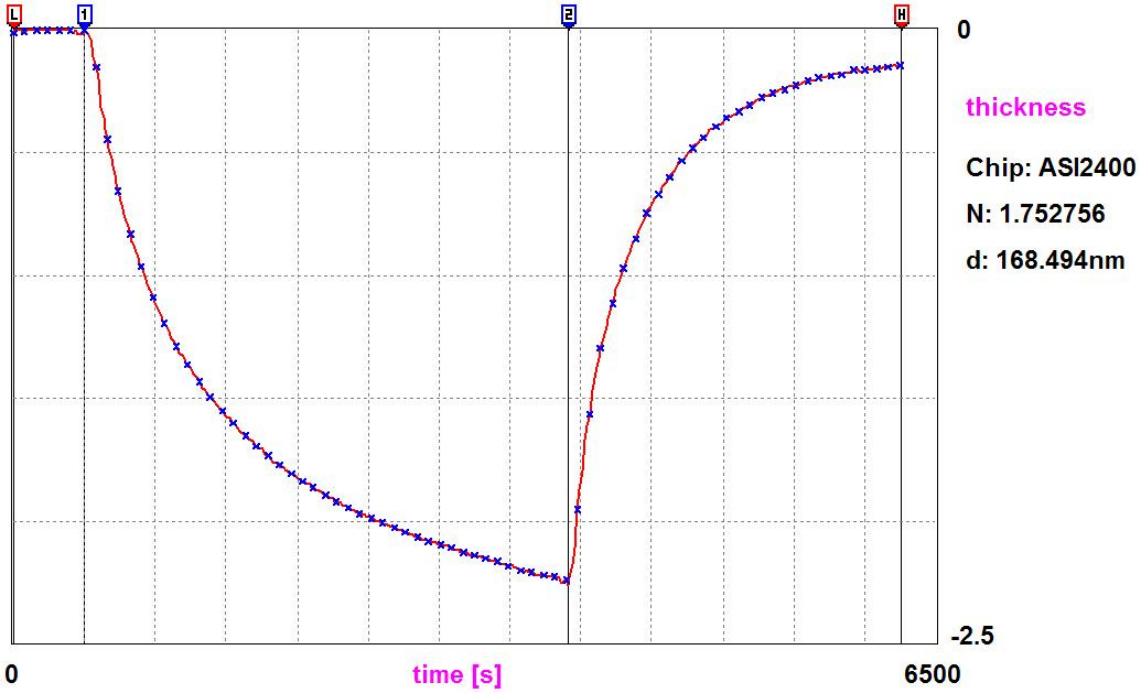

Figure 9.24 Thickness calculated from the plot shown in Figure 9.23 and the accompanying N_{TM} data. Marker 1 is at the start of FAR-42 adsorption on the waveguide; marker 2 is at the start of washing by DMSO. [Experimental code: NF4200B].

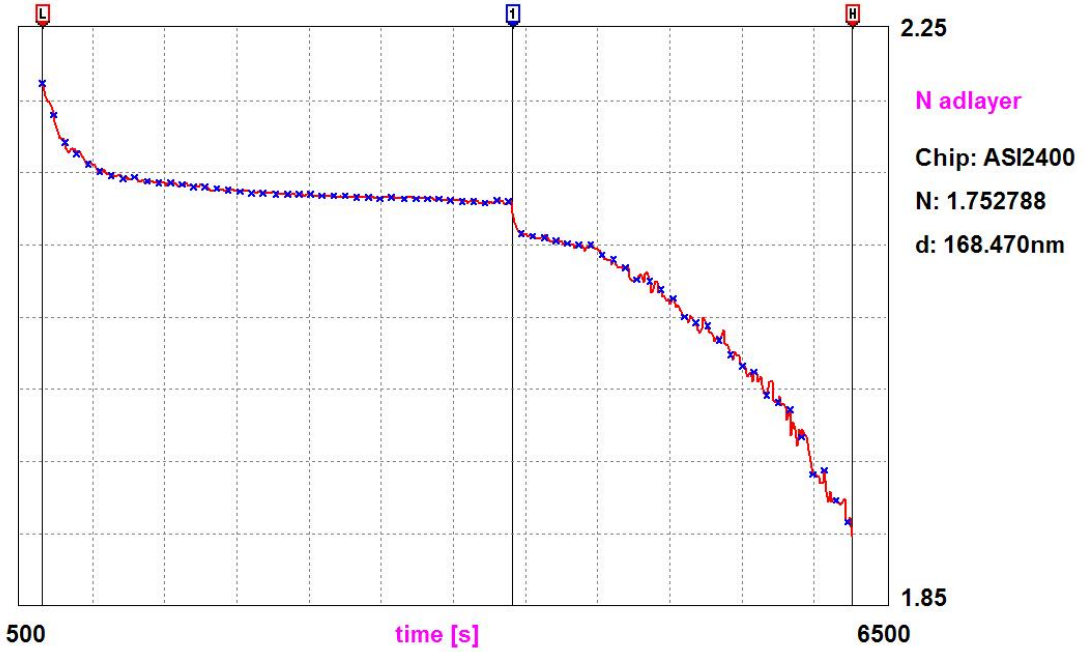

Figure 9.25 Refractive index of adlayer calculated from the plot shown in Figure 9.23 and the accompanying N_{TM} data. Marker L is at the start of FAR-42 adsorption on the waveguide; marker 1 is at the start of washing by DMSO. [Experimental code: NF4200B]

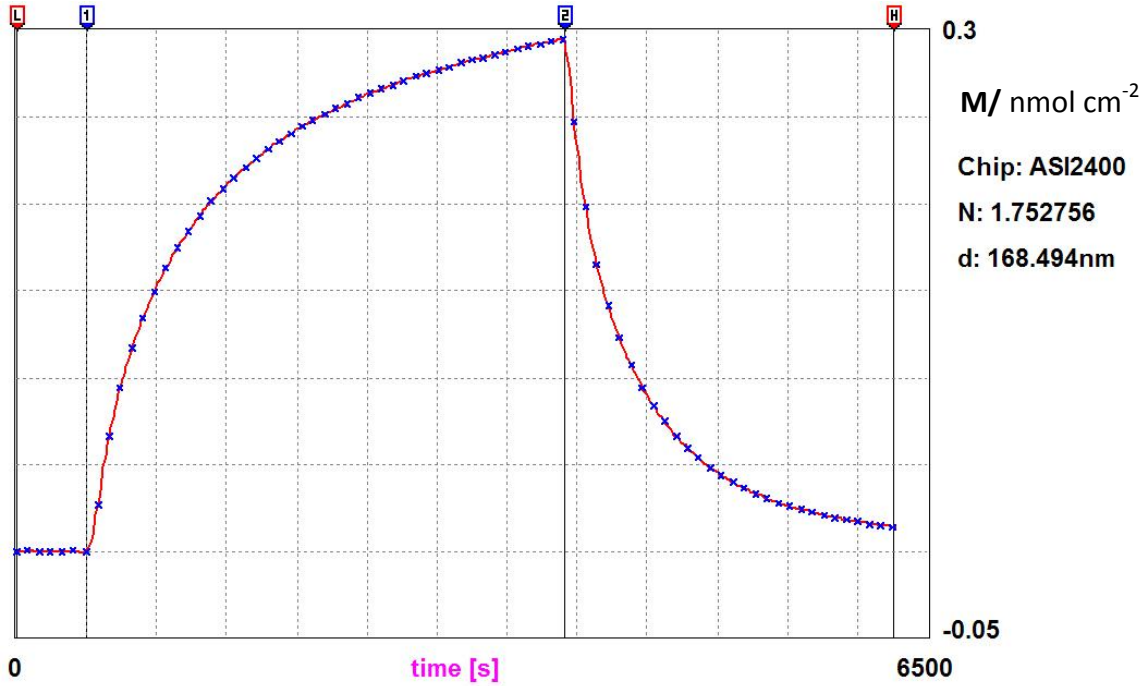

Figure 9.26 Calculated from the data shown in Figures 9.24 and 9.25. Marker 1 is at the start of FAR-42 adsorption on the waveguide; marker 2 is at the start of washing by DMSO.

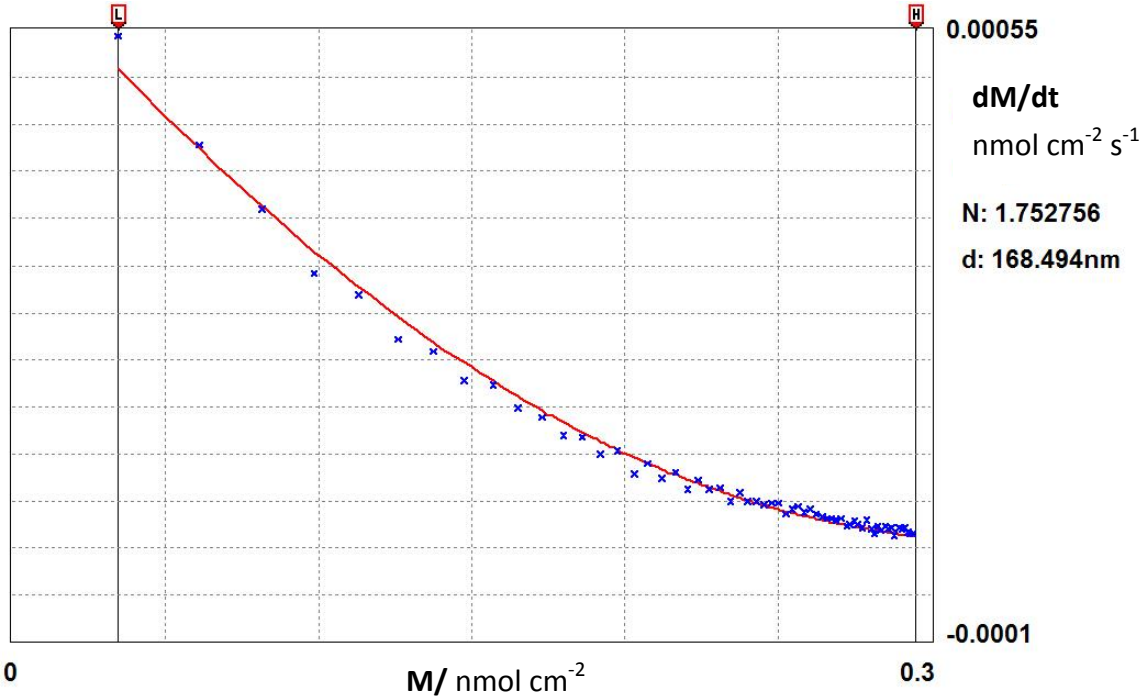

Figure 9.27 Numerically differentiated data from the adsorption part of Figure 9.23 plotted against M (with best fitting of Equation (6.4) A=2.65 and B=0.00063). by solving $A= a/\theta_J$ and $B=k_a c_b$, a is equal to 1.43 nm^2.

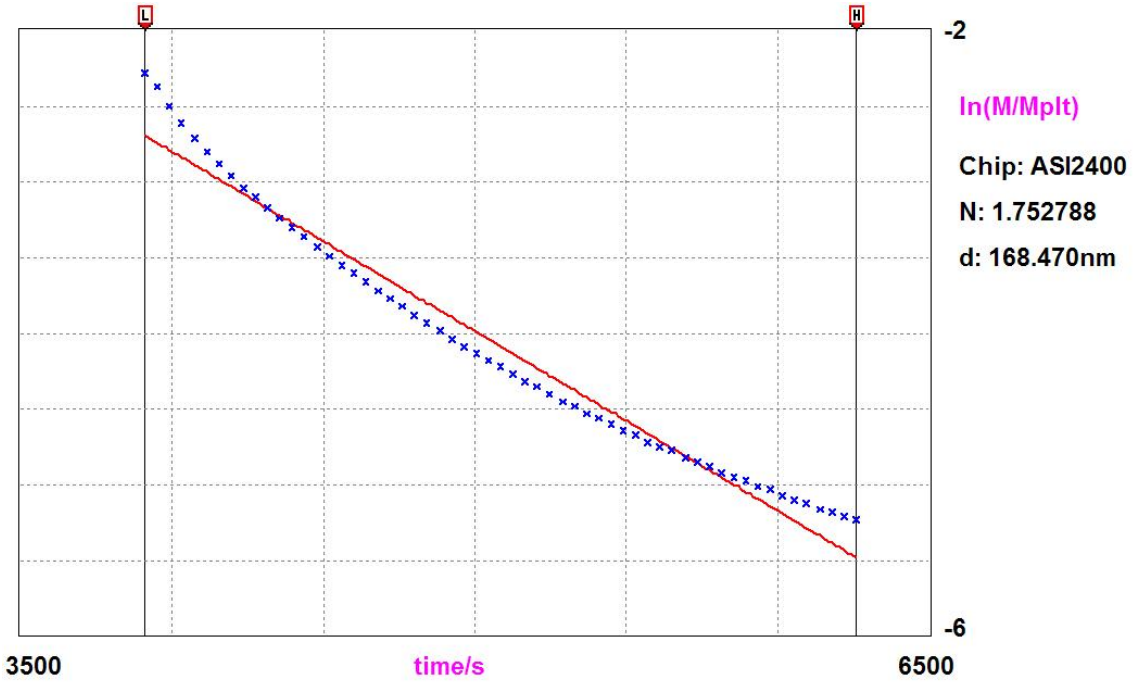

Figure 9.28 Plot of ln(M(t)/M_{sat}) vs time(data from Figure 9.23).

[FAR-41]

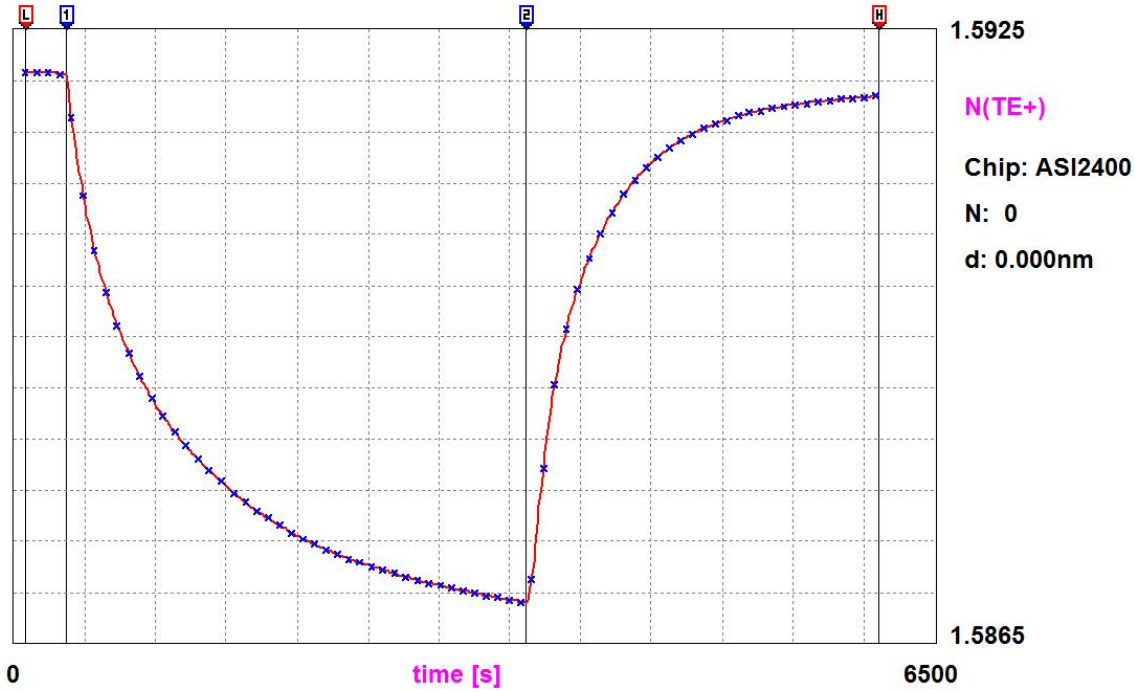

Figure 9.29 The N(TE) versus time raw data of FAR-41 at c_b = 0.2 mM in pure DMSO at T=30.6 ^{o}C. Marker 1 is at the start of FAR-1 adsorption on the waveguide; marker 2 is at the start of washing by DMSO. [Experimental code: NF41200B].

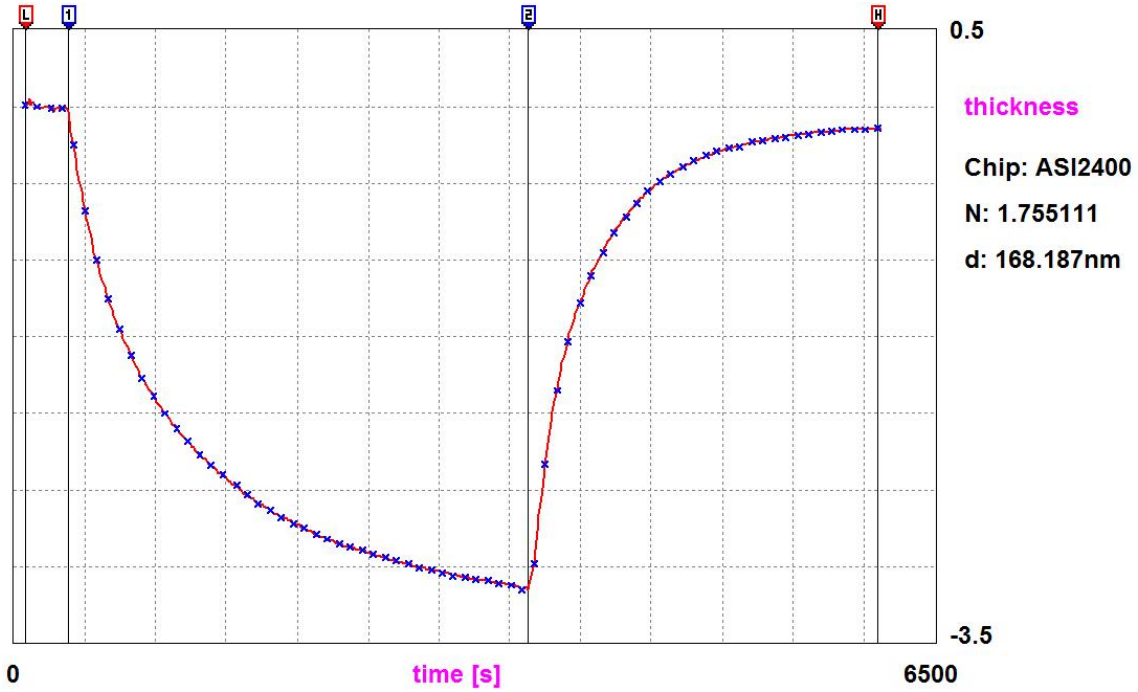

Figure 9.30 Thickness calculated from the plot shown in Figure 9.29 and the accompanying N_{TM} data. Marker 1 is at the start of FAR-41 adsorption on the waveguide; marker 2 is at the start of washing by DMSO. [Experimental code: NF41200B].

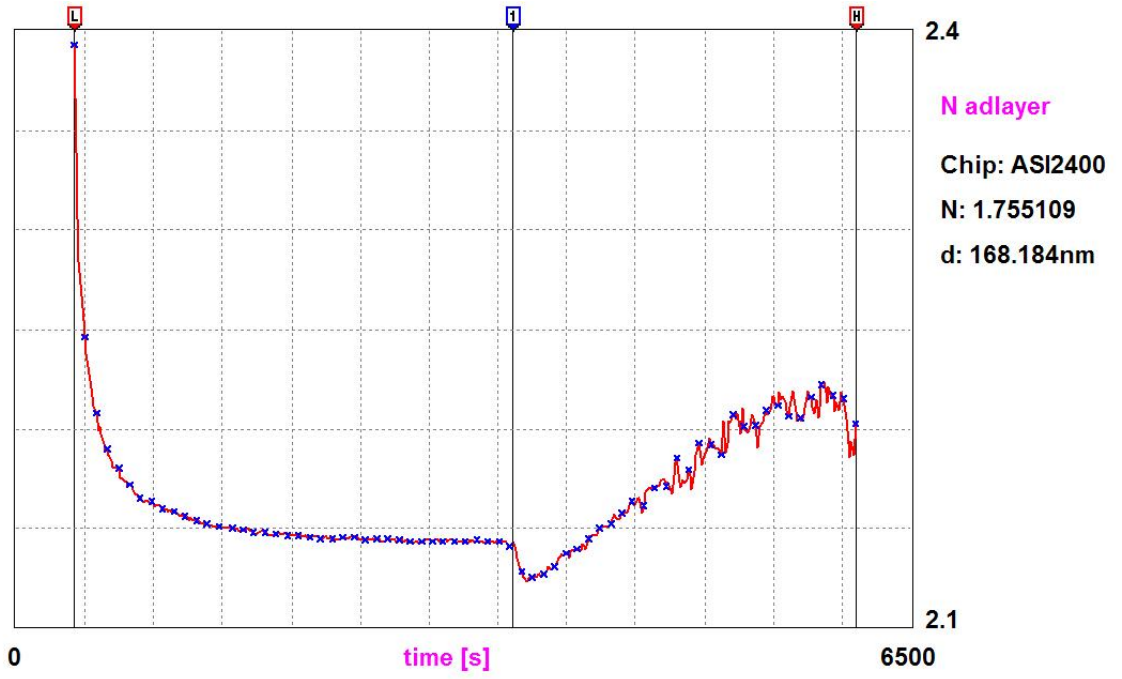

Figure 9.31 Refractive index of adlayer calculated from the plot shown in Figure 9.29 and the accompanying N_{TM} data. Marker L is at the start of FAR-41 adsorption on the waveguide; marker 1 is at the start of washing by DMSO. [Experimental code:

NF41200B]

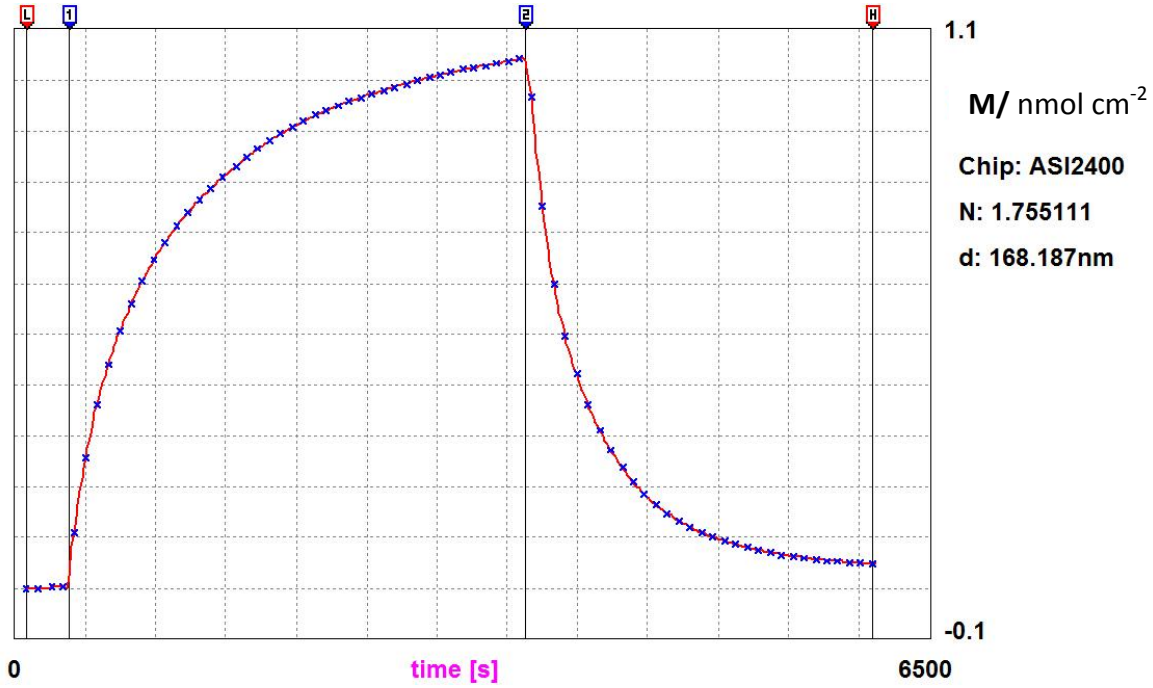

Figure 9.32 Calculated from the data shown in Figures 9.30 and 9.31. Marker 1 is at the start of FAR-41 adsorption on the waveguide; marker 2 is at the start of washing by DMSO.

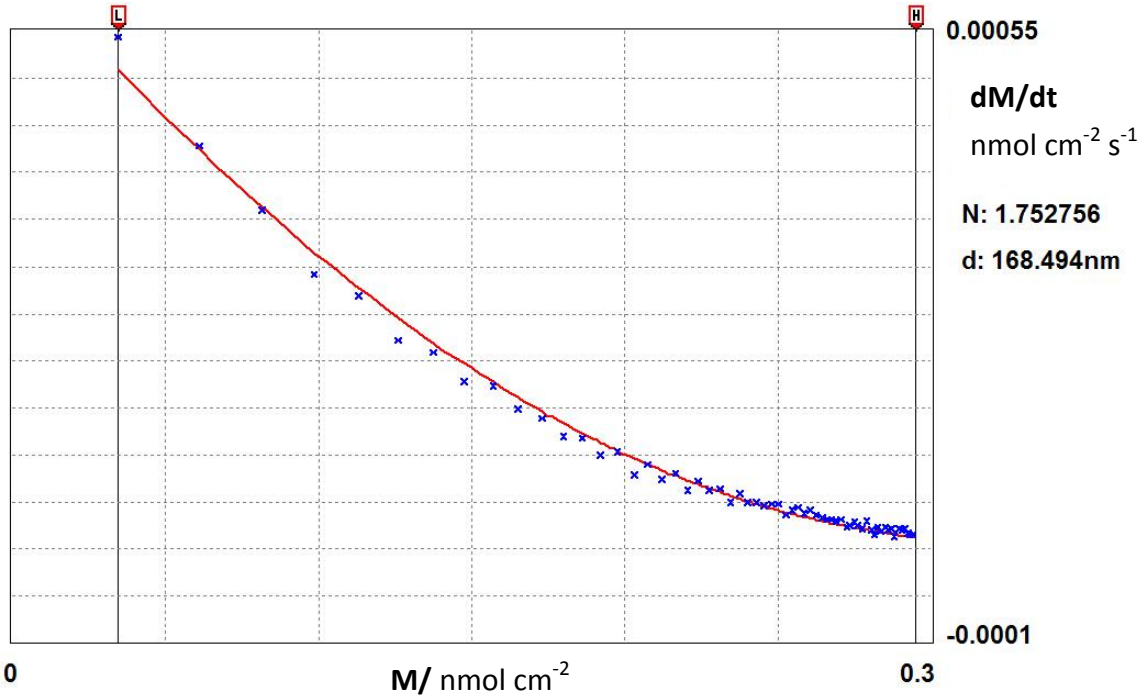

Figure 9.33 Numerically differentiated data from the adsorption part of Figure 9.29 plotted against M (with best fitting of Equation (6.4) A=0.75 and B=0.00245). by solving $A= a/\theta_J$ and $B=k_a c_b$, a is equal to 0.405 nm^2.

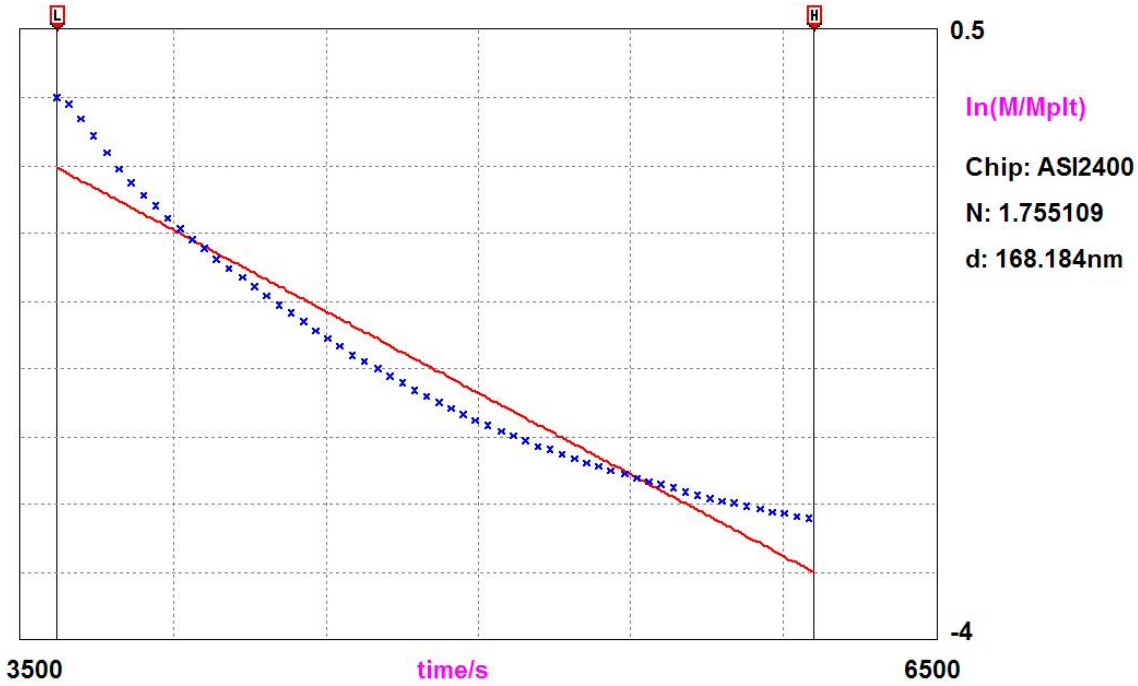

Figure 9.34 Plot of ln(M(t)/M_{sat}) vs time(data from Figure 9.29).

[FAR-6]

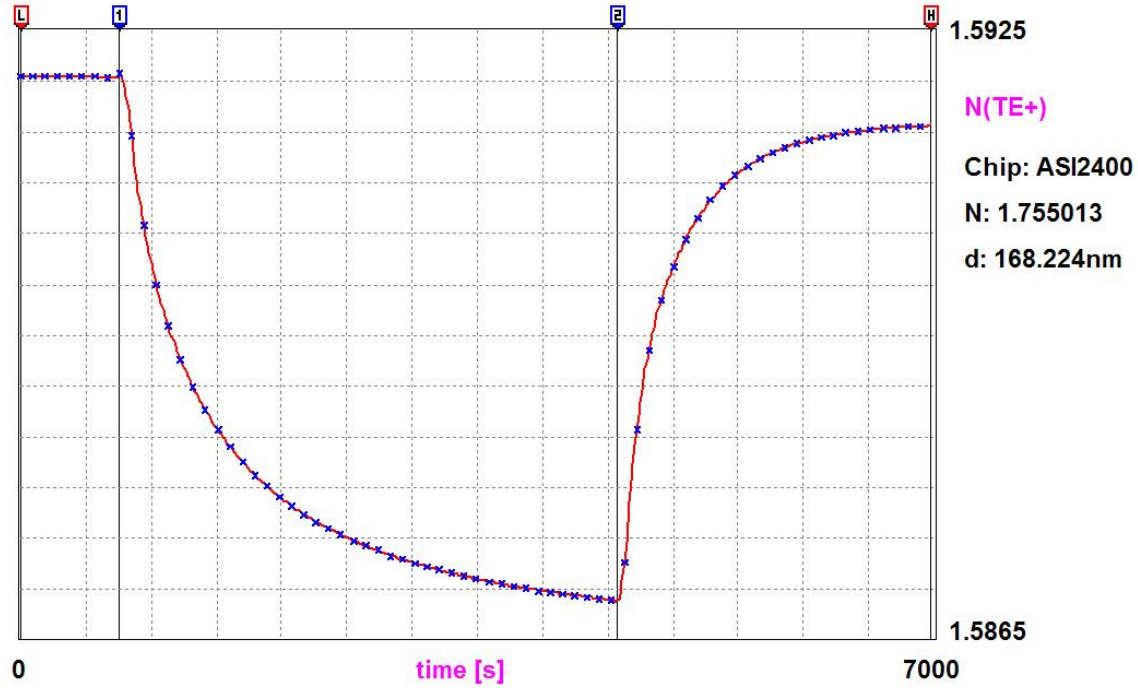

Figure 9.35 The N(TE) versus time raw data of FAR-6 at c_b = 0.2 mM in pure DMSO at T=28.5 ^{o}C. Marker 1 is at the start of FAR-1 adsorption on the waveguide; marker 2 is at the start of washing by DMSO. [Experimental code: NF6200B].

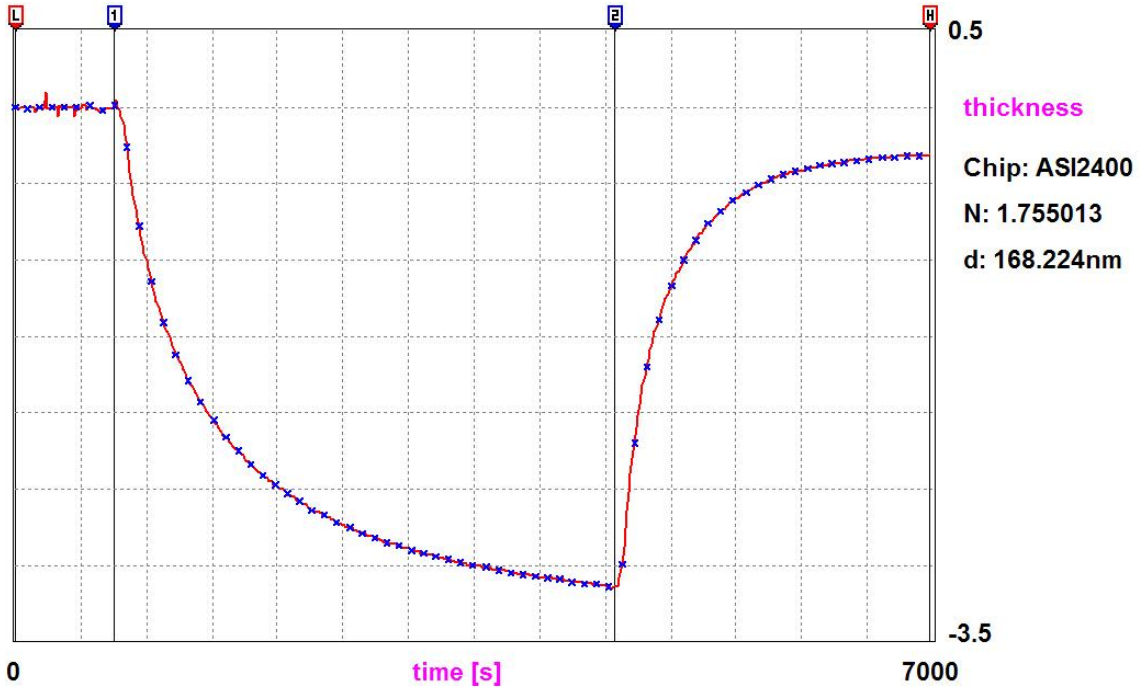

Figure 9.36 Thickness calculated from the plot shown in Figure 9.35 and the accompanying N_{TM} data. Marker 1 is at the start of FAR-6 adsorption on the waveguide; marker 2 is at the start of washing by DMSO. [Experimental code: NF6200B].

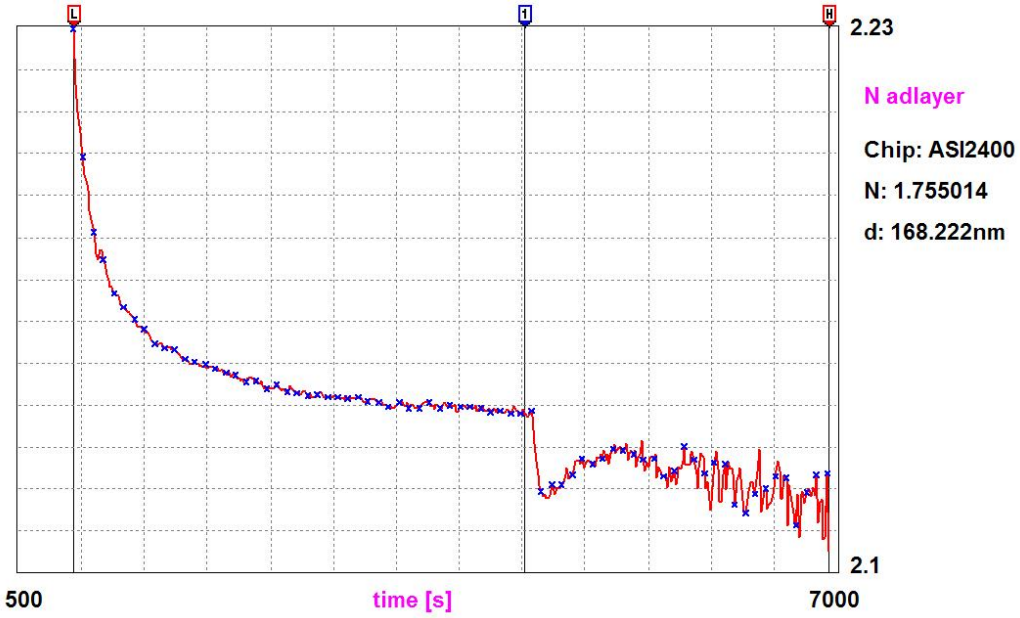

Figure 9.37 Refractive index of adlayer calculated from the plot shown in Figure 9.35 and the accompanying N_{TM} data. Marker L is at the start of FAR-6 adsorption on the waveguide; marker 1 is at the start of washing by DMSO. [Experimental code: NF6200B]

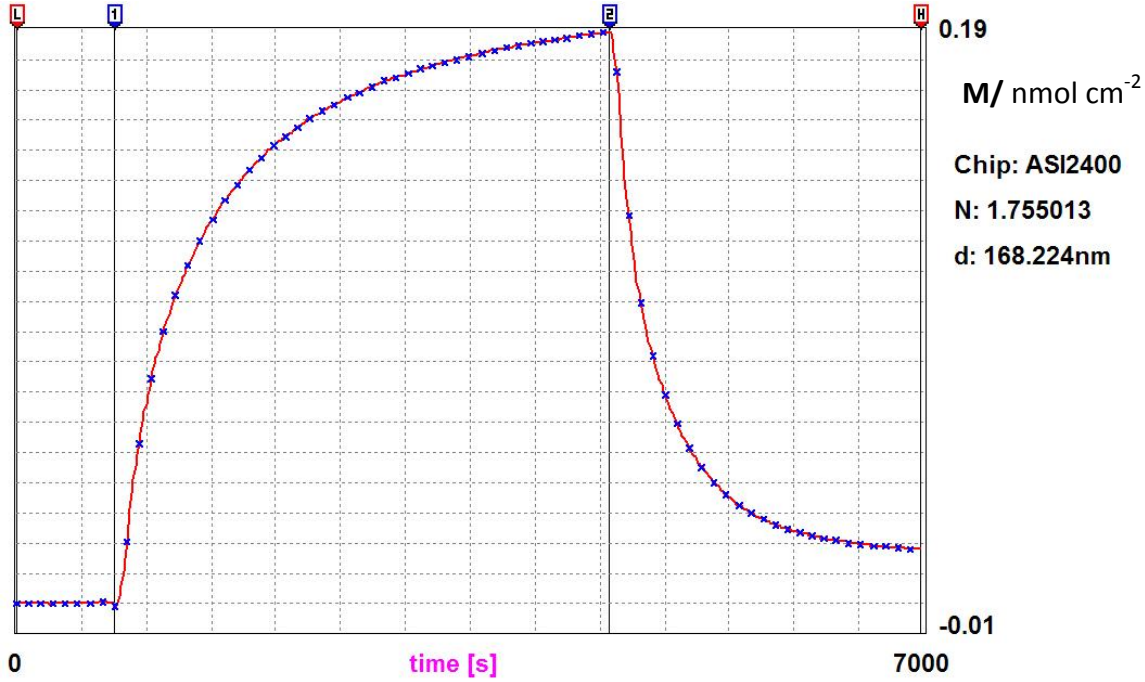

Figure 9.38 Calculated from the data shown in Figures 9.36 and 9.37. Marker 1 is at the start of FAR-6 adsorption on the waveguide; marker 2 is at the start of washing by DMSO.

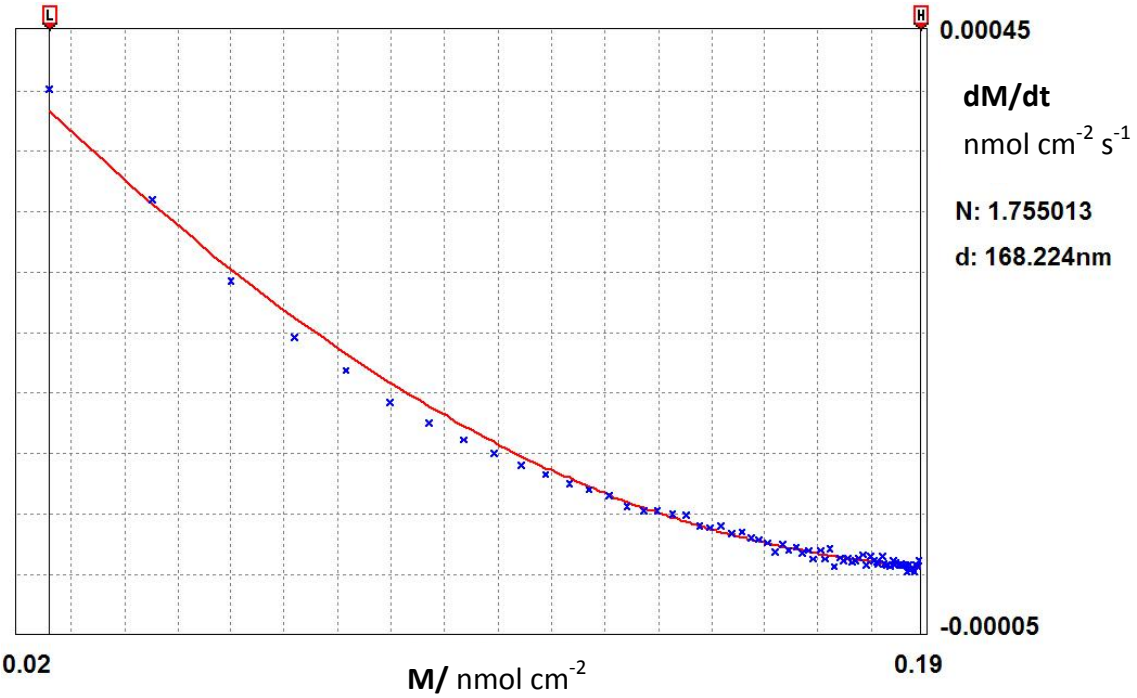

Figure 9.39 Numerically differentiated data from the adsorption part of Figure 9.35 plotted against M (with best fitting of Equation (6.4) A=4.3 and B=0.0005) by solving $A=a/\theta_J$ and $B=k_a c_b$, a is equal to 2.32 nm^2.

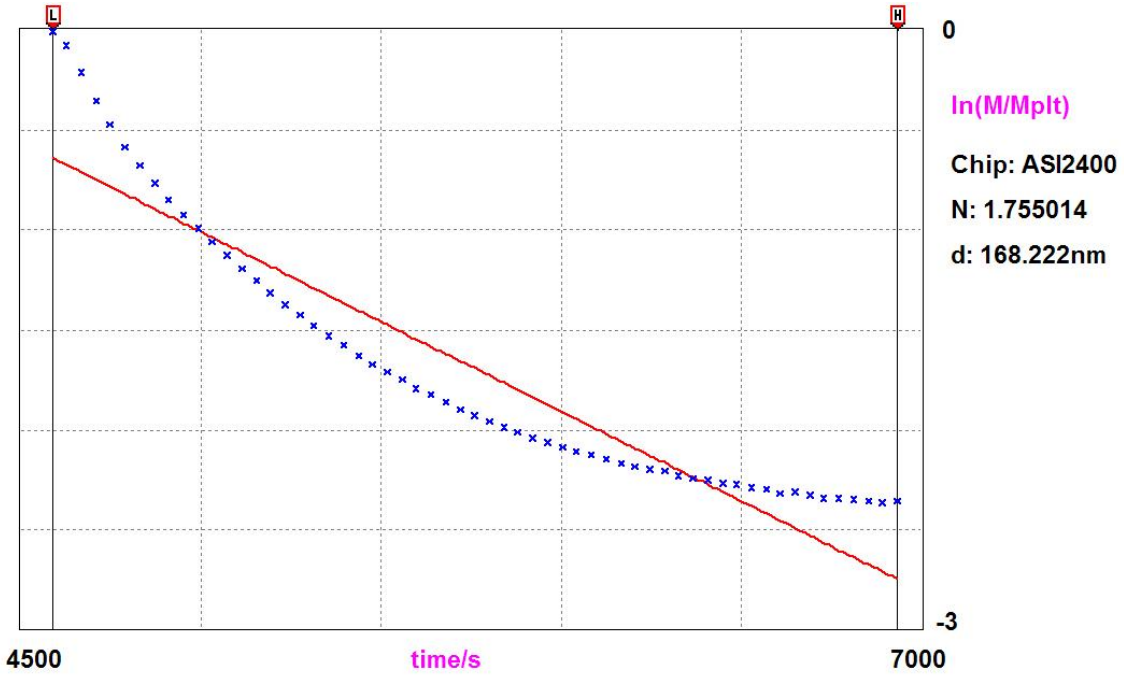

Figure 9.40 Plot of ln(M(t)/M_{sat}) vs time(data from Figure 9.35).

Table 9.9 Summy of the fitted parameters.

Compound	M_r*	M_{plat} /nmol cm^{-2}	d_A /nm	a /nm2	10^{-7} k_a /cm s^{-1}	$10^{-4}k_d$ /s^{-1}	k_a/k_d /μm
FAR-1	564	0.09	2.2	0.73	6.5	9.5	6.8
FAR-A	427	0.31	2.6	0.24	27.5	8.4	33
FAR-6	671	0.19	3.2	0.39	25	8.97	28
FAR-18	474	0.62	1.4	0.11	49	6.56	74
FAR-41	661	1.04	3.1	0.07	123	12.0	103
FAR-42	578	2.9	2.3	0.24	31	11.8	26
Typical Uncertainty	---	±0.005	±0.1	±0.05	±2x10^{-8}	±0.0005	---

* Molecular weight.

We discuss these data rather briefly here, focusing on reasons for extreme values; e.g. although all the compounds fall in the range of M_r =427 to 671, M_{plat} varies from 0.09 to 2.9 nmol/cm^2 (conversely, a from 0.73 to 0.07 nm^2). Adsorption rate constant varied from 6.5x10^{-7} to 123x10^{-7} cm/s, but desorption constants from 6.6x10^{-4} to 12x10^{-4} s^{-1}. Certainly the molecule structures do not obviously reveal these behavioural features, except that the thickness roughly follows the molecular weight. The ratio k_a/k_d measures the adsorption/desorption balance, which is least favourable for FAR-1, but FAR-42, which has the biggest M_{plat}, has the next least favourable value. Evidently FAR-41 can pack into a layer with a very small footprint. A next step -- but beyond the scope of this thesis -- would be to use Brownian dynamics investigate how these molecules randomly adsorb. Note that we can use this data to get estimates of the molecular volume $v=d_Aa$.

9.8 Adsorption in DMSO-water mixtures

Since the compounds desorbed from the substrata in the DMSO environment, but are insoluble in water, we can predict that at intermediate solvent compositions we should get irreversible adsorption, which is what we need for our original purpose of generating novel substrata for bacterial adsorption. Figure 9.41 demonstrates that this proposition is correct.

Figure 9.41 shows N(TE) vs time for FAR-6 (20 µm) deposition in 50% DMSO-50% water.

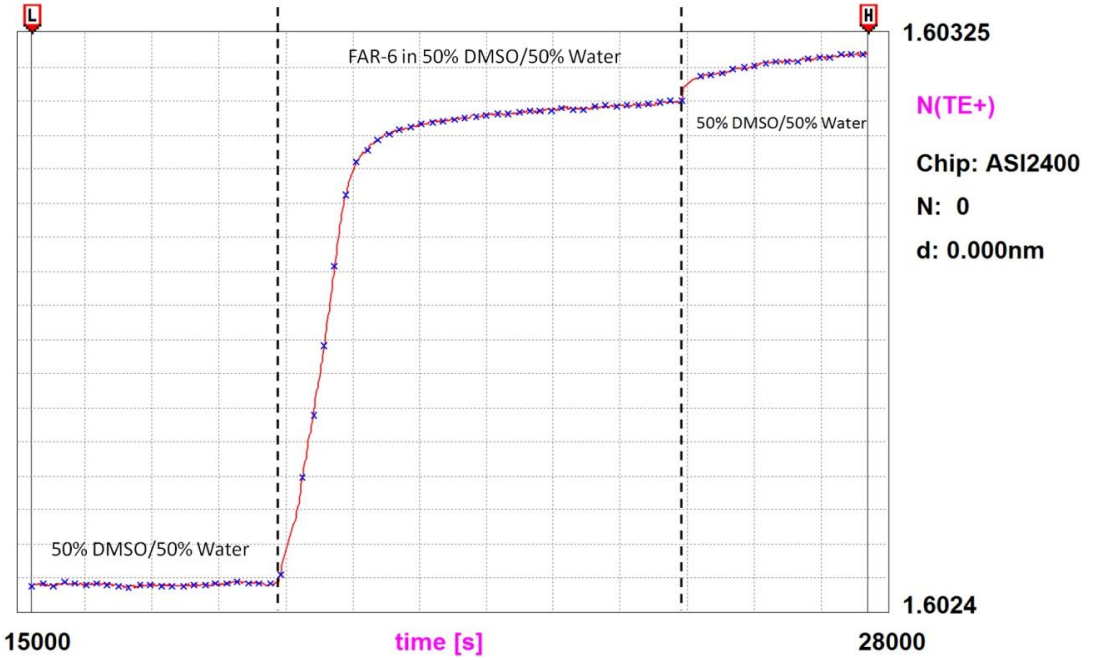

Figure 9.41 N(TE) vs time for FAR-6 (20 µm) deposition in 50% DMSO-50% water [Experimental code: 011007-1].

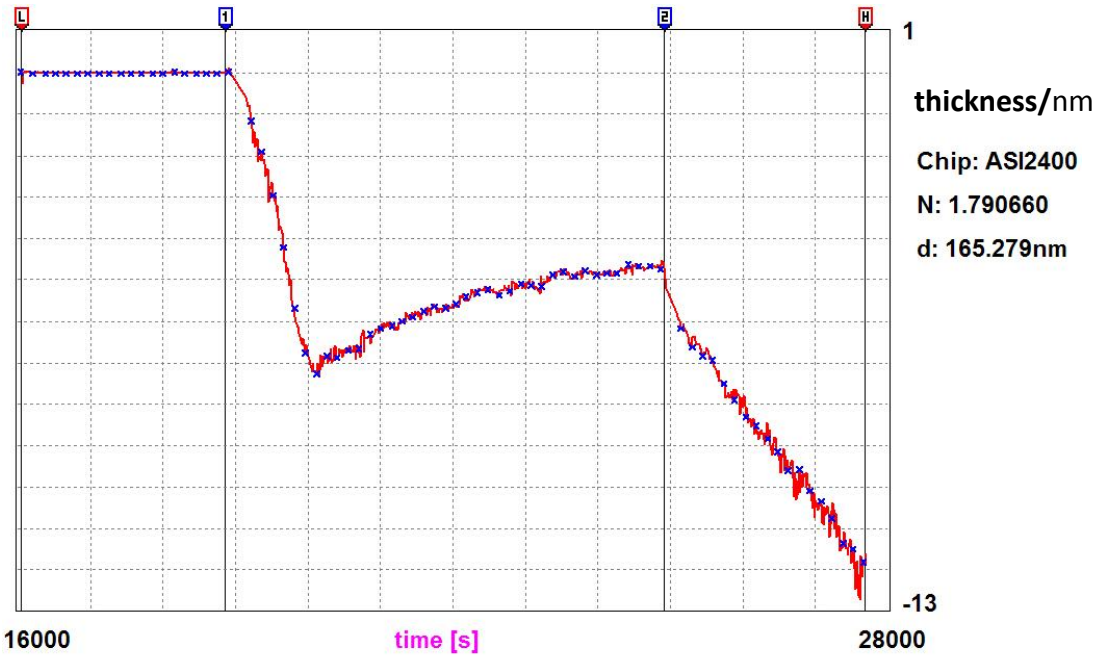

Figure 9.42 Thickness of 20 µM FAR -6 on 50% DMSO-50% water. Marker 1 is at the start of FAR-6 in adsorption on the waveguide in 50% DMSO-50% water; marker 2 is at the start of washing by 50% DMSO-50% water.

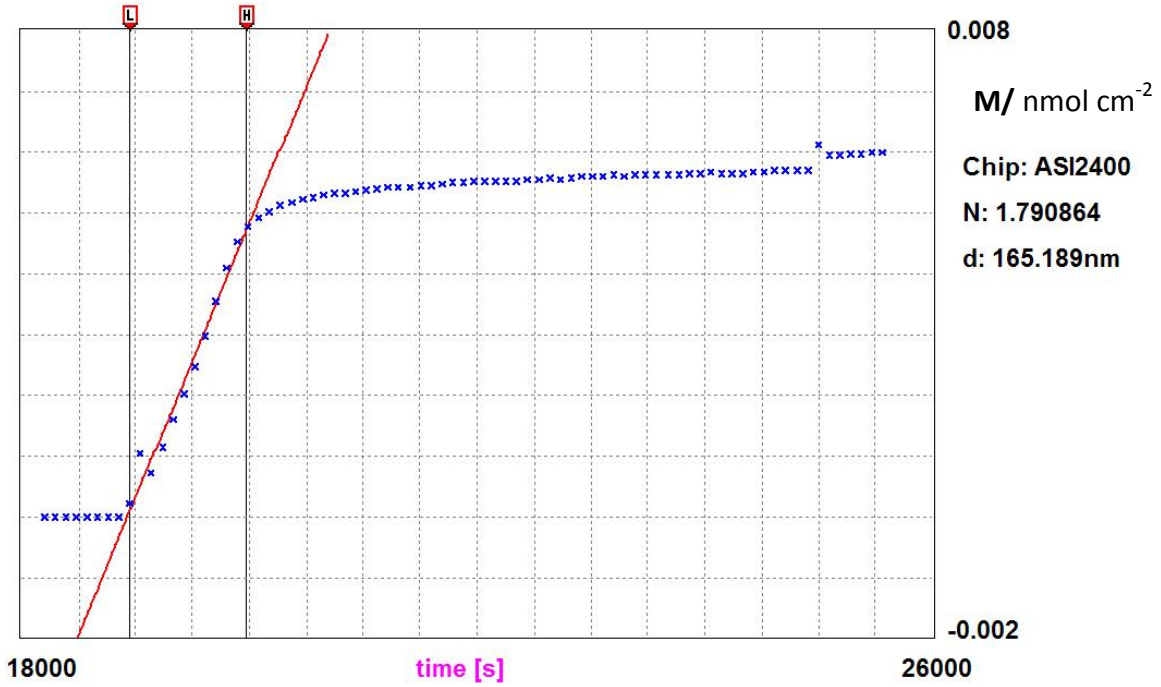

Figure 9.43 Mass vs time of 20 µM FAR -6 on 50% DMSO-50% water. The refractive index of 20 µM FAR-6 in 50% DMSO-50% water is 1.10946 and the refractive index of 50% DMSO-50% water is 1.40932, hence dn/dc=(1.40946 - 1.40932)/0.00002=7.

The detail of mechanism operating are likely to be quite complex, and we also have to take into account the strong propensity of the water to hydrogen-bond to the silica-titania substratum. Initial adsorption rate is 4.4×10^{-6} nmol $cm^{-2}s^{-1}$, M_{sat}=0.0056 nmol cm^{-2} and giving $k_a=2.2 \times 10^{-7}$ cm/s.

Figure 9.42 and 9.43 (thickness and mass) are calculated.

Features are

- Adsorption is indeed irreversible.
- The apparent mass increase after flooding with solvent and the dramatic thickness increase, suggest significant intralayer rearrangement. Maybe the assumption of isotropy is a poor one.
- Adsorption does not follow a random sequential mechanism.
- The plateau (saturation) mass is significantly (more than 30 %) less than in pure DMSO (only 0.0056 nmol cm^2, as opposed to 0.19 despite the irreversibility.

Chapter 10 Principal Conclusions

[Hypothesis 1]

All bacteria have a characteristic surface chemical signature (p. 3).

=>Evidence in Chapter 2.

[Hypothesis 2]

Bacterial interfacial energies are deducible from the adsorption kinetics (p. 26).

=>Evidence in Chapter 6.

[Hypothesis 3]

RSA describes bacterial adsorption (p. 61) (not in all case).

=>Evidence in Chapter6. Bacteria adsorb according to a random sequential addition process and the interaction can be well predicted by the appropriate equations. The rate of adsorption as characterized by the adsorption rate constant k_a is inversely proportional to the integral of the bacterium-substratum interfacial free energy ΔG_{123}. The results are correlatable with interfacial free energy predicted from saturated surface tension, considering that a fairly unsophisticated approximation approach was used in the calculations. Hence, we may be reasonably confident about expanding the approach to design new biomaterial surfaces for discriminating between different bacteria.

[Hypothesis 4]

If chemical and topographical features at least approximately match those of the bacterium surface, adhesion could be enhanced (or diminished) (p. 25). I.e., the lateral and normal interaction energy profiles between bacterium and substrate in Chapter 2 specifically match characteristic features on the bacterium, resulting in specific binding. No evidence adduced.

[Hypothesis 5]

Only one millionth of the nominal area of the bacterial surface interacts with a smooth planar substratum. (p. 101)

=> Evidence in Chapter 6; only one of at least three alternative explanations.

[Hypothesis 6]

Bacterial interfacial energies depend on and culture conditions and bacterium age. (p. 67) =>Evidence in Chapter 6

Organometallic complexes can be self-assembled to form a monolayer.

In summary

1. Bacterial adsorption displays well defined kinetics (follows random sequential adsorption).

2. The adsorption kinetics can be parametrized to provide a numerical representation.

3. The adsorption rate coefficient k_a is a key parameter that is related to the bacterial surface energy ΔG.

4. In order to identify an unknown bacterium, one should first create a database of k_a values for different substrata under different solution conditions. The strategy to identify the bacteria in an uncharacterized sample will be to establish the profile of adsorption parameters to a series of substrata; i.e., like the strategy of olfaction in mammals, for example.

5. A comparison of the ΔG values we derived from our measured k_a with published bacterial surface tension data reveals discrepancies, which raise the issue of how reliable are the published data. Inter alia they may depend on culture conditions, etc.

6. The minimum number of "standard" substrata needed to differentiate between different bacteria depends on what bacteria are anticipated to be present in the sample.

7. As well as using "standard" substrata (i.e., pure metal oxides) sophisticated "designer" substrata have been investigated with the ultimate aim of providing a greater variety of interfacial energies.

8. A further parameter extracted from the adsorption kinetics is the area a per bacterium. Simple RSA theory predicts that it should not change with the substratum and should moreover coincide with the area ā determined from micrography. The fact that it does not and it raises a variety of pertinent issues that will need resolution before advancing further in this direction.

9. Complex organometallic compound adlayer formation has been characterized.

My results are consistent with the main hypothesis (No. 1), according to which artificial nonbiological, possibly nanotextured, surfaces can selectively bind diverse bacteria, and hence differential binding can be used as the basis of strain identification. In use, an unknown sample would be exposed to a variety of nanotextured surfaces; the rest of those retaining them would be characteristic of the bacteria in the sample (cf. the mammalian olfactory system). The knowledge acquired through the fulfilment of this aim is also expected to be useful for designing surfaces that deliberately repel or attract bacteria.

There are some unexplained observations comparing bacterial adsorption in phosphate with other salts. This would need more extensive systematic investigation with other Hofmeister salts.

If Hypothesis 6 is correct, then the reliability of published interfacial energies for bacteria (see e.g. Table 2.1) is very questionable because insufficient details of culture, age, etc. are given.

Key contributions to knowledge

1. Quantitative analysis of bacterial adsorption including method development and data evaluation.
   1.1 Demonstration of applicability of RSA to bacterial adsorption.
   1.2 Demonstration that bacteria can selectively bind to different surfaces.
   1.3 Simple barrier model used for nano-objects NOT applicable to bacteria.
   1.4 Inverse correlation of a with ΔG_{123} demonstrated and explained.
   1.5 Evidence for variability of bacterial surface properties with age and culture conditions.

2. Elucidation of organometallic thin layer self-assembly
   2.1 Discovery of how to make a stable layer of certain organophosphine palladium complexs.

Chapter 11 Future Work

What I would like to have done had there been more time

Use the Langmuir trough for determining bacterial surface tension.

Systematic investigation of the efforts of different Hofmeister salts on bacterial adsorption.

Systematic investigation of the influence of the age of a bacterium on the surface properties.

Systematic investigation of the spread of surface properties within a culture population.

Systematic investigation of the effect of bulk bacterial concentration on adsorption behaviour.

More extensive investigation of adsorption/desorption of the complex organometallic (Kaleem Khosa) compounds at different water:DMSO ratios .

Analysis of nonexponential desorption kinetics of complex organometallic compounds.

Analysis of adlayer anisotropy of complex organometallic compounds.

Brownian dynamics of the complex organometallic compounds.

Interaction of bacteria with layers made from the Kaleem Khosa organometallic compounds.

Test Hypothesis 4.

Appendix A

List of abbreviations

AFM	Atomic Force Microscopy
DLVO	Derjaguin and Landau, Verwey and Overbeek
DMSO	Dimethyl Sulphoxide
EGCG	Epigallocatechin Gallate
ESEM	Environmental Scanning Electron Microscope
GBD	Generalized Ballistic Deposition
LPS	Lipopolysaccharide
MATS	Microbial adhesion to solvents
MATH	Microbial adhesion to hydrocarbons
OWLI	Optical Waveguide Lightmode Interferometry
OWLS	Optical Waveguide Lightmode Spectroscopy
PBS	Phosphate Buffered Saline
PCR	Polymerase Chain Reaction
RSA	Random Sequential Adsorption
S-layer	Surface Layer (specific protein layer of certain bacteria)
SCCM	Standard Cubic Centimeters per Minute
SEM	Scanning Electron Microscope
TE	Transverse Electric
TM	Transverse Magnetic
UTFA	Uniform Thin-Film Approximation

Appendix B

The standard four-layer mode equations for the determination of adlayer (n_A and d_A) (Máté and Ramsden, 1998):

$$n_A = n_C n_F N_{TM} R^{1/2} \tag{B.1}$$

and

$$d_A = \frac{(n_F^2 - n_C^2)\left[\lambda R_E - 2\pi d_F\left(n_F^2 - N_{TE}^2\right)^{1/2}\right]}{2\pi(n_A^2 - n_C^2)\left(n_F^2 - N_{TE}^2\right)^{1/2}} \tag{B.2}$$

where,

$$R = \frac{\left(n_F^2 - N_{TM}^2\right)^{1/2}\left[R_E - 2\pi d_F\left(n_F^2 - N_{TE}^2\right)^{1/2}/\lambda\right]}{D_1 - D_2 - D_3} \tag{B.3}$$

$$D_1 = \left(n_F^2 - N_{TE}^2\right)^{1/2}\left(N_{TM}^2 n_F^2 + N_{TM}^2 n_C^2 - n_F^2 n_C^2\right)R_M \tag{B.4}$$

$$D_2 = n_F^2\left(n_F^2 - N_{TM}^2\right)^{1/2}\left(N_{TM}^2 - n_C^2\right)R_M \tag{B.5}$$

$$D_3 = 2\pi d_F\left(n_F^2 - N_{TE}^2\right)^{1/2}\left(n_F^2 - N_{TM}^2\right)^{1/2} N_{TM}^2 n_C^2/\lambda \tag{B.6}$$

$$R_E = \tan^{-1}\left(\frac{N_{TE}^2 - n_S^2}{n_F^2 - N_{TE}^2}\right)^{1/2} + \tan^{-1}\left(\frac{N_{TE}^2 - n_C^2}{n_F^2 - N_{TE}^2}\right)^{1/2} \tag{B.7}$$

$$R_M = \tan^{-1}\left[\left(\frac{n_F}{n_S}\right)^2\left(\frac{N_{TM}^2 - n_S^2}{n_F^2 - N_{TM}^2}\right)^{1/2}\right] + \tan^{-1}\left[\left(\frac{n_F}{n_C}\right)^2\left(\frac{N_{TM}^2 - n_C^2}{n_F^2 - N_{TM}^2}\right)^{1/2}\right] \tag{B.8}$$

References

Acharya, G., Chang, C.-L. and Savran, C. (2006). An Optical Biosensor for Rapid and Label-Free Detection of Cells. *Journal of the American Chemical Society.* 128**,** p. 3862-3863.

Aggarwal, N., Lawson, K., Kershaw, M., Horvath, R. and Ramsden, J. (2009). Protein adsorption on heterogeneous surfaces. *Applied Physics Letters.* 94**,** p. 083110-3.

Al-Homoud, A. and Hondzo, M. (2008). Enhanced uptake of dissolved oxygen and glucose by *Escherichia coli* in a turbulent flow. *Applied Microbiology and Biotechnology.* 79**,** p. 643-655.

Alava, J. I., Garagorri, N., Briz, N. and Mendicute, J. (2005). Effects of bacterial adhesion with respect to the type of material, structure and design of intraocular lenses. *J Mater Sci Mater Med.* 16**,** p. 313-317.

Alcamo, I. E. (2001). *Fundamentals of microbiology,* Sudbury, Mass., Jones and Bartlett.

Allen, A. and Snary, D. (1972). The structure and function of gastric mucus. *Gut.* 13**,** p. 666-672.

Alverdi, V., Giovagnini, L., Marzano, C., Seraglia, R., Bettio, F., Sitran, S., Graziani, R. and Fregona, D. (2004). Characterization studies and cytotoxicity assays of Pt(II) and Pd(II) dithiocarbamate complexes by means of FT-IR, NMR spectroscopy and mass spectrometry. *Journal of Inorganic Biochemistry.* 98**,** p. 1117-1128.

Arnold, J. W., Boothe, D. H., Suzuki, O. and Bailey, G. W. (2004). Multiple imaging techniques demonstrate the manipulation of surfaces to reduce bacterial contamination and corrosion. *Journal of Microscopy.* 216**,** p. 215-221.

Aronson, A. I. and Fitz-James, P. (1976). Structure and morphogenesis of the bacterial spore coat. *Microbiol. Mol. Biol. Rev.,* 40**,** p. 360-402.

Ball, V. and Ramsden, J. J. (1997). Absence of Surface Exclusion in the First Stage of Lysozyme Adsorption Is Driven through Electrostatic Self-Assembly. *The Journal of Physical Chemistry B.* 101**,** p. 5465-5469.

Bansil, R. and Turner, B. S. (2006). Mucin structure, aggregation, physiological functions and biomedical applications. *Current opinion in colloid & interface science.* 11**,** p. 164-170.

Baveja, J. K., Willcox, M. D. P., Hume, E. B. H., Kumar, N., Odell, R. and Poole-Warren, L. A. (2004). Furanones as potential anti-bacterial coatings on biomaterials. *Biomaterials.* 25**,** p. 5003-5012.

Beis, K., Collins, R. F., Ford, R. C., Kamis, A. B., Whitfield, C. and Naismith, J. H. (2004). Three-dimensional Structure of Wza, the Protein Required for Translocation of Group 1 Capsular Polysaccharide across the Outer Membrane of *Escherichia coli*. *Journal of Biological Chemistry.* 279**,** p. 28227-28232.

Bellon-Fontaine, M. N., Rault, J. and van Oss, C. J. (1996). Microbial adhesion to solvents: a novel method to determine the electron-donor/electron-acceptor or Lewis acid-base properties of microbial cells. *Colloids and Surfaces B: Biointerfaces.* 7**,** p. 47-53.

Bernstein, J. M. and Reddy, M. (2000). Bacteria-mucin interaction in the upper aerodigestive tract shows striking heterogeneity: Implications in otitis media, rhinosinusitis, and pneumonia. *Otolaryngology - Head and Neck Surgery.* 122**,** p. 514-520.

Bertoluzza, A., Monti, P., Arciola, C. R. and Pizzoferrato, A. (1991). Structural properties and biocompatibility of polymers used in ophthalmology. *Clinical Materials.* 8**,** p. 165-169.

Bond, A. M. and Martin, R. L. (1984). Electrochemistry and redox behaviour of transition metal dithiocarbamates. *Coordination Chemistry Reviews.* 54**,** p. 23-98.

Briandet, R., Meylheuc, T., Maher, C. and Bellon-Fontaine, M. N. (1999). Listeria monocytogenes Scott A: Cell Surface Charge, Hydrophobicity, and Electron Donor and Acceptor Characteristics under Different Environmental Growth Conditions. *Appl. Environ. Microbiol.,* 65**,** p. 5328-5333.

Bromberg, L. E. and Barr, D. P. (2000). Self-Association of Mucin. *Biomacromolecules.* 1**,** p. 325-334.

Cacace, M. G., Landau, E. M. and Ramsden, J. J. (1997). The Hofmeister series: salt and solvent effects on interfacial phenomena. *Q Rev Biophys.* 30**,** p. 241-77.

Chada, V., Sanstad, E., Wang, R. and Driks, A. (2003). Morphogenesis of Bacillus spore surfaces. *J Bacteriol.* 185**,** p. 6255 - 6261.

Chien, H. H., Ma, K. J., Yeh, Y. P. and Liao, W. T. (2005). Fabrication of Microfluidic System by Hot Embossing and Selective Plasma Surface Modification Method. *International Symposium on Nano Bioengineering-Quantum Dots for Live Cells, in vivo Imaging, and Diagnostics.* Taiwan.

Clerc, D. and Lukosz, W. (1997). Real-time analysis of avidin adsorption with an integrated-optical output grating coupler: adsorption kinetics and optical anisotropy of adsorbed monomolecular layers. *Biosensors and Bioelectronics.* 12**,** p. 185-194.

Constable, E. C., Harverson, P. and Ramsden, J. J. (1997). Adsorption of ruthenadendrimers to silica–titania surfaces studied by optical waveguide lightmode spectroscopy (OWLS). *Chem. Commun.***,** p. 1683 - 1684.

Coupe, B., Evangelista, M. E., Yeung, R. M. and Chen, W. (2001). Surface Modification of Poly(tetrafluoroethylene-co-hexafluoropropylene) by Adsorption of Functional Polymers. *Langmuir.* 17**,** p. 1956-1960.

Cowie, J. M. G. and Toporowski, P. M. (1961). Association in The Binary Liquid System Dimethyl Sulphoxide - Water. *Canadian Journal of Chemistry.* 39**,** p. 2240-2243.

Csúcs, G. and Ramsden, J. J. (1998a). Generalized ballistic deposition of small buoyant particles. *The Journal of Chemical Physics.* 109**,** p. 779-781.

Csúcs, G. and Ramsden, J. J. (1998b). Solubilization of planar bilayers with detergent. *Biochimica et Biophysica Acta (BBA) - Biomembranes.* 1369**,** p. 304-308.

Curtis, A. (2004). Tutorial on the biology of nanotopography. *NanoBioscience, IEEE Transactions on.* 3**,** p. 293-295.

Curtis, A. and Wilkinson, C. (1997). Topographical control of cells. *Biomaterials.* 18**,** p. 1573-1583.

Curtis, A. and Wilkinson, C. (2001). Nantotechniques and approaches in biotechnology. *Trends in Biotechnology.* 19**,** p. 97-101.

Deisingh, A. K. and Thompson, M. (2004). Biosensors for The Detection of Bacteria. *Canadian Journal of Microbiology.* 50**,** p. 69-77.

Diaz, C., Cortizo, M. C., Schilardi, P. L., Saravia, S. G. G. D. and Mele, M. A. F. L. D. (2007). Inluence of the Nano-micro Structure of the Surface on Bacterial Adhesion. *Materials Research.* 10**,** p. 11-14.

Duc, L., Hong, H., Fairweather, N., Ricca, E. and Cutting, S. (2003). Bacterial spores as vaccine vehicles. *Infect Immun.* 71**,** p. 2810 - 2818.

Edwards, K. J. and Rutenberg, A. D. (2001). Microbial response to surface microtopography: the role of metabolism in localized mineral dissolution. *Chemical Geology.* 180**,** p. 19-32.

F.S Colwell, T. C. O., M.E Delwiche, D Chandler, J.K Fredrickson, Q.-J Yao, J.P Mckinley, D.R Boone, R Griffiths, T.J Phelps, D Ringelberg, D.C White, L Lafreniere, D Balkwill, R.M Lehman, J Konisky, P.E Long, (1997). Microorganisms from deep, high temperature sandstones: constraints on microbial colonization. *FEMS Microbiology Reviews.* 20**,** p. 425-435.

Faraglia, G., Fregona, D., Sitran, S., Giovagnini, L., Marzano, C., Baccichetti, F., Casellato, U. and Graziani, R. (2001). Platinum(II) and palladium(II) complexes with dithiocarbamates and amines: synthesis, characterization and cell assay. *Journal of Inorganic Biochemistry.* 83**,** p. 31-40.

Feijter, J. A. D., Benjamins, J. and Veer, F. A. (1978). Ellipsometry as a tool to study the adsorption behavior of synthetic and biopolymers at the air-water interface. *Biopolymers.* 17**,** p. 1759-1772.

Fleminger, G. and Shabtai, Y. (1995). Direct and Rapid Analysis of the Adhesion of Bacteria to Solid Surfaces: Interaction of Fluorescently Labeled Rhodococcus Strain GIN-1 (NCIMB 40340) Cells with Titanium-Rich Particles. *Appl Environ Microbiol.* 61**,** p. 4357-4361.

Fux, C. A., Costerton, J. W., Stewart, P. S. and Stoodley, P. (2005). Survival strategies of infectious biofilms. *Trends in Microbiology.* 13**,** p. 34-40.

Gfeller, K. Y., Nugaeva, N. and Hegner, M. (2005). Rapid Biosensor for Detection of Antibiotic-Selective Growth of *Escherichia coli*. *Appl. Environ. Microbiol.,* 71**,** p. 2626-2631.

Gladstone, J. H. (1896). The Relation between the Refraction of the Elements and Their Chemical Equivalents. *Proceedings of the Royal Society of London.* 60**,** p. 140-146.

Good, N. E., Winget, G. D., Winter, W., Connolly, T. N., Izawa, S. and Singh, R. M. M. (1966). Hydrogen Ion Buffers for Biological Research*. *Biochemistry.* 5**,** p. 467-477.

Gould, G. W., Stubbs, J. M. and King, W. L. (1970). Structure and Composition of Resistant Layers in Bacterial Spore Coats. *J Gen Microbiol.* 60**,** p. 347-355.

Grossman, H. L., Myers, W. R., Vreeland, V. J., Bruehl, R., Alper, M. D., Bertozzi, C. R. and Clarke, J. (2004). Detection of bacteria in suspension by using a superconducting quantum interference device. *Proceedings of the National Academy of Sciences of the United States of America.* 101**,** p. 129-134.

Haake, H. M., Schütz, A. and Gauglitz, G. (2000). Label-free detection of biomolecular interaction by optical sensors. *Fresenius' Journal of Analytical Chemistry.* 366**,** p. 576-585.

Hammond, E. and Lundberg, W. (1954). Molar refraction, molar volume, and refractive index of fatty acid esters and related compounds in the liquid state. *Journal of the American Oil Chemists' Society.* 31**,** p. 427-432.

Hanisch, F.-G. and Muller, S. (2000). MUC1: the polymorphic appearance of a human mucin. *Glycobiology.* 10**,** p. 439-449.

Harris, L. G., Tosatti, S., Wieland, M., Textor, M. and Richards, R. G. (2004). Staphylococcus aureus adhesion to titanium oxide surfaces coated with non-functionalized and peptide-functionalized poly(-lysine)-grafted-poly(ethylene glycol) copolymers. *Biomaterials.* 25**,** p. 4135-4148.

Healy, T. W. and White, L. R. (1978). Ionizable surface group models of aqueous interfaces. *Advances in Colloid and Interface Science.* 9**,** p. 303-345.

Henriques, A. and Moran, C. (2000). Structure and assembly of the bacterial endospore coat. *Methods, a Companion to Methods in Enzymology.* 20**,** p. 95 - 110.

Hermansson, M. (1999). The DLVO Theory in Microbial Adhesion. *Colloids and Surfaces B: Biointerfaces.* 14**,** p. 105-119.

Hillman, H. (2009). Procedures used in modern cell biology ignore natural laws *The Journal of Biological Physics and Chemistry.* 9(3)**,** p. 130-135.

Horváth, R., McColl, J., Yakubov, G. E. and Ramsden, J. J. (2008). Structural hysteresis and hierarchy in adsorbed glycoproteins. *The Journal of Chemical Physics.* 129**,** p. 071102.

Horváth, R., Pedersen, H. C., Skivesen, N., Selmeczi, D. and Larsen, N. B. (2003). Optical waveguide sensor for on-line monitoring of bacteria. *Opt. Lett.,* 28**,** p. 1233-1235.

Howell, S. W., Inerowicz, H. D., Regnier, F. E. and Reifenberger, R. (2003). Patterned Protein Microarrays for Bacterial Detection. *Langmuir.* 19**,** p. 436-439.

Hug, T. S. (2000). Optical Waveguide Lightmode Spectroscopy as a Biosensor to Monitor Adhesion and Metabolic State of Anchorage-dependent Cells. *SWISS FEDERAL INSTITUTE OF TECHNOLOGY ZURICH (ETHZ)* Switzerland, SWISS FEDERAL INSTITUTE OF TECHNOLOGY ZURICH (ETHZ)

Ikigai, H., Nakae, T., Hara, Y. and Shimamura, T. (1993). Bactericidal catechins damage the lipid bilayer. *Biochimica et Biophysica Acta (BBA) - Biomembranes.* 1147**,** p. 132-136.

Ivnitski, D., Abdel-Hamid, I., Atanasov, P. and Wilkins, E. (1999). Biosensors for Detection of Pathogenic Bacteria. *Biosensors and Bioelectronics.* 14**,** p. 599-624.

Jin, F.-L., Kim, H.-Y. and Park, S.-J. (2007). Effect of fluorine functional groups on surface and mechanical interfacial properties of epoxy resins. *Journal of Fluorine Chemistry.* 128**,** p. 184-189.

Johnson, F. H. and Harvey, E. N. (1937). The osmotic and surface properties of marine luminous bacteria. *Journal of Cellular and Comparative Physiology.* 9**,** p. 363-380.

Kessler, D. and Theato, P. (2009). Reactive Surface Coatings Based on Polysilsesquioxanes: Defined Adjustment of Surface Wettability. *Langmuir.* 25**,** p. 14200-14206.

Kolari, M., Schmidt, U., Kuismanen, E. and Salkinoja-Salonen, M. S. (2002). Firm but Slippery Attachment of Deinococcus geothermalis. *J. Bacteriol.,* 184**,** p. 2473-2480.

Kotra, L. P., Golemi, D., Amro, N. A., Liu, G. Y. and Mobashery, S. (1999). Dynamics of the lipopolysaccharide assembly on the surface of *Escherichia coli*. *Journal of the American Chemical Society.* 121**,** p. 8707-8711.

Kurrat, R., Ramsden, J. J. and Prenosil, J. E. (1994). Kinetic model for serum albumin adsorption : experimental verification. *J. Chem. Soc., Faraday Trans.,* 90**,** p. 587-590.

Lau, K. K. S., Bico, J., Teo, K. B. K., Chhowalla, M., Amaratunga, G. A. J., Milne, W. I., Mckinley, G. H. and Gleason, K. K. (2003). Superhydrophobic Carbon Nanotube Forests. *Nano Letters.* 3**,** p. 1701-1705.

Levich, V. G. (1962). *Physicochemical Hydrodynamics,* Englewood Cliffs, New Jersey, Prentice-Hall.

Liao, S., Kao, Y.-H. and Hiipakka, R. A. (2001). Green tea: Biochemical and biological basis for health benefits. In: *Vitamins & Hormones,* edited., Academic Press, p. 1-94.

Liao, S., Umekita, Y., Guo, J., Kokontis, J. M. and Hiipakka, R. A. (1995). Growth inhibition and regression of human prostate and breast tumors in athymic mice by tea epigallocatechin gallate. *Cancer Letters.* 96**,** p. 239-243.

Lower, S. K., Tadanier, C. J. and Hochella, M. F. (2000). Measuring interfacial and adhesion forces between bacteria and mineral surfaces with biological force microscopy. *Geochimica et Cosmochimica Acta.* 64**,** p. 3133-3139.

Lukosz, W. (1995). Integrated optical chemical and direct biochemical sensors. *Sensors and Actuators B: Chemical.* 29**,** p. 37-50.

Lukosz, W., Nellen, P. M. and Tiefenthaler, K. (1988). Integrated optical input grating couplers as biochemical sensors. *Sensors and Actuators.* 15**,** p. 285-295.

Macgregor, W. S. (1967). The chemical and physical properties of DMSO. *Annals of the New York Academy of Sciences.* 141**,** p. 3-12.

Magnani, A., Priamo, A., Pasqui, D. and Barbucci, R. (2003). Cell behaviour on chemically microstructured surfaces. *Materials Science and Engineering: C.* 23**,** p. 315-328.

Mann, E. K. (2001). Evaluating Optical Techniques for Determining Film Structure: Optical Invariants for Anisotropic Dielectric Thin Films. *Langmuir.* 17**,** p. 5872-5881.

Mann, E. K., Heinrich, L. and Schaaf, P. (1997). Validity of the Uniform Thin-Film Approximation for the Optical Analysis of Particulate Films. *Langmuir.* 13**,** p. 4906-4909.

Martin, D., Weise, A. and Niclas, H.-J. (1967). The Solvent Dimethyl Sulfoxide. *Angewandte Chemie International Edition in English.* 6**,** p. 318-334.

Máté, M. and Ramsden, J. J. (1998). Addition of Particles of Alternating Charge. *J. Chem. Soc., Faraday Trans.,* 94**,** p. 2813 - 2816.

McColl, J., Yakubov, G. E. and Ramsden, J. J. (2007). Complex Desorption of Mucin from Silica. *Langmuir.* 23**,** p. 7096-7100.

McColl, J., Yakubov, G. E. and Ramsden, J. J. (2008). Temperature Dependence of Mucin Adsorption. *Langmuir.* 24**,** p. 902-905.

Meinders, J. M., van der Mei, H. C. and Busscher, H. J. (1995). Deposition Efficiency and Reversibility of Bacterial Adhesion under Flow. *Journal of Colloid and Interface Science.* 176**,** p. 329-341.

Mentré, P. (2004). Interfacial water: a modulator of biological activity *Journal of Biological Physics and Chemistry.* 4**,** p. 115-123.

Mital, R., Jain, N. and Srivastava, T. S. (1989). Synthesis, characterization and cytotoxic studies of diamine and diimine palladium(II) complexes of diethyldithiocarbamate and binding of these and analogous platinum(II) complexes with DNA. *Inorganica Chimica Acta.* 166**,** p. 135-140.

Nagao, P. E. and Benchetrit, L. C. (1999). Virulent and Avirulent Strains of Group B Streptococci from Rio de Janeiro, Brazil: Relationship between Differences in Surface Hydrophobicity, Sialic Acid Content and Macrophage Interaction. *Memóias do Instituto Oswaldo Cruz.* 94**,** p. 497-498.

Nakajima, A., Fujishima, A., Hashimoto, K. and Watanabe, T. (1999). Preparation of Transparent Superhydrophobic Boehmite and Silica Films by Sublimation of Aluminum Acetylacetonate. *Advanced Materials.* 11**,** p. 1365-1368.

Nellen, P. M. and Lukosz, W. (1990). Integrated optical input grating couplers as chemo- and immunosensors. *Sensors and Actuators B: Chemical.* 1**,** p. 592-596.

Nellen, P. M. and Lukosz, W. (1991). Model experiments with integrated optical input grating couplers as direct immunosensors. *Biosensors and Bioelectronics.* 6**,** p. 517-525.

Neu, T. (1996). Significance of bacterial surface-active compounds in interaction of bacteria with interfaces. *Microbiol. Rev.,* 60**,** p. 151-166.

Nicholson, W. (2002). Roles of Bacillus endospores in the environment. *Cell Mol Life Sci.* 59**,** p. 410 - 416.

Nicholson, W., Munakata, N., Horneck, G., Melosh, H. and Setlow, P. (2000). Resistance of Bacillus endospores to extreme terrestial and extraterrestrial environments. *Microbiol Mol Biol Rev.* 64**,** p. 548 - 572.

Ong, Y.-L., Razatos, A., Georgiou, G. and Sharma, M. M. (1999). Adhesion Forces between E. coli Bacteria and Biomaterial Surfaces. *Langmuir.* 15**,** p. 2719-2725.

Otto, K. (2008). Biophysical approaches to study the dynamic process of bacterial adhesion. *Research in Microbiology.* 159**,** p. 415-422.

Otto, K., Elwing, H. and Hermansson, M. (1999). Effect of Ionic Strength on Initial Interactions of *Escherichia coli* with Surfaces, Studied On-Line by a Novel Quartz Crystal Microbalance Technique. *J. Bacteriol.,* 181**,** p. 5210-5218.

Paul Messner, G. A., Christina Schäffer, Thomas Wugeditsch, Sylvie Lortal, Helmut König, Ruth Niemetz, Maria Dorner (1997). III. Biochemistry of S-layers. *FEMS Microbiology Reviews.* 20**,** p. 25-46.

Pelczar, M. J., Chan, E. C. S. and Krieg, N. R. (1993). *Microbiology : concepts and applications,* New York; London, McGraw-Hill.

Pelletier, C., Bouley, C., Cayuela, C., Bouttier, S., Bourlioux, P. and Bellon-Fontaine, M. (1997). Cell surface characteristics of *Lactobacillus casei subsp. casei*, *Lactobacillus paracasei subsp. paracasei*, and *Lactobacillus rhamnosus* strains. *Appl. Environ. Microbiol.,* 63**,** p. 1725-1731.

Rammler, D. H. and Zaffaroni, A. (1967). Biological implications of DMSO based on a review of its chemical properties. *Annals of the New York Academy of Sciences.* 141**,** p. 13-23.

Ramsden, J. J. (1993). Review of new experimental techniques for investigating random sequential adsorption. *Journal of Statistical Physics.* 73**,** p. 853-877.

Ramsden, J. J. (1994). Experimental methods for investigating protein adsorption kinetics at surfaces. *Q Rev Biophys.* 27**,** p. 41-105.

Ramsden, J. J. (1997). Optical biosensors. *Journal of Molecular Recognition.* 10**,** p. 109-120.

Ramsden, J. J. (1998). Kinetics of Protein Adsorption. In: *Biopolymers At Interfaces,* edited by Malmsten, M. 1st ed., Marcel Dekker, p. 322-361.

Ramsden, J. J. (2006). From Kinetics to Structure: High Resolution Molecular Microscopy. In: *Proteins at Solid-Liquid Interfaces,* edited by Déjardin, P., Heidelberg: Springer-Verlag, p. 23-49.

Ramsden, J. J. (2008). *Biomedical Surfaces*, Artech House Publishers.

Ramsden, J. J. (2009). *Bioinformatics: An Introduction, 2nd Edn.*, Springer.

Ramsden, J. J., Li, S.-Y., Heinzle, E. and Prenosil, J. E. (1995). Optical method for measurement of number and shape of attached cells in real time. *Cytometry.* 19**,** p. 97-102.

Ramsden, J. J. and Máté, M. (1998). Kinetics of monolayer particle deposition. *J. Chem. Soc., Faraday Trans.,* 94**,** p. 783 - 788.

Razatos, A., Ong, Y.-L., Sharma, M. M. and Georgiou, G. (1998). Molecular determinants of bacterial adhesion monitored by atomic force microscopy. *Proceedings of the National Academy of Sciences of the United States of America.* 95**,** p. 11059-11064.

Razatos, A., Ong, Y. L., Boulay, F., Elbert, D. L., Hubbell, J. A., Sharma, M. M. and Georgiou, G. (2000). Force Measurements between Bacteria and Poly(ethylene glycol)-Coated Surfaces. *Langmuir.* 16**,** p. 9155-9158.

Reid, G., Mei, H. C., Tieszer, C. and Busscher, H. J. (1996). Uropathogenic *Escherichia coli* adhere to urinary catheters without using fimbriae. *FEMS Immunology & Medical Microbiology.* 16**,** p. 159-162.

Reinhard Rachel, D. P., Jan 0160marda, Jan Šmarda, Jir0131769 Komrska, Vladislav Krzyzáek, Gertraud Rieger, Karl O Stetter, (1997). II. Fine structure of S-layers. *FEMS Microbiology Reviews.* 20**,** p. 13-23.

Ricca, E. and Cutting, S. (2003). Emerging Applications of Bacterial Spores in Nanobiotechnology. *Journal of Nanobiotechnology.* 1**,** p. 6.

Ricci, S. M., Talbot, J., Tarjus, G. and Viot, P. (1992). Random sequential adsorption of anisotropic particles. II. Low coverage kinetics. *The Journal of Chemical Physics.* 97**,** p. 5219-5228.

Rijnaarts, H. H. M., Norde, W., Bouwer, E. J., Lyklema, J. and Zehnder, A. J. B. (1993). Bacterial Adhesion under Static and Dynamic Conditions. *Appl. Environ. Microbiol.,* 59**,** p. 3255-3265.

Rosenberg, M., Gutnick, D. and Rosenberg, E. (1980). Adherence of bacteria to hydrocarbons: A simple method for measuring cell-surface hydrophobicity. *FEMS Microbiology Letters.* 9**,** p. 29-33.

S. Chumakov, C. Belapurkar, C. Putonti, T.-B. Li, B. M. Pettitt, G. E. Fox, Willson, R. C. and Fofanov, Y. (2005). The Theoretical Basis of Universal Identification Systems For Bacteria And Viruses. *Journal of Biological Physics and Chemistry.* 5(4)**,** p. 121-128.

Sára, M. and Sleytr, U. B. (1996). Crystalline bacterial cell surface layers (S-layers): From cell structure to biomimetics. *Progress in Biophysics and Molecular Biology.* 65**,** p. 83-111.

Satriano, C., Messina, G. M. L., Carnazza, S., Guglielmino, S. and Marletta, G. (2006). Bacterial adhesion onto nanopatterned polymer surfaces. *Materials Science and Engineering: C.* 26**,** p. 942-946.

Satyaprasad, A., Jain, V. and Nema, S. K. (2007). Deposition of superhydrophobic nanostructured Teflon-like coating using expanding plasma arc. *Applied Surface Science.* 253**,** p. 5462-5466.

Sayre, R. (1964). The Molar Refraction of Liquid Organosilicon Compounds. *Journal of Chemical & Engineering Data.* 9**,** p. 146-153.

Schaaf, P. and Talbot, J. (1989). Surface exclusion effects in adsorption processes. *The Journal of Chemical Physics.* 91**,** p. 4401-4409.

Schar-Zammaretti, P. and Ubbink, J. (2003). The Cell Wall of Lactic Acid Bacteria: Surface Constituents and Macromolecular Conformations. *Biophys. J.,* 85**,** p. 4076-4092.

Schuster, B. and Sleytr, U. B. (2000). S-layer-supported lipid membranes. *Reviews in Molecular Biotechnology.* 74**,** p. 233-254.

Schwarz-Linek, U., Werner, J. M., Pickford, A. R., Gurusiddappa, S., Kim, J. H., Pilka, E. S., Briggs, J. A. G., Gough, T. S., Hook, M., Campbell, I. D. and Potts, J. R. (2003). Pathogenic bacteria attach to human fibronectin through a tandem [beta]-zipper. *Nature.* 423**,** p. 177-181.

Shaheen, F., Badshah, A., Gielen, M., Dusek, M., Fejfarova, K., De Vos, D. and Mirza, B. (2007a). Synthesis, characterization, antibacterial and cytotoxic activity of new palladium(II) complexes with dithiocarbamate ligands: X-ray structure of bis(dibenzyl-1-S:S'-dithiocarbamato)Pd(II). *Journal of Organometallic Chemistry.* 692**,** p. 3019-3026.

Shaheen, F., Badshah, A., Gielen, M., Gieck, C. and Vos, D. D. (2007b). Synthesis, characterization and *in vitro* cytotoxicity of palladium(II) complexes with mixed ligands. X-ray diffraction study of $C_{31}H_{36}ClNPPdS_2$. *Applied Organometallic Chemistry.* 21**,** p. 633-640.

Shang, H. M., Wang, Y., Limmer, S. J., Chou, T. P., Takahashi, K. and Cao, G. Z. (2005). Optically transparent superhydrophobic silica-based films. *Thin Solid Films.* 472**,** p. 37-43.

Slomiany, B. L., Murty, V. L. N., Piotrowski, J. and Slomiany, A. (1996). Salivary mucins in oral mucosal defense. *General Pharmacology: The Vascular System.* 27**,** p. 761-771.

Spielman, L. A. and Friedlander, S. K. (1974). Role of the electrical double layer in particle deposition by convective diffusion. *Journal of Colloid and Interface Science.* 46**,** p. 22-31.

Spina, M., Cuccioloni, M., Mozzicafreddo, M., Montecchia, F., Pucciarelli, S., Eleuteri, A. M., Fioretti, E. and Angeletti, M. (2008). Mechanism of inhibition of wt-dihydrofolate reductase from *E. coli* by tea epigallocatechin-gallate. *Proteins: Structure, Function, and Bioinformatics.* 72**,** p. 240-251.

Swientoslawski, W. (1920). Atomic Refraction. *Journal of the American Chemical Society.* 42**,** p. 1945-1951.

Tadanaga, K., Katata, N. and Minami, T. (1997). Formation Process of Super-Water-Repellent Al_2O_3 Coating Films with High Transparency by the Sol-Gel Method. *Journal of the American Ceramic Society.* 80**,** p. 3213-3216.

Talbot, J. (1996). Time dependent desorption: A memory function approach. *Adsorption.* 2**,** p. 89-94.

Terrance J Beveridge, P. H. P., Margit Sára, Anja Kotiranta, Kari Lounatmaa, Kirsti Kari, Eero Kerosuo, Markus Haapasalo, Eva M Egelseer, Ingrid Schocher, Uwe B Sleytr, Lorenzo Morelli, Maria-Luisa Callegari, John F Nomellini, Wade H Bingle, John Smit, Emmanuelle Leibovitz, Marc Lemaire, Isabelle Miras, Sylvie Salamitou, Pierre Béguin [I] , Hélène Ohayon, Pierre Gounon, Markus Matuschek, Kerstin Sahm, Hubert Bahl, Rosemary Grogono-Thomas, Joel Dworkin, Martin J Blaser, Ralph M Woodland, Diane G Newell, Martin Kessel, Susan F Koval (1997). V. Functions of S-layers. *FEMS Microbiology Reviews.* 20**,** p. 99-149.

Tiefenthaler, K. and Lukosz, W. (1989). Sensitivity of grating couplers as integrated-optical chemical sensors. *J. Opt. Soc. Am. B.* 6**,** p. 209-220.

Tien, P. K. (1977). Integrated optics and new wave phenomena in optical waveguides. *Reviews of Modern Physics.* 49**,** p. 361.

Torimura, M., Ito, S., Kano, K., Ikeda, T., Esaka, Y. and Ueda, T. (1999). Surface characterization and on-line activity measurements of microorganisms by capillary zone electrophoresis. *Journal of Chromatography B: Biomedical Sciences and Applications.* 721**,** p. 31-37.

Uwe B Sleytr (1997). I. Basic and applied S-layer research: an overview. *FEMS Microbiology Reviews.* 20**,** p. 5-12.

van der Mei, H. C., Bos, R. and Busscher, H. J. (1998). A reference guide to microbial cell surface hydrophobicity based on contact angles. *Colloids and Surfaces B: Biointerfaces.* 11**,** p. 213-221.

van der Mei, H. C., van De Belt-Gritter, B., Reid, G., Bialkowska-Hobrzanska, H. and Busscher, H. J. (1997). Adhesion of coagulase-negative staphylococci grouped according to physico-chemical surface properties. *Microbiology.* 143**,** p. 3861-3870.

van Houdt, R. and Michiels, C. W. (2005). Role of bacterial cell surface structures in *Escherichia coli* biofilm formation. *Research in Microbiology.* 156**,** p. 626-633.

van Loosdrecht, M. C. M., Norde, W. and Zehnder, A. J. B. (1990). Physical Chemical Description of Bacterial Adhesion. *J Biomater Appl.* 5**,** p. 91-106.

van Oss, C. J. (1997). Hydrophobicity and hydrophilicity of biosurfaces. *Current opinion in colloid & interface science* 2**,** p. 503-512.

van Oss, C. J. (2006). *Interfacial Forces in Aqueous Media, 2nd Edition.* CRC Press.

van Oss, C. J., Docoslis, A., Wu, W. and Giese, R. F. (1999). Influence of macroscopic and microscopic interactions on kinetic rate constants - I. Role of the extended DLVO theory in determining the kinetic adsorption constant of proteins in aqueous media, using von Smoluchowski's approach. *Colloids and Surfaces B: Biointerfaces.* 14**,** p. 99-104.

van Oss, C. J., Ju, L., Chaudhury, M. K. and Good, R. J. (1989). Estimation of the polar parameters of the surface tension of liquids by contact angle measurements on gels. *Journal of Colloid and Interface Science.* 128**,** p. 313-319.

Vilain, S. and Brozel, V. S. (2006). Multivariate Approach to Comparing Whole-Cell Proteomes of Bacillus cereus Indicates a Biofilm-Specific Proteome. *Journal of Proteome Research.* 5**,** p. 1924-1930.

Viot, P., Tarjus, G., Ricci, S. M. and Talbot, J. (1992). Random sequential adsorption of anisotropic particles. I. Jamming limit and asymptotic behavior. *The Journal of Chemical Physics.* 97**,** p. 5212-5218.

Vörös.J., Ramsden, J. J., Csúcs, G., Szendro, I., De Paul, S. M., Textor, M. and Spencer, N. D. (2002). Optical grating coupler biosensors. *Biomaterials.* 23**,** p. 3699-3710.

Walker, S. L., Redman, J. A. and Elimelech, M. (2004). Role of Cell Surface Lipopolysaccharides in *Escherichia coli* K12 Adhesion and Transport. *Langmuir.* 20**,** p. 7736-7746.

Wang, J. and Wang, L. (2006). The lower surface free energy achievements from ladder polysilsesquioxanes with fluorinated side chains. *Journal of Fluorine Chemistry.* 127**,** p. 287-290.

Webster, T. J., Liu, J. X. and Banks, M. K. (2004). More Efficient Capture of Bacteria on Nanostructured Materials IN Cato T. Laurencin and Botchwey, E. A. (Eds.) *Nanoscale Materials Science in Biology and Medicine.* MRS Proceedings.

Wiencek, K. and Fletcher, M. (1995). Bacterial adhesion to hydroxyl- and methyl-terminated alkanethiol self- assembled monolayers. *J. Bacteriol.,* 177**,** p. 1959-1966.

Wiggins, P. M. (2002). Enzyme reactions and two-state water. *Journal of Biological Physics and Chemistry.* 2**,** p. 25-37.

Wong, J. Y., Leach, J. B. and Brown, X. Q. (2004). Balance of chemistry, topography, and mechanics at the cell-biomaterial interface: Issues and challenges for assessing the role of substrate mechanics on cell response. *Surface Science.* 570**,** p. 119-133.

Y.F. Missirlis and Katsikogianni, M. (2004). Concise Review of Mechanisms of Bacterial Adhesion to Biomaterials and of Techniques Used in Estimating Bacteria-Material Interactions. *Eur Cell Mater.* 8**,** p. 37-57.

Yang, C. S. and Wang, Z.-Y. (1993). Tea and Cancer. *J. Natl. Cancer Inst.,* 85**,** p. 1038-1049.